Crystal Plasticity Finite Element Simulation of Deformation and Fracture in Polycrystalline Microstructures

by

Ahmad Shahba

A dissertation submitted to The Johns Hopkins University in conformity with the requirements for the degree of Doctor of Philosophy.

Baltimore, Maryland

September, 2018

Abstract

The mechanical response of metals and their alloys are governed by the deformation mechanisms in the underlying microstructure. High-fidelity modeling of deformation in metals requires development of proper constitutive laws at single crystal scale. Image-based crystal plasticity FE framework is regarded as one of the most powerful tools for deformation simulations, allowing the modelers to explicitly represent the elastic and plastic anisotropy of the material using physics-based laws in a computational domain which statistically represents the morphological and crystallographic properties of the microstructure.

In this work, a thermodynamically-consistent coupled crystal plasticity-crack phase field framework is derived to model fracture prcoess in polycrystalline microstructures. The governing differential equations for the displacement and crack phase field are coupled via the Helmholtz free energy density (HFED). Using the volumetric-deviatoric decomposition of the elastic deformation gradient, a new HFED formulation is proposed which respects the unilateral damage conditions (tension-compression asymmetry of material response in the presence of cracks) and can be used for mod-

eling fracture in anisotropic media under finite deformation conditions.

Numerical modeling of fracture is computationally daunting, partly due to the frequent convergence issues and occurrence of instabilities. Recognizing that the instabilities take place due to an excess energy, three viscous stabilization methods are proposed in this work to dissipate this excess energy and effectively overcome the instabilities. Unlike arc-length methods, the viscous stabilization is applicable for rate-dependent constitutive models and its implementation into any existing FE code is straightforward.

Crystal plasticity simulations of polycrystalline are generally carried out with linear tetrahedral elements due to their capability in conforming to complex geometries. These elements are known to suffer from volumetric locking in modeling (nearly-) incompressible materials, leading to numerical artifacts such as underestimation of displacements and overestimation of pressure levels. A modified F-bar-patch technique is developed in this work to alleviate volumetric locking in phase field modeling of ductile fracture.

In the course of plastic deformation, the local strain rate experienced by different material points in the microstructure could be orders of magnitude different from the applied macroscopic strain rate. It is of paramount significance to develop a unified crystal plasticity law which could be applied for a wide range of strain rates. Using the dislocation glide mechanisms in *hcp* metals, a unified flow rule is developed by combining the thermally-activated and drag-dominated processes. This unified law

can be employed to model deformation over a wide range of strain rates and its explicit dependence of temperature makes it suitable for modeling high rate deformation of metals where adiabatic heating is significant.

Thesis Committee

Professor Somnath Ghosh (Primary Advisor)

Departments of Civil and Mechanical Engineering

Johns Hopkins Whiting School of Engineering

Professor Todd C. Hufnagel

Department of Material Science and Engineering

Johns Hopkins Whiting School of Engineering

Professor James K. Guest

Department Civil Engineering

Johns Hopkins Whiting School of Engineering

Professor Jaafar El-Awady

Department Mechanical Engineering

Johns Hopkins Whiting School of Engineering

Acknowledgments

I would like to begin by expressing my gratitude to my PhD advisor, Professor Ghosh, for enriching my life with thoughts and ideas. His drive, passion for research and courage to solve formidable problems was undoubtedly an essential part of my work. This work would have been impossible if it was not for his constant support, encouragement, supervision and thrust to push the boundaries.

I am grateful to Professors Hufnagel, Guest and El-Awady for serving as members of my thesis committee. I would like to thank the members of the PETSc team, specifically Drs. Barry Smith and Matthew Knepley, for helping me out by answering my questions on the implementation of the PETSc package in our parallel FE code.

Many thanks to the past and present members of the Computational Mechanics Research Laboratory (CMRL) from whom I learn about through our frequent discussions. Thank you for always being there in my moments of despair when codes, algorithms and etc did not work. Our discussions were priceless as they helped me realize that codes, algorithms and etc **do** work if I go an extra mile and be a little bit more patient.

And my heartfelt thanks to Zohreh, my wife, for always supporting me and putting up with my late night coding and debugging. I could not have got here without her sacrifices. Many thanks to my parents, Nayyereh and Gholamreza, and my siblings, Ali, Amin, Mohammad and Arezoo, for their unwavering love and support.

I am very grateful to the Office of Naval Research SBA Structures and Materials Program and Army Research Office for the financial support. The computer support provided by the Homewood High Performance Computing Center (HHPC) and Maryland Advanced Research Computing Center (MARCC) is gratefully acknowledged.

dedicated to

Nayyereh** & **Gholamreza

for their lifelong sacrifice

&

Zohreh

for her unwavering support

Contents

List of Tables

List of Figures

Chapter 1

Introduction

Metals and their alloys are widely used in the components of structures in automotive, aviation and defense industries. During their lifetime, these components undergo permanent deformation (plasticity) and possibly failure under service load conditions. One may study deformation and failure from a macroscopic point of view at the structural scale; however, a more detailed robust study involves investigating these phenomena at the microscale where different mechanisms such as dislocation glide and twinning are active and the mechanical response of the material is governed by the microstructural features.

Crystal plasticity FE (CPFE) modeling is deemed to be one of the most powerful numerical tools for modeling problems at the microscale since its framework allows the modelers to develop physics-based constitutive models to represent the effects of different deformation mechanisms on the material behavior [6, 7]. Within the past

two decades, there have been significant improvements to the CP theory and modeling tools. One can mention the development of image-based CP models where the virtual computational domain is obtained by matching the morphological and crystallographic statistics with electron back-scattered diffraction (EBSD) data [8]. The EBSD data could be simply surface data or volumetric data obtained by serial sectioning using focused-ion beam (FIB) [9]. The most notable tool which has made image-based CP modeling possible is DREAM.3d software [10, 11]. These tools have made the concept of statistically equivalent representative volume element (SERVE) a reality and improved the predictive capability of CP models by constructing realistic computational domains. It is worthy to note that the development of meshing softwares [12], capable of discretizing complex geometries, has been instrumental in paving the way for simulating realistic computational domains.

The developments in CP modeling of metals have not been limited to computer tools. The CP constitutive laws have been an area of development as researchers have tried to incorporate different deformation mechanisms into the CP framework. One can mention the research works on simulating twin nucleation and propagation in *hpc* metals [13–16]. Another area of development in CP modeling of deformation focuses on the computational aspects and costs of the simulations. The fast-Fourier transformation (FFT) based method [17–19] is one of the methods proposed to decrease the computational cost associated with CP models. The efficiency of FFT solvers is due to the low complexity of spectral solvers with operations of convolution. An adaptive

wavelet-enriched hierarchical finite element has been recently proposed by Azdoud et al. [20, 21] to lower the computational costs associated with CPFE modeling. This method employs wavelet basis functions to adaptively create an optimal discretization space conforming to the solution profile.

Due to the anisotropic elastic and plastic response of materials, the local strain rate experienced at different material points in the microstructure could be orders of magnitude different from the applied macroscopic strain rate. This drastic variation in local strain rate poses a problem in CP modeling of material response since the majority of the available constitutive models are limited to a certain range of strain rates. For example, the power-law and Arrhenius-type flow rules are applicable to low strain rate deformation where the dislocation glide is governed by thermally-activated processes. On the other hand, the linear flow rule is applicable to high strain rate deformations where the drag-dominated processes define the dislocation mobility. It is clear that development of unified flow rules which can be applied to a wide range of strain rates is significantly important. In this work, a unified flow rule is developed in the context of dislocation density-based CP framework by combining the thermal activation and drag mechanisms to obtain an average dislocation velocity which can seamlessly transcend decades of strain rates.

There is a body of work in the literature on unified flow rules that are based on alternative formulations for average dislocation velocity. Frost and Ashby [22] were the first to propose a dislocation velocity formulation based on combining thermal

activation and drag mechanisms. Inertial models of dislocations have been developed to model plasticity in superconductors in [23]. Hiratani and Nadgorny [24] have developed a unified model to study dislocation motion in 2D through an array of obstacles in an *fcc* metal. A similar unified model has been implemented in a discrete dislocation dynamics code to model dislocation behavior in *fcc* metals under creep conditions in [25]. Unified flow rules have been developed in the context of macroscale J_2 plasticity for modeling deformation behavior of *bcc* vanadium and tantalum [26,27]. Recently, Austin et al. [28] and Lloyd et al. [29] have developed unified flow rules to model viscoplastic deformation in fcc alloys under shock loading. Cereceda et al. [30] developed a unified flow rule to study the dependence of yield strength on temperature in *bcc* tungsten within a CP framework. Most of the studies on unified flow rules have been in the realm of analytical models or discrete dislocation motion in a 2D array of obstacles. There are very few studies that have investigated the capability of these unified flow rules for crystal plasticity-based modeling of deformation in polycrystalline aggregates.

The polycrystalline microstructures of many metals and alloys are quite complex with sharp and tortuous grain boundaries and multiple grain junctions. Discretization of these domains is best accomplished using three-dimensional four-node tetrahedral or TET4 elements, which conform to the complex geometries. However, it has been commonly observed e.g. in [31–35] that TET4 elements suffer from severe volumetric locking when simulating deformation of incompressible or nearly incompressible ma-

terials. A metric that is used to understand element performance for incompressible or nearly incompressible deformations is termed as the *incompressibility constraint ratio*. It is defined as the ratio of number of available degrees of freedom (DOF) to the number of incompressibility constraints in a finite element mesh. Low incompressibility constraint ratio associated with TET4 elements can lead to prediction of large spurious hydrostatic stresses in plastically deforming metallic materials. This volumetric phenomenon is commonly ignored by most CPFE modelers who have been focused on the development of constitutive laws. This work aims at developing stable, locking-free TET4 element formulations for efficient and accurate CPFE modeling and simulations.

A variety of methods have been proposed for the stabilization and control of volumetric locking in TET4 elements. A major idea in these methods is to associate nodal points with patches corresponding to an assembly of surrounding sub-elements, and subsequently integrate the weak form over these patches, thus reducing the incompressibility constraint ratio. An average nodal pressure technique has been proposed for dynamic explicit formulations in [36], where the volumetric strain energy is integrated over the patch for each node. In [32], a node-based uniform strain (NUS) formulation is introduced for four-node tetrahedral elements associated with linear elasticity problems. The volumetric and deviatoric strain energy components are integrated over nodal patches in this formulation. Spurious zero energy modes were identified with this approach in [37], and consequently an additional stabilization

term with a modified constitutive law was added to the potential energy functional. This approach was further extended in [38] into a locally integrated weighted strain formulation, where numerical integration is done at local Gauss points instead of nodes. In [33], the fact that instability is linked only to the isochoric strain energy contribution was exploited through a stress splitting operation, to stabilize the formulation in [32]. A generalized node-based, smoothed finite element method (NS-FEM) has been proposed in [39] that adopts an arbitrary polygonal element domain discretization. This method provides an upper-bound solution for the strain energy and is shown to reduce to the formulation in [32] for the special case of linear tetrahedral elements. The strain smoothing operation in NS-FEM is later extended to edge-based smoothed finite element method (ES-FEM) [40, 41] and face-based smoothed finite element method (FS-FEM) [42]. The above methods are however not suitable for anisotropic crystal plasticity finite element formulations, since the stress or the elasto-plastic tangent stiffness tensor cannot be split into isochoric and deviatoric components. An element formulation with a F-bar patch method has been introduced in [34, 35] to overcome volumetric locking in TET4 elements for finite deformation problems. The original F-bar formulation in [43] was developed for four-node quadrilateral and eight-noded hexahedral elements. This simple and effective model can be used for any constitutive law and can be easily implemented in any standard displacement-based finite element code. Other competing strategies in developing locking-free linear tetrahedral elements include stabilizing NUS formulation

with additional higher order support function [44], and mixed enhanced elements [31] in which additional augmentation strain fields are used in conjunction with a linearly interpolated pressure field to treat the incompressible constraints. Mahnken et al. [45, 46] used volume and area bubble functions to enrich the displacement field and strain field with an additional stabilization.

In this work, an F-bar patch (FP) element is developed in the context of CPFE analysis. The requirements for patch creation in polycrystalline medium are delineated. Moreover, the necessary modifications for utilization of FP element in ductile fracture simulations are discussed and relevant FE derivations are given.

In the past few decades, there has been an ever increasing demand from industries to optimize components and build structures with optimal weight and performance. These optimizations should be achieved without compromising on the load-bearing capacity of components and structural integrity of the system. Often numerous experiments are required to validate the new designs, thus incurring considerable costs on high-tech industries such as aviation sector where raw materials are expensive. High-fidelity fracture models with reliable predictive capabilities can be helpful. These model should minimize the number of required experiments and assist engineers in identifying the most critical experiments.

Multiple approaches to modeling fracture have been proposed in the literature. One can mention approaches such as J-integral and its variants [47, 48] and critical crack tip opening displacement (CTOD) or angle (CTOA) [49, 50] where the state

of crack tip is characterized by one or a few parameters. An alternative is the *discrete* approach where cracks are idealized as surfaces in the computational domain. The extended FEM (XFEM) [51] belongs to this group of methods which suppresses the need to remesh the discontinuity by adding discontinuous functions to the solution space. These methods need to be equipped with additional criteria for crack nucleation and propagation. The cohesive zone models (CZM) [52–54] are another instance of the discrete approach where cohesive elements with certain constitutive description are embedded in between neighboring finite elements. In problems where the crack path is not known a priori, one needs to add cohesive elements in the entire simulation domain, incurring a significant amount of computational expense.

Continuum approaches to fracture are another class of methods to model degradation in materials. These methods generally work by introducing a variable representing degradation state at the constitutive level affecting elasticity or plasticity at the integration points. Gurson–Tvergaard–Needleman (GTN) [55, 56] and continuum damage mechanics [57–59] are categorized as continuum methods of fracture modeling. To overcome mesh sensitivity associated with the continuum approaches, nonlocal damage formulations with a material length scale [60–62] have been proposed.

Crack phase field modeling (PFM) has received significant attention from the fracture modeling community in the last decade. In the PF framework, cracks are idealized by an *order parameter*, say s, which smoothly changes from 0 to 1 to repre-

sent the transition of damage from intact to fully-broken state, respectively [63, 64]. PFM is generally considered as a *smeared* approach since it represents sharp cracks with a smeared (regularized) field of finite thickness. PFM implicitly tracks cracks in the computational domain without the need to remesh or introduce explicit fracture surfaces. This is achieved through solving a governing differential equation which is coupled to the displacement field via the Helmholtz free energy density. Phase field approaches have shown promising results in modeling brittle [65–67] and ductile [68–72] fracture. A critical comparison of PFM and linear fracture mechanics has been done in [73].

PFM can be implemented in FE-based commercial sofeware packages [74]. One may choose alternative numerical tools to solve crack phase field problems, such as isogeometric analysis [75] and material point method [76, 77]. Massive parallelization of PFM via GPU technology was successfully done in [78].

In this work, a thermodynamically-consistent coupled crystal plasticity-crack phase field framework is derived to model fracture in polycrystalline metals. The governing differential equations are obtained by using the principle of virtual power and the first and second laws of thermodynamics. It is shown that the governing equations for the displacement and crack phase field are coupled via the Helmholtz free energy density (HFED). Using the volumetric-deviatoric decomposition of the elastic deformation gradient, a new HFED formulation is proposed for modeling fracture in anisotropic media under finite deformation conditions. Furthermore, this model respects the

tension-compression asymmetry in material response in the presence of cracks; that is, a cracked material loses its load-bearing capacity under tension whereas it retains part of this capacity under compression.

Numerical modeling of fracture is computationally daunting, partly due to the frequent convergence issues and occurrence of instabilities. These instabilities are attributed to an excess energy which cannot be dissipated out of the system. Different arc-length methods [79–81] have been developed to overcome these instabilities in the phase field modeling community [82, 83]. Implementing the arc-length method requires some modifications to the finite element solver. Moreover, since the concept of time is replaced with an arc length, application of the arc-length method for modeling fracture in rate-dependent materials (i.e. rate-sensitive plasticity) is ambiguous [84, 85]. It is worthy to note that unstable equilibrium path could be followed by a stable one; therefore, it is required to propose some criteria to switch from the arc-length methodology (for the unstable path) to the regular time increment-based solver (for the stable path) and vice-versa [83]. In this work, an alternative approach based on viscous stabilization is proposed to overcome these instabilities. Unlike the arc-length methods, the viscous stabilization is applicable for time-dependent materials and its implementation into any existing FE code is straightforward.

The layout of this document is as follows. Chapter 2 discusses the fundamental concepts in crystal plasticity theory. Using principles of thermodynamics, the coupled governing equations for displacement and crack phase field are derived in Chapter 3.

This chapter also discusses the viscous stabilization schemes to overcome instabilities in fracture simulations. The nonlinear FE solution of the governing equations and F-bar-patch formulation are outlined in Chapter 4. The cornerstone of this formulation, i.e. Helmholtz free energy density, is defined in Chapter 5. The numerical implementation of PFM and some fracture examples are given in Chapters 6 and 7, respectively. Development of the unified crystal plasticity model is detailed in Chapter 8. The concluding remarks and future works are given in Chapter 9.

Chapter 2

Finite-strain crystal plasticity theory

In the past few decades, crystal plasticity (CP) theory has received significant attention from material scientists and mechanical engineers for modeling metals under different service conditions. CP theory enables modelers to relate the material response to the morphological and crystallographic properties of the underlying microstructure. This chapter reviews the theory of crystal plasticity within a finite-strain framework.

2.1 Description of deformation

Consider a continuum body initially occupying volume Ω_0 bounded by surface Γ_0. This configuration is referred to as the *reference configuration*. Under certain loading conditions, the body deforms and assumes the *current configuration* as time t, characterized by volume Ω bounded by surface Γ. The position vector of an arbitrary material point P in the reference and current configurations are respectively denoted by $\mathbf{X}$ and $\mathbf{x}$. The current position vector $\mathbf{x}$ can be written in terms of the reference one as:

$$\mathbf{x} = \mathbf{X} + \mathbf{u} \tag{2.1}$$

where $\mathbf{u}$ denotes the displacement vector of the material point P, as shown in Figure 2.1.

Let's define deformation gradient tensor, $\mathbf{F}$, which linearly transforms vector $d\mathbf{X}$ in the reference configuration to $d\mathbf{x}$ in the current configuration as:

$$d\mathbf{x} = \mathbf{F}\, d\mathbf{X} \tag{2.2}$$

Using Equation 2.1, one can also express the deformation gradient tensor in terms of displacements as

$$\mathbf{F} = \frac{\partial \mathbf{x}}{\partial \mathbf{X}} = \mathbf{I} + \boldsymbol{\nabla}_{\mathbf{X}} \mathbf{u} \tag{2.3}$$

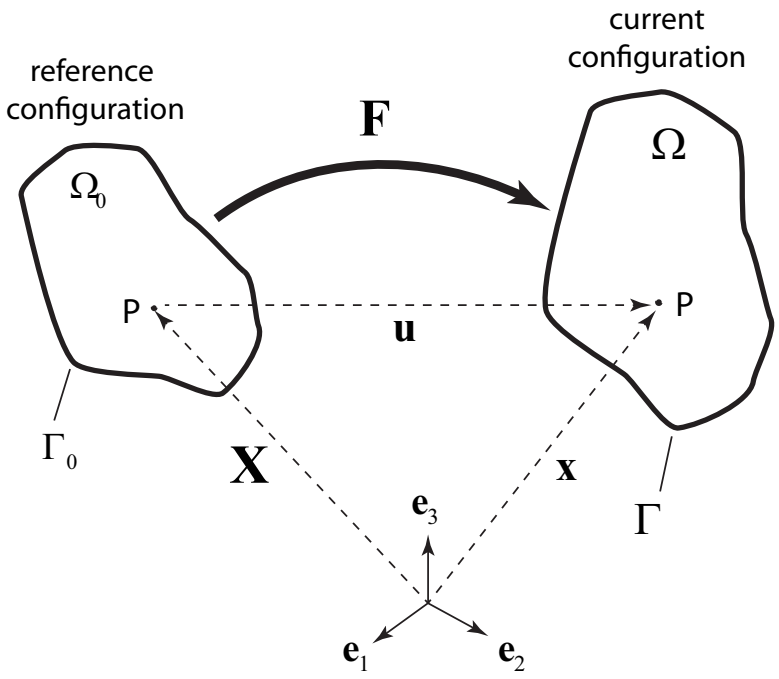

Figure 2.1: Illustration of configuration and motion of a continuum body

Here **I** denotes the second order identity tensor.

In the finite strain theory of plasticity, the deformation gradient is multiplicatively decomposed into elastic and plastic components as [86]:

$$\mathbf{F} = \mathbf{F}^e \, \mathbf{F}^p \tag{2.4}$$

Here $\mathbf{F}^e$ accounts for the elastic stretching and rigid body rotations, whereas $\mathbf{F}^p$ corresponds to the isochoric plastic part of deformation; that is, $\det \mathbf{F}^p = 1$. As shown in Figure 2.2, plastic deformation gradient $\mathbf{F}^p$ can be thought of as a linear map which transforms vectors in the reference configuration to the corresponding ones in a fictitious configuration, traditionally referred to as *intermediate configuration*. The

elastic deformation gradient maps the vectors in the intermediate configuration to the corresponding one in the current configuration.

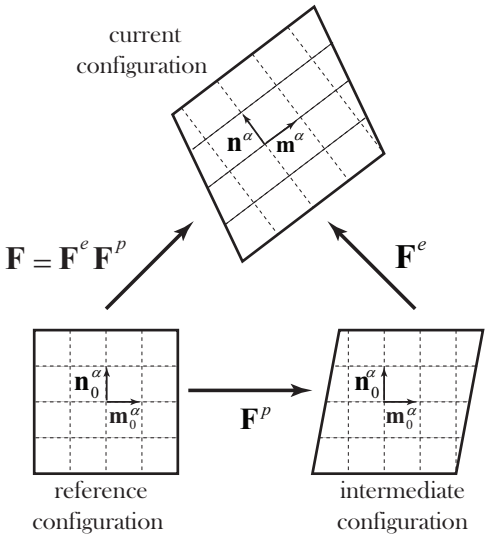

Figure 2.2: Multiplicative decomposition of deformation gradient into elastic and plastic components

2.2 Crystal plasticity theory

The crystal plasticity theory attributes the inelastic deformation of metals to glide of dislocations in certain directions (i.e. *slip direction*) on specific planes (i.e. *slip planes*). Description of the kinematics of this theory is largely due to the seminal work of Asaro and Rice [7]. According to this theory, $\mathbf{F}^p$ is associated with pure slip in an unrotated undistorted lattice. Using the kinematics of dislocation glide, the plastic velocity gradient tensor $\mathbf{L}^p$ in the intermediate configuration is obtained

as [7]:

$$\mathbf{L}^p = \dot{\mathbf{F}}^p \mathbf{F}^{p-1} = \sum_{\alpha=1}^{n_{slip}} \dot{\gamma}^\alpha \mathbf{m}_0^\alpha \otimes \mathbf{n}_0^\alpha \tag{2.5}$$

where $\mathbf{m}_0^\alpha$ and $\mathbf{n}_0^\alpha$ are respectively the slip direction and slip plane normal in the reference configuration for the slip system α. The summation is over all the slip systems n_{slip}. The dyadic product of the slip system direction and normal is referred to as *Schmid tensor*, $\mathbf{S}_0^\alpha = \mathbf{m}_0^\alpha \otimes \mathbf{n}_0^\alpha$. $\dot{\gamma}^\alpha$ denotes the slip rate on slip system α.

2.3 Flow rule

Flow rule in crystal plasticity theory is the core part of the constitutive model. Flow rule describes the dependence of the slip rates on individual slip systems as a function of the local stress state and relevant internal state variables. In order to formulate the flow rule, one can either follow a dislocation density-based or a phenomenological approach.

In the dislocation density-based approach, the resistance to dislocation slip is explicitly expressed in terms of the dislocation densities ρ^α on different slip systems. In this approach, different dislocation interactions, such as multiplication, thermal and athermal annihilation and etc, are introduced and the dislocation densities are evolved accordingly [87]. Since the dislocation densities are known, the Orowan equation is generally used to express the slip rate in terms of dislocation density and the average

dislocation velocity v^α as:

$$\dot{\gamma}^\alpha = \rho^\alpha b^\alpha v^\alpha \text{sign}\left(\tau_p^\alpha\right) \tag{2.6}$$

where b^α is the magnitude of Burgers vector. τ_p^α is the resolved shear stress on the slip system in the intermediate configuration:

$$\tau_p^\alpha = \left(\mathbf{C}^e \mathbf{S}_p^{nv}\right) : \mathbf{S}_0^\alpha \tag{2.7}$$

$\mathbf{C}^e = \mathbf{F}^{eT}\mathbf{F}^e$ is the right elastic Cauchy-Green deformation tensor and $\mathbf{S}_p^{nv}$ denotes the non-viscous part of the second Piola-Kirchhoff stress in the intermediate configuration. The average dislocation velocity is generally governed on thermally-activated processes in low stress levels (and low strain rates) whereas the drag dominated processes control the dislocation glide at high stress levels (and high strain rates). We will discuss dislocation density-based approaches in more details in Chapter 8.

In the phenomenological models, the effective resistance to dislocation motion is evolved through some phenomenological evolution laws. In this approach, one cannot use the Orowan equation since the dislocation densities are not known. A general form used for the flow rule reads as:

$$\dot{\gamma}^\alpha = a_{\dot{\gamma}} v^\alpha \tag{2.8}$$

in which $a_{\dot{\gamma}}$ is material parameter. At lower levels of stress and strain rate, one may formulate the dislocation velocity using the thermally activated law, i.e. Arrhenius-

type relationship, which relates the average dislocation velocity to the resolved shear stress and the thermal s^{α}_{th} and athermal s^{α}_{ath} resistances to dislocation glide [88–90]. Defining an effective shear stress $\tau^{\alpha}_{eff} = \left|\tau^{\alpha}_{p} - \chi^{\alpha}\right| - s^{\alpha}_{ath}$, the average dislocation velocity is expressed as:

$$v^{\alpha}_{th} = \begin{cases} 0 & \text{if} \quad \tau^{\alpha}_{eff} \leq 0 \\ \nu_{att} b^{\alpha} c_j \exp\left(\frac{-Q^{\alpha}}{K_B T}\left[1 - \left(\frac{\tau^{\alpha}_{eff}}{s^{\alpha}_{th}}\right)^{p}\right]^{q}\right) \text{sign}\left(\tau^{\alpha}_{p} - \chi^{\alpha}\right) & \text{if} \quad \tau^{\alpha}_{eff} > 0 \end{cases} \tag{2.9}$$

where ν_{att}, c^{α}_{2}, Q^{α}, K_B and T are frequency of attack, dislocation jump width, activation energy, Boltzmann constant and temperature, respectively. χ^{α} corresponds to the backstress which accounts for kinematic hardening. $0 \leq p \leq 1$ and $1 \leq q \leq 2$ are material constants to account for different barrier profiles [91].

At higher levels of stress and strain rate where drag processes govern dislocation glide, the average dislocation velocity is linearly dependent on the resolved shear stress [88]:

$$v^{\alpha}_{d} = \begin{cases} 0 & \text{if} \quad \tau^{\alpha}_{eff} \leq 0 \\ \frac{\tau^{\alpha}_{eff} b^{\alpha}}{B_0} \text{sign}\left(\tau^{\alpha}_{p} - \chi^{\alpha}\right) & \text{if} \quad \tau^{\alpha}_{eff} > 0 \end{cases} \tag{2.10}$$

in which B_0 is the drag coefficient.

Using molecular dynamics and dislocation dynamics simulations, Becker et al. [27] suggested a unified dislocation velocity formulation by combining the thermally activated and drag processes.

$$v^{\alpha} = \frac{v_{th}^{\alpha}\, v_{d}^{\alpha}}{[(v_{th}^{\alpha})^{r_v} + (v_{d}^{\alpha})^{r_v}]^{\frac{1}{r_v}}} \tag{2.11}$$

Here r_v is set to 2. Using the material properties given in Table 2.1, Figure 2.3 shows how the unified average dislocation velocity changes with the effective shear stress. It is observed that at low stresses v^{α} matches the thermally activated velocity v_{th}^{α} since thermal activation is the dominant dislocation glide mechanism. At higher levels of stress where drag-dominated processes are dominant, v^{α} follows v_{d}^{α}.

Parameter	unit	value
ν_{att}	s^{-1}	10^{10}
b^{α}	m	2.49×10^{-10}
c_2^{α}	$-$	10^{4}
Q^{α}	J	6.5×10^{-19}
T	K	300
s_{th}^{α}	MPa	481.2×10^{6}
p	$-$	0.78
q	$-$	1.15
B_0	$Pa\ s$	5×10^{-4}

Table 2.1: material properties used to generate Figure 2.3

For phase field modeling of ductile fracture, it is strongly recommended to utilize the unified dislocation velocity law even if the macroscopic strain rate and stress lev-

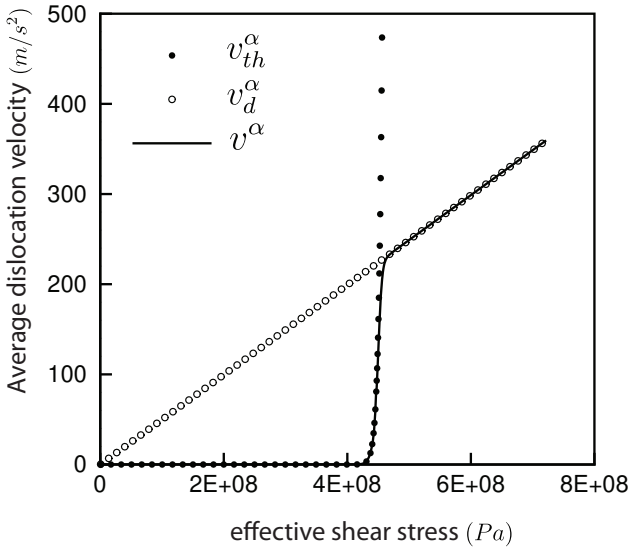

Figure 2.3: comparison of average dislocation velocity according to the unified, thermally activated and drag-dominated laws

els are low. It is known that the stress levels ahead of the crack tip are high and the dislocation glide could be potentially governed by the drag-dominated processes. It is clearly seen in Figure 2.3 that if the thermally activated dislocation velocity law is used at high stress levels, significant slip rates will be obtained. From a numerical standpoint, appearance of high slip rates is catastrophic as the time integration of constitutive law will most likely fail, making the simulation take smaller time increments. The unified flow rule would fix this issue by smoothly transitioning the dislocation velocity from the thermally activated mode to the drag-dominated one where more reasonable slip rates are calculated at high stress levels.

2.4 Evolution of slip system resistances

Dislocation populations are traditionally divided into two classes, viz. statistically stored dislocations (SSDs) that are characterized by a net vanishing Burgers vector, and geometrically necessary dislocations (GNDs) characterized by a non-zero net Burgers vector [92]. In the course of plastic deformation, SSDs evolve by various mechanisms such as multiplication, thermal and athermal annihilation and etc. [87]. GNDs on the other hand, correspond to the storage of polarized dislocation densities and account for crystal lattice curvatures near grain boundaries of polycrystalline aggregates.

As the dislocation density evolves, their entanglements and interactions with each other increase, causing strain hardening in the material. The stress field around dislocations exerts influence on the motion of other dislocations via long-range and short-range interactions. In crystal plasticity framework, thermal and athermal resistances to dislocation glide are introduced to account for long-range and short-range interactions, respectively [93].

$$s^{\alpha}_{ath} = s^{\alpha}_{0,ath} + \frac{K^{\alpha}}{\sqrt{D_g}} + \int_{t'=0}^{t'=t} \sum_{\beta=1}^{n_{slip}} h^{\alpha\beta}_{ath} \left| \dot{\gamma}^{\beta} \sin\left(\mathbf{n}^{\alpha}_{0}, \mathbf{m}^{\beta}_{0}\right) \right| dt' + c^{\alpha}_{1} \mu^{\alpha} b^{\alpha} \sqrt{\rho^{\alpha}_{\mathrm{GND,P}}} \tag{2.12a}$$

$$s^{\alpha}_{th} = s^{\alpha}_{0,th} + \int_{t'=0}^{t'=t} \sum_{\beta=1}^{n_{slip}} h^{\alpha\beta}_{th} \left| \dot{\gamma}^{\beta} \cos\left(\mathbf{n}^{\alpha}_{0}, \mathbf{m}^{\beta}_{0}\right) \right| dt' + \frac{Q^{\alpha}}{c^{\alpha}_{2} c^{\alpha}_{3} {b^{\alpha}}^{2}} \sqrt{\rho^{\alpha}_{\mathrm{GND,F}}} \tag{2.12b}$$

Here $s^{\alpha}_{0,ath}$ and $s^{\alpha}_{0,th}$ are respectively the initial athermal and thermal resistances to dislocation glide. The resistance term $K^{\alpha}/\sqrt{D_g}$ accounts for the dependence of athermal stress on the grain size D_g [94], i.e. the Hall-Petch effect. $K^{\alpha} = \sqrt{\frac{(2-\nu)\pi\tau^{*}\mu b^{\alpha}}{2(1-\nu)}}$ is a Hall-Petch coefficient with ν, μ and τ^{*} as the Poisson's ratio, shear modulus and grain boundary barrier strength, respectively [95]. Material constant c^{α}_{1} is for the long-range impeding stresses arising due to GNDs, while c^{α}_{2} and c^{α}_{3} respectively correspond to the jump and obstacle width [87]. $\rho^{\alpha}_{\mathrm{GND,P}}$ and $\rho^{\alpha}_{\mathrm{GND,F}}$ are respectively the parallel and forest GND densities, calculated as:

$$\rho^{\alpha}_{\mathrm{GND,P}} = \sum_{\beta=1}^{n_{slip}} \chi^{\alpha\beta} \left[\left| \rho^{\beta}_{\mathrm{GNDs}} \sin\left(\mathbf{n}^{\alpha}_{0}, \mathbf{m}^{\beta}_{0}\right) \right| + \left| \rho^{\beta}_{\mathrm{GNDet}} \sin\left(\mathbf{n}^{\alpha}_{0}, \mathbf{t}^{\beta}_{0}\right) \right| + \left| \rho^{\beta}_{\mathrm{GNDen}} \sin\left(\mathbf{n}^{\alpha}_{0}, \mathbf{n}^{\beta}_{0}\right) \right| \right] \tag{2.13a}$$

$$\rho^{\alpha}_{\mathrm{GND,F}} = \sum_{\beta=1}^{n_{slip}} \chi^{\alpha\beta} \left[\left| \rho^{\beta}_{\mathrm{GNDs}} \cos\left(\mathbf{n}^{\alpha}_{0}, \mathbf{m}^{\beta}_{0}\right) \right| + \left| \rho^{\beta}_{\mathrm{GNDet}} \cos\left(\mathbf{n}^{\alpha}_{0}, \mathbf{t}^{\beta}_{0}\right) \right| + \left| \rho^{\beta}_{\mathrm{GNDen}} \cos\left(\mathbf{n}^{\alpha}_{0}, \mathbf{n}^{\beta}_{0}\right) \right| \right] \tag{2.13b}$$

in which $\chi^{\alpha\beta}$ is an interaction factor, defining the strengthening effect of slip system β on slip system α.

$$\chi^{\alpha\beta} = \begin{cases} 1 & \text{if} \quad \alpha = \beta \\ 1.4 & \text{if} \quad \alpha \neq \beta \end{cases} \tag{2.14}$$

$\rho^{\alpha}_{\mathrm{GNDs}}$, $\rho^{\alpha}_{\mathrm{GNDen}}$ and $\rho^{\alpha}_{\mathrm{GNDet}}$ are vector components of the GND density on slip system α with Burgers vector along $\mathbf{m}^{\alpha}_{0}$, and line tangents respectively along directions $\mathbf{m}^{\alpha}_{0}$, $\mathbf{n}^{\alpha}_{0}$

and $\mathbf{t}_0^\alpha = \mathbf{m}_0^\alpha \times \mathbf{n}_0^\alpha$ [87]. For more details on calculation of GNDs, interested readers are referred to [93, 96].

The hardening matrix $h_{(a)th}^{\alpha\beta}$ which accounts for the self and latent hardening is given by:

$$h_{(a)th}^{\alpha\beta} = \chi^{\alpha\beta} h_{ref,(a)th}^{\beta} \left| 1 - \frac{s_{(a)th}^{\beta}}{s_{sat,(a)th}^{\beta}} \right|^{r^\alpha} \text{sign}\left(1 - \frac{s_{(a)th}^{\beta}}{s_{sat,(a)th}^{\beta}} \right) \tag{2.15}$$

where r^α, and $h_{ref,(a)th}^{\beta}$ are material constants and $s_{sat,(a)th}^{\beta}$ denotes the saturation stress on slip system β.

In order to capture the Bauschinger effect in cyclic loading, it is required to consider kinematic hardening via the backstress. An evolution equation for the backstress is given by [97, 98]:

$$\dot{\chi}^\alpha = c_\chi^\alpha \dot{\gamma}^\alpha - d_\chi^\alpha \chi^\alpha \left| \dot{\gamma}^\alpha \right| \tag{2.16}$$

where c_χ^α and d_χ^α are the direct hardening and dynamic recovery coefficients, respectively.

Chapter 3

Governing differential equations

In this chapter, the differential equations governing deformation and fracture of a solid body undergoing an arbitrary loading are obtained using the principle of virtual power and the fundamental laws of thermodynamics. The derivations in this chapter are valid regardless of the material behavior; therefore, the governing equations could be used for modeling elastic and plastic deformation of materials.

3.1 Boundary conditions

The order parameter (e.g. crack phase field) at P is denoted by s where $s \in [0, 1]$. Intact and fully broken material states respectively correspond to $s = 0$ and $s = 1$.

The continuum body is generally subject to some boundary conditions. For multi-field problems, like crack phase field modeling of fracture, the boundary conditions

should be specified for each solution field separately. The Dirichlet conditions on the displacement and crack phase fields are specified as:

$$\mathbf{u} = \overline{\mathbf{u}} \qquad \text{on } \Gamma_{0u} \tag{3.1a}$$

$$s = \overline{s} \qquad \text{on } \Gamma_{0s} \tag{3.1b}$$

where Γ_{0u} and Γ_{0s} refer to the part of boundary in the initial configuration where Dirichlet conditions on displacement ($\overline{\mathbf{u}}$) and order parameter ($\overline{s}$) are imposed, respectively. Moreover, the body is subject to external traction loading as:

$$\mathbf{T} = \overline{\mathbf{T}} \qquad \text{on } \Gamma_{0T} \tag{3.2a}$$

$$\lambda_0 = \overline{\lambda}_0 \qquad \text{on } \Gamma_{0\lambda} \tag{3.2b}$$

where Γ_{0T} and $\Gamma_{0\lambda}$ refer respectively to the part of boundary in the initial configuration where traction loading is applied on displacement ($\overline{\mathbf{T}}$) and order parameter ($\overline{\lambda}_0$). It is noteworthy that

$$\Gamma_{0T} \cap \Gamma_{0u} = \emptyset \ , \quad \Gamma_{0T} \cup \Gamma_{0u} = \Gamma_0 \tag{3.3a}$$

$$\Gamma_{0\lambda} \cap \Gamma_{0s} = \emptyset \ , \quad \Gamma_{0\lambda} \cup \Gamma_{0s} = \Gamma_0 \tag{3.3b}$$

Besides the external traction loadings, the body is subject to body forces $\mathbf{B}$ and $\mathbf{l_0}$ on respectively the displacement and crack phase fields.

3.2 Principle of virtual power

Principle of virtual power (PVP) is one of the fundamental concepts in the mechanics of materials. It states that a necessary and sufficient condition for a continuous body to be in equilibrium is [99]:

$$\delta P_{int} = \delta P_{ext} \tag{3.4}$$

where δP_{int} and δP_{ext} are respectively the virtual internal and external powers induced by a kinematically admissible virtual velocity $\delta\dot{\mathbf{u}}$ (i.e. $\delta\dot{\mathbf{u}} = \mathbf{0}$ on Γ_{0u}) and an admissible virtual rate of order parameter $\delta\dot{s}$ (i.e. $\delta\dot{s} = 0$ on $\Gamma 0s$).

In this section, we assume the existence of microforce balance laws to derive the governing equations for the crack phase field [100]. The virtual internal and external powers can be written in the reference configuration as:

$$\delta P_{int} = \int_{\Omega_0} \boldsymbol{\xi}_0 \cdot \boldsymbol{\nabla}_{\mathbf{X}} \delta\dot{s} \, d\Omega_0 + \int_{\Omega_0} \pi_0 \, \delta\dot{s} \, d\Omega_0 + \int_{\Omega_0} \mathbf{P} : \delta\dot{\mathbf{F}} \, d\Omega_0 + \int_{\Omega_0} \rho_0 \ddot{\mathbf{u}} \cdot \delta\dot{\mathbf{u}} \, d\Omega_0 \tag{3.5a}$$

$$\delta P_{ext} = \int_{\Gamma_{0\lambda}} \lambda_0 \, \delta\dot{s} \, d\Gamma_{0\lambda} + \int_{\Omega_0} l_0 \, \delta\dot{s} \, d\Omega_0 + \int_{\Gamma_{0T}} \mathbf{T} \cdot \delta\dot{\mathbf{u}} \, d\Gamma_{0T} + \int_{\Omega_0} \mathbf{B} \cdot \delta\dot{\mathbf{u}} \, d\Omega_0 \tag{3.5b}$$

Here the overdot $(\cdot)$ denotes differentiation with respect to time t. π_0 and $\boldsymbol{\xi}_0$ are the internal microforces, power-conjugate to $\dot{s}$ and $\boldsymbol{\nabla}_{\mathbf{X}}\dot{s}$, respectively. $\mathbf{P}$ is the first Piola-Kirchhoff stress which is power-conjugate to $\dot{\mathbf{F}} = \boldsymbol{\nabla}_{\mathbf{X}}\dot{\mathbf{u}}$. The initial mass density is denoted by ρ_0.

Setting $\delta\dot{s} = 0$ in Equation 3.4 and recognizing that $\delta\mathbf{u} = \mathbf{0}$ on Γ_{0u}, one obtains:

$$\begin{aligned}
&\int_{\Gamma_{0T}} \mathbf{T} \cdot \delta\dot{\mathbf{u}}\, d\Gamma_{0T} + \int_{\Omega_0} \mathbf{B} \cdot \delta\dot{\mathbf{u}}\, d\Omega_0 \\
&\quad = \int_{\Omega_0} \mathbf{P} : \boldsymbol{\nabla}_{\mathbf{X}} \delta\dot{\mathbf{u}}\, d\Omega_0 + \int_{\Omega_0} \rho_0 \ddot{\mathbf{u}} \cdot \delta\dot{\mathbf{u}}\, d\Omega_0 \\
&\quad = \int_{\Omega_0} \boldsymbol{\nabla}_{\mathbf{X}} \cdot (\delta\dot{\mathbf{u}}\, \mathbf{P})\; d\Omega_0 - \int_{\Omega_0} \delta\dot{\mathbf{u}} \cdot (\boldsymbol{\nabla}_{\mathbf{X}} \cdot \mathbf{P})\; d\Omega_0 + \int_{\Omega_0} \rho_0 \ddot{\mathbf{u}} \cdot \delta\dot{\mathbf{u}}\, d\Omega_0 \\
&\quad = \int_{\Gamma_0} \delta\dot{\mathbf{u}}\, \mathbf{P} \cdot \mathbf{N}\, d\Gamma_0 - \int_{\Omega_0} \delta\dot{\mathbf{u}} \cdot (\boldsymbol{\nabla}_{\mathbf{X}} \cdot \mathbf{P})\; d\Omega_0 + \int_{\Omega_0} \rho_0 \ddot{\mathbf{u}} \cdot \delta\dot{\mathbf{u}}\, d\Omega_0 \\
&\quad = \int_{\Gamma_{0T}} \delta\dot{\mathbf{u}}\, \mathbf{P} \cdot \mathbf{N}\, d\Gamma_{0T} - \int_{\Omega_0} \delta\dot{\mathbf{u}} \cdot (\boldsymbol{\nabla}_{\mathbf{X}} \cdot \mathbf{P})\; d\Omega_0 + \int_{\Omega_0} \rho_0 \ddot{\mathbf{u}} \cdot \delta\dot{\mathbf{u}}\, d\Omega_0
\end{aligned} \tag{3.6}$$

This equation should hold for any kinematically admissible $\delta\dot{\mathbf{u}}$ over an arbitrary volume Ω_0 bounded by Γ_0 with unit outward normal $\mathbf{N}$. Therefore, one obtains the governing equation of motion and traction law for the displacement field in the reference configuration as:

$$\boldsymbol{\nabla}_{\mathbf{X}} \cdot \mathbf{P} + \mathbf{B} = \rho_0 \ddot{\mathbf{u}} \qquad \forall \mathbf{X} \in \Omega_0 \tag{3.7a}$$

$$\mathbf{T} = \mathbf{P}\, \mathbf{N} \qquad \forall \mathbf{X} \in \Gamma_{0T} \tag{3.7b}$$

Setting $\delta\dot{\mathbf{u}} = \mathbf{0}$ in Equation 3.4 and recognizing that $\delta s = 0$ on Γ_{0s}, one obtains:

$$
\begin{aligned}
&\int_{\Gamma_{0\lambda}} \lambda_0 \, \delta\dot{s} \, d\Gamma_{0\lambda} + \int_{\Omega_0} l_0 \, \delta\dot{s} \, d\Omega_0 \\
&\quad = \int_{\Omega_0} \boldsymbol{\xi}_0 \cdot \boldsymbol{\nabla}_{\mathbf{X}} \delta\dot{s} \, d\Omega_0 + \int_{\Omega_0} \pi_0 \, \delta\dot{s} \, d\Omega_0 \\
&\quad = \int_{\Omega_0} \boldsymbol{\nabla}_{\mathbf{X}} \cdot (\delta\dot{s}\boldsymbol{\xi}_0) \; d\Omega_0 - \int_{\Omega_0} \delta\dot{s} \; \boldsymbol{\nabla}_{\mathbf{X}} \cdot \boldsymbol{\xi}_0 \, d\Omega_0 + \int_{\Omega_0} \pi_0 \, \delta\dot{s} \, d\Omega_0 \\
&\quad = \int_{\Gamma_0} \delta\dot{s}\boldsymbol{\xi}_0 \cdot \mathbf{N} \, d\Gamma_0 - \int_{\Omega_0} \delta\dot{s} \; \boldsymbol{\nabla}_{\mathbf{X}} \cdot \boldsymbol{\xi}_0 \, d\Omega_0 + \int_{\Omega_0} \pi_0 \, \delta\dot{s} \, d\Omega_0 \\
&\quad = \int_{\Gamma_{0\lambda}} \delta\dot{s}\boldsymbol{\xi}_0 \cdot \mathbf{N} \, d\Gamma_{0\lambda} - \int_{\Omega_0} \delta\dot{s} \; \boldsymbol{\nabla}_{\mathbf{X}} \cdot \boldsymbol{\xi}_0 \, d\Omega_0 + \int_{\Omega_0} \pi_0 \, \delta\dot{s} \, d\Omega_0
\end{aligned}
\tag{3.8}
$$

Since this equation should hold for any admissible $\delta\dot{s}$ over an arbitrary volume, the governing equation and traction law for the crack phase field in the reference configuration are obtained as:

$$
\boldsymbol{\nabla}_{\mathbf{X}} \cdot \boldsymbol{\xi}_0 - \pi_0 + l_0 = 0 \qquad \forall \mathbf{X} \in \Omega_0 \tag{3.9a}
$$

$$
\lambda_0 = \boldsymbol{\xi}_0 \cdot \mathbf{N} \qquad \forall \mathbf{X} \in \Gamma_{0\lambda} \tag{3.9b}
$$

3.3 First law of thermodynamics

The first law of thermodynamics, also referred to as *conservation of energy*, requires that [101]:

$$
\frac{d}{dt}\left(E + K\right) = Q + P_{ext} \tag{3.10}
$$

for any arbitrary volume. Here E, K, Q and P_{ext} are respectively the total internal energy, total kinetic energy, net heat flux into the solid and rate of external work done on the solid (external power). These quantities can be calculated as:

$$E = \int_{\Omega_0} \rho_0 e \; d\Omega_0 \tag{3.11a}$$

$$K = \int_{\Omega_0} \frac{1}{2} \rho_0 \dot{\mathbf{u}} \cdot \dot{\mathbf{u}} \; d\Omega_0 \tag{3.11b}$$

$$Q = \int_{\Omega_0} \rho_0 r \; d\Omega_0 - \int_{\Gamma_0} \mathbf{Q} \cdot \mathbf{N} \; d\Gamma_0 \tag{3.11c}$$

$$P_{ext} = \int_{\Gamma_0} \mathbf{T} \cdot \dot{\mathbf{u}} \; d\Gamma_0 + \int_{\Omega_0} \mathbf{B} \cdot \dot{\mathbf{u}} \; d\Omega_0 + \int_{\Omega_0} l_0 \dot{s} \; d\Omega_0 + \int_{\Gamma_0} \lambda_0 \dot{s} \; d\Gamma_0 \tag{3.11d}$$

in which e, r, $\mathbf{Q}$ refer to the specific internal energy, rate of heat generation per unit mass and outward heat flux per unit reference area, respectively. Using Equations 3.7 and 3.9 and divergence theorem, Equation 3.10 can be simplified as:

$$\rho_0 \dot{e} = \mathbf{P} : \dot{\mathbf{F}} + \boldsymbol{\xi}_0 \cdot \boldsymbol{\nabla}_{\mathbf{X}} \dot{s} + \pi_0 \dot{s} + \rho_0 r - \boldsymbol{\nabla}_{\mathbf{X}} \cdot \mathbf{Q} \qquad \forall \mathbf{X} \in \Omega_0 \tag{3.12}$$

3.4 Second law of thermodynamics

The second law of thermodynamics, also referred to as *dissipation principle*, states that the net entropy production within any given volume should be non-negative [101], i.e.

$$\frac{dS}{dt} - \frac{dH}{dt} \geq 0 \tag{3.13}$$

where the total entropy S and the net rate of external entropy supplied to the body $dH\,/\,dt$ are given by

$$S = \int_{\Omega_0} \rho_0 \eta \; d\Omega_0 \tag{3.14a}$$

$$\frac{dH}{dt} = \int_{\Omega_0} \frac{\rho_0 r}{T} \; d\Omega_0 - \int_{\Gamma_0} \frac{\mathbf{Q}\cdot\mathbf{N}}{T} \; d\Gamma_0 \tag{3.14b}$$

Here η and T denote the specific entropy and temperature, respectively. Using divergence theorem and Equation 3.12, Equation 3.13 can be rewritten as:

$$\int_{\Omega_0} \left(\rho_0 T\dot{\eta} + \mathbf{P} : \dot{\mathbf{F}} + \boldsymbol{\xi}_0 \cdot \boldsymbol{\nabla}_{\mathbf{X}} \dot{s} + \pi_0 \dot{s} - \rho_0 \dot{e} - \frac{\mathbf{Q}\cdot\boldsymbol{\nabla}_{\mathbf{X}} T}{T} \right) \; d\Omega_0 \geq 0 \tag{3.15}$$

Separating the mechanical and thermal problems, the entropy production inequality for the mechanical problem is obtained as:

$$\int_{\Omega_0} \left[\rho_0 T\dot{\eta} + \mathbf{P} : \dot{\mathbf{F}} + \boldsymbol{\xi}_0 \cdot \boldsymbol{\nabla}_{\mathbf{X}} \dot{s} + \pi_0 \dot{s} - \rho_0 \dot{e} \right] \; d\Omega_0 \geq 0 \tag{3.16}$$

Defining the Helmholtz free energy density as $\psi = e - T\eta$, Equation 3.16 is rewritten as:

$$\int_{\Omega_0} \left[\rho_0 \left(-\dot{T}\eta - \dot{\psi} \right) + \mathbf{P} : \dot{\mathbf{F}} + \boldsymbol{\xi}_0 \cdot \boldsymbol{\nabla}_{\mathbf{X}} \dot{s} + \pi_0 \dot{s} \right] \; d\Omega_0 \geq 0 \tag{3.17}$$

The Helmholtz free energy density is generally a function of elastic deformations $\mathbf{F}^e$, some internal state variables $\boldsymbol{\zeta}$, order parameter and its gradient [68]; i.e.

$$\rho_0\psi = \rho_0\psi\left(\mathbf{F}^e,\ s,\ \boldsymbol{\nabla}_{\mathbf{X}}s,\ \boldsymbol{\zeta}\right) = \rho_0\psi\left(\mathbf{F},\ \mathbf{F}^p,\ s,\ \boldsymbol{\nabla}_{\mathbf{X}}s,\ \boldsymbol{\zeta}\right) \tag{3.18}$$

Using Equation 3.18 and assuming isothermal conditions, i.e. $\dot{T} = 0$, the dissipation inequality given in Equation 3.17 is further simplified as:

$$\begin{aligned}\int_{\Omega_0}\Bigg[\left(\mathbf{P} - \rho_0\frac{\partial\psi}{\partial\mathbf{F}}\right) : \dot{\mathbf{F}} - \rho_0\frac{\partial\psi}{\partial\mathbf{F}^p} : \dot{\mathbf{F}}^p - \rho_0\frac{\partial\psi}{\partial\boldsymbol{\zeta}}\cdot\dot{\boldsymbol{\zeta}} + \\ \left(\pi_0 - \rho_0\frac{\partial\psi}{\partial s}\right)\dot{s} + \left(\boldsymbol{\xi}_0 - \rho_0\frac{\partial\psi}{\partial\boldsymbol{\nabla}_{\mathbf{X}}s}\right)\cdot\boldsymbol{\nabla}_{\mathbf{X}}\dot{s}\Bigg]\, d\Omega_0 \geq 0\end{aligned} \tag{3.19}$$

Considering that the dissipation should be zero for a purely elastic deformation and recognizing that Equation 3.19 is valid for any $\dot{\mathbf{F}}$, $\dot{\mathbf{F}}^p$, $\dot{\boldsymbol{\zeta}}$, $\dot{s}$ and $\boldsymbol{\nabla}_{\mathbf{X}}\dot{s}$, one can obtain the following equation for the first Piola-Kirchhoff stress:

$$\mathbf{P} = \rho_0\frac{\partial\psi}{\partial\mathbf{F}} \tag{3.20}$$

Equation 3.20 is the constitutive equation for the first Piola-Kirchhoff stress and is valid for both elasticity and plasticity. Following classical arguments of thermodynamics and enforcing the dissipation inequality in Equation 3.19 on the deformation and crack phase field separately, it yields:

$$\int_{\Omega_0}\left[-\rho_0\frac{\partial\psi}{\partial\mathbf{F}^p} : \dot{\mathbf{F}}^p - \rho_0\frac{\partial\psi}{\partial\boldsymbol{\zeta}}\cdot\dot{\boldsymbol{\zeta}}\right]\, d\Omega_0 \geq 0 \tag{3.21a}$$

$$\int_{\Omega_0} \left[\left(\pi_0 - \rho_0 \frac{\partial \psi}{\partial s} \right) \dot{s} + \left(\boldsymbol{\xi}_0 - \rho_0 \frac{\partial \psi}{\partial \boldsymbol{\nabla}_{\mathbf{X}} s} \right) \cdot \boldsymbol{\nabla}_{\mathbf{X}} \dot{s} \right] \, d\Omega_0 \geq 0 \tag{3.21b}$$

Equation 3.21a denotes the standard integral form of the dissipation inequality for the displacement field. One can enforce this inequality in a point-wise sense; that is,

$$- \rho_0 \frac{\partial \psi}{\partial \mathbf{F}^p} : \dot{\mathbf{F}}^p - \rho_0 \frac{\partial \psi}{\partial \boldsymbol{\zeta}} \cdot \dot{\boldsymbol{\zeta}} \geq 0 \tag{3.22}$$

Following some simple mathematical operations, the dissipation inequality for the crack phase field in Equation 3.21b can be rewritten as:

$$\begin{aligned} \int_{\Omega_0} \left[\left(\pi_0 - \rho_0 \frac{\partial \psi}{\partial s} \right) \dot{s} + \left(\boldsymbol{\xi}_0 - \rho_0 \frac{\partial \psi}{\partial \boldsymbol{\nabla}_{\mathbf{X}} s} \right) \cdot \boldsymbol{\nabla}_{\mathbf{X}} \dot{s} \right] \, d\Omega_0 = \\ \int_{\Omega_0} \left[\pi_0 - \rho_0 \frac{\partial \psi}{\partial s} - \boldsymbol{\nabla}_{\mathbf{X}} \cdot \left(\boldsymbol{\xi}_0 - \rho_0 \frac{\partial \psi}{\partial \boldsymbol{\nabla}_{\mathbf{X}} s} \right) \right] \dot{s} \, d\Omega_0 \quad + \\ \int_{\Gamma_0} \left(\boldsymbol{\xi}_0 - \rho_0 \frac{\partial \psi}{\partial \boldsymbol{\nabla}_{\mathbf{X}} s} \right) \cdot \mathbf{N} \dot{s} \, d\Gamma_0 \geq 0 \end{aligned} \tag{3.23}$$

Making the dissipation disappear over the domain boundary, one obtains the internal microforce $\boldsymbol{\xi}_0$ as:

$$\boldsymbol{\xi}_0 = \rho_0 \frac{\partial \psi}{\partial \boldsymbol{\nabla}_{\mathbf{X}} s} \tag{3.24}$$

Therefore, the dissipation inequality for phase field given in Equation 3.23 is further reduced to:

$$\int_{\Omega_0} \left(\pi_0 - \rho_0 \frac{\partial \psi}{\partial s} \right) \dot{s} \, d\Omega_0 \geq 0 \tag{3.25}$$

This equation can be enforced in a point-wise sense as:

$$\left(\pi_0 - \rho_0 \frac{\partial \psi}{\partial s}\right) \dot{s} \geq 0 \tag{3.26}$$

3.5 Instability and convergence issues

Convergence of nonlinear solvers in fracture simulations is challenging due to the inherent instabilities associated with the gradual loss of material integrity. These instabilities are not unique to phase field modeling of fracture and have been also reported for other fracture modeling frameworks such as cohesive interface models. Snap-back and snap-through are two of the main instabilities observed in fracture modeling. If not treated, these instabilities can cause early termination of the simulations due to the inability of solver to converge.

In the following, first a simple 1D problem is set up to show that instabilities take place when there is an excess energy which cannot be dissipated through any of the available dissipative mechanisms. Then the local and global viscous stabilization for phase field modeling of fracture are introduced as a means to dissipate this excess energy and therefore effectively overcome instabilities. Local stabilization is applied to the constitutive model for the displacement field, whereas, the global stabilization is added to the governing equations for both the displacement and crack phase fields.

It is worthy to mention that, in addition to the snap-back and snap-through, frac-

ture simulations could suffer from numerical precision issues due to the ill-conditioning of the tangent stiffness matrix [102]. The ill-conditioning could be attributed to the significant disparity in eigenvalues of the system in problems where the material degradation, i.e. fracture, is very localized. This issue could be addressed by either designing appropriate preconditioners to enhance the condition number of the stiffness matrix or dividing the problem into separate subregions (cracks and uncracked regions) and solving each subregion separately and the solutions on the interfaces.

3.5.1 Instabilities in modeling degradable materials

This section discusses the source of instabilities occuring in modeling degradable materials using a simple 1D deformation model. Consider a uniform bar consisting of three segments undergoing uniaxial extension, as shown in Figure 3.1a. A linear constitutive model is used for segments 1 and 3, as shown in Figure 3.1b. To mimic material degradation, it is assumed that segment 2 experiences softening once the uniaxial strain exceeds ϵ_c, as shown in Figure 3.1c.

All bar segments experience the same level of stress since they are acting in serial. Following simple structural mechanics calculations, one can obtain the stress in terms of the applied displacement as:

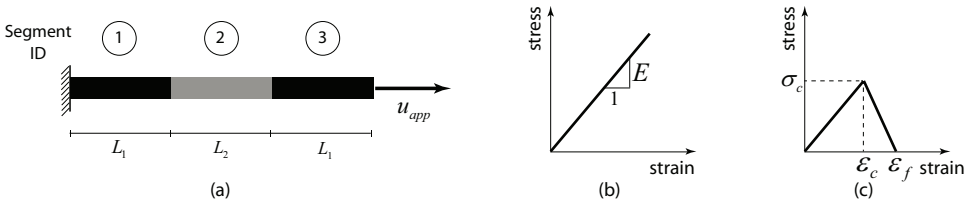

Figure 3.1: 1D deformation model to study the occurrence of instabilities, (a) geometry and boundary conditions for the bar problem, (b) linear constitutive model for segments 1 and 3, (c) constitutive model for segment 2

$$\sigma = \begin{cases} \frac{u_{app}}{2\frac{L_1}{E}+\frac{\epsilon_c L_2}{\sigma_c}} & \text{if} \quad 0 \leq \epsilon_2 \leq \epsilon_c \\ \\ \frac{u_{app}-\epsilon_f L_2}{2\frac{L_1}{E}-L_2\frac{\epsilon_f-\epsilon_c}{\sigma_c}} & \text{if} \quad \epsilon_c \leq \epsilon_2 \leq \epsilon_f \end{cases} \tag{3.27}$$

Plugging the constitutive model for segment 2 into the stress results in Equation 3.27, the applied displacement can be expressed in terms of the strain in segment 2 as:

$$u_{app} = \begin{cases} \left(2\frac{\sigma_c L_1}{E\epsilon_c} + L_2\right)\epsilon_2 & \text{if} \quad 0 \leq \epsilon_2 \leq \epsilon_c \\ 2\frac{\sigma_c L_1}{E} + \epsilon_c L_2 - \frac{\sigma_c}{\epsilon_f-\epsilon_c}\left(2\frac{L_1}{E} - L_2\frac{\epsilon_f-\epsilon_c}{\sigma_c}\right)(\epsilon_2-\epsilon_c) & \text{if} \quad \epsilon_c \leq \epsilon_2 \leq \epsilon_f \end{cases} \tag{3.28}$$

It is expected that the strain in all segments (including segment 2) increase with the applied displacement; in other words, the linear relationship between the applied displacement and ϵ_2 should have a positive slope, otherwise the solution is unphysical and unacceptable. This requirement yields the following stability condition:

$$2\frac{L_1}{E} - L_2\frac{\epsilon_f - \epsilon_c}{\sigma_c} < 0 \tag{3.29}$$

This stability condition can be rewritten as

$$\frac{\sigma_c^2 L_1}{E} < \frac{\epsilon_f - \epsilon_c}{2}\sigma_c L_2 \tag{3.30}$$

The LHS of this inequality corresponds to the sum of elastic energy stored in segments 1 and 3 up to the point where segment 2 starts to degrade. The RHS of this inequality denotes the elastic energy stored in segment 2 from the initiation of degradation ($\epsilon_2 = \epsilon_c$) up to the full failure ($\epsilon_2 = \epsilon_f$). This inequality indicates that the solution is stable (feasible) if the degradable segment 2 can absorb the elastic energies released from segments 1 and 3 as it undergoes degradation. If this inequality does not hold, there would be an excess energy in the system and no static equilibrium path exists. Therefore, (quasi-)static numerical solvers will not be able to find a feasible solution and solvers experience convergence issues. This is consistent with the conclusions in [103–105] where this excess energy is introduced as the source of convergence issues and instabilities in the equilibrium path.

Equation 3.29 clearly signifies that instabilities can be triggered in simulations depending on the choice of geometrical (L_1 and L_2) and constitutive (E, ϵ_f, ϵ_c and σ_c) parameters. This explains why some, but not all, simulations involving material degradation experience instabilities and convergence issues. It is also worthy to mention that these types of instabilities cannot be overcome by simply refining the finite

element discretization.

3.5.2 Local viscous stabilization of displacement field

Viscous stabilization is an effective remedy for overcoming the instabilities. Viscous stabilization can be done at the local (constitutive model) and global (governing differential equation) levels. The artificial viscosity allows the system to dissipate the excess energy and therefore avoid the instabilities. The competency of local viscous stabilization has been explored extensively in the context of cohesive models [104,106].

In order to introduce local viscous stabilization to the displacement field, one needs to introduce an artificial viscosity in the constitutive model. One can introduce viscosity in a finite-strain setting by augmenting the multiplicative decomposition of deformation gradient in Equation 2.4 with an additional deformation gradient corresponding to the viscous elasticity, as outline in [107]. This treatment of viscoelasticity is rigorous and suitable for developing crack phase models for modeling fracture in viscoelastic media. Given that, in this work, the introduction of *artificial* viscosity to the constitutive model is merely due to numerical necessity (i.e. the material does not have inherent viscoelastic response), a simpler approach is taken here to incorporate viscosity into the constitutive model which is less computationally involved compared to the framework in [107].

Using the definition of first Piola-Kirchhoff stress in Equation 3.20, the second Piola-Kirchhoff stress in the reference configuration is derived as:

$$\mathbf{S}_0 = \mathbf{F}^{-1}\ \rho_0 \frac{\partial \psi}{\partial \mathbf{F}} \tag{3.31}$$

A simple viscosity law is considered where the second Piola-Kirchhoff stress is assumed to be linearly dependent on the rate of its power-conjugate, i.e. Green-Lagrange strain tensor $\mathbf{E}$. The stabilized second Piola-Kirchhoff stress reads as:

$$\mathbf{S}_0 = \mathbf{F}^{-1}\ \rho_0 \frac{\partial \psi}{\partial \mathbf{F}} + \beta_{lu}\ \dot{\mathbf{E}} \tag{3.32}$$

in which β_{lu} is the artificial local viscosity for the displacement field. The stabilized first Piola-Kirchhoff stress can be easily obtained as:

$$\mathbf{P} = \rho_0 \frac{\partial \psi}{\partial \mathbf{F}} + \beta_{lu}\ \mathbf{F}\ \dot{\mathbf{E}} \tag{3.33}$$

The first and second terms on the RHS of Equations 3.32 and 3.33 are regarded as the non-viscous and viscous contributions to the stress tensor, respectively.

3.5.3 Global viscous stabilization of displacement field

Another approach for overcoming the instabilities is the introduction of viscous forces, i.e. damping, in the governing differential equation of motion. This method has

proved to be effective in modeling deformation of degradable materials [85]. Viscous forces can be thought of as body forces and incorporated into the stress equilibrium equation as:

$$\boldsymbol{\nabla}_{\mathbf{X}} \cdot \mathbf{P} + \mathbf{B} - \beta_{gu}\, \dot{\mathbf{u}} = \rho_0 \ddot{\mathbf{u}} \tag{3.34}$$

in which β_{gu} stands for the artificial global viscosity parameter for the displacement field. Viscous forces are a linear function of velocity. The magnitude of viscous forces should be small for stable deformation; however, when a local region in the computational domain becomes unstable and nodal velocities increase drastically, the viscous forces will play a key role to stabilize the solution. As discussed in [85], β_{gu} may have spatial and temporal dependence and can be adaptively modified to obtain the optimum performance. In this work, we assume a linear dependence between the artificial global viscosity and order parameter. That is,

$$\beta_{gu} = \beta_{gu0}\, s \tag{3.35}$$

Here β_{gu0} is the reference global viscosity parameter. This treatment will ensure that the viscous stabilization is applied to regions in the computational domain where material integrity is lost; i.e. regions with non-zero crack phase field.

3.5.4 Global viscous stabilization of crack phase field

One can address the convergence issues associated with instabilities by performing global viscous stabilization on the governing equation for the crack phase field. Global stabilization of the phase field model will render the fracture process rate-sensitive [65,66]. Viscosity can be introduced in the crack phase field problem by decomposing the internal microforce π_0 into energetic π_0^{en} and dissipative π_0^{dis} components [69] as:

$$\pi_0 = \pi_0^{en} + \pi_0^{dis} \tag{3.36}$$

where

$$\pi_0^{en} = \rho_0 \frac{\partial \psi}{\partial s} \tag{3.37a}$$

$$\pi_0^{dis} = \beta_{gs}\, \dot{s} \tag{3.37b}$$

Here β_{gs} is the non-negative viscous parameter for the global stabilization of the crack phase field. It is clear that setting β_{gs} to zero will make the fracture process rate-insensitive. Plugging Equations 3.36 and 3.37 into Equation 3.26, yields:

$$\beta_{gs}\, \dot{s}^2 \geq 0 \tag{3.38}$$

This inequality always holds regardless of the state of crack phase field evolution since β_{gs} is non-negative.

3.6 Governing differential equations

In this section, the derivations in Sections 3.2, 3.3, 3.4 and 3.5 are consolidated to establish the differential equations governing the displacement and crack phase fields. The strong form of the boundary-value problem at any given time can be stated as:

$$\boldsymbol{\nabla}_{\mathbf{X}} \cdot \mathbf{P} + \mathbf{B} - \beta_{gu}\, \dot{\mathbf{u}} = \mathbf{0} \qquad on \quad \Omega_0 \tag{3.39a}$$

$$\boldsymbol{\nabla}_{\mathbf{X}} \cdot \rho_0 \frac{\partial \psi}{\partial \boldsymbol{\nabla}_{\mathbf{X}} s} - \rho_0 \frac{\partial \psi}{\partial s} = \beta_{gs}\, \dot{s} \qquad on \quad \Omega_0 \tag{3.39b}$$

$$\mathbf{T} = \mathbf{P}\,\mathbf{N} = \overline{\mathbf{T}} \qquad on \quad \Gamma_{0T} \tag{3.39c}$$

$$\lambda_0 = \rho_0 \frac{\partial \psi}{\partial \boldsymbol{\nabla}_{\mathbf{X}} s} \cdot \mathbf{N} = 0 \qquad on \quad \Gamma_{0\lambda} \tag{3.39d}$$

$$\mathbf{u} = \overline{\mathbf{u}} \qquad on \Gamma_{0u} \tag{3.39e}$$

$$s = \overline{s} \qquad on \Gamma_{0s} \tag{3.39f}$$

It is worthy to note that the term $\rho_0 \ddot{\mathbf{u}}$ is dropped in Equation 3.39a since we are interested in quasi-static simulations in this work. Moreover, the external traction and body microforces on the crack phase field, i.e. λ_0 and l_0 respectively, are assumed to be zero.

Chapter 4

Nonlinear finite element framework

This chapter focuses on solving the partial differential equations governing the displacement and crack phase fields derived in Chapter 3. Nonlinear finite element (FE) method is used to solve the governing equations given in Equation 3.39b. In the following, the structure of a staggered solver for coupled problems is laid out in Section 4.1 before the basic formulation of finite element method is explained in Section 4.2. Volumetric locking associated with modeling incompressible materials is discussed and the possible remedies are explained in Section 4.3. The linearization of the governing equations for the displacement and crack phase fields will be discussed in Sections 4.4 and 4.5, respectively.

4.1 Staggered scheme for solving coupled problems

As observed in Chapter 3, the displacement and crack phase field problems are two-way coupled since their governing equations are both functions of the Helmholtz free energy density. In order to solve this two-way coupled problem, one may follow either a monolithic or staggered solver scheme. In the monolithic scheme, both the displacement and crack phase field degrees of freedom (DOFs) are solved simultaneously and it involves solution of a system of equations as:

$$\begin{bmatrix} [K_{uu}] & [K_{us}] \\ [K_{su}] & [K_{ss}] \end{bmatrix} \begin{Bmatrix} \{d_u\} \\ \{d_s\} \end{Bmatrix} = \begin{Bmatrix} \{R_u\} \\ \{R_s\} \end{Bmatrix} \tag{4.1}$$

where $[K_{uu}]$ and $[K_{ss}]$ are respectively the intrinsic stiffness matrices for the displacement and crack phase field. $[K_{us}]$ and $[K_{su}]$ correspond to the cross-stiffness matrices. The residual force vectors for the displacement and crack phase field are denoted by $\{R_u\}$ and $\{R_s\}$, respectively. On the other hand, in the staggered scheme, each field is solved separately while keeping the other field fixed. Coupling of the solution fields is taken care of in the post-processing step after one field is solved by passing relevant data, here referred to as *inter-field information*, in between the two fields, as shown in Figure 4.1. This approach leads to systems of equations involving only either

displacement or crack phase field DOFs as:

$$[K_{uu}]\{d_u\} = \{R_u\} \tag{4.2a}$$

$$[K_{ss}]\{d_s\} = \{R_s\} \tag{4.2b}$$

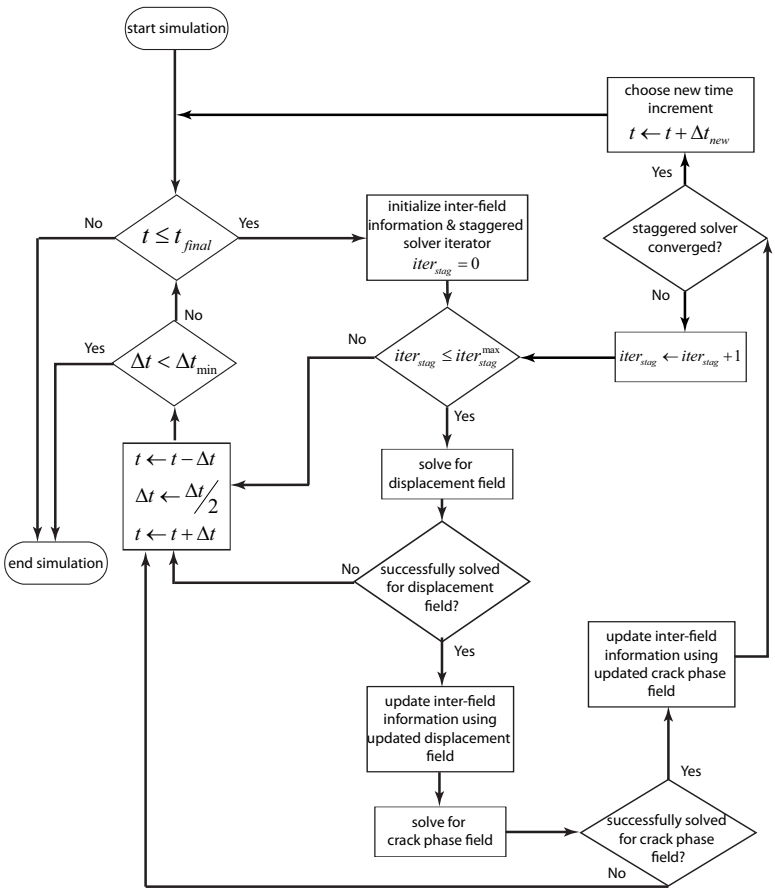

Figure 4.1: schematics of the staggered solver for the coupled displacement-crack phase field problem

The energy functional corresponding to phase field modeling of fracture is typically non-convex in $(\mathbf{u}, s)$. This fact poses issues for the convergence of monolithic solvers

as they try to find the solution to energy minimization problem since there might be many local minimizers [108]. On the other hand, the energy functional is convex w.r.t. each of $\mathbf{u}$ and s separately; therefore, the staggered schemes are generally more favorable for phase field simulations of fracture and experience less convergence issues compared to the monolithic ones. Besides the convexity issue, the following reasons may motivate one to choose the staggered solvers over the monolithic one.

- Since the two fields are solved together in the monolithic approach, one should pay caution to the condition number of the coefficient matrix since the order of magnitude of the displacement and order parameter could be drastically different. One may utilize scaling to bring the two types of DOF to the same order.

- Given that the DOFs and their corresponding residual forces have different units, extra caution should be practiced in checking for convergence of the solver. This concern is valid for problems in which DOFs represent different physical quantities [109].

- Staggered solvers are generally more memory efficient since the cross-stiffness terms $[K_{us}]$ and $[K_{su}]$ are neither calculated nor stored.

It is worthy to mention that recently there have been efforts to improve the performance of staggered [102] and monolithic [108] solvers by employing over-relaxation and specialized line search techniques. It should be pointed out that the algorithm

given in Figure 4.1 is usually referred to as the *multi-pass* staggered scheme since it involves multiple iterations of the staggered solver until convergence is reached. One may simplify this scheme and utilize the *single-pass* staggered scheme where it is deemded that the staggered solver converges after only one iteration [66,67]. It can be readily seen that the single-pass scheme is faster compared to the multi-pass one; however, based on our experience, the multi-pass staggered solver is more robust and larger time increments can be taken without loss of accuracy.

4.2 Finite element method

Finite element method is a powerful numerical tool for solving differential equations arising in engineering and mathematical physics. In order to conduct an FE analysis, one needs to discretize the computational domain into non-overlapping subdomain, namely *elements*. Elements generally have simple geometrical shapes such as tetrahedrons. Each element is associated with n_{npe} nodes and its volume at time t is denoted by $\Omega_{e,t}$. Each degree of freedom (DOF), i.e. displacements and order parameter, is interpolated within an element as:

$$q = \sum_{i=1}^{n_{npe}} N_i^e q_i^e \tag{4.3}$$

in which q is a degree of freedom. q_i^e and N_i^e respectively denote the DOF and shape function corresponding to the *i-th* node of the element. There are in general

4 DOFs in 3D simulations of crack phase modeling, 3 DOFs corresponding to the 3 displacement components along the Cartesian axes and 1 DOF corresponding to the order parameter. Following Equation 4.3, the displacement $\mathbf{u} = [u_x, u_y, u_z]^T$ and order parameter s can be interpolated within an element as:

$$\mathbf{u} = [N_u^e]\,\{u^e\} \tag{4.4a}$$

$$s = [N_s^e]\,\{s^e\} \tag{4.4b}$$

where

$$[N_u^e] = \begin{bmatrix} N_1^e & 0 & 0 & N_2^e & 0 & 0 & \cdots & N_{n_{npe}}^e & 0 & 0 \\ 0 & N_1^e & 0 & 0 & N_2^e & 0 & \cdots & 0 & N_{n_{npe}}^e & 0 \\ 0 & 0 & N_1^e & 0 & 0 & N_2^e & \cdots & 0 & 0 & N_{n_{npe}}^e \end{bmatrix} \tag{4.5a}$$

$$[N_s^e] = \begin{bmatrix} N_1^e & N_2^e & \cdots & N_{n_{npe}}^e \end{bmatrix} \tag{4.5b}$$

$$\{u^e\} = \begin{bmatrix} u_{x1}^e & u_{y1}^e & u_{z1}^e & u_{x2}^e & u_{y2}^e & u_{z2}^e & \vdots & u_{x\,n_{npe}}^e & u_{y\,n_{npe}}^e & u_{z\,n_{npe}}^e \end{bmatrix}^T \tag{4.5c}$$

$$\{s^e\} = \begin{bmatrix} s_1^e & s_2^e & \vdots & s_{n_{npe}}^e \end{bmatrix}^T \tag{4.5d}$$

It is often required to calculate the gradient of DOFs within an element. It can readily seen that the gradient of displacement and order parameter within an element

can be obtained as:

$$\frac{\partial \mathbf{u}}{\partial \mathbf{X}} = \begin{bmatrix} \frac{\partial u_x}{\partial x} & \frac{\partial u_x}{\partial y} & \frac{\partial u_x}{\partial z} & \cdots & \frac{\partial u_z}{\partial x} & \frac{\partial u_z}{\partial y} & \frac{\partial u_z}{\partial z} \end{bmatrix}^T = [G^e_{ux}] \{u^e\} \tag{4.6a}$$

$$\frac{\partial s}{\partial \mathbf{X}} = \begin{bmatrix} \frac{\partial s}{\partial x} & \frac{\partial s}{\partial y} & \frac{\partial s}{\partial z} \end{bmatrix}^T = [G^e_{sx}] \{s^e\} \tag{4.6b}$$

with

$$[G^e_{ux}] = \begin{bmatrix} \frac{\partial N^e_1}{\partial \mathbf{x}} & \mathbf{0} & \mathbf{0} & \frac{\partial N^e_2}{\partial \mathbf{x}} & \mathbf{0} & \mathbf{0} & \cdots & \frac{\partial N^e_{nnpe}}{\partial \mathbf{x}} & \mathbf{0} & \mathbf{0} \\ \mathbf{0} & \frac{\partial N^e_1}{\partial \mathbf{x}} & \mathbf{0} & \mathbf{0} & \frac{\partial N^e_2}{\partial \mathbf{x}} & \mathbf{0} & \cdots & \mathbf{0} & \frac{\partial N^e_{nnpe}}{\partial \mathbf{x}} & \mathbf{0} \\ \mathbf{0} & \mathbf{0} & \frac{\partial N^e_1}{\partial \mathbf{x}} & \mathbf{0} & \mathbf{0} & \frac{\partial N^e_2}{\partial \mathbf{x}} & \cdots & \mathbf{0} & \mathbf{0} & \frac{\partial N^e_{nnpe}}{\partial \mathbf{x}} \end{bmatrix} \tag{4.7a}$$

$$[G^e_{sx}] = \begin{bmatrix} \frac{\partial N^e_1}{\partial \mathbf{x}} & \frac{\partial N^e_2}{\partial \mathbf{x}} & \cdots & \frac{\partial N^e_{nnpe}}{\partial \mathbf{x}} \end{bmatrix} \tag{4.7b}$$

$[G^e_{ux}]$ and $[G^e_{sx}]$ are respectively referred to as the gradient operator for the displacement and order parameter in the current configuration. Replacing $\mathbf{x}$ with $\mathbf{X}$ in Equation 4.7, one can obtain the gradient operators in the reference configuration, i.e. $[G^e_{uX}]$ and $[G^e_{sX}]$.

4.3 Volumetric locking in linear tetrahedral elements

Image-based crystal plasticity finite element analysis of metallic alloys have received significant attention from the material modeling community since it allows the underlying microstructure to directly affect the mechanical response [8, 110]. This enables the modelers to understand the sensitivity of mechanical properties to the morphological and crystallographic attributes of the polycrystalline microstructure. The statistically equivalent representative volume elements (SERVEs) often consist of grains with complex irregular geometries. Enforcing the conformity of finite element mesh to these complex morphologies makes it almost impossible for commercial mesh generating software packages to discretize the computational domain into brick elements [12]. Tetrahedral elements, on the other hand, can properly conform to these geometries. Moreover, implementation of linear tetrahedral elements (TET4) into any existing FE code is straight-forward due to their simple formulation.

It is been observed that linear tetrahedral elements suffer from severe volumetric locking in modeling (nearly-) incompressible materials [31–35]. This is of great significance for crystal plasticity simulations since plasticity in metals is essentially isochoric. *Incompressibility constraint ratio*, defined as the ratio of number of available DOFs to the number of incompressibility constraints in a finite element mesh, is a metric, used for evaluating the performance of an element in modeling incompressible

or nearly incompressible deformations. An optimal value for the incompressibility constraint ratio is 3 in 3D meshes. Low incompressibility constraint ratio denotes a mesh where there are not enough DOFs to accommodate the incompressibility conditions and therefore causing the volumetric locking. Large spurious hydrostatic stresses, checker-board patterned pressure field and under-estimation of displacement field are the main artifacts of volumetric locking observed in finite element simulations. This volumetric phenomenon, commonly ignored by most CPFE modelers who focus on the development of constitutive laws, can be detrimental to the simulation results and result in erroneous predictions. In this section, a simple example is first outlined to show volumetric locking in TET4 elements. Then the concept of F-bar-patch element is introduced and it is shown how this element can help one overcome volumetric locking in crystal plasticity simulations. The formulation and results for F-bar-patch element has been published in [111].

4.3.1 Demonstration of volumetric locking

A simple example is given in this section to demonstrate the presence of volumetric locking in TET4 elements in modeling (nearly-) incompressible materials. Consider an elastic bar of dimensions $4 \times 2 \times 2$ units with Young's modulus $E = 1\ GPa$. Poisson's ratio is set to 0.4999 to impose incompressibility. The bar is discretized into 6 TET4 elements, as shown in Figure 4.2, and the nodal coordinates and element connectivity list are given in Table 4.1.

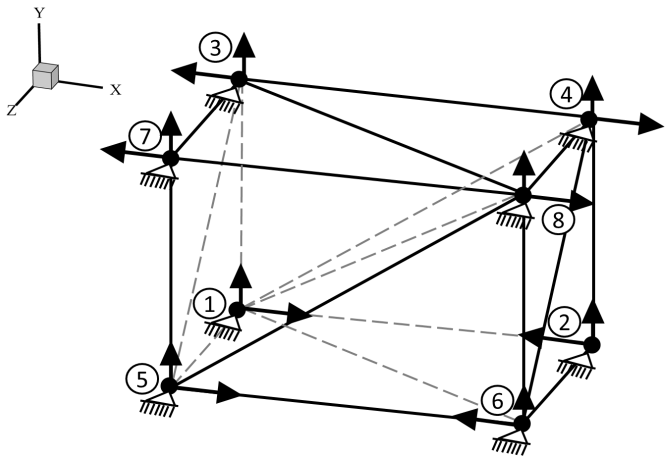

Figure 4.2: elastic bar consisting of 6 TET4 elements subject to nodal displacements

Node ID	1	2	3	4	5	6	7	8
Coordinates	-2,-1,-1	2,-1,-1	-2, 1,-1	2, 1,-1	-2,-1,1	2,-1,1	-2,1,1	2,1,1

Element ID	1	2	3	4	5	6
Connectivity	1, 3, 8, 4	1, 3, 5, 8	3, 5, 8, 7	1, 2, 4, 6	1, 6, 8, 5	1, 4, 8, 6

Table 4.1: Nodal coordinates and element connectivity for the FE model in Figure 4.2

All the nodal points are subjected to Dirichlet conditions prescribed by:

$$u_x = \frac{xy}{2}, \qquad u_y = \frac{x^2}{4} - \frac{\nu}{4(1-\nu)}y^2, \qquad u_z = 0 \tag{4.8}$$

The normal components of the linear strain tensor are analytically obtained as:

$$e_{xx} = \frac{y}{2},\ e_{yy} = -\frac{\nu y}{2(1-\nu)},\ e_{zz} = 0 \tag{4.9}$$

The volumetric strain is given as $e_{xx} + e_{yy} + e_{zz} = \frac{1-2\nu}{2(1-\nu)}y$ which is clearly dependent on the Poisson's ratio ν and position y. Under incompressibility conditions, i.e. $\nu = 0.4999$, the volumetric strain is nearly zero. However, for TET4 elements, the volumetric strain is clearly non-zero as listed in table 4.2. The large volumetric strains induce high spurious dilatational energy, resulting in element locking and high stresses. This simple example highlights the importance of alleviating volumetric locking in problems involving incompressible modes of deformation.

Strain Component	Element ①	Element ②	Element ③	Element ④	Element ⑤	Element ⑥
e_{xx}	0.5	0.5	0.5	-0.5	-0.5	-0.5
e_{yy}	0	0	0	0	0	0
Volumetric	0.5	0.5	0.5	-0.5	-0.5	-0.5

Table 4.2: Strain components for each TET4 element of the FE model in Figure 4.2

4.3.2 F-bar-patch element

In an FE mesh, the incompressibility requirements are enforced at every integration point of an element. If there are insufficient number of DOFs to accommodate these incompressibility requirements, the problem would be over-constrained and volumetric locking occurs. This volumetric phenomenon takes place in all elements such as brick and tetrahedral elements. Volumetric locking could be alleviated if the number of incompressibility enforcements is reduced for a given number of DOFs.

de Souza Neto et al. [43] proposed *F-bar element* to overcome volumetric locking in brick elements. The idea behind F-bar formulation is to perform the constitutive calculation with a modified deformation gradient such that the incompressibility constraint is only enforced at the centroid of the element instead of enforcing it at all the integration points. In order to achieve this goal, deformation gradient evaluated at a given integration point is first multiplicatively decomposed into volumetric $\mathbf{F}_{vol}$ and isochoric (deviatoric) $\mathbf{F}_{iso}$ components as

$$\mathbf{F} = \mathbf{F}_{iso}\,\mathbf{F}_{vol} \quad \text{where} \quad \mathbf{F}_{iso} = (\det \mathbf{F})^{-\frac{1}{3}}\,\mathbf{F} \quad \text{and} \quad \mathbf{F}_{vol} = (\det \mathbf{F})^{\frac{1}{3}}\,\mathbf{I} \tag{4.10}$$

The modified deformation gradient, *F-bar*, is then obtained by replacing $\mathbf{F}_{vol}$ evaluated at the integration point by the corresponding one evaluated at the centroid of the element $(\mathbf{F}_0)_{vol}$; that is,

$$\bar{\mathbf{F}} = \mathbf{F}_{iso}\left(\mathbf{F}_0\right)_{vol} = \left(\frac{\det \mathbf{F}_0}{\det \mathbf{F}}\right)^{\frac{1}{3}} \mathbf{F} \tag{4.11}$$

Here $\mathbf{F}_0$ denotes the deformation gradient at the centroid of the element. One can immediately see that utilization of this modified deformation gradient in the constitutive calculations will result in enforcement of incompressibility at the centroid of the element. In brick elements with 8 integration points per element, this approach reduces the number of incompressibility constraints by 8 times.

While the F-bar formulation is very effective for elements with multiple integrations points, this formulation would not alleviate volumetric locking for linear tetrahedral elements. It can be easily observed that $\bar{\mathbf{F}}$ will be equal to $\mathbf{F}$ in TET4 elements with only 1 integration point per element; that is, the number of incompressibility constraints is not reduced. de Souza Neto et al. [34] proposed *F-bar-patch* element (FP element) to overcome volumetric locking in meshes of TET4 elements. The idea behind F-bar-patch formulation is very similar to the F-bar one but it revolves around reducing the number of incompressibility constraints by enforcing these constraints over *patches* of elements. F-bar-patch formulation requires the elements in the mesh be assigned to non-overlapping patches, as illustrated in Figure 4.3 for a 2D mesh of triangular elements. The modified deformation gradient of element e in a patch $\mathscr{P}$ is obtained as:

$$\bar{\mathbf{F}}_e = \left(\frac{\Omega_{\mathscr{P},t}}{\Omega_{\mathscr{P},0}\ \det \mathbf{F}_e}\right)^{\frac{1}{3}} \mathbf{F}_e \tag{4.12}$$

where $\Omega_{\mathscr{P},0}$ and $\Omega_{\mathscr{P},t}$ are respectively the reference and current volumes of the patch $\mathscr{P}$, calculated as:

$$\Omega_{\mathscr{P},0} = \sum_{e \in \mathscr{P}} \Omega_{e,0} \tag{4.13a}$$

$$\Omega_{\mathscr{P},t} = \sum_{e \in \mathscr{P}} \Omega_{e,t} \tag{4.13b}$$

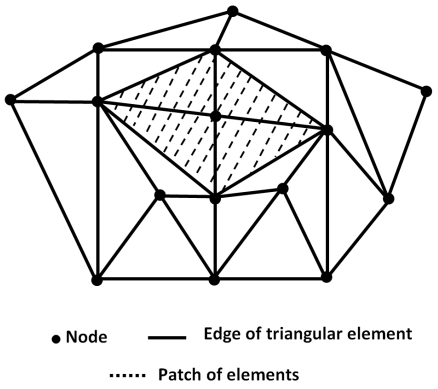

Figure 4.3: Illustration of a patch of elements in 2D

***Remark* 1** *Volumetric locking is reduced further as more elements are added to the patch. However, caution should be practiced as it has been observed that the presence of too many elements in a patch may result in spurious energy modes. It was inferred through numerical experimentation that 8 elements per patch is adequate for 3D problems to alleviate volumetric locking without inciting spurious mechanisms [35]*

***Remark* 2** *It can be readily seen that the F-bar-patch formulation reduces to the conventional tetrahedral element formulation if each element is identified with a patch.*

***Remark* 3** *The slip systems are not continuous across the grain boundaries in polycrystalline microstructures; therefore, the plastic strain is not continuous across the grain boundaries. Since the elements on either side of the grain boundary experience different levels of plasticity, it is not logical to include elements belonging to different grains in one patch. In other words, element patches should conform to grain structure and may not cross the grain boundaries.*

4.3.3 Numerical examples

Before studying the effectiveness of F-bar-patch formulation in fracture problems, it is instructive to investigate the competency of this formulation in alleviating volumetric locking in non-degrading materials. In this section, we solve problems involving only the displacement field. Two alloys, namely Ti6Al and magensium AZ31, are considered for this study. The material properties and details of the constitutive models are given in Cheng et al [111]. The results of the F-bar-patch element are compared with brick elements with B-bar stabilization (when possible) and locally integrated B-bar TET4 (LIB) element presented in [111].

4.3.3.1 Element patch test

Patch test in finite element method is a simple indicator whether an element can replicate a piece-wise linear solution field [112]. It is a necessary condition for any element to pass the patch test. A $20 \times 20 \times 40$ cube is discretized into 48 TET4

elements with 8 nodes on the outer surfaces and 13 nodes inside the cube. The material is assumed to be isotropic, linear elastic. Nodal displacements on the outer surfaces are prescribed using linear functions as:

$$\triangle u_x = \frac{z+20}{200} - \frac{x-10}{100}, \qquad \triangle u_y = \frac{z+20}{200} - \frac{y-10}{100}, \qquad \triangle u_z = 0 \tag{4.14}$$

A norm of the displacement error is defined as:

$$\overline{err}_{dis} = \frac{\sum_{\alpha=1}^{8}\sum_{i=1}^{3}\left(\mathbf{u}_{\alpha\ i}^{exact} - \mathbf{u}_{\alpha\ i}^{FE}\right)^2}{\sum_{\alpha=1}^{8}\sum_{i=1}^{3}\left(\mathbf{u}_{\alpha\ i}^{exact}\right)^2} \tag{4.15}$$

The error norm for FP element is less than 2.22×10^{-15}; hence, it passes the standard patch test.

4.3.3.2 Bending of an elastic beam

In this example, deformation of a nearly incompressible elastic beam under bending is studied, as shown in Figure 4.4. The material is isotropic, linear elastic with Young's modulus $E = 300MPa$ and Poisson ratio $\nu = 0.4999$. Dimensions of the beam are $4m \times 1m \times 1m$ and is discretized into 31758 elements with 6513 nodes.

To generate a *reference solution*, the beam is also discretized into 4000 brick elements and B-bar stabilization is utilized to overcome volumetric locking [113]. The maximum tip deflections for different elements are reported in Table 4.3 where it can be clearly shown that the standard TET4 element suffers from severe volumetric locking and thus resulting in very stiff behavior. The result predicted by the FP elements

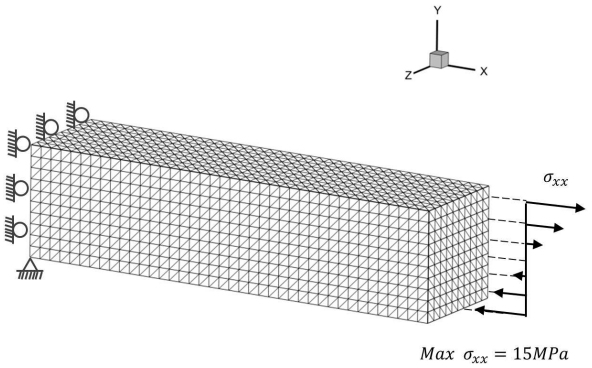

Figure 4.4: Mesh and boundary conditions for the elastic beam bending problem

is comparable with those of the reference solution and LIB element, indicating that volumetric locking is successfully overcome.

	brick element with B-bar stabilization	Standard TET4 element	LIB element	FP element
tip deflection	0.785m	0.271m	0.773m	0.779m

Table 4.3: Maximum tip deflection in the elastic beam bending problem using different element formulations

Convergence rate of the FP element is studied next. 5 different meshes consisting of 343, 845, 1246, 2929, 6513 nodes are constructed. Figure 4.5 shows the tip deflection predicted by the FP elements with a patch size of 4 (FP4) and 8 tetrahedrons (FP8). The dashed-line denotes the reference solution obtained through 8-noded brick

elements with B-bar stabilization. As expected, FP8 element shows a softer response compared to that of FP4 since FP8 element reduces the incompressibility constraints further.

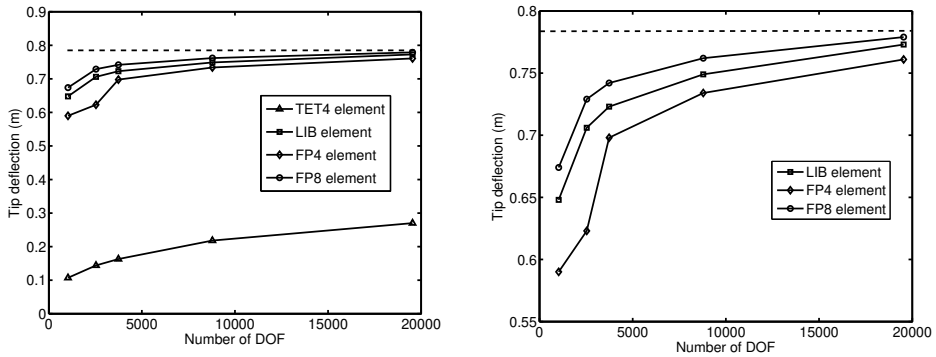

(a) (b)

Figure 4.5: (a) Convergence of the tip deflection for different element formulations. The dashed line corresponds to the reference solution predicted by 8-noded brick element with B-bar stabilization. (b) zoom-in view of (a) showing the difference between LIB, FP4 and FP8 elements.

4.3.3.3 Bicrystal compression test

To investigate the detrimental effects of volumetric locking in crystal plasticity simulations, uniaxial compression of a bicrystal Mg AZ31 sample of size $20\mu m \times 20\mu m \times 10\mu m$ is simulated. Seven meshes of tetrahedral elements, consisting of 766, 1106, 1583, 2742, 4400, 6421 and 11862 nodes are generated. The boundary conditions

are shown in Figure 4.6a. The Bunge Euler angles for crystal 1 and 2 are $[0°, 0°, 0°]$ and $[0°, 90°, 0°]$, respectively. From Schmid factor analysis, plastic deformation is expected to occur primarily on $\langle c+a \rangle$ pyramidal plane in crystal 1 and $\langle a \rangle$ prismatic plane in crystal 2. Due to the presence of grain boundary in the sample, the stress state deviates from the uniform uniaxial one close to the grain boundary, promoting slip activity on other slip planes in the vicinity of the grain boundary.

The distribution of loading direction stress σ_{zz} is shown in Figure 4.6. It is observed that very high stress concentrations are predicted using the standard TET4 elements close to the grain boundary. Accepting the results predicted by the brick element as the reference solution, the Cauchy stress error measure is defined as:

$$\|e\|_{L2} = \frac{\left[\int_\Omega \left(\sigma_{ij} - \sigma_{ij}^{ref}\right)\left(\sigma_{ij} - \sigma_{ij}^{ref}\right) d\Omega\right]^{\frac{1}{2}}}{\left(\int_\Omega \sigma_{ij}\sigma_{ij} d\Omega\right)^{\frac{1}{2}}} \tag{4.16}$$

where $\boldsymbol{\sigma}$ and $\boldsymbol{\sigma}^{ref}$ are the solution and reference Cauchy stress tensors, respectively. The error plots for different elements with increasing mesh densities are shown in Figure 4.7. The average convergence rate for LIB and FP elements is 0.75. It is clear that the FP element exhibits better results compared to the standard TET4 elements in CPFE simulations.

The hydrostatic stress at the grain boundary is plotted in Figure 4.8 where large hydrostatic stresses are observed with conventional TET4 elements. Consistent with the results of the 8-noded brick element, FP elements significantly alleviate this problem and exhibit a saturation of the hydrostatic stress. It is observed that all element

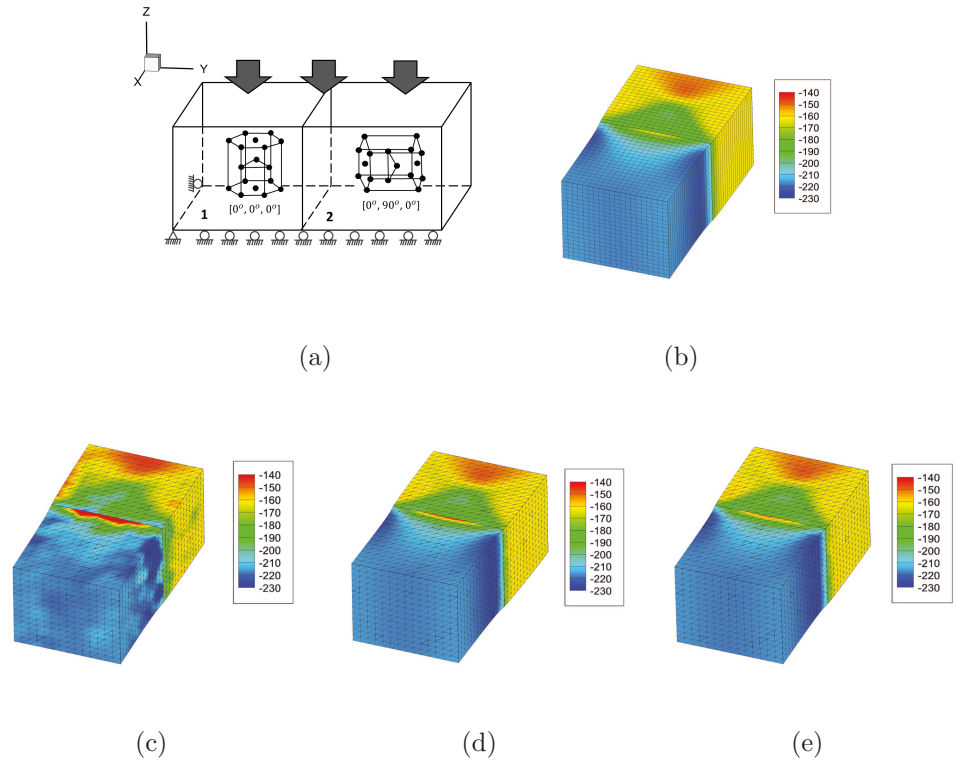

Figure 4.6: (a) Illustration of the boundary conditions and the crystallographic orientations for the constant strain rate compression test on a magnesium AZ31 alloy bicrystal; distribution of loading direction stress σ_{zz} in the deformed configuration at 5% strain using simulation results of: (b) 8-noded brick element using B-bar method with a mesh of 18081 nodes, (c) standard TET4 element with a mesh of 11862 nodes, (d) LIB element with a mesh of 11862 nodes, and (e) FP element with a mesh of 11862 nodes.

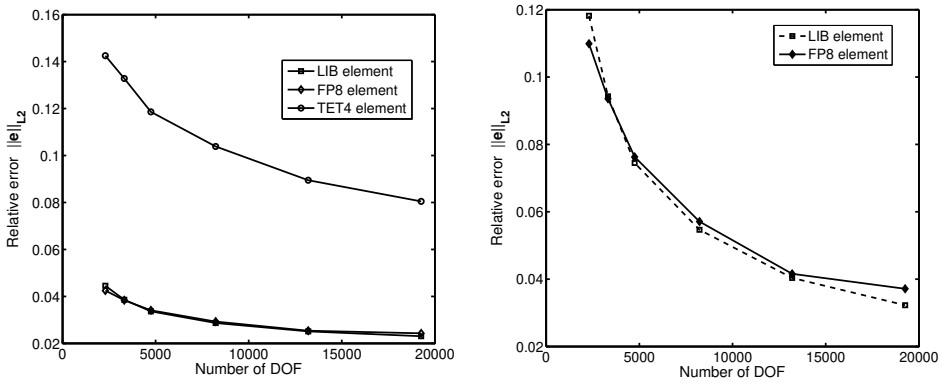

(a) (b)

Figure 4.7: (a) Error plot of $\|e\|_{L2}$ with increasing degrees of freedom (DOF). (b) zoom-in view of (a) to compare the error between FP8 element and LIB element

formulations predict nearly the same values of the von Mises stress, signifying that the deviatoric strain energy is nearly unaffected by the volumetric locking in this bicrystal problem.

4.3.3.4 Bending of a polycrystalline cantilever beam

The effect of volumetric locking on bending of a polycrystalline $Ti6Al$ cantilever beam is investigated in this example. The beam is $2000\mu m$ long with a square cross-section of $300 \times 300\mu m^2$, consisting of 327 grains. The beam is discretized into 276544 TET4 elements as shown in Figure 4.9. The beam is clamped on the left end and a linearly increasing shear traction is imposed in the Y direction on the right end to bend the beam mainly about Z direction.

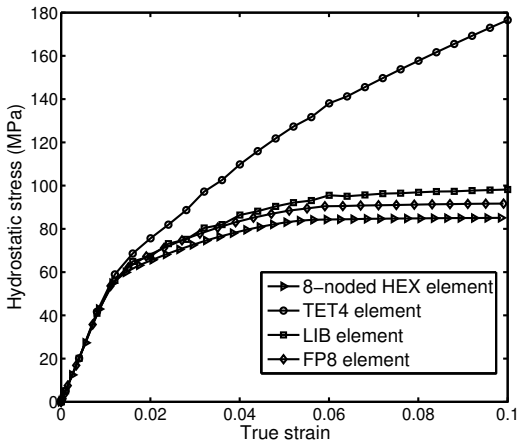

Figure 4.8: Evolution of maximum of local hydrostatic stress with strain for different element formulations.

Figure 4.9 shows the distribution of the effective plastic strain predicted by different element formulations. The response is primarily elastic at the early stages of deformation; hence, all element formulations perform equally well. At later stages of deformation, plasticity occurs close to the clamped end where maximum bending moment takes place. This facilitates the formation of a plastic hinge near the clamped end, promoting further rotation of the beam. Volumetric locking leads to less plastic strain in TET4 element and significant under-prediction of the tip deflection.

As mentioned before, checker-board distribution pattern of pressure is an artifact of volumetric locking. Figure 4.10 shows the checker-board patter of pressure in TET4 results, specifically close to the clamped end where plastic deformation occurs. These fluctuations are nearly alleviated in the results predicted by the FP and LIB elements.

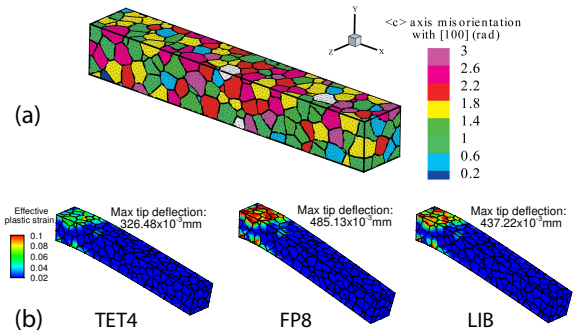

Figure 4.9: (a) Schematic of a 327-grain $Ti6Al$ polycrystalline beam showing misorientation distribution; (b) distribution of effective plastic strain for different element formulations after $324s$

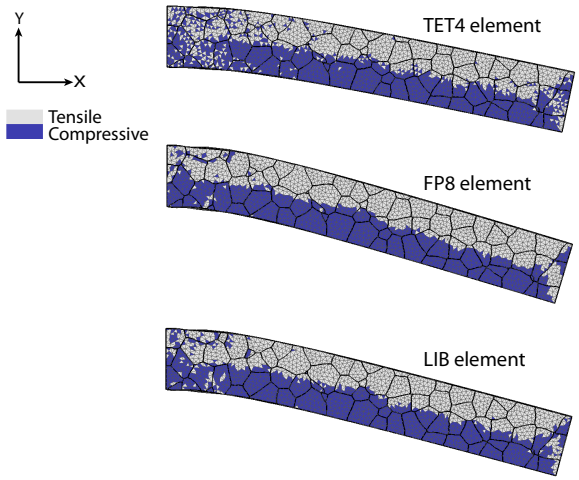

Figure 4.10: Distribution of hydrostatic stress on XY face of the beam after $324s$ using different element formulations.

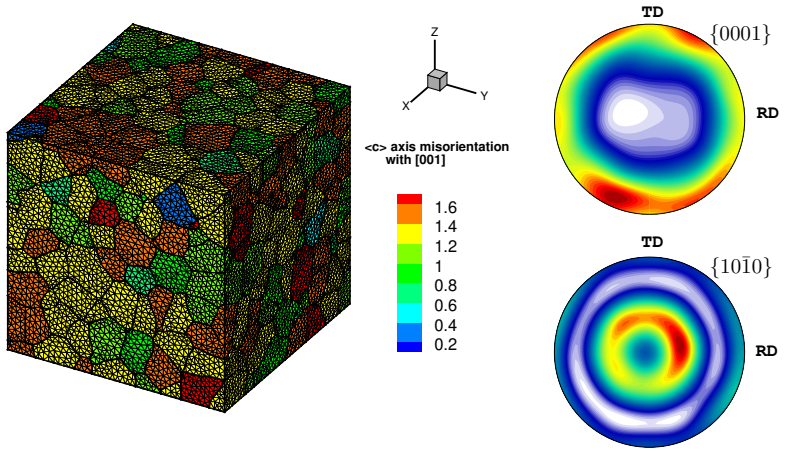

(a) (b)

Figure 4.11: A 540-grain polycrystalline microstructure of Ti6Al alloy discretized into 583432 TET4 elements.

4.3.3.5 Constant strain-rate deformation of a polycrystalline microstructure

A statistically equivalent $680 \times 680 \times 680 \mu m^3$ $Ti6Al$ polycrystalline microstructure is reconstructed. This microstructure consists of 540 grains and is discretized into 583432 TET4 elements, as shown in Figure 4.11. A constant rate of deformation $\dot{\epsilon} = 9 \times 10^{-5} s^{-1}$ is applied in the [001] direction.

Figure 4.12a shows the results of CPFE simulations using different element formulations. As expected, all elements perform equally well in the elastic regime since the material is elastically compressible. With increasing plasticity, the response obtained from TET4 element suffers volumetric locking, showing a stiffer response with

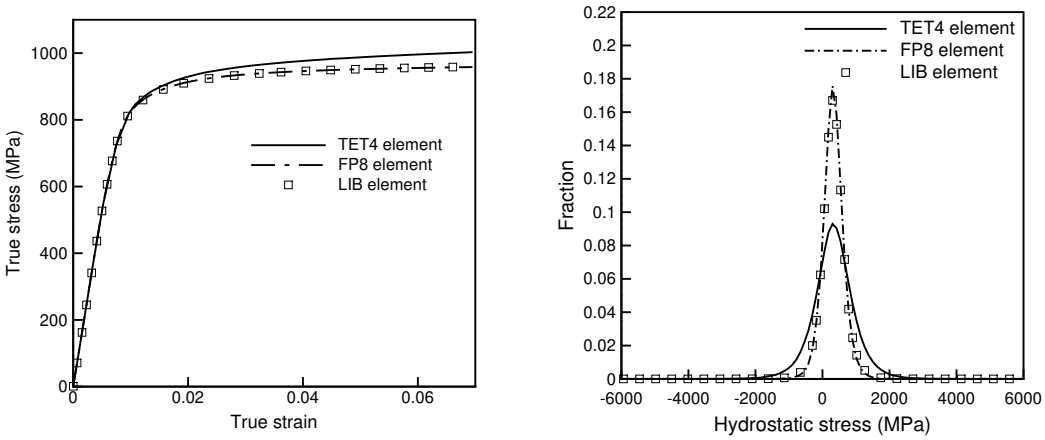

(a) (b)

Figure 4.12: Comparison of (a) loading-direction true stress-strain response of polycrystalline Ti-6Al alloy under uniaxial tension in the [001] direction, and (b) distribution of hydrostatic stress in the polycrystalline microstructure after 800s, by different methods.

a higher rate of hardening in comparison with the response predicted by FP8 and LIB elements. The distribution of hydrostatic stress after $800s$, corresponding to nearly %7 strain, is plotted in Figure 4.12b. It is clearly shown that TET4 element tends to over-predict hydrostatic stresses.

4.3.4 Modification of F-bar-patch element for fracture simulations

In finite element method, the mechanical response of an element is dependent on the state of material at its integration points. As the order parameter in the integration point of an element increases from 0 to 1, the material integrity is gradually lost and the element loses its ability to withstand volumetric expansions. In other words, if the material is undamaged ($s = 0$), volumetric expansion of the element gives rise to stress. However, if the material is fully damaged ($s = 1$), volumetric expansion of the element would not induce any stress. It is worthy to note that the material point will induce stress under volumetric contraction, regardless of the value of order parameter. This argument on the volumetric changes of degrading materials is the premise of development of the elastic free energy density described in Section 5.2.

Application of F-bar-patch formulation could be theoretically and numerically problematic if, in a patch, there are degraded elements which can easily undergo volumetric expansions. In order to comprehend the numerical problem with the F-bar-patch formulation in fracture simulations, consider a patch $\mathscr{P}$ consisting of several elements. Let a few elements in the patch be fully damaged, unable to withstand volumetric expansions while the other elements in the patch are undamaged. Due to the presence of these damaged elements, the current volume of the patch, $\Omega_{\mathscr{P},t}$

in Equation 4.13b, could be much larger compared to the reference volume of the patch, $\Omega_{\mathscr{P},0}$ in Equation 4.13a. It can be easily seen from Equation 4.12 that this will yield unreasonable modified deformation gradient tensors for the undamaged elements in the patch. Moreover, the stress in the degraded elements drop as the order parameter increases; therefore, damaged elements primarily experience elastic deformation. With this consideration, it is not justifiable from a theoretical point of view to keep compressible elastic damaged elements in the same patch with the incompressible plastic undamaged elements.

In order to address this issue in F-bar-patch elements, one needs to modify the formulation such that elements experiencing damage gradually leave the patch as the order parameter increases. This can be thought as an adaptive restructuring of patches as fracture evolves in the computational domain. This can be achieved by introducing the order parameter in the F-bar-patch formulation. The modified F-bar-patch for element e in patch $\mathscr{P}$ is given as:

$$\bar{\mathbf{F}}_e = \left(\frac{v_{r\mathscr{P}}}{\det \mathbf{F}_e} \right)^{\frac{1}{3} g_{\mathscr{P}}(s_e)} \mathbf{F}_e \tag{4.17}$$

where $v_{r\mathscr{P}}$ is the ratio of current effective volume of the patch to its reference effective volume:

$$v_{r\mathscr{P}} = \frac{\sum\limits_{e \in \mathscr{P}} g_{\mathscr{P}}(s_e) \Omega_{e,t}}{\sum\limits_{e \in \mathscr{P}} g_{\mathscr{P}}(s_e) \Omega_{e,0}} \tag{4.18}$$

Here s_e denotes the order parameter at the integration point of an element. $g_{\mathscr{P}}$ is

a function of order parameter such that $g_{\mathscr{P}}(0) = 1$ and $g_{\mathscr{P}}(1) = 0$. In this work, a polynomial of order m is used to represent $g_{\mathscr{P}}$:

$$g_{\mathscr{P}}(s) = (1 - s)^m \tag{4.19}$$

where m is a positive integer number, here taken to be 10.

To understand how the modification of F-bar-patch formulation given in Equation 4.17 automatically restructures the patch, a simple example is set up. Let's consider a patch $\mathscr{P}$ consisting of three elements. Table 4.4 describes how this modification works for different scenarios.

4.4 Nonlinear FE derivations for displacement field

Assuming that the internal state variables, displacement and crack phase fields are known at time $t - \triangle t$, it is shown in this section how one can use the nonlinear FEM to obtain the solution field at time t. Subscripts $t - \triangle t$ and 0 are used to denote variables at time $t - \triangle t$ and 0, respectively. Unless explicitly mentioned, the subscript t is dropped from all variables pertaining to the current time, for the sake of brevity.

scenario	$v_{r\mathscr{P}}$	F-bar in Equation 4.17	comments
$s_1 = 0$ $s_2 = 0$ $s_3 = 0$	$\frac{\Omega_{1,t}+\Omega_{2,t}+\Omega_{3,t}}{\Omega_{1,0}+\Omega_{2,0}+\Omega_{3,0}}$	$\bar{\mathbf{F}}_1 = \left(\frac{v_{r\mathscr{P}}}{\det \mathbf{F}_1}\right)^{\frac{1}{3}} \mathbf{F}_1$ $\bar{\mathbf{F}}_2 = \left(\frac{v_{r\mathscr{P}}}{\det \mathbf{F}_2}\right)^{\frac{1}{3}} \mathbf{F}_2$ $\bar{\mathbf{F}}_3 = \left(\frac{v_{r\mathscr{P}}}{\det \mathbf{F}_3}\right)^{\frac{1}{3}} \mathbf{F}_3$	When all elements are undamaged, the modified F-bar-patch formulation reduces to the original one given in Equation 4.12
$s_1 = 1$ $s_2 = 0$ $s_3 = 0$	$\frac{\Omega_{2,t}+\Omega_{3,t}}{\Omega_{2,0}+\Omega_{3,0}}$	$\bar{\mathbf{F}}_1 = \mathbf{F}_1$ $\bar{\mathbf{F}}_2 = \left(\frac{v_{r\mathscr{P}}}{\det \mathbf{F}_2}\right)^{\frac{1}{3}} \mathbf{F}_2$ $\bar{\mathbf{F}}_3 = \left(\frac{v_{r\mathscr{P}}}{\det \mathbf{F}_3}\right)^{\frac{1}{3}} \mathbf{F}_3$	Element 1 leaves the patch and is treated as a standard TET4 element. Incompressibility is enforced over the new patch consisting of elements 2 and 3
$s_1 = 1$ $s_2 = 1$ $s_3 = 1$	$\frac{\Omega_{1,t}+\Omega_{2,t}+\Omega_{3,t}}{\Omega_{1,0}+\Omega_{2,0}+\Omega_{3,0}}$	$\bar{\mathbf{F}}_1 = \mathbf{F}_1$ $\bar{\mathbf{F}}_2 = \mathbf{F}_2$ $\bar{\mathbf{F}}_3 = \mathbf{F}_3$	When all elements are fully damaged, the patch is virtually destructed and each element is treated as a standard TET4 element

Table 4.4: results of the modified F-bar-patch formulation given in Equation 4.17 for different scenarios

4.4.1 Derivation of weak form

The weak form corresponding to the Equation 3.39a is obtained as:

$$R_u\left(\mathbf{u}, \mathbf{w_u}\right) = \int_{\Omega_0} \left(\boldsymbol{\nabla}_{\mathbf{X}} \cdot \mathbf{P}\left(\mathbf{u}\right) + \mathbf{B} - \beta_{gu}\, \dot{\mathbf{u}}\right) \cdot \mathbf{w_u}\, d\Omega_0 = 0 \tag{4.20}$$

where $\mathbf{w_u}$ is the so-called *weight function* corresponding to the displacement field. Applying simple mathematical operations and using Equation 3.39c, the weak form can be rewritten as:

$$\begin{aligned} R_u\left(\mathbf{u}, \mathbf{w_u}\right) &= \int_{\Omega_0} \left[\boldsymbol{\nabla}_{\mathbf{X}} \cdot \left(\mathbf{w_u}\mathbf{P}\right) - \mathbf{P} \colon \boldsymbol{\nabla}_{\mathbf{X}}\mathbf{w_u} + \mathbf{B} \cdot \mathbf{w_u} - \beta_{gu}\, \dot{\mathbf{u}} \cdot \mathbf{w_u}\right]\, d\Omega_0 \\ &= \int_{\Omega_0} \left[-\mathbf{P} \colon \boldsymbol{\nabla}_{\mathbf{X}}\mathbf{w_u} + \mathbf{B} \cdot \mathbf{w_u} - \beta_{gu}\, \dot{\mathbf{u}} \cdot \mathbf{w_u}\right]\, d\Omega_0 + \int_{\Gamma_{0T}} \left(\mathbf{w_u}\mathbf{P}\right) \cdot \mathbf{N}\, d\Gamma_{0T} \\ &= \int_{\Omega_0} \left[-\mathbf{P} \colon \boldsymbol{\nabla}_{\mathbf{X}}\mathbf{w_u} + \mathbf{B} \cdot \mathbf{w_u} - \beta_{gu}\, \dot{\mathbf{u}} \cdot \mathbf{w_u}\right]\, d\Omega_0 + \int_{\Gamma_{0T}} \mathbf{T} \cdot \mathbf{w_u}\, d\Gamma_{0T} = 0 \end{aligned} \tag{4.21}$$

4.4.2 Linearization considering F-bar-patch formulation

The F-bar-patch element is used in the finite element simulations to alleviate volumetric locking. The procedure outlined in [34] is followed here to Linearize the weak form. As mentioned in Section 4.3.2, the modified deformation gradient given in Equation 4.17 is used for the constitutive calculations. Feeding $\bar{\mathbf{F}}$ to the constitutive model, one obtains the modified first Piola-Kirchhoff stress $\bar{\mathbf{P}} = \bar{\mathbf{P}}\left(\bar{\mathbf{F}}\right)$. Using Equa-

tion 4.17 and Piola transformation, one can express the first Piola-Kirchhoff stress $\mathbf{P}$ in terms of $\bar{\mathbf{P}}$ as:

$$\mathbf{P} = \left(\frac{v_{r\mathscr{P}}}{J}\right)^{-\frac{2}{3}g_{\mathscr{P}}} \bar{\mathbf{P}}\left(\bar{\mathbf{F}}\right) \tag{4.22}$$

where $J = \det \mathbf{F}$ is the Jacobian of deformation. Plugging Equation 4.22 into 4.21, one obtains

$$R_u\left(\mathbf{u}, \mathbf{w_u}\right) = \int_{\Omega_0} \left[-\left(\frac{v_{r\mathscr{P}}}{J}\right)^{-\frac{2}{3}g_{\mathscr{P}}} \bar{\mathbf{P}} \colon \boldsymbol{\nabla}_{\mathbf{X}} \mathbf{w_u} + \mathbf{B} \cdot \mathbf{w_u} - \beta_{gu}\, \dot{\mathbf{u}} \cdot \mathbf{w_u} \right] d\Omega_0 + \int_{\Gamma_{0T}} \mathbf{T} \cdot \mathbf{w_u}\, d\Gamma_{0T} = 0 \tag{4.23}$$

Since the first Piola-Kirchhoff stress is in general a nonlinear function of the displacement field, one needs to linearize the weak form. However before linearizing the weak form, it is beneficial to calculate the directional derivative of a few quantities which are functions of the displacement field $\mathbf{u}$. Table 4.5 tabulates the directional derivative of some scalar-valued and tensor-valued functions of $\mathbf{u}$ in direction $\mathbf{d_u}$.

Linearizing Equation 4.23 at $\mathbf{u}$ in direction $\mathbf{d_u}$, yields

$$\begin{aligned} R_u\left(\mathbf{u} + \mathbf{d_u}, \mathbf{w_u}\right) &= R_u\left(\mathbf{u}, \mathbf{w_u}\right) + DR_u\left(\mathbf{u}, \mathbf{w_u}\right)\left[\mathbf{d_u}\right] \\ &= R_u\left(\mathbf{u}, \mathbf{w_u}\right) + \left.\frac{d}{d\epsilon}\right|_{\epsilon=0} R_u\left(\mathbf{u} + \epsilon \mathbf{d_u}, \mathbf{w_u}\right) = 0 \end{aligned} \tag{4.24}$$

It is worthy to note that here linearization is not done w.r.t. the order parameter since a staggered solver is utilized and the order parameter is kept frozen. If one were

scalar-valued/tensor-valued function $\mathscr{A}(\mathbf{u})$	directional derivative $D\mathscr{A}(\mathbf{u})[\mathbf{d_u}] = \frac{d}{d\epsilon}\big\vert_{\epsilon=0} \mathscr{A}(\mathbf{u}+\epsilon\mathbf{d_u})$
$\mathbf{F} = \mathbf{I} + \boldsymbol{\nabla}_{\mathbf{X}}\mathbf{u}$	$\boldsymbol{\nabla}_{\mathbf{X}}\mathbf{d_u}$
$J = \det \mathbf{F}$	$J\mathbf{F}^{-T} \colon \boldsymbol{\nabla}_{\mathbf{X}}\mathbf{d_u}$
$v_{r\mathscr{P}} = \frac{\sum_{i\in\mathscr{P}} g_{\mathscr{P}i}\Omega_{i,t}}{\sum_{i\in\mathscr{P}} g_{\mathscr{P}i}\Omega_{i,0}} = \frac{\sum_{i\in\mathscr{P}} g_{\mathscr{P}i}J_i\Omega_{i,0}}{\sum_{i\in\mathscr{P}} g_{\mathscr{P}i}\Omega_{i,0}}$	$\frac{\sum_{i\in\mathscr{P}} g_{\mathscr{P}i}\Omega_{i,t}\mathbf{F}_i^{-T} \colon \boldsymbol{\nabla}_{\mathbf{X}}\mathbf{d}_{\mathbf{u}i}}{\sum_{i\in\mathscr{P}} g_{\mathscr{P}i}\Omega_{i,0}}$
$\frac{v_{r\mathscr{P}}}{J}$	$\frac{\sum_{i\in\mathscr{P}} g_{\mathscr{P}i}\Omega_{i,t}\left(\mathbf{F}_i^{-T} \colon \boldsymbol{\nabla}_{\mathbf{X}}\mathbf{d}_{\mathbf{u}i} - \mathbf{F}^{-T} \colon \boldsymbol{\nabla}_{\mathbf{X}}\mathbf{d_u}\right)}{J\sum_{i\in\mathscr{P}} g_{\mathscr{P}i}\Omega_{i,0}}$
$\bar{\mathbf{F}} = \left(\frac{v_{r\mathscr{P}}}{J}\right)^{\frac{1}{3}g_{\mathscr{P}}}\mathbf{F}$	$\frac{1}{3}g_{\mathscr{P}}\left(\frac{v_{r\mathscr{P}}}{J}\right)^{\frac{1}{3}g_{\mathscr{P}}-1}\frac{\sum_{i\in\mathscr{P}} g_{\mathscr{P}i}\Omega_{i,t}\left(\mathbf{F}_i^{-T} \colon \boldsymbol{\nabla}_{\mathbf{X}}\mathbf{d}_{\mathbf{u}i} - \mathbf{F}^{-T} \colon \boldsymbol{\nabla}_{\mathbf{X}}\mathbf{d_u}\right)}{J\sum_{i\in\mathscr{P}} g_{\mathscr{P}i}\Omega_{i,0}}\mathbf{F} + \left(\frac{v_{r\mathscr{P}}}{J}\right)^{\frac{1}{3}g_{\mathscr{P}}}\boldsymbol{\nabla}_{\mathbf{X}}\mathbf{d_u}$

Table 4.5: directional derivative of scalar-valued and tensor-valued functions of $\mathbf{u}$ in direction $\mathbf{d_u}$

interested in employing monolithic solvers, it would be necessary to linearize Equation 4.24 w.r.t. the order parameter, as well, to obtain the cross-stiffness matrix.

Following conventional finite element methodology, one can break the weak form integral over Ω_0 into integrals over individual elements $\Omega_{e,0}$ and then add up the resulting matrices and vectors using standard assembly techniques [112]. Therefore, in the following, weak form will be integrated over an element. Using the product rule and directional derivatives given in Table 4.5, the directional derivative of weak form in Equation 4.24 over element e can be expanded as:

$$
\begin{aligned}
&DR_{ue}\left(\mathbf{u}, \mathbf{w}_{\mathbf{u}}\right)\left[\mathbf{d}_{\mathbf{u}}\right] = \\
&\int_{\Omega_{e,0}} \left[\frac{2}{3} g_{\mathscr{P}} \left(\frac{v_{r\mathscr{P}}}{J}\right)^{-\frac{2}{3}g_{\mathscr{P}}-1} \boldsymbol{\nabla}_{\mathbf{X}}\mathbf{w}_{\mathbf{u}} \colon \frac{\sum\limits_{i\in\mathscr{P}} g_{\mathscr{P}i}\Omega_{i,t}\left(\mathbf{F}_i^{-T} \colon \boldsymbol{\nabla}_{\mathbf{X}}\mathbf{d}_{\mathbf{u}i} \;-\; \mathbf{F}^{-T} \colon \boldsymbol{\nabla}_{\mathbf{X}}\mathbf{d}_{\mathbf{u}}\right)}{J\sum\limits_{i\in\mathscr{P}} g_{\mathscr{P}i}\Omega_{i,0}} \bar{\mathbf{P}} \right] d\Omega_{e,0} - \\
&\int_{\Omega_{e,0}} \left[\frac{1}{3} g_{\mathscr{P}} \left(\frac{v_{r\mathscr{P}}}{J}\right)^{-\frac{1}{3}g_{\mathscr{P}}-1} \boldsymbol{\nabla}_{\mathbf{X}}\mathbf{w}_{\mathbf{u}} \colon \mathbb{A} \colon \frac{\sum\limits_{i\in\mathscr{P}} g_{\mathscr{P}i}\Omega_{i,t}\left(\mathbf{F}_i^{-T} \colon \boldsymbol{\nabla}_{\mathbf{X}}\mathbf{d}_{\mathbf{u}i} \;-\; \mathbf{F}^{-T} \colon \boldsymbol{\nabla}_{\mathbf{X}}\mathbf{d}_{\mathbf{u}}\right)}{J\sum\limits_{i\in\mathscr{P}} g_{\mathscr{P}i}\Omega_{i,0}} \mathbf{F} \right] d\Omega_{e,0} - \\
&\int_{\Omega_{e,0}} \left[\left(\frac{v_{r\mathscr{P}}}{J}\right)^{-\frac{1}{3}g_{\mathscr{P}}} \boldsymbol{\nabla}_{\mathbf{X}}\mathbf{w}_{\mathbf{u}} \colon \mathbb{A} \colon \boldsymbol{\nabla}_{\mathbf{X}}\mathbf{d}_{\mathbf{u}} \right] d\Omega_{e,0} - \\
&\int_{\Omega_{e,0}} \left[\mathbf{w}_{\mathbf{u}} \cdot \frac{\beta_{gu}}{\triangle t}\mathbf{d}_{\mathbf{u}} \right] d\Omega_{e,0}
\end{aligned}
\tag{4.25}
$$

Here the velocity field is approximated using backward difference method $\dot{\mathbf{u}} = \left(\mathbf{u} - \mathbf{u}_{t-\triangle t}\right)/\triangle t$. $\mathbb{A} = \partial\bar{\mathbf{P}}/\partial\bar{\mathbf{F}}$ is the first elasticity tensor [114]. It can be shown that the identity

$$
\left(\mathbf{F}^{-T} \colon \boldsymbol{\nabla}_{\mathbf{X}}\mathbf{r}\right)\mathbf{M} = \left(\mathbf{M} \otimes \mathbf{I}\right) : \boldsymbol{\nabla}_{\mathbf{x}}\mathbf{r} \tag{4.26}
$$

is valid for an arbitrary vector $\mathbf{r}$ and second order tensor $\mathbf{M}$. Using this identity, Equation 4.25 can be rewritten as:

$$
\begin{aligned}
&DR_{ue}\left(\mathbf{u},\mathbf{w_u}\right)\left[\mathbf{d_u}\right] = \\
&\int_{\Omega_{e,0}} \left[\frac{2}{3} g_{\mathscr{P}} \left(\frac{v_{r\mathscr{P}}}{J}\right)^{-\frac{2}{3}g_{\mathscr{P}}-1} \boldsymbol{\nabla}_{\mathbf{X}}\mathbf{w_u} \colon \left(\bar{\mathbf{P}} \otimes \mathbf{I}\right) : \frac{\sum\limits_{i\in\mathscr{P}} g_{\mathscr{P}i}\Omega_{i,t}\left(\boldsymbol{\nabla}_{\mathbf{x}}\mathbf{d_u}_i \; - \; \boldsymbol{\nabla}_{\mathbf{x}}\mathbf{d_u}\right)}{J\sum\limits_{i\in\mathscr{P}} g_{\mathscr{P}i}\Omega_{i,0}} \right] d\Omega_{e,0} - \\
&\int_{\Omega_{e,0}} \left[\frac{1}{3} g_{\mathscr{P}} \left(\frac{v_{r\mathscr{P}}}{J}\right)^{-\frac{1}{3}g_{\mathscr{P}}-1} \boldsymbol{\nabla}_{\mathbf{X}}\mathbf{w_u} \colon \mathbb{A} \colon \left(\mathbf{F} \otimes \mathbf{I}\right) : \frac{\sum\limits_{i\in\mathscr{P}} g_{\mathscr{P}i}\Omega_{i,t}\left(\boldsymbol{\nabla}_{\mathbf{x}}\mathbf{d_u}_i \; - \; \boldsymbol{\nabla}_{\mathbf{x}}\mathbf{d_u}\right)}{J\sum\limits_{i\in\mathscr{P}} g_{\mathscr{P}i}\Omega_{i,0}} \right] d\Omega_{e,0} - \\
&\int_{\Omega_{e,0}} \left[\left(\frac{v_{r\mathscr{P}}}{J}\right)^{-\frac{1}{3}g_{\mathscr{P}}} \boldsymbol{\nabla}_{\mathbf{X}}\mathbf{w_u} \colon \mathbb{A} \colon \boldsymbol{\nabla}_{\mathbf{X}}\mathbf{d_u} \right] d\Omega_{e,0} - \\
&\int_{\Omega_{e,0}} \left[\mathbf{w_u} \cdot \frac{\beta_{gu}}{\triangle t}\mathbf{d_u} \right] d\Omega_{e,0}
\end{aligned}
\tag{4.27}
$$

The spatial version of Equation 4.27 can be obtained by utilizing $\boldsymbol{\nabla}_{\mathbf{X}}\mathbf{w_u} = \left(\boldsymbol{\nabla}_{\mathbf{x}}\mathbf{w_u}\right)\mathbf{F}$, $\bar{\mathbf{F}} = \left(v_{r\mathscr{P}}/J\right)^{g_{\mathscr{P}}/3}\mathbf{F}$ and $\bar{J} = \det\bar{\mathbf{F}} = J\left(v_{r\mathscr{P}}/J\right)^{g_{\mathscr{P}}}$. In the following, the spatial version of each integral on the RHS of Equation 4.27 is obtained separately to simplify the derivations.

- The spatial version of the fourth integral on RHS of Equation 4.27

$$
\int_{\Omega_{e,0}} \left[\mathbf{w_u} \cdot \frac{\beta_{gu}}{\triangle t}\mathbf{d_u} \right] d\Omega_{e,0} = \int_{\Omega_{e,t}} \left[\mathbf{w_u} \cdot \frac{\beta_{gu}}{J\triangle t}\mathbf{d_u} \right] d\Omega_{e,t} \tag{4.28}
$$

- The spatial version of the third integral on RHS of Equation 4.27

$$
\begin{aligned}
&\int_{\Omega_{e,0}} \left[\left(\frac{v_{r\mathscr{P}}}{J} \right)^{-\frac{1}{3} g_{\mathscr{P}}} \boldsymbol{\nabla}_{\mathbf{X}} \mathbf{w}_{\mathbf{u}} \colon \mathbb{A} \colon \boldsymbol{\nabla}_{\mathbf{X}} \mathbf{d}_{\mathbf{u}} \right] \, d\Omega_{e,0} = \\
&\int_{\Omega_{e,t}} \left[\frac{1}{J} \left(\frac{v_{r\mathscr{P}}}{J} \right)^{-\frac{1}{3} g_{\mathscr{P}}} (\boldsymbol{\nabla}_{\mathbf{x}} \mathbf{w}_{\mathbf{u}} \, \mathbf{F}) : \mathbb{A} \colon (\boldsymbol{\nabla}_{\mathbf{x}} \mathbf{d}_{\mathbf{u}} \, \mathbf{F}) \right] \, d\Omega_{e,t} = \\
&\int_{\Omega_{e,t}} \left[\bar{J}^{-1} \left(\frac{\partial \mathbf{w}_{\mathbf{u}}}{\partial \mathbf{x}} \right)_{am} \mathbb{A}_{abkl} \left(\frac{\partial \mathbf{d}_{\mathbf{u}}}{\partial \mathbf{x}} \right)_{kn} \bar{F}_{mb} \bar{F}_{nl} \right] \, d\Omega_{e,t} = \\
&\int_{\Omega_{e,t}} \left[\left(\frac{\partial \mathbf{w}_{\mathbf{u}}}{\partial \mathbf{x}} \right)_{am} \mathbb{a}_{amkn} \left(\frac{\partial \mathbf{d}_{\mathbf{u}}}{\partial \mathbf{x}} \right)_{kn} \right] \, d\Omega_{e,t} = \\
&\int_{\Omega_{e,t}} \left[\boldsymbol{\nabla}_{\mathbf{x}} \mathbf{w}_{\mathbf{u}} \colon \mathbb{a} \colon \boldsymbol{\nabla}_{\mathbf{x}} \mathbf{d}_{\mathbf{u}} \right] \, d\Omega_{e,t}
\end{aligned}
\tag{4.29}
$$

where

$$
\mathbb{a}_{amkn} = \bar{J}^{-1} \mathbb{A}_{abkl} \bar{F}_{mb} \bar{F}_{nl} \tag{4.30}
$$

is the first spatial elasticity tensor.

- The spatial version of the second integral on RHS of Equation 4.27

$$\int_{\Omega_{e,0}} \left[\tfrac{1}{3} g_{\mathscr{P}} \left(\tfrac{v_{r\mathscr{P}}}{J}\right)^{-\frac{1}{3} g_{\mathscr{P}}{}^{-1}} \boldsymbol{\nabla}_{\mathbf{X}} \mathbf{w}_{\mathbf{u}} \colon \mathbb{A} \colon (\mathbf{F} \otimes \mathbf{I}) : \frac{\sum\limits_{i \in \mathscr{P}} g_{\mathscr{P}} i \Omega_{i,t} (\boldsymbol{\nabla}_{\mathbf{x}} \mathbf{d}_{\mathbf{u}i} - \boldsymbol{\nabla}_{\mathbf{x}} \mathbf{d}_{\mathbf{u}})}{J \sum\limits_{i \in \mathscr{P}} g_{\mathscr{P}} i \Omega_{i,0}} \right] d\Omega_{e,0} =$$

$$\int_{\Omega_{e,t}} \left[\tfrac{1}{3} g_{\mathscr{P}} \bar{J}^{-1} v_{r\mathscr{P}}^{-1} \left(\tfrac{\partial \mathbf{w}_{\mathbf{u}}}{\partial \mathbf{x}}\right)_{am} \bar{F}_{mb} \mathbb{A}_{abkl} \bar{F}_{kl} \delta_{rs} \frac{\sum\limits_{i \in \mathscr{P}} g_{\mathscr{P}} i \Omega_{i,t} \left(\frac{\partial \mathbf{d}_{\mathbf{u}i}}{\partial \mathbf{x}} - \frac{\partial \mathbf{d}_{\mathbf{u}}}{\partial \mathbf{x}}\right)_{rs}}{\sum\limits_{i \in \mathscr{P}} g_{\mathscr{P}} i \Omega_{i,0}} \right] d\Omega_{e,t} =$$

$$\int_{\Omega_{e,t}} \left[\tfrac{1}{3} g_{\mathscr{P}} \bar{J}^{-1} v_{r\mathscr{P}}^{-1} \left(\tfrac{\partial \mathbf{w}_{\mathbf{u}}}{\partial \mathbf{x}}\right)_{am} \bar{F}_{mb} \mathbb{A}_{abkl} \bar{F}_{nl} \delta_{kn} \delta_{rs} \frac{\sum\limits_{i \in \mathscr{P}} g_{\mathscr{P}} i \Omega_{i,t} \left(\frac{\partial \mathbf{d}_{\mathbf{u}i}}{\partial \mathbf{x}} - \frac{\partial \mathbf{d}_{\mathbf{u}}}{\partial \mathbf{x}}\right)_{rs}}{\sum\limits_{i \in \mathscr{P}} g_{\mathscr{P}} i \Omega_{i,0}} \right] d\Omega_{e,t} =$$

$$\int_{\Omega_{e,t}} \left[\frac{g_{\mathscr{P}}}{3 \sum\limits_{i \in \mathscr{P}} g_{\mathscr{P}} i \Omega_{i,t}} \boldsymbol{\nabla}_{\mathbf{x}} \mathbf{w}_{\mathbf{u}} \colon \mathbb{a} \colon (\mathbf{I} \otimes \mathbf{I}) : \sum_{i \in \mathscr{P}} g_{\mathscr{P}} i \Omega_{i,t} (\boldsymbol{\nabla}_{\mathbf{x}} \mathbf{d}_{\mathbf{u}i} - \boldsymbol{\nabla}_{\mathbf{x}} \mathbf{d}_{\mathbf{u}}) \right] d\Omega_{e,t} =$$

$$\int_{\Omega_{e,t}} \left[\frac{g_{\mathscr{P}}}{3 \sum\limits_{i \in \mathscr{P}} g_{\mathscr{P}} i \Omega_{i,t}} \boldsymbol{\nabla}_{\mathbf{x}} \mathbf{w}_{\mathbf{u}} \colon \mathbb{a} \colon (\mathbf{I} \otimes \mathbf{I}) : \sum_{i \in \mathscr{P}} g_{\mathscr{P}} i \Omega_{i,t} \boldsymbol{\nabla}_{\mathbf{x}} \mathbf{d}_{\mathbf{u}i} \right] d\Omega_{e,t} -$$

$$\int_{\Omega_{e,t}} \left[\tfrac{g_{\mathscr{P}}}{3} \boldsymbol{\nabla}_{\mathbf{x}} \mathbf{w}_{\mathbf{u}} \colon \mathbb{a} \colon (\mathbf{I} \otimes \mathbf{I}) : \boldsymbol{\nabla}_{\mathbf{x}} \mathbf{d}_{\mathbf{u}} \right] d\Omega_{e,t} \tag{4.31}$$

- The spatial version of the first integral on RHS of Equation 4.27

$$\int_{\Omega_{e,0}} \left[\frac{2}{3} g_{\mathscr{P}} \left(\frac{v_{r\mathscr{P}}}{J}\right)^{-\frac{2}{3} g_{\mathscr{P}}{}^{-1}} \boldsymbol{\nabla}_{\mathbf{X}} \mathbf{w}_{\mathbf{u}} \colon \left(\bar{\mathbf{P}} \otimes \mathbf{I}\right) : \frac{\sum\limits_{i \in \mathscr{P}} g_{\mathscr{P}} i \Omega_{i,t} \left(\boldsymbol{\nabla}_{\mathbf{x}} \mathbf{d}_{\mathbf{u}i} - \boldsymbol{\nabla}_{\mathbf{x}} \mathbf{d}_{\mathbf{u}}\right)}{J \sum\limits_{i \in \mathscr{P}} g_{\mathscr{P}} i \Omega_{i,0}} \right] d\Omega_{e,0} =$$

$$\int_{\Omega_{e,t}} \left[\frac{2}{3} g_{\mathscr{P}} \bar{J}^{-1} v_{r\mathscr{P}}^{-1} \left(\frac{\partial \mathbf{w}_{\mathbf{u}}}{\partial \mathbf{x}}\right)_{am} \bar{F}_{mb} \bar{\mathbf{P}}_{ab} \delta_{kl} \frac{\sum\limits_{i \in \mathscr{P}} g_{\mathscr{P}} i \Omega_{i,t} \left(\frac{\partial \mathbf{d}_{\mathbf{u}i}}{\partial \mathbf{x}} - \frac{\partial \mathbf{d}_{\mathbf{u}}}{\partial \mathbf{x}}\right)_{kl}}{\sum\limits_{i \in \mathscr{P}} g_{\mathscr{P}} i \Omega_{i,0}} \right] d\Omega_{e,t} =$$

$$\int_{\Omega_{e,t}} \left[\frac{2\, g_{\mathscr{P}}}{3 \sum\limits_{i \in \mathscr{P}} g_{\mathscr{P}} i \Omega_{i,t}} \boldsymbol{\nabla}_{\mathbf{x}} \mathbf{w}_{\mathbf{u}} \colon (\boldsymbol{\sigma} \otimes \mathbf{I}) : \sum_{i \in \mathscr{P}} g_{\mathscr{P}} i \Omega_{i,t} (\boldsymbol{\nabla}_{\mathbf{x}} \mathbf{d}_{\mathbf{u}i} - \boldsymbol{\nabla}_{\mathbf{x}} \mathbf{d}_{\mathbf{u}}) \right] d\Omega_{e,t} =$$

$$\int_{\Omega_{e,t}} \left[\frac{2\, g_{\mathscr{P}}}{3 \sum\limits_{i \in \mathscr{P}} g_{\mathscr{P}} i \Omega_{i,t}} \boldsymbol{\nabla}_{\mathbf{x}} \mathbf{w}_{\mathbf{u}} \colon (\boldsymbol{\sigma} \otimes \mathbf{I}) : \sum_{i \in \mathscr{P}} g_{\mathscr{P}} i \Omega_{i,t} \boldsymbol{\nabla}_{\mathbf{x}} \mathbf{d}_{\mathbf{u}i} \right] d\Omega_{e,t} -$$

$$\int_{\Omega_{e,t}} \left[\frac{2\, g_{\mathscr{P}}}{3} \boldsymbol{\nabla}_{\mathbf{x}} \mathbf{w}_{\mathbf{u}} \colon (\boldsymbol{\sigma} \otimes \mathbf{I}) : \boldsymbol{\nabla}_{\mathbf{x}} \mathbf{d}_{\mathbf{u}} \right] d\Omega_{e,t} \tag{4.32}$$

Using Equations 4.28, 4.29, 4.31 and 4.32, one can write the spatial form of the directional derivative of weak form as:

$$
\begin{aligned}
DR_{ue}\left(\mathbf{u}, \mathbf{w_u}\right)[\mathbf{d_u}] = \\
&- \Bigg[\int_{\Omega_{e,t}} \boldsymbol{\nabla}_{\mathbf{x}} \mathbf{w_u} \colon \mathbb{a} \colon \boldsymbol{\nabla}_{\mathbf{x}} \mathbf{d_u} \, d\Omega_{e,t} + \int_{\Omega_{e,t}} \boldsymbol{\nabla}_{\mathbf{x}} \mathbf{w_u} \colon \mathbb{d}_l \colon \boldsymbol{\nabla}_{\mathbf{x}} \mathbf{d_u} \, d\Omega_{e,t} + \\
&\sum_{j \in \mathscr{P}, j \neq e} \int_{\Omega_{e,t}} \boldsymbol{\nabla}_{\mathbf{x}} \mathbf{w_u} \colon \mathbb{d}^j_{nl} \colon \boldsymbol{\nabla}_{\mathbf{x}} \mathbf{d_u}_j \, d\Omega_{e,t} + \int_{\Omega_{e,t}} \mathbf{w_u} \cdot \frac{\beta_{gu}}{J \triangle t} \mathbf{d_u} \, d\Omega_{e,t} \Bigg]
\end{aligned}
\tag{4.33}
$$

where

$$
\mathbb{d}_l = \left(\frac{g_{\mathscr{P}} \Omega_{e,t}}{\sum\limits_{i \in \mathscr{P}} g_{\mathscr{P}i} \Omega_{i,t}} - 1 \right) \left[\frac{g_{\mathscr{P}}}{3} \mathbb{a} \colon \left(\mathbf{I} \otimes \mathbf{I} \right) - \frac{2\, g_{\mathscr{P}}}{3} \left(\boldsymbol{\sigma} \otimes \mathbf{I} \right) \right] \tag{4.34a}
$$

$$
\mathbb{d}^j_{nl} = \frac{g_{\mathscr{P}j} \Omega_{j,t}}{\sum\limits_{i \in \mathscr{P}} g_{\mathscr{P}i} \Omega_{i,t}} \left[\frac{g_{\mathscr{P}}}{3} \mathbb{a} \colon \left(\mathbf{I} \otimes \mathbf{I} \right) - \frac{2\, g_{\mathscr{P}}}{3} \left(\boldsymbol{\sigma} \otimes \mathbf{I} \right) \right] \tag{4.34b}
$$

The nonlinear solver for the displacement field, i.e. the Newton-Raphson solver, can be obtained by (a) plugging Equation 4.33 into Equation 4.24, (b) using Galerkin method where both $\mathbf{w_u}$ and $\mathbf{d_u}$ are interpolated using the same shape functions and (c) recognizing the arbitrariness of the weight function. The *i-th* iteration of Newton-Raphson scheme is obtained as

$$
[K_u]\{d_u\} = \{f_u^{ext}\} - \{f_u^{int}\} \tag{4.35a}
$$

$$
\{u\}^{i+1} = \{u\}^i + \{d_u\} \tag{4.35b}
$$

where $[K_u]$, $\{f_u^{ext}\}$ and $\{f_u^{int}\}$ are respectively the global tangent stiffness matrix, external and internal force vectors. The local $[K_{ue}^l]$ and nonlocal $[K_{ue}^{nl}]$ elemental tangent stiffness matrices and internal force vector $\{f_{ue}^{int}\}$ are given by:

$$[K_{ue}^l] = \underbrace{\int_{\Omega_{e,t}} [G_{ux}^e]^T \, \mathrm{F}_{9x9}^{UP}(\mathrm{a}) \, [G_{ux}^e] \; d\Omega_{e,t}}_{\text{contribution from local material behavior}} + \underbrace{\int_{\Omega_{e,t}} [G_{ux}^e]^T \, \mathrm{F}_{9x9}^{UP}(\mathrm{d}_l) \, [G_{ux}^e] \; d\Omega_{e,t}}_{\text{patch contribution to the local stiffness}} + \underbrace{\int_{\Omega_{e,t}} [N_u^e]^T \, \frac{\beta_{gu}}{J\triangle t} \, [N_u^e] \; d\Omega_{e,t}}_{\text{contribution from global viscous stabilization}} \tag{4.36a}$$

$$[K_{ue}^{nl}] = \underbrace{\sum_{j \in \mathscr{P}, j \neq e} \int_{\Omega_{e,t}} [G_{ux}^e]^T \, \mathrm{F}_{9x9}^{UP}\left(\mathrm{d}_{nl}^j\right) \left[G_{ux}^j\right] \; d\Omega_{e,t}}_{\text{patch contribution to the nonlocal stiffness}} \tag{4.36b}$$

$$\{f_{ue}^{int}\} = \underbrace{\int_{\Omega_{e,t}} [G_{ux}^e]^T \, \{\sigma\} \; d\Omega_{e,t}}_{\text{contribution from local material behavior}} + \underbrace{\int_{\Omega_{e,t}} [N_u^e]^T \, \beta_{gu} \{\dot{u}\} \; d\Omega_{e,t}}_{\text{contribution from global viscous stabilization}} \tag{4.36c}$$

Here $\{\sigma\} = [\sigma_{11} \; \sigma_{12} \; \sigma_{13} \; \sigma_{21} \; \sigma_{22} \; \sigma_{23} \; \sigma_{31} \; \sigma_{32} \; \sigma_{33}]^T$ and $\{\dot{u}\} = [\dot{u}_x \; \dot{u}_y \; \dot{u}_z]^T$. Moreover, F_{9x9}^{UP} is function that unpacks a fourth order tensor into a 9 by 9 matrix as:

$$\mathrm{F}_{9x9}^{UP}(\mathrm{a}) = \begin{bmatrix} \mathrm{a}_{1111} & \mathrm{a}_{1112} & \mathrm{a}_{1113} & \mathrm{a}_{1121} & \mathrm{a}_{1122} & \mathrm{a}_{1123} & \mathrm{a}_{1131} & \mathrm{a}_{1132} & \mathrm{a}_{1133} \\ \mathrm{a}_{1211} & \mathrm{a}_{1212} & \mathrm{a}_{1213} & \mathrm{a}_{1221} & \mathrm{a}_{1222} & \mathrm{a}_{1223} & \mathrm{a}_{1231} & \mathrm{a}_{1232} & \mathrm{a}_{1233} \\ & \vdots & & & \ddots & & & \vdots & \\ \mathrm{a}_{3311} & \mathrm{a}_{3312} & \mathrm{a}_{3313} & \mathrm{a}_{3321} & \mathrm{a}_{3322} & \mathrm{a}_{3323} & \mathrm{a}_{3331} & \mathrm{a}_{3332} & \mathrm{a}_{3333} \end{bmatrix} \tag{4.37}$$

It is clearly seen that application of F-bar-patch formulation gives rise to a non-local stiffness matrix since the volume of all elements in the patch appears in the

modified deformation gradient given in Equation 4.17. The rows of this nonlocal stiffness matrix correspond to the DOFs of element e whereas its columns correspond to the DOFs of element $j \in \mathscr{P}, j \neq e$. It is worthy to note that the presence of this nonlocal stiffness matrix will render the global stiffness matrix non-symmetric value-wise; however, it would still remain structurally symmetric.

As pointed out in [34], the bandwidth of the global stiffness matrix corresponding to the F-bar-patch formulation is larger compared to the conventional TET4 element; hence, more operations would be needed for LU factorizations. Cheng et al [111] have shown that the computational cost associated with these added operations during factorization is negligible.

***Remark* 4** *Although the derivations presented in this section were on the premise of using F-bar-patch formulation for tetrahedral elements, following a similar procedure, one can derive the tangent stiffness matrix and internal force vector for any other types of elements, such as conventional TET4 and brick elements, as:*

$$[K^l_{ue}] = \underbrace{\int_{\Omega_{e,t}} [G^e_{ux}]^T \, F^{UP}_{9x9}\,(\mathbb{a})\, [G^e_{ux}] \; d\Omega_{e,t}}_{\textit{contribution from local material behavior}} + \underbrace{\int_{\Omega_{e,t}} [N^e_u]^T \, \frac{\beta_{gu}}{J\triangle t}\, [N^e_u] \; d\Omega_{e,t}}_{\textit{contribution from global viscous stabilization}} \tag{4.38a}$$

$$\{f^{int}_{ue}\} = \underbrace{\int_{\Omega_{e,t}} [G^e_{ux}]^T \, \{\sigma\} \; d\Omega_{e,t}}_{\textit{contribution from local material behavior}} + \underbrace{\int_{\Omega_{e,t}} [N^e_u]^T \, \beta_{gu} \{\dot{u}\} \; d\Omega_{e,t}}_{\textit{contribution from global viscous stabilization}} \tag{4.38b}$$

***Remark* 5** *It can be readily seen that if each element is considered as a patch (size of patch is 1),* $\mathbb{d}_l$ *and* $[K^{nl}_{ue}]$ *will disappear and the stiffness matrix reduces to the one*

for conventional tetrahedral elements.

***Remark* 6** *If an element within a multi-element patch is fully degraded ($s = 1$), $\mathbb{d}_l$ and $\mathbb{d}_{nl}^j$ tensors will disappear and the tangent stiffness matrix for the conventional tetrahedral element is recovered.*

4.4.3 Stabilization of displacement field

As the simulations experience convergence issues, it is generally advised to decrease the time increment to bring the solution within the radius of convergence of the Newton-Raphson scheme. However, if these convergence issues are due to the occurrence of instabilities, cutting back the time increment would not be helpful as the radius of convergence shrinks down to zero at the point of instability [104]. Utilizing the stabilization techniques discussed in Section 3.5 helps one overcome the instabilities by improving the state of tangent stiffness matrix at the points of instabilities. It is clearly seen from Equation 4.36a that as $\triangle t$ decreases, both $\mathbb{a}$ and the viscous tangent stiffness matrix increase. These stabilization contributions to the stiffness matrix will restore its positive-definiteness at sufficiently small time increments.

In this section, deformation of the 1D bar discussed in Section 3.5.1 is revisited. The effectiveness of local and global stabilizations of the displacement field in overcoming instabilities is investigated. The bar is assumed to have a uniform cross section with area $A = 1m^2$. The applied displacement is set to increase linearly with time as $u_{app} = 4 \times 10^{-4}t$. The other necessary geometrical and constitutive model

parameters are given in Table 4.6.

parameters	value	unit
L_1	1	m
L_2	1	m
E	200	GPa
ϵ_c	0.001	-
ϵ_f	0.002	-
σ_c	400	MPa

Table 4.6: geometrical and constitutive model parameters for the 1D bar problem in Figure 3.1a

For FE analysis of this system, each bar segment is idealized as a linear 2-noded bar element. The parameters given in Table 4.6 are chosen such that the stability inequality in Equation 3.29 is violated. In the simulations with no stabilization, once degradation initiated in the middle segment, the tangent stiffness matrix lost its positive-definiteness and the simulation failed due to the emergence of convergence issues.

To investigate the competency of stabilization techniques, local and global stabilization of displacement field are employed separately to simulate deformation of this bar. Figure 4.13 depicts the displacement-reaction force plots for different values of local and global viscosity parameters. It is seen that addition of a small amount of

viscosity to the model can effectively overcome the instabilities. Over a wide range of viscosity, the mechanical response is observed to be almost insensitive to the chosen value of viscous stabilization parameter. It is instructive to remember that utilization of the viscous stabilization is merely out of numerical necessity and the value used for viscosity should be as small as possible. Performing sensitivity analysis of mechanical response on the viscous parameter can help the modeler choose an appropriate value for viscosity.

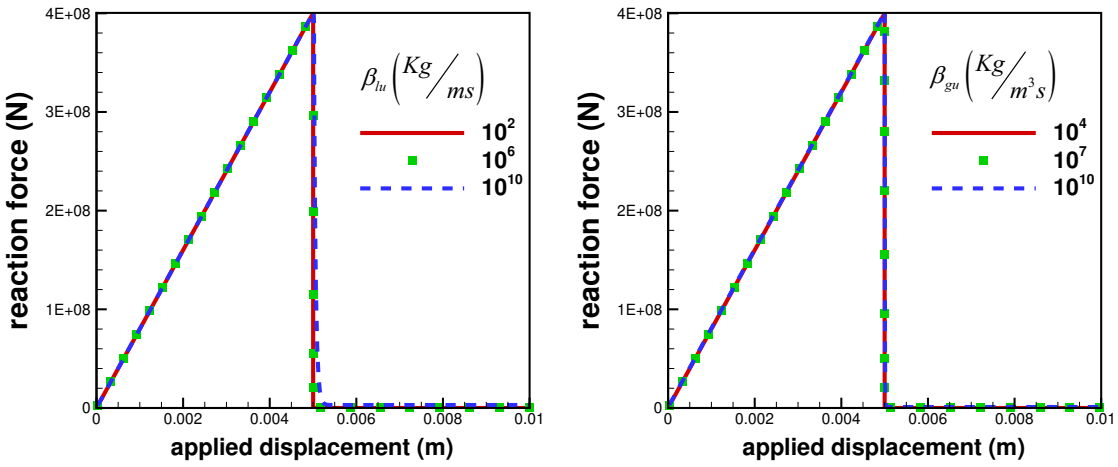

Figure 4.13: load-displacement plot for the 1D bar using (a) local and (b) global stabilization of the displacement field

In the stabilized simulations, at the onset of degradation of the middle segment, the system is unstable and multiple time increment reductions are necessary to amplify the viscous contributions to the system of equations. For a sufficiently small time increment, the positive-definiteness of the tangent stiffness matrix is restored and the

solver converges. For $\beta_{gu} = 10^{10} Kg/m^3 s$, Figure 4.14 shows how the minimum eigenvalue of the tangent stiffness matrix changes at the onset of degradation for different time increments. It is observed that the positive-definiteness of the system is restored at $\triangle t \approx 0.0025s$ when the minimum eigenvalue of the tangent stiffness matrix becomes positive. For time increments less than $0.002s$, the two smallest eigenvalues do not change with time increment; whereas, the other eigenvalues still increase with further reduction in time increment.

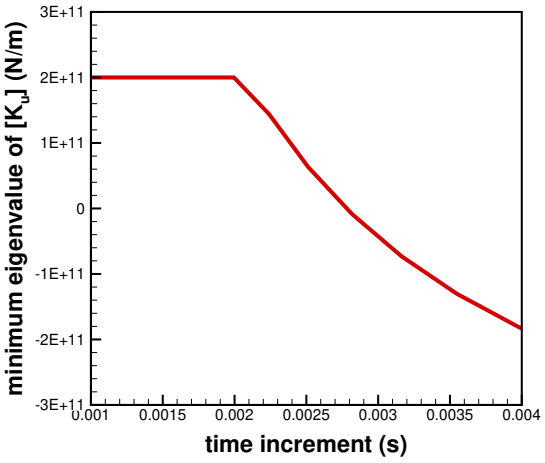

Figure 4.14: dependence of the minimum eigenvalue of tangent stiffness matrix on time increment at the point of instability in the 1D bar problem

One can expect that with higher values of viscosity the simulation will march through the unstable equilibrium path with larger time increments. Figure 4.15 shows the average time increment taken by the simulation during degradation of the middle segment. Both local and global stabilization schemes show a nearly linear relationship

between the average time increment and the viscosity parameter.

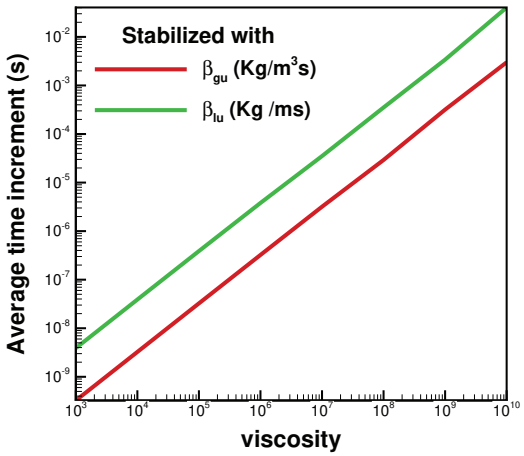

Figure 4.15: average time increment taken by the simulation during degradation of the middle segment in the 1D bar using (a) local and (b) global stabilization of the displacement field

4.5 Nonlinear FE derivations for crack phase field

In this section, the tangent stiffness matrix and residual vector for the crack phase field are derived. The weak form for the governing differential equation for the crack phase field, given in Equation 3.39b, can be written as:

$$R_s\left(s, w_s\right) = \int_{\Omega_0} \left[\beta_{gs}\dot{s} - \boldsymbol{\nabla}_{\mathbf{X}} \cdot \left(\rho_0 \frac{\partial \psi}{\partial \boldsymbol{\nabla}_{\mathbf{X}} s}\right) + \rho_0 \frac{\partial \psi}{\partial s}\right] w_s \, d\Omega_0 = 0 \tag{4.39}$$

where w_s is the *weight function* corresponding to the crack phase field. Setting the crack phase field traction $\lambda_0 = \rho_0 \frac{\partial \psi}{\partial \boldsymbol{\nabla}_{\mathbf{X}} s} \cdot \mathbf{N}$ to zero and employing the backward difference method, Equation 4.39 can be rewritten as:

$$\begin{aligned}
&R_s\left(s, w_s\right) = \\
&\int_{\Omega_0} \left[\beta_{gs} \frac{s - s_{t-\triangle t}}{\triangle t} w_s - \boldsymbol{\nabla}_{\mathbf{X}} \cdot \left(\rho_0 \frac{\partial \psi}{\partial \boldsymbol{\nabla}_{\mathbf{X}} s}\right) w_s + \rho_0 \frac{\partial \psi}{\partial s} w_s\right] \, d\Omega_0 = \\
&\int_{\Omega_0} \left[\beta_{gs} \frac{s - s_{t-\triangle t}}{\triangle t} w_s - \boldsymbol{\nabla}_{\mathbf{X}} \cdot \left(w_s \rho_0 \frac{\partial \psi}{\partial \boldsymbol{\nabla}_{\mathbf{X}} s}\right) + \rho_0 \frac{\partial \psi}{\partial \boldsymbol{\nabla}_{\mathbf{X}} s} \cdot \boldsymbol{\nabla}_{\mathbf{X}} w_s + \rho_0 \frac{\partial \psi}{\partial s} w_s\right] \, d\Omega_0 = \\
&\int_{\Omega_0} \left[\left(\beta_{gs} \frac{s - s_{t-\triangle t}}{\triangle t} + \rho_0 \frac{\partial \psi}{\partial s}\right) w_s + \rho_0 \frac{\partial \psi}{\partial \boldsymbol{\nabla}_{\mathbf{X}} s} \cdot \boldsymbol{\nabla}_{\mathbf{X}} w_s\right] \, d\Omega_0 - \int_{\Gamma_0} w_s \rho_0 \frac{\partial \psi}{\partial \boldsymbol{\nabla}_{\mathbf{X}} s} \cdot \mathbf{N} \, d\Gamma_0 = \\
&\int_{\Omega_0} \left[\left(\beta_{gs} \frac{s - s_{t-\triangle t}}{\triangle t} + \rho_0 \frac{\partial \psi}{\partial s}\right) w_s + \rho_0 \frac{\partial \psi}{\partial \boldsymbol{\nabla}_{\mathbf{X}} s} \cdot \boldsymbol{\nabla}_{\mathbf{X}} w_s\right] \, d\Omega_0 = 0
\end{aligned} \tag{4.40}$$

Regardless of the form chosen for the Helmholtz free energy density, one can linearize Equation 4.40 and solve for the crack phase field with an iterative solver. One can easily verify that for simple quadratic degradation functions as in [65], the weak form would be linear in terms of the order parameter;therefore, one iteration of Newton-Raphson would yield the solution. However, for non-quadratic degradation functions, such as the ones proposed in [68, 69, 115, 116], the term $\rho_0 \frac{\partial \psi}{\partial s}$ would be a nonlinear function of the order parameter and a few Newton-Raphson iterations might be needed to obtain the solution. As pointed out in Section 4.4.2, one can

break the integral over volume Ω_0 into integrals over individual element volumes $\Omega_{e,0}$. Linearization of Equation 4.40 in direction d_s over an element e reads as:

$$\begin{aligned} &R_{se}\left(s+d_s, w_s\right) = R_{se}\left(s, w_s\right) + DR_{se}\left(s, w_s\right)\left[d_s\right] = \\ &\quad R_{se}\left(s, w_s\right) + \left.\frac{d}{d\epsilon}\right|_{\epsilon=0} R_{se}\left(s+\epsilon d_s, w_s\right) = \\ &\quad R_{se}\left(s, w_s\right) + \int_{\Omega_{e,0}} w_s \left(\frac{\beta_{gs}}{\triangle t} + \rho_0 \frac{\partial^2 \psi}{\partial s^2}\right) d_s \; d\Omega_{e,0} + \int_{\Omega_{e,0}} \boldsymbol{\nabla}_{\mathbf{X}} w_s \cdot \mathbf{A}_s \boldsymbol{\nabla}_{\mathbf{X}} d_s \; d\Omega_{e,0} = 0 \end{aligned} \tag{4.41}$$

Here $\mathbf{A}_s = \frac{\partial}{\partial \boldsymbol{\nabla}_{\mathbf{X}} s}\left(\rho_0 \frac{\partial \psi}{\partial \boldsymbol{\nabla}_{\mathbf{X}} s}\right)$. The linearized weak form could be rewritten as:

$$\begin{aligned} &\int_{\Omega_{e,0}} w_s \left(\frac{\beta_{gs}}{\triangle t} + \rho_0 \frac{\partial^2 \psi}{\partial s^2}\right) d_s \; d\Omega_{e,0} + \int_{\Omega_{e,0}} \boldsymbol{\nabla}_{\mathbf{X}} w_s \cdot \mathbf{A}_s \boldsymbol{\nabla}_{\mathbf{X}} d_s \; d\Omega_{e,0} \\ &\quad = -\int_{\Omega_{e,0}} \left[\left(\beta_{gs} \frac{s - s_{t-\triangle t}}{\triangle t} + \rho_0 \frac{\partial \psi}{\partial s}\right) w_s + \rho_0 \frac{\partial \psi}{\partial \boldsymbol{\nabla}_{\mathbf{X}} s} \cdot \boldsymbol{\nabla}_{\mathbf{X}} w_s\right] \; d\Omega_{e,0} \end{aligned} \tag{4.42}$$

Using the Galerkin method where both d_s and w_s are interpolated using the same shape functions and recognizing the arbitrariness of weight function, one can derive the elemental tangent stiffness matrix $[K_{se}]$ and internal force vector $\{f_{se}^{int}\}$ for the crack phase field as:

$$[K_{se}] = \int_{\Omega_{e,0}} [N_s^e]^T \left(\frac{\beta_{gs}}{\triangle t} + \rho_0 \frac{\partial^2 \psi}{\partial s^2}\right) [N_s^e] \; d\Omega_{e,0} + \int_{\Omega_{e,0}} [G_{sX}^e]^T \mathbf{A}_s [G_{sX}^e] \; d\Omega_{e,0} \tag{4.43a}$$

$$\{f_{se}^{int}\} = \int_{\Omega_{e,0}} [N_s^e]^T \left(\beta_{gs} \frac{s - s_{t-\triangle t}}{\triangle t} + \rho_0 \frac{\partial \psi}{\partial s}\right) \; d\Omega_{e,0} + \int_{\Omega_{e,0}} [G_{sX}^e]^T \rho_0 \frac{\partial \psi}{\partial \boldsymbol{\nabla}_{\mathbf{X}} s} \; d\Omega_{e,0} \tag{4.43b}$$

Following the conventional assembly process, one can obtain the global stiffness matrix $[K_s]$ and internal force vector $\{f_s^{int}\}$. The *i-th* iteration of Newton-Raphson scheme for the crack phase field is obtained as:

$$[K_s]\{d_s\} = -\{f_s^{int}\} \tag{4.44a}$$

$$\{s\}^{i+1} = \{s\}^i + \{d_s\} \tag{4.44b}$$

It is worthy to note that there is no external loading vector associated with the crack phase field since $\lambda_0 = 0$.

Chapter 5

Helmholtz free energy density

As observed in Chapter 5, the displacement and crack phase field problems are coupled via the Helmholtz free energy density. Once the free energy density is defined, one can calculate the first Piola-Kirchhoff stress in Equation 3.33 and obtain the final form of the governing equations 3.39. For phase field modeling of fracture in ductile materials, the Helmholtz free energy density (HFED) is composed of three distinct terms as:

$$\rho_0\psi = \rho_0\psi_e + \rho_0\psi_p + \rho_0\psi_c \tag{5.1}$$

The energy stored due to the elastic stretching of the body is denoted by $\rho_0\psi_e$. The defect energy causing work hardening during plasticity is represented by $\rho_0\psi_p$. The crack surface energy density is denoted by $\rho_0\psi_c$. In this chapter, these three contributions to the HFED are discussed in details.

5.1 Crack surface energy density

Definition of the crack surface energy density in terms of an order parameter and its gradient is the core idea behind the phase field modeling of fracture. The simple 1D example given in [65] is used here to define an appropriate energy density term which can represent a sharp crack. Consider an infinite bar with cross-section A_0 and position vector X. To mimic a sharp crack, assume that the bar is cracked at $X = 0$ and is intact (unbroken) in the rest of the domain. An order parameter s in defined such that $s = 0$ denotes an intact state, whereas $s = 1$ corresponds to a fully broken state. The fracture state of the bar can be expressed in terms of s as:

$$s = \begin{cases} 1 & \text{if} \quad X = 0 \\ \\ 0 & \text{otherwise} \end{cases} \tag{5.2}$$

Since this strong discontinuity is not amenable to numerical computations, one may regularize this discontinuity and represent this discontinuous function with a smooth one. This can be achieved by an exponential function as:

$$s(X) = e^{-\frac{|X|}{l_c}} \tag{5.3}$$

in which l_c is the regularization length, controlling the sharpness of the regularized function. Figure 5.1 illustrates how the regularized function approximates the sharp discontinuous one.

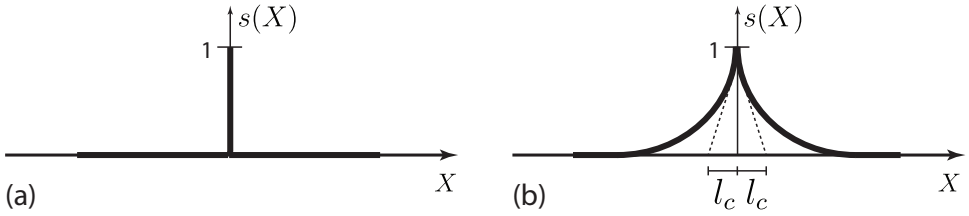

Figure 5.1: fracture in 1D bar (a) discontinuous sharp crack, (b) regularized representation of sharp crack

One can easily see that the regularized function in Equation 5.3 is the solution of the homogeneous differential equation:

$$s - l_c^2 \frac{d^2 s}{dX^2} = 0 \tag{5.4}$$

subject to boundary conditions $s(0) = 1$ and $s(\pm\infty) = 0$. Using variational calculus, it can be seen that this differential equation is the Euler equation of functional

$$\Pi_s = \frac{1}{2} \int_{\Omega_0} \left\{ s^2 + l_c^2 \left(\frac{ds}{dX} \right)^2 \right\} \, d\Omega_0 \tag{5.5}$$

Plugging Equation 5.3 in Equation 5.5 and using $d\Omega_0 = A_0 dX$, it is observed that the functional Π_s is related to the crack surface A_0 and regularization length l_c as:

$$\Pi_s = A_0 \, l_c \tag{5.6}$$

Consequently, one can introduce an alternative functional to represent crack surface whose minimization yields the same exponential regularization in Equation 5.3. This alternative functional reads as:

$$A_{s0} = \frac{\Pi_s}{l_c} = \frac{1}{2l_c} \int_{\Omega_0} \left\{ s^2 + l_c^2 \left(\frac{ds}{dX} \right)^2 \right\} \, d\Omega_0 \tag{5.7}$$

Introducing g_c as the critical Griffith-type fracture energy per unit area, the total fracture surface energy can be calculated as

$$g_c A_{s0} = \frac{g_c}{2l_c} \int_{\Omega_0} \left\{ s^2 + l_c^2 \left(\frac{ds}{dX} \right)^2 \right\} \, d\Omega_0 \tag{5.8}$$

Extending this equation to multi-dimensional solids, one can derive the crack surface energy density as:

$$\rho_0 \psi_c = \frac{g_c}{2l_c} \left(s^2 + l_c^2 \, \boldsymbol{\nabla}_{\mathbf{X}} s \cdot \boldsymbol{\nabla}_{\mathbf{X}} s \right) \tag{5.9}$$

Equation 5.9 is by far the most commonly used form of crack surface energy density for the phase field modeling of fracture. This formulation, however, allows for material degradation upon straining; in other words, the order parameter assumes non-zero values (although the values might be small) as the solid body starts to deform. As an alternative, a different form of $\rho_0 \psi_c$ has been proposed and used in the literature [67, 117, 118] which is linearly dependent on the order parameter.

$$\rho_0 \psi_c = 2w_c \left(s + \frac{l_c^2}{2} \boldsymbol{\nabla}_{\mathbf{X}} s \cdot \boldsymbol{\nabla}_{\mathbf{X}} s \right) \tag{5.10}$$

in which w_c is the specific fracture energy per unit volume. This modified formulation declares a threshold on the initiation of fracture and order parameter starts to evolve only after a specific amount of energy density is stored in the material.

5.2 Stored elastic energy density

As the material deforms under loading conditions, part of the deformation is accommodated by elastic deformations which is quantified by the elastic deformation gradient $\mathbf{F}^e$. The energy corresponding to the elastic deformation is stored in the material. For an intact material point, a conventional hyperelastic law expresses the stored elastic energy density (SEED) as a quadratic function of the elastic Green-Lagrange strain tensor [86]:

$$\rho_0 \hat{\psi}_e = \frac{1}{2} \mathbf{E}^e : \mathbb{C}^e : \mathbf{E}^e \tag{5.11}$$

Here $\rho_0 \hat{\psi}_e$ is the stored elastic energy density in an intact material state and $\mathbb{C}^e$ denotes the fourth-order anisotropic elasticity tensor with major and minor symmetries. The elastic Green-Lagrange strain tensor is defined as:

$$\mathbf{E}^e = \frac{1}{2} \left(\mathbf{F}^{e^T} \mathbf{F}^e - \mathbf{I} \right) \tag{5.12}$$

Given that SEED plays a key role as the driving force for fracture, it is necessary to define how the crack phase field interacts with the elastic deformation. To formulate this interaction, it is instructive to determine what type of behavior should be expected when the order parameter is at either end of its bounding limits; that is, $s = 0$ and $s = 1$. It is clearly expected that SEED for damaged materials should be formulated such that it reduces down to the one in Equation 5.11 when $s = 0$.

When the material is fully damaged; i.e. $s = 1$, it is expected that the material loses part of its capability to store elastic energy. In the literature, it has been argued extensively that the load-bearing capacity of a material point (its capability to store elastic energy) at the fully broken state is dependent on the compressive/tensile state of strain. It is generally considered that the cracks close under compression, allowing the load/stress to be transmitted across the crack surfaces and therefore the material can still deform elastically and store energy. Whereas in tension, the crack surfaces open up and load-bearing capacity is lost. This phenomenon is referred to as *unilateral condition* [119].

5.2.1 Overview of available models

Most of the formulations in the literature on phase field modeling of fracture are developed for isotropic elastic materials under small deformation conditions. Using small strain elasticity ($\boldsymbol{\epsilon}^e = 1/2(\boldsymbol{\nabla}_{\mathbf{X}}\mathbf{u} + \boldsymbol{\nabla}_{\mathbf{X}}\mathbf{u}^T)$) and assuming isotropy ($\mathbb{C}^e_{ijkl} = \lambda\delta_{ij}\delta_{kl} + \mu\left(\delta_{ik}\delta_{jl} + \delta_{il}\delta_{jk}\right)$), SEED in Equation 5.11 is simplified as:

$$\rho_0\hat{\psi}_e = \frac{\lambda}{2}\,\mathrm{tr}^2(\boldsymbol{\epsilon}^e) + \mu\,\mathrm{tr}(\boldsymbol{\epsilon}^{e2}) \tag{5.13}$$

in which λ and μ are the Lame's constants, respectively. One may rewrite this equation in terms of the bulk κ and shear μ moduli as:

$$\rho_0\hat{\psi}_e = \frac{\kappa}{2}\,\mathrm{tr}^2(\boldsymbol{\epsilon}^e) + \mu\,\mathrm{tr}(\boldsymbol{\epsilon}^{e2}_{dev}) \tag{5.14}$$

Here $\boldsymbol{\epsilon}^e_{dev}$ is the deviatoric elastic strain tensor. The term $\kappa/2\,\mathrm{tr}^2(\boldsymbol{\epsilon}^e)$ and $\mu\,\mathrm{tr}(\boldsymbol{\epsilon}^{e2}_{dev})$ correspond to purely volumetric and deviatoric parts of SEED, respectively. It is worthy to note that such decomposition of SEED into purely volumetric and deviatoric components is not generally possible for anisotropic materials.

The simplest form of SEED for degradable materials is referred to as *full degradation* [64]:

$$\rho_0\psi_e = (1-s)^2\rho_0\hat{\psi}_e \tag{5.15}$$

This form of $\rho_0\psi_e$ does not respect the unilateral condition since SEED disappears for $s = 1$ regardless of the state of strain. One consequence of this formulation is that under mode II phase field modeling of fracture will predict an unrealistic crack branching, as shown in Figure 5.2. This is an artifact of the choice of SEED which allows compressive strains to drive fracture.

A more sophisticated model is due to the seminal work of Miehe et al. [65] where SEED is written as:

$$\rho_0\psi_e = (1-s)^2\rho_0\hat{\psi}^+_e + \rho_0\hat{\psi}^-_e \tag{5.16}$$

$\rho_0\hat{\psi}^+_e$ and $\rho_0\hat{\psi}^-_e$ are SEEDs due to tension and compression, respectively, calculated in terms of the principal strains ϵ^e_1, ϵ^e_2 and ϵ^e_3 as:

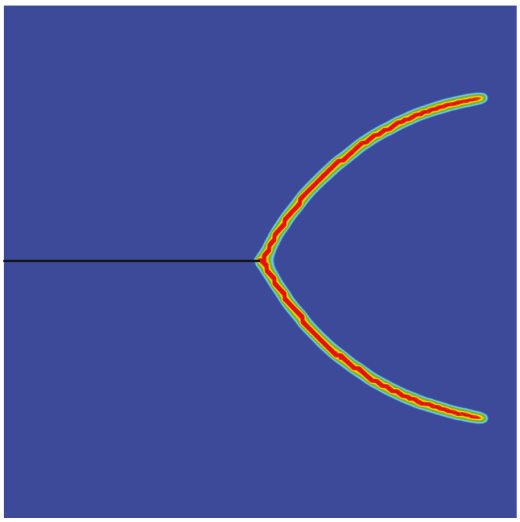

Figure 5.2: unrealistic crack branching under mode II due to violation of the unilateral condition in full degradation formulation

$$\rho_0\hat{\psi}_e^{\pm} = \frac{\lambda}{2}\left\langle \epsilon_1^e + \epsilon_2^e + \epsilon_3^e \right\rangle_{\pm}^2 + \mu\left(< \epsilon_1^e >_{\pm}^2 + < \epsilon_2^e >_{\pm}^2 + < \epsilon_3^e >_{\pm}^2 \right) \tag{5.17}$$

in which $< x >_{\pm} = (x \pm |x|)/2$. This type of SEED formulation respects the unilateral condition as it only makes $\rho_0\hat{\psi}_e^{+}$ disappear at the fully broken stage while not degrading $\rho_0\hat{\psi}_e^{-}$. Based on this formulation, only the tensile part of the energy contributes to crack phase field evolution. While this method is effective, its application is limited to isotropic materials where this specific form of $\rho_0\hat{\psi}_e$ is available.

Using Equation 5.14, Amor et al. [63] proposed a different SEED formulation:

$$\rho_0\psi_e = (1-s)^2\left[\frac{\kappa}{2} < \mathrm{tr}(\boldsymbol{\epsilon}^e) >_{+}^2 \; + \mu\,\mathrm{tr}(\boldsymbol{\epsilon}_{dev}^{e2})\right] + \frac{\kappa}{2} < \mathrm{tr}(\boldsymbol{\epsilon}^e) >_{-}^2 \tag{5.18}$$

In this formulation, the deviatoric part of SEED is always degraded, regardless of

the state of strain. However, the volumetric part of SEED is only degraded only if the material is under hydrostatic tension, i.e. volumetric strain $\mathrm{tr}(\boldsymbol{\epsilon}^e)$ is positive. It is clear that this formulation is only applicable to isotropic materials as it requires decomposition of SEED into purely volumetric and deviatoric components.

Clayton and Knap [120] extended the formulation in [63] to anisotropic materials.

$$\rho_0 \psi_e = \frac{1}{2} \epsilon^e \colon \mathbb{C}_s^e \colon \epsilon^e \tag{5.19}$$

where $\mathbb{C}_s^e$ is the degraded fourth-order elasticity tensor, defined as:

$$\mathbb{C}^e_{s_{ijkl}} = (1-s)^2 \mathbb{C}^e_{ijkl} + \left(1 - (1-s)^2\right) \kappa \delta_{ij} \delta_{kl} \mathcal{H}\left(-\mathrm{tr}(\boldsymbol{\epsilon}^e)\right) \tag{5.20}$$

in which $\mathcal{H}(x)$ represents the Heaviside step function. Except for the bulk modulus which is degraded only if the volume change is tensile, this model permits degradation of all elastic moduli with order parameter regardless of the nature of volume change.

5.2.2 Degradation of stored elastic energy density

In this work, we are interested in modeling fracture in anisotropic solids under finite strain conditions. Therefore, the formulations presented in Section 5.2.1 are not applicable since they are limited to isotropic materials undergoing infinitesimal strains. In this section, a new degradation formulation for SEED is developed in finite strain framework which is suitable for phase field modeling of fracture in anisotropic

materials. The key idea behind our approach is to degrade the elastic strain tensor with the order parameter rather than degrading the fourth-order anisotropic elasticity tensor. The proposed SEED formulation reads as:

$$\rho_0 \psi_e = \frac{1}{2} \tilde{\mathbf{E}}^e : \mathbb{C}^e : \tilde{\mathbf{E}}^e \tag{5.21}$$

where $\tilde{\mathbf{E}}^e$ is the degraded elastic Green-Lagrange strain tensor. In order to calculate $\tilde{\mathbf{E}}^e$, one needs to decompose the elastic deformation gradient $\mathbf{F}^e$ into volumetric $\mathbf{F}^e_{vol}$ and isochoric $\mathbf{F}^e_{iso}$ components as:

$$\mathbf{F}^e = \mathbf{F}^e_{iso} \, \mathbf{F}^e_{vol} \tag{5.22}$$

in which

$$\mathbf{F}^e_{iso} = (\det \mathbf{F}^e)^{-\frac{1}{3}} \, \mathbf{F}^e \tag{5.23a}$$

$$\mathbf{F}^e_{vol} = (\det \mathbf{F}^e)^{\frac{1}{3}} \, \mathbf{I} \tag{5.23b}$$

Using Equation 5.22 to calculate the elastic Green-Lagrange strain tensor, one obtains

$$\mathbf{E}^e = \frac{1}{2} \left(\mathbf{F}^{eT} \mathbf{F}^e - \mathbf{I} \right) = \mathbf{F}^{eT}_{vol} \, \mathbf{E}^e_{iso} \, \mathbf{F}^e_{vol} + \mathbf{E}^e_{vol} \tag{5.24}$$

where the volumetric $\mathbf{E}^e_{vol}$ and isochoric $\mathbf{E}^e_{iso}$ elastic Green-Lagrange strain tensors

are given by:

$$\mathbf{E}^e_{vol} = \frac{1}{2}\left(\mathbf{F}^{eT}_{vol}\mathbf{F}^e_{vol} - \mathbf{I}\right) \tag{5.25a}$$

$$\mathbf{E}^e_{iso} = \frac{1}{2}\left(\mathbf{F}^{eT}_{iso}\mathbf{F}^e_{iso} - \mathbf{I}\right) \tag{5.25b}$$

To obtain the degraded elastic Green-Lagrange strain tensor, it is assumed that the isochoric strain tensor $\mathbf{E}^e_{iso}$ is linearly degraded with the order parameter irrespective of the nature of volume change. However, the volumetric strain tensor is degraded only if the volume change is tensile ($J^e = \det \mathbf{F}^e > 1$). The degraded elastic Green-Lagrange strain tensor reads as:

$$\tilde{\mathbf{E}}^e = (1-s)\mathbf{F}^{eT}_{vol}\,\mathbf{E}^e_{iso}\,\mathbf{F}^e_{vol} + \left[1 - s\mathcal{H}\left(J^e - 1\right)\right]\mathbf{E}^e_{vol} \tag{5.26}$$

Using Equations 5.23 and 5.25, one can rewrite Equation 5.26 as:

$$\begin{aligned}\tilde{\mathbf{E}}^e =& (1-s)\frac{1}{2}\left(\mathbf{F}^{eT}\mathbf{F}^e - \mathbf{I}\right) + \left[1 - \mathcal{H}\left(J^e - 1\right)\right] s\frac{1}{2}\left(J^{e\frac{2}{3}} - 1\right)\mathbf{I} \\ =& (1-s)\mathbf{E}^e + \left[1 - \mathcal{H}\left(J^e - 1\right)\right] s\mathbf{E}^e_{vol}\end{aligned} \tag{5.27}$$

Equation 5.27 provides another chance to re-interpret the degraded elastic Green-Lagrange strain tensor. According to Equation 5.27, $\tilde{\mathbf{E}}^e$ can be obtained by first ignoring the unilateral condition and degrading the entire elastic strain tensor (both volumetric and isochoric components); that is $\tilde{\mathbf{E}}^e = (1-s)\mathbf{E}^e$. In the second step, if

it is realized that the volume change is compressive, an appropriate volumetric elastic strain ($[1-\mathcal{H}\left(J^e-1\right)]\, s\mathbf{E}^e_{vol}$) is also added to $\tilde{\mathbf{E}}^e$ such that the improper degradation of volumetric strain in the first step is undone.

***Remark* 7** *Under small strain conditions ($\mathbf{F}^e \simeq \mathbf{I}$), the degraded elastic Green-Lagrange strain tensor in Equation 5.27 reduces to the degraded linear elastic strain tensor $\tilde{\boldsymbol{\epsilon}}^e$ as:*

$$\tilde{\boldsymbol{\epsilon}}^e = (1-s)\boldsymbol{\epsilon}^e + [1-\mathcal{H}\left(\operatorname{tr}\boldsymbol{\epsilon}^e\right)]\, s\frac{\operatorname{tr}\boldsymbol{\epsilon}^e}{3}\mathbf{I} \tag{5.28}$$

Replacing $\tilde{\mathbf{E}}^e$ in Equation 5.21 with $\tilde{\boldsymbol{\epsilon}}^e$ and assuming isotropy, SEED is calculated as:

$$\begin{aligned}
\rho_0\psi_e =& \frac{\kappa}{2}\operatorname{tr}^2\left(\tilde{\boldsymbol{\epsilon}}^e\right) + \mu\operatorname{tr}\left(\tilde{\boldsymbol{\epsilon}}^{e2}_{dev}\right) \\
=& \frac{\kappa}{2}\operatorname{tr}^2\left[(1-s)\boldsymbol{\epsilon}^e + [1-\mathcal{H}\left(\operatorname{tr}\boldsymbol{\epsilon}^e\right)]\, s\frac{\operatorname{tr}\boldsymbol{\epsilon}^e}{3}\mathbf{I}\right] + \mu\operatorname{tr}\left[(1-s)^2\boldsymbol{\epsilon}^{e2}_{dev}\right] \\
=& \frac{\kappa}{2}\left[(1-s)\operatorname{tr}(\boldsymbol{\epsilon}^e) + [1-\mathcal{H}\left(\operatorname{tr}\boldsymbol{\epsilon}^e\right)]\, s\operatorname{tr}(\boldsymbol{\epsilon}^e)\right]^2 + \mu(1-s)^2\operatorname{tr}\left(\boldsymbol{\epsilon}^{e2}_{dev}\right) \\
=& \frac{\kappa}{2}\left[1-\mathcal{H}\left(\operatorname{tr}\boldsymbol{\epsilon}^e\right)s\right]^2\operatorname{tr}^2\left(\boldsymbol{\epsilon}^e\right) + \mu(1-s)^2\operatorname{tr}\left(\boldsymbol{\epsilon}^{e2}_{dev}\right) \\
=& (1-s)^2\left[\frac{\kappa}{2} < \operatorname{tr}(\boldsymbol{\epsilon}^e) >_+^2 \; + \mu\operatorname{tr}(\boldsymbol{\epsilon}^{e2}_{dev})\right] + \frac{\kappa}{2} < \operatorname{tr}(\boldsymbol{\epsilon}^e) >_-^2
\end{aligned} \tag{5.29}$$

It is observed that the proposed SEED in Equation 5.21 reduces to the formulation in Equation 5.18 under small strain isotropic elasticity conditions. Therefore, the proposed SEED formulation could be deemed as the anisotropic finite-strain analog of the formulation in [63].

***Remark* 8** *Consider a fully degraded material point ($s=1$) subject to a strain state*

corresponding to volumetric expansion. Using either the SEED formulation proposed here or the ones mentioned in Section 5.2.1, one can readily verify that $\rho_0\psi_e$ is zero. This leads to occurrence of numerical problems under quasi-static conditions due to disappearance of the local stiffness of the material and the discretized problem could suffer from ill-posedness [64]. To circumvent this issue, a sufficiently small positive parameter κ_s can be introduced in SEED formulation to leave an artificial elastic energy density in the material at the fully broken state [63–65]. With this in mind, one can rewrite Equation 5.27 such that the degraded elastic strain tensor, and hence SEED, would not disappear at $s = 1$.

$$\tilde{\mathbf{E}}^e = g_2(s)\,\mathbf{E}^e + g_1(J^e, s)\,\mathbf{E}^e_{vol} \tag{5.30}$$

with $g_1(J^e, s) = [1 - \mathcal{H}(J^e - 1)](1 - \kappa_s)s$ and $g_2(s) = [1 - (1 - \kappa_s)s]$.

***Remark* 9** *Plugging Equation 5.22 into 2.4, one obtains*

$$\mathbf{F} = \mathbf{F}^e_{iso}\,\mathbf{F}^e_{vol}\,\mathbf{F}^p \tag{5.31}$$

It is readily observed that the volumetric-isochoric split of elastic deformation gradient in Equation 5.22 leads to introduction of a new configuration, namely elastically dilated configuration. Figure 5.3 depicts the multiplicative decomposition of deformation gradient in Equation 5.31. One can interpret $\mathbf{F}^e_{vol}$ as a deformation gradient which linearly maps vectors in the intermediate configuration to the corresponding one in

the elastically dilated one. $\mathbf{F}^e_{iso}$ *is the tensor which linearly maps vectors in elastically dilated configuration to the corresponding one in the current configuration.*

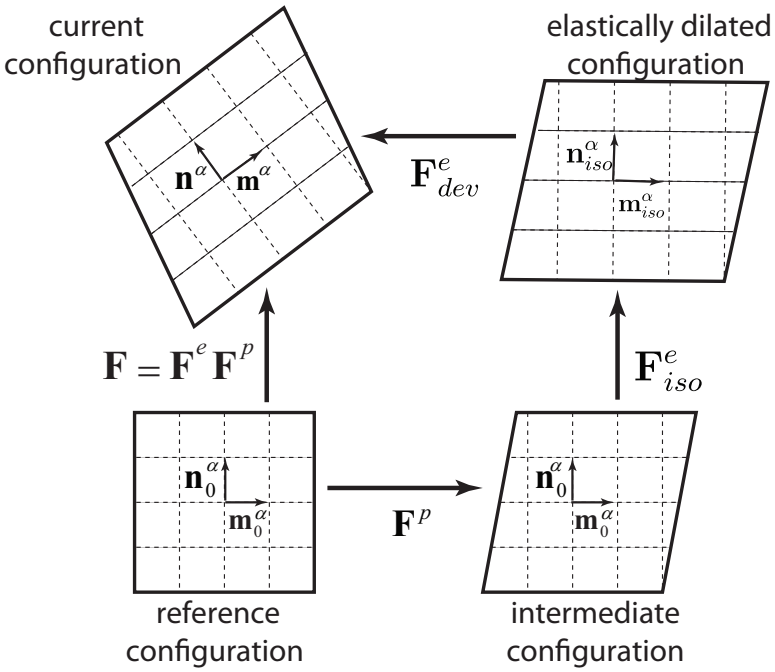

Figure 5.3: Multiplicative decomposition of deformation gradient into elastic isochoric, elastic volumetric and plastic components

5.3 Stored plastic energy density

Plastic deformation is an exothermic process, releasing energy in the form of heat. A significant fraction of the plastic work is dissipated and converted into heat, while the rest is stored as defect energy [86, 121]. The contribution of plastic work to the free energy density in a degradable material can be formulated as

$$\rho_0 \psi_p = (1-s)^2 \frac{\beta_p}{2} \sum_{\alpha=1}^{nslip} \left(s_{ath}^{\alpha} + s_{th}^{\alpha}\right) \gamma_{acc}^{\alpha} \tag{5.32}$$

in which $\gamma_{acc}^{\alpha} = \int_0^t |\dot{\gamma}^{\alpha}|\, dt$ is the total accumulated slip on slip system α. As mentioned in Section 2.4, s_{ath}^{α} and s_{th}^{α} correspond to the athermal and thermal resistances to dislocation glide, respectively. β_p is a material constant which should be chosen carefully such that the contribution of plastic work to free energy density does not exceed the total plastic work [86].

5.4 Stress measures

With the Helmholtz free energy density defined, one can calculate the first Piola-Kirchhoff stress using Equation 3.33.

$$\mathbf{P} = \rho_0 \frac{\partial \psi}{\partial \mathbf{F}} + \beta_{lu}\, \mathbf{F}\, \dot{\mathbf{E}} = \rho_0 \frac{\partial \psi}{\partial \tilde{\mathbf{E}}^e} : \frac{\partial \tilde{\mathbf{E}}^e}{\partial \mathbf{F}^e} : \frac{\partial \mathbf{F}^e}{\partial \mathbf{F}} + \beta_{lu}\, \mathbf{F}\, \dot{\mathbf{E}} \tag{5.33}$$

where

$$\rho_0 \frac{\partial \psi}{\partial \tilde{\mathbf{E}}^e} = \mathbb{C}^e : \tilde{\mathbf{E}}^e \tag{5.34a}$$

$$\left(\frac{\partial \tilde{\mathbf{E}}^e}{\partial \mathbf{F}^e}\right)_{ijkl} = \frac{1}{3} g_1\left(J^e, s\right) J^{e\,\frac{2}{3}} \delta_{ij} F_{lk}^{e\,-1} + \frac{1}{2} g_2\left(s\right) \left(F_{ki}^e \delta_{jl} + F_{kj}^e \delta_{il}\right) \tag{5.34b}$$

$$\left(\frac{\partial \mathbf{F}^e}{\partial \mathbf{F}}\right)_{ijkl} = \delta_{ik} F_{lj}^{p\,-1} \tag{5.34c}$$

Plugging Equation 5.34 into Equation 5.33, an analytical form for the first Piola-Kirchhoff stress is obtained as:

$$\mathbf{P} = \frac{1}{3} g_1\left(J^e, s\right) J^{e\,\frac{2}{3}} \left(\mathbf{I} \colon \mathbb{C}^e \colon \tilde{\mathbf{E}}^e\right) \mathbf{F}^{-T} + g_2\left(s\right) \mathbf{F}^e \left(\mathbb{C}^e \colon \tilde{\mathbf{E}}^e\right) \mathbf{F}^{p\,-T} + \beta_{lu}\, \mathbf{F}\, \dot{\mathbf{E}} \tag{5.35}$$

For crystal plasticity constitutive calculations, one needs to compute the second Piola-Kirchhoff stress in the intermediate configuration $\mathbf{S}_p$. Using Equation 5.35, $\mathbf{S}_p$ is derived as:

$$\mathbf{S}_p = \underbrace{\frac{1}{3} g_1\left(J^e, s\right) J^{e\,\frac{2}{3}} \left(\mathbf{I} \colon \mathbb{C}^e \colon \tilde{\mathbf{E}}^e\right) \mathbf{C}^{e\,-1} + g_2\left(s\right) \mathbb{C}^e \colon \tilde{\mathbf{E}}^e}_{\mathbf{S}_p^{nv}} + \underbrace{\beta_{lu} \mathbf{F}^p \dot{\mathbf{E}} \mathbf{F}^{p\,T}}_{\mathbf{S}_p^{v}} \tag{5.36}$$

where $\mathbf{S}_p^{nv}$ and $\mathbf{S}_p^{v}$ are the non-viscous and viscous components of $\mathbf{S}_p$, respectively.

Chapter 6

Numerical implementation details

This chapter discusses the details of implementation of the phase field modeling of fracture in a nonlinear finite element framework. Specifically, the following topics will be covered.

- A simple technique to ensure the irreversibility of crack phase field is discussed.
- Time integration of the CP constitutive model is explained.
- The required variables to evaluate the tangent stiffness and internal force vector for both displacement and crack phase fields are computed.

This chapter will conclude with a few suggestions to accelerate the fracture simulations. Throughout this chapter, it is assumed that the problem state (displacement $\mathbf{u}$, order parameter s and the internal state variable (ISV)) is known at time $t - \triangle t$ and one would like to obtain the problem state at time t using Newton-Raphson scheme.

Moreover, *inter-field information* (IFI) is introduced which stores the most updated state of variables needed for coupling of the fields. This variable is updated after each field is solved during the staggered iterations, as shown in Figure 4.1. Besides IFI and ISV, at each iteration of the Newton-Raphson, the constitutive models for the displacement and crack phase field problems should be solved for a candidate deformation gradient $\mathbf{F}$ and order parameter s, respectively.

6.1 Implementation of crack phase field model without threshold

Plugging Equation 5.1 into Equation 3.39b, the differential equation governing crack phase field is obtained as:

$$\beta_{gs}\,\dot{s} = \underbrace{\left(-\rho_0 \frac{\partial \psi_e}{\partial s} - \rho_0 \frac{\partial \psi_p}{\partial s}\right)}_{\text{mechanical driving force}} - \underbrace{\frac{g_c}{l_c}\left(s - l_c^2 \boldsymbol{\nabla}_{\mathbf{X}} \cdot \boldsymbol{\nabla}_{\mathbf{X}} s\right)}_{\text{geometric resistance}} \tag{6.1}$$

Note that here the crack surface energy density corresponding to the model without threshold is used. The first term on RHS is only dependent on the state of displacement field and is, therefore, called the *mechanical driving force* for fracture [67]. Given that both $\rho_0\psi_e$ and $\rho_0\psi_p$ decrease as order parameter increases, one can verify that the mechanical driving force is always non-negative. Using Equations 5.21, 5.30 and 5.32, the mechanical driving force is calculated as:

$$
\begin{aligned}
f_{mech}\left(\mathbf{F}^e, \hat{W}^p, s\right) =& -\rho_0 \frac{\partial \psi_e\left(\mathbf{F}^e, s\right)}{\partial s} - \rho_0 \frac{\partial \psi_p\left(\hat{W}^p, s\right)}{\partial s} \\
=& (1-\kappa_s)\Big(\mathbb{C}^e : \tilde{\mathbf{E}}^e\left(\mathbf{F}^e, s\right)\Big) : \\
& \Big(\mathbf{E}^e\left(\mathbf{F}^e\right) - \left[1 - \mathcal{H}\left(J^e - 1\right)\right] \mathbf{E}^e_{vol}\left(\mathbf{F}^e\right)\Big) + 2(1-s)\hat{W}^p
\end{aligned} \tag{6.2}
$$

For the sake of brevity, here we use $\hat{W}^p = \beta_p/2 \sum_{\alpha=1}^{nslip} \left(s^\alpha_{ath} + s^\alpha_{th}\right) \gamma^\alpha_{acc}$ to represent the stored plastic energy density in an undamaged material.

In order to compute the internal force vector for the crack phase field given by Equation 4.43b, one needs to derive the derivative of HFED w.r.t. to the order parameter and its gradient.

$$
\pi_0^{en}\left(\mathbf{F}^e, \hat{W}^p, s\right) = \rho_0 \frac{\partial \psi}{\partial s} = \frac{g_c}{l_c} s - f_{mech}\left(\mathbf{F}^e, \hat{W}^p, s\right) \tag{6.3a}
$$

$$
\boldsymbol{\xi}_0\left(s\right) = \rho_0 \frac{\partial \psi}{\partial \boldsymbol{\nabla}_{\mathbf{X}} s} = g_c l_c \boldsymbol{\nabla}_{\mathbf{X}} s \tag{6.3b}
$$

Moreover, it is required to calculate the second derivative of HFED w.r.t. to the order parameter and its gradient to compute the stiffness matrix for the crack phase field given in Equation 4.43a.

$$
\frac{\partial \pi_0^{en}\left(\mathbf{F}^e, \hat{W}^p, s\right)}{\partial s} = \rho_0 \frac{\partial^2 \psi}{\partial s^2} = \frac{g_c}{l_c} - \frac{\partial f_{mech}\left(\mathbf{F}^e, \hat{W}^p, s\right)}{\partial s} \tag{6.4a}
$$

$$
\mathbf{A}_s = \frac{\partial}{\partial \boldsymbol{\nabla}_{\mathbf{X}} s} \boldsymbol{\xi}_0 = \frac{\partial}{\partial \boldsymbol{\nabla}_{\mathbf{X}} s} \left(\rho_0 \frac{\partial \psi}{\partial \boldsymbol{\nabla}_{\mathbf{X}} s}\right) = g_c l_c \mathbf{I} \tag{6.4b}
$$

The proposed phase field modeling of fracture does not enforce irreversibility; e.g. cracks could heal upon unloading of the system. Therefore, it needs to be modified

such that $\dot{s} \geq 0$. Different methods have been proposed in the literature to enforce irreversibility. Bourdin et al. [64] suggested a Dirichlet-type condition approach to enforce irreversibility. According to their approach, if the order parameter at an FE node at time t^* becomes 1, a Dirichlet condition of $s = 1$ can be applied on this node for $t > t^*$. This approach ensures that the crack at a fully fractured node does not recover; however, it does not enforce irreversibility at nodes where order parameter is $0 < s < 1$. Wick [122] suggested an incremental formulation where the irreversibility constraint is enforced using an augmented Lagrangian penalization. A simple and yet effective solution was proposed by Miehe et al. [66] where a local history field of maximum positive energy density was introduced to enforce irreversibility condition. Positive energy density signifies the part of HFED which is degraded by the crack phase field and thus drives the evolution of order parameter. This history field is stored as a state variable and monitors the maximum positive energy density experienced by the material point during the history of deformation. Irreversibility is enforced by solving the crack phase field problem using this local history field. In this work, an approach similar to the local history field in [66, 67] is adopted to enforce irreversibility. Here, f_{mech} as well as the elastic strain tensor and stored plastic work corresponding to the maximum f_{mech} in deformation history are stored as ISV. The most updated elastic strain tensor and stored plastic work are stored in IFI to inform the crack phase field of the most updated state of displacement field. The constitutive calculation at an integration point for crack phase field incorporating the

irreversibility constraint is illustrated in Figure 6.1.

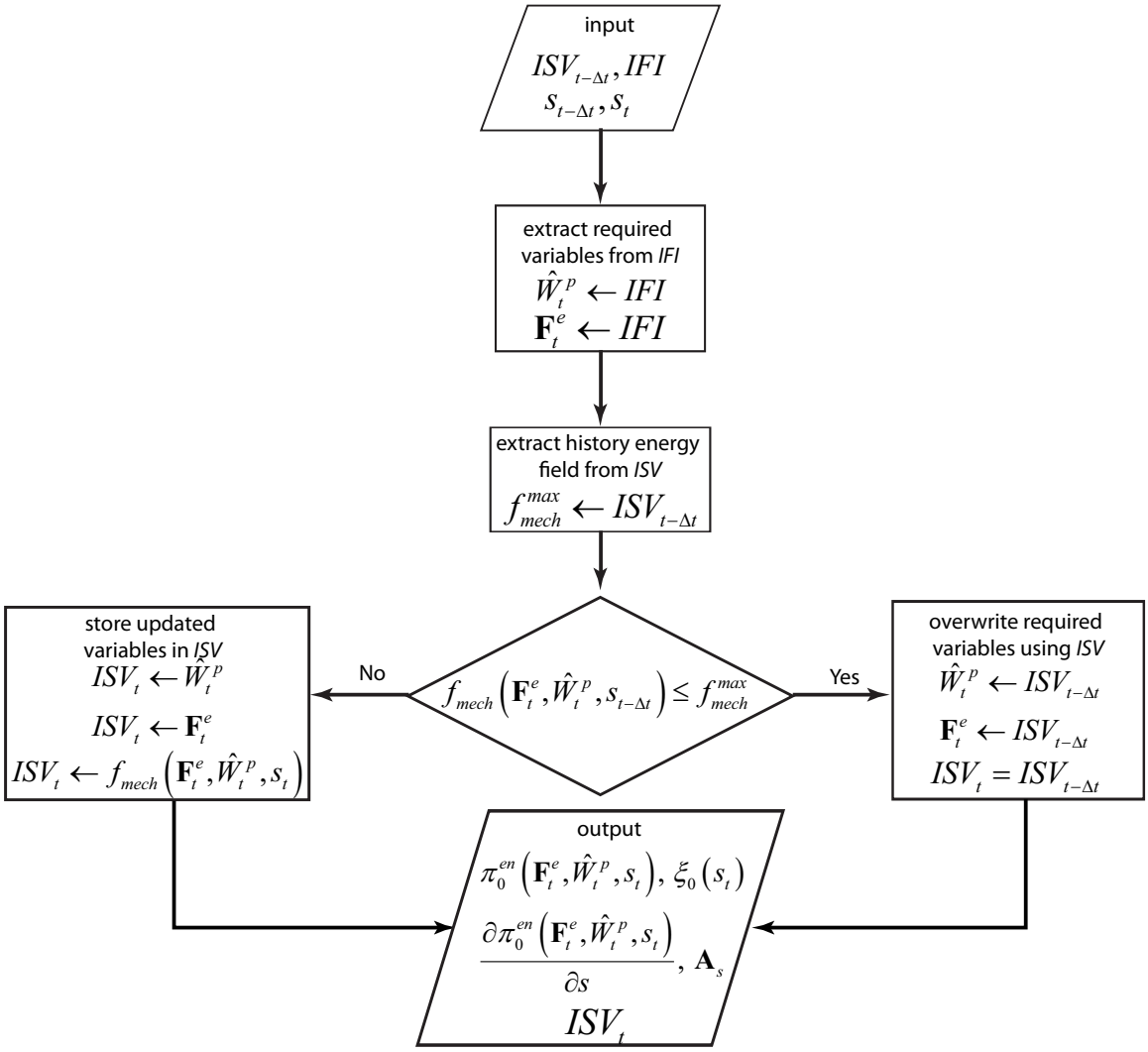

Figure 6.1: schematics of the constitutive calculation at an integration point for crack phase field model without threshold

6.2 Implementation of crack phase field model with threshold

Constitutive calculations and imposing irreversibility condition for the crack phase field model with threshold is very similar to the one discussed in the previous section. Using Equation 5.10 as the crack surface energy density, the differential equation governing crack phase field with threshold can be cast into a form similar to the one in Equation 6.1.

$$\begin{aligned}\beta_{gs}\,\dot{s} &= -\rho_0\frac{\partial\psi_e}{\partial s} - \rho_0\frac{\partial\psi_p}{\partial s} - 2w_c + 2w_c l_c^2\boldsymbol{\nabla}_{\mathbf{X}}\cdot\boldsymbol{\nabla}_{\mathbf{X}}s \\ &= -\rho_0\frac{\partial\psi_e}{\partial s} - \rho_0\frac{\partial\psi_p}{\partial s} - 2w_c\left[s+(1-s)\right] + 2w_c l_c^2\boldsymbol{\nabla}_{\mathbf{X}}\cdot\boldsymbol{\nabla}_{\mathbf{X}}s \\ &= \underbrace{\left(-\rho_0\frac{\partial\psi_e}{\partial s} - \rho_0\frac{\partial\psi_p}{\partial s}\right)}_{\text{mechanical driving force}} - \underbrace{2w_c(1-s)}_{\text{threshold force}} - \underbrace{2w_c\left(s - l_c^2\boldsymbol{\nabla}_{\mathbf{X}}\cdot\boldsymbol{\nabla}_{\mathbf{X}}s\right)}_{\text{geometric resistance}}\end{aligned} \tag{6.5}$$

To start fracture once a certain amount of energy density is stored in the material, one should require the mechanical driving force to exceed the threshold force $f_{th}(s)$. Therefore, the governing equation should be modified as [67]:

$$\beta_{gs}\,\dot{s} = \left\langle\left(-\rho_0\frac{\partial\psi_e}{\partial s} - \rho_0\frac{\partial\psi_p}{\partial s}\right) - 2w_c(1-s)\right\rangle_+ - 2w_c\left(s - l_c^2\boldsymbol{\nabla}_{\mathbf{X}}\cdot\boldsymbol{\nabla}_{\mathbf{X}}s\right) \tag{6.6}$$

Due to this modification in the strong form of the crack phase field problem, one needs to redo the linearization process. Following a similar procedure as in Section

4.5, one can derive the elemental tangent stiffness matrix $[K_{se}]$ and internal force vector $\{f_{se}^{int}\}$ for the crack phase field with threshold as:

$$[K_{se}] = \int_{\Omega_{e,0}} [N_s^e]^T \left(\frac{\beta_{gs}}{\triangle t} + \frac{\partial \tilde{\pi}_0^{en}}{\partial s} \right) [N_s^e] \, d\Omega_{e,0} + \int_{\Omega_{e,0}} [G_{sX}^e]^T \frac{\partial \tilde{\boldsymbol{\xi}}_0}{\partial \boldsymbol{\nabla}_{\mathbf{X}} s} [G_{sX}^e] \, d\Omega_{e,0} \tag{6.7a}$$

$$\{f_{se}^{int}\} = \int_{\Omega_{e,0}} [N_s^e]^T \left(\beta_{gs} \frac{s - s_{t-\triangle t}}{\triangle t} + \tilde{\pi}_0^{en} \right) \, d\Omega_{e,0} + \int_{\Omega_{e,0}} [G_{sX}^e]^T \tilde{\boldsymbol{\xi}}_0 \, d\Omega_{e,0} \tag{6.7b}$$

where

$$\tilde{\pi}_0^{en} \left(\mathbf{F}^e, \hat{W}^p, s \right) = \begin{cases} 2w_c s & \text{if} \quad f_{mech} \leq f_{th} \\ 2w_c - f_{mech} \left(\mathbf{F}^e, \hat{W}^p, s \right) & \text{if} \quad f_{mech} > f_{th} \end{cases} \tag{6.8a}$$

$$\tilde{\boldsymbol{\xi}}_0(s) = 2w_c l_c^2 \, \boldsymbol{\nabla}_{\mathbf{X}} s \tag{6.8b}$$

$$\frac{\partial \tilde{\pi}_0^{en} \left(\mathbf{F}^e, \hat{W}^p, s \right)}{\partial s} = \begin{cases} 2w_c & \text{if} \quad f_{mech} \leq f_{th} \\ -\frac{\partial f_{mech} \left(\mathbf{F}^e, \hat{W}^p, s \right)}{\partial s} & \text{if} \quad f_{mech} > f_{th} \end{cases} \tag{6.8c}$$

$$\frac{\partial \tilde{\boldsymbol{\xi}}_0}{\partial \boldsymbol{\nabla}_{\mathbf{X}} s} = 2w_c l_c^2 \, \mathbf{I} \tag{6.8d}$$

The algorithm used to calculate the constitutive response for the crack phase field with threshold is very similar to the one given in Figure 6.1. The only difference is the output box in the algorithm where the output variables should be $\tilde{\pi}_0^{en}$, $\tilde{\boldsymbol{\xi}}_0$, $\partial \tilde{\pi}_0^{en} / \partial s$, $\partial \tilde{\boldsymbol{\xi}}_0 / \partial \boldsymbol{\nabla}_{\mathbf{X}} s$ and ISV_t.

6.3 Time integration of CP constitutive model

Different algorithms have been designed to perform time integration for crystal plasticity constitutive models. An excellent summary of the most important algorithms is provided in [123]. In this work, a semi-implicit time integration algorithm is devised to solve a set of 9 nonlinear equations, corresponding to the components of elastic deformation gradient $\mathbf{F}^e$. In this section, unless explicitly mentioned, the subscript t is dropped from all variables pertaining to the current time.

Solving the evolution equation for $\mathbf{F}^p$ in Equation 2.5, the plastic deformation gradient at time t is obtained as [124]:

$$\mathbf{F}^p = \exp\left(\sum_{\alpha=1}^{n_{slip}} \triangle\gamma^\alpha \mathbf{S}_0^\alpha\right) \mathbf{F}^p_{t-\triangle t} \tag{6.9}$$

with $\triangle\gamma^\alpha = \dot{\gamma^\alpha}\triangle t$. For $|\triangle\gamma^\alpha| \ll 1$, this equation can be approximated as [125]:

$$\mathbf{F}^p \approx \left(\mathbf{I} + \sum_{\alpha=1}^{n_{slip}} \triangle\gamma^\alpha \mathbf{S}_0^\alpha\right) \mathbf{F}^p_{t-\triangle t} \tag{6.10}$$

The inverse of plastic deformation gradient can be obtained as:

$$\mathbf{F}^{p\,-1} \approx \mathbf{F}^{p\,-1}_{t-\triangle t}\left(\mathbf{I} - \sum_{\alpha=1}^{n_{slip}} \triangle\gamma^\alpha \mathbf{S}_0^\alpha\right) \tag{6.11}$$

Using Equations 2.4 and 6.11, the elastic deformation gradient is obtained as:

$$\mathbf{F}^e = \mathbf{F}\mathbf{F}^{p^{-1}} = \mathbf{F}^{e\,tr} - \sum_{\alpha=1}^{n_{slip}} \triangle\gamma^\alpha \left(\mathbf{F}^e, ISV\right) \mathbf{B}^\alpha \tag{6.12}$$

where

$$\mathbf{F}^{e\,tr} = \mathbf{F}\ \mathbf{F}_{t-\triangle t}^{p\,-1} \tag{6.13a}$$

$$\mathbf{B}^\alpha = \mathbf{F}\ \mathbf{F}_{t-\triangle t}^{p\,-1}\ \mathbf{S}_0^\alpha \tag{6.13b}$$

A two-stage Newton-Raphson scheme is employed to solve Equation 6.12 since the slip increment $\triangle\gamma^\alpha$ has a nonlinear dependence on $\mathbf{F}^e$. In the first stage (*inner loop*), Equation 6.12 is solved for $\mathbf{F}^e$ while freezing the slip system resistances. Following Maniatty et al. [126], an adaptive scheme is implemented to restrict the change of $\mathbf{F}^e$ between iterations when the residual starts to increase. In the second stage (*outer loop*), the slip system resistances are evolved using the slip increments calculated in the first stage. This two-stage iterative solver is repeated until both elastic deformation gradient and the resistances converge.

The i-th iteration of Newton-Raphson in the inner loop reads as:

$$\mathbf{F}^{e\,i+1} = \mathbf{F}^{e\,i} - \mathbb{J}^{-1} : \mathbf{R}^i \tag{6.14}$$

where the residual $\mathbf{R}$ and Jacobian $\mathbb{J}$ are computed as:

$$\mathbf{R}^i = \mathbf{F}^{e\,i} - \mathbf{F}^{e\,tr} + \sum_{\alpha=1}^{n_{slip}} \triangle\gamma^\alpha \left(\mathbf{F}^{e\,i}, ISV\right) \mathbf{B}^\alpha \tag{6.15a}$$

$$\mathbb{J} = \mathbb{I} + \sum_{\alpha=1}^{n_{slip}} \frac{\partial \triangle\gamma^{\alpha}}{\partial \tau_p^{\alpha}} \mathbf{B}^{\alpha} \otimes \frac{\partial \tau_p^{\alpha}}{\partial \mathbf{F}^e} \tag{6.15b}$$

Here $\mathbb{I}_{ijkl} = \delta_{ik}\delta_{jl}$ is the fourth order identity tensor. Calculation of $\partial \triangle\gamma^{\alpha}/\partial \tau_p^{\alpha}$ is straightforward; however, derivation of $\partial \tau_p^{\alpha}/\partial \mathbf{F}^e$ is more analytically involved and is given in details in Section 6.4. The sequence of computational operations needed for time integration of the CP constitutive relations is given in Table 6.1.

6.4 Derivation of $\frac{\partial \tau_p^{\alpha}}{\partial \mathbf{F}^e}$

Using Equation 2.7, the derivative of resolved shear stress in the intermediate configuration with respect to the elastic deformation gradient is obtained as

$$\frac{\partial \tau_p^{\alpha}}{\partial \mathbf{F}^e} = \left(\mathbf{S}_0^{\alpha}\mathbf{S}_p^{nv}\right) : \frac{\partial \mathbf{C}^e}{\partial \mathbf{F}^e} + \left(\mathbf{C}^e\mathbf{S}_0^{\alpha}\right) : \frac{\partial \mathbf{S}_p^{nv}}{\partial \mathbf{F}^e} \tag{6.16}$$

where

$$\left(\partial \mathbf{C}^e/\partial \mathbf{F}^e\right)_{ijkl} = F_{ki}^e\delta_{jl} + F_{kj}^e\delta_{il} \tag{6.17}$$

Using Equations 5.36, the derivative of $\mathbf{S}_p^{nv}$ with respect to the elastic deformation gradient is calculated as:

Step **A**	**Determine elastic deformation gradient and slip increments**
I	*Initialize relevant quantities for the Newton-Raphson algorithm*:
	$\mathbf{F}^{e\,0} = \mathbf{F}^{e}_{t-\triangle t}, \quad \mathbf{F}^{p\,0} = \mathbf{F}^{p}_{t-\triangle t}\ , \quad s^{\alpha}_{th} = s^{\alpha}_{th,t-\triangle t}, \quad s^{\alpha}_{ath} = s^{\alpha}_{ath,t-\triangle t}, \quad \chi^{\alpha} = \chi^{\alpha}_{t-\triangle t}$
II	*For the i-th iteration in the Newton-Raphson algorithm*:
	(a) Calculate $\tilde{\mathbf{E}}^{e}$ using Equation 5.30
	(b) Calculate $\mathbf{S}_p$ and τ^{α}_{p} using Equations 5.36 and 2.7, respectively
	(c) Calculate slip rates using Equations 2.8
	(d) Calculate residual and Jacobian using Equation 6.15
	(e) if $i = 0$ or $\parallel \mathbf{R}^{i} \parallel < \parallel \mathbf{R}^{i-1} \parallel$; continue to step (f)
	if $i \neq 0$ and $\parallel \mathbf{R}^{i} \parallel > \parallel \mathbf{R}^{i-1} \parallel$; scale back $\mathbf{F}^{e\,i}$
	$\mathbf{F}^{e\,i} \longleftarrow \frac{1}{2}\left(\mathbf{F}^{e\,i} + \mathbf{F}^{e\,i-1}\right)$
	and go to step (a)
	(f) update elastic deformation gradient using Equation 6.14
	(g) Check for convergence: if no, return to step (a); if yes, proceed to step III.
Step **B**	**Update slip system resistances.**
III	*Compute hardening matrix using Equation* 2.15
IV	*Update slip system resistances using Equation* 2.12
V	*Check for convergence of slip system resistances: if no, return to step II; if yes, proceed to step VI*
VI	*return updated ISVs, Cauchy stress and first spatial elasticity tensor*

Table 6.1: Sequence of computational operations for time integration of the crystal plasticity constitutive model

$$\left(\frac{\partial \mathbf{S}_p^{nv}}{\partial \mathbf{F}^e}\right)_{ijkl} = \frac{1}{3} g_1\left(J^e, s\right) J^{e\,\frac{2}{3}} \mathbb{C}^e_{nnrs} \left[\frac{2}{3} F^{e\,-1}_{lk} \tilde{E}^e_{rs} C^{e\,-1}_{ij} + \left(\frac{\partial \tilde{\mathbf{E}}^e}{\partial \mathbf{F}^e}\right)_{rskl} C^{e\,-1}_{ij} + \tilde{E}^e_{rs} \left(\frac{\partial \mathbf{C}^{e\,-1}}{\partial \mathbf{F}^e}\right)_{ijkl}\right] + g_2(s) \mathbb{C}^e_{ijrs} \left(\frac{\partial \tilde{\mathbf{E}}^e}{\partial \mathbf{F}^e}\right)_{rskl} \tag{6.18}$$

The term $\partial \tilde{\mathbf{E}}^e / \partial \mathbf{F}^e$ is already given in Equation 5.34. One can calculate $\partial \mathbf{C}^{e\,-1} / \partial \mathbf{F}^e$ using Equation 6.17 and tensor identity $\left(\partial \mathbf{C}^{e\,-1} / \partial \mathbf{F}^e\right)_{ijkl} = -C^{e\,-1}_{ir} \left(\partial \mathbf{C}^e / \partial \mathbf{F}^e\right)_{rmkl} C^{e\,-1}_{mj}$.

6.5 Derivation of first spatial elasticity tensor

In order to evaluate the stiffness matrix in Equation 4.36a, one needs to calculate the first spatial elasticity tensor $\mathbb{a}$. It can be readily seen that $\mathbb{a}$ can be expressed in terms of $\mathbb{A} = \partial \mathbf{P} / \partial \mathbf{F}$ (see Equation 4.30). Before starting to calculate $\mathbb{A}$, it is observed that the formulation for $\mathbf{P}$ in Equation 5.35 can be modified such that it is only dependent on $\mathbf{F}^e$ and $\mathbf{F}$.

$$\mathbf{P} = \frac{1}{3} g_1\left(J^e, s\right) J^{e\,\frac{2}{3}} \left(\mathbf{I} \colon \mathbb{C}^e \colon \tilde{\mathbf{E}}^e\right) \mathbf{F}^{-T} + g_2\left(s\right) \mathbf{F}^e \left(\mathbb{C}^e \colon \tilde{\mathbf{E}}^e\right) \mathbf{F}^{e\,T} \mathbf{F}^{-T} + \beta_{lu}\, \mathbf{F}\, \dot{\mathbf{E}} \tag{6.19}$$

Using chain rule, derivative of $\mathbf{P}$ with respect to $\mathbf{F}$ is obtained as:

$$\mathbb{A} = \frac{\partial \mathbf{P}}{\partial \mathbf{F}} = \left.\frac{\partial \mathbf{P}}{\partial \mathbf{F}}\right|_{\mathbf{F}^e} + \left.\frac{\partial \mathbf{P}}{\partial \mathbf{F}^e}\right|_{\mathbf{F}} : \frac{\partial \mathbf{F}^e}{\partial \mathbf{F}} \tag{6.20}$$

Holding $\mathbf{F}^e$ fixed, derivative of $\mathbf{P}$ with respect to $\mathbf{F}$ is obtained as:

$$\begin{aligned}\left(\frac{\partial \mathbf{P}}{\partial \mathbf{F}}\right)_{ijkl}\Bigg|_{\mathbf{F}^e} =& -\frac{1}{3} g_1\left(J^e, s\right) J^{e\,\frac{2}{3}} \mathbb{C}^e_{pprs} \tilde{E}^e_{rs} F^{-1}_{jk} F^{-1}_{li} - \\ & g_2\left(s\right) F^e_{ip} \mathbb{C}^e_{pqrs} \tilde{E}^e_{rs} F^e_{tq} F^{-1}_{jk} F^{-1}_{lt} + \\ & \frac{\beta_{lu}}{\triangle t}\left[\delta_{ik}\left(E_{lj} - E_{t-\triangle t\, lj}\right) + \frac{1}{2} F_{il} F_{kj} + \frac{1}{2}\delta_{jl} F_{ir} F_{kr}\right]\end{aligned} \tag{6.21}$$

Holding $\mathbf{F}$ fixed, derivative of $\mathbf{P}$ with respect to $\mathbf{F}^e$ is obtained as:

$$\begin{aligned}\left(\frac{\partial \mathbf{P}}{\partial \mathbf{F}^e}\right)_{ijkl}\Bigg|_{\mathbf{F}} =& \frac{1}{3} g_1\left(J^e, s\right) J^{e\,\frac{2}{3}} \mathbb{C}^e_{pprs} F^{-1}_{ji}\left[\frac{2}{3} F^{e\,-1}_{lk} \tilde{E}^e_{rs} + \left(\frac{\partial \tilde{\mathbf{E}}^e}{\partial \mathbf{F}^e}\right)_{rskl}\right] + \\ & g_2\left(s\right) \mathbb{C}^e_{pqrs} F^{-1}_{jn}\left[\delta_{ik}\delta_{pl}\tilde{E}^e_{rs} F^e_{nq} + F^e_{ip} F^e_{nq}\left(\frac{\partial \tilde{\mathbf{E}}^e}{\partial \mathbf{F}^e}\right)_{rskl} + \delta_{kn}\delta_{ql}\tilde{E}^e_{rs} F^e_{ip}\right]\end{aligned} \tag{6.22}$$

The last term which needs to be calculated in Equation 6.20 is derivative of $\mathbf{F}^e$ with respect to $\mathbf{F}$. In order to obtain the consistent tangent moduli, it is essential to use the nonlinear Equation 6.12.

$$\frac{\partial \mathbf{F}^e}{\partial \mathbf{F}} = \frac{\partial \mathbf{F}^{e\,tr}}{\partial \mathbf{F}} - \sum_{\alpha=1}^{n_{slip}} \triangle\gamma^\alpha \frac{\partial \mathbf{B}^\alpha}{\partial \mathbf{F}} - \sum_{\alpha=1}^{n_{slip}} \frac{d\triangle\gamma^\alpha}{d\tau^\alpha_p} \mathbf{B}^\alpha \otimes \left(\frac{\partial \tau^\alpha_p}{\partial \mathbf{F}^e} : \frac{\partial \mathbf{F}^e}{\partial \mathbf{F}}\right) \tag{6.23}$$

in which

$$\left(\frac{\partial \mathbf{F}^{e\,tr}}{\partial \mathbf{F}}\right)_{ijkl} = \delta_{ik} F^{p\,-1}_{t-\triangle t\, lj} \tag{6.24a}$$

$$\left(\frac{\partial \mathbf{B}^{\alpha}}{\partial \mathbf{F}}\right)_{ijkl} = \delta_{ik} F^{p\,-1}_{t-\triangle t\; ln} S^{\alpha}_{0_{nj}} \tag{6.24b}$$

Equation 6.23 can be rewritten as

$$\left(\mathbb{I} + \sum_{\alpha=1}^{n_{slip}} \frac{d\triangle\gamma^{\alpha}}{d\tau_p^{\alpha}} \mathbf{B}^{\alpha} \otimes \frac{\partial \tau_p^{\alpha}}{\partial \mathbf{F}^e}\right) : \frac{\partial \mathbf{F}^e}{\partial \mathbf{F}} = \frac{\partial \mathbf{F}^{e\,tr}}{\partial \mathbf{F}} - \sum_{\alpha=1}^{n_{slip}} \triangle\gamma^{\alpha} \frac{\partial \mathbf{B}^{\alpha}}{\partial \mathbf{F}} \tag{6.25}$$

This system of equations can be simply solved by inverting the fourth-order coefficient tensor.

$$\frac{\partial \mathbf{F}^e}{\partial \mathbf{F}} = \left(\mathbb{I} + \sum_{\alpha=1}^{n_{slip}} \frac{d\triangle\gamma^{\alpha}}{d\tau_p^{\alpha}} \mathbf{B}^{\alpha} \otimes \frac{\partial \tau_p^{\alpha}}{\partial \mathbf{F}^e}\right)^{-1} : \left(\frac{\partial \mathbf{F}^{e\,tr}}{\partial \mathbf{F}} - \sum_{\alpha=1}^{n_{slip}} \triangle\gamma^{\alpha} \frac{\partial \mathbf{B}^{\alpha}}{\partial \mathbf{F}}\right) \tag{6.26}$$

Table 6.2 summarizes the procedure to compute the first spatial elasticity tensor.

6.6 Accelerating fracture simulations

Generally phase field modeling of fracture is time-consuming due to requirements on convergence of the staggered solver, time increments and mesh size. In this section, three tactics are proposed to accelerate crack phase field simulations and minimize the number of cutbacks (reductions in time increment) as much as possible.

tactic I: During the fracture simulations, the elements in the vicinity of cracks may experience severe deformation. The crystal plasticity time integration often fails in these elements for different reasons such as divergence of inner and outer loops or get-

I	calculate $\frac{\partial \tilde{\mathbf{E}}^e}{\partial \mathbf{F}^e}$ using Equation 5.34
II	use results of step I to calculate $\frac{\partial \tau_p^\alpha}{\partial \mathbf{F}^e}$ using Equation 6.16
III	calculate $\frac{\partial \mathbf{F}^{e\,tr}}{\partial \mathbf{F}}$ and $\frac{\partial \mathbf{B}^\alpha}{\partial \mathbf{F}}$ using Equation 6.24
IV	use results of step II and III to calculate $\frac{\partial \mathbf{F}^e}{\partial \mathbf{F}}$ using Equation 6.26
V	use result of step I to calculate $\frac{\partial \mathbf{P}}{\partial \mathbf{F}^e}\big\vert_{\mathbf{F}}$ using Equation 6.22
VI	calculate $\frac{\partial \mathbf{P}}{\partial \mathbf{F}}\big\vert_{\mathbf{F}^e}$ using Equation 6.21
VII	use results of step IV, V and VI to calculate $\mathbb{A}$ using Equation 6.20
VIII	calculate $\mathbb{a}$ using Equation 4.30

Table 6.2: Sequence of computational operations to calculate the first spatial elasticity tensor

ting large slip increments invalidating the $\mathbf{F}^p$ approximation in Equation 6.10. Given that fracture is a localized phenomenon, a few percentage of elements in the entire FE discretization suffer from failure of constitutive model update and require a small time increment whereas the majority of elements can handle large time increments. The classical approach is to march in time with the minimum time increment required by the elements; therefore, one has to restart the time step with a sufficiently smaller time increment such that time integration can be successfully carried out for all elements in the mesh.

This time-marching approach is obviously not efficient. Consider a case where all elements in the mesh can take a time increment of $\triangle t$ except for one element which

requires a time increment of $\triangle t/10$. Following the aforementioned approach, to know the mechanical response after $\triangle t$ seconds, one has to simulate 10 time steps where at each time step the FE nonlinear solver is performed for all the elements in the mesh. This is a computational burden and can be overcome by utilizing a simple *substepping* technique [127]. In the sub-stepping technique, the entire FE problem takes a time increment of $\triangle t$ and each element may march through this time increment in multiple steps. Knowing the deformation gradient and order parameter at time $t - \triangle t$ and t, $\mathbf{F}$ and s are linearly interpolated with time whereas the state variables are simply passed from one step to the next. In this work, an adaptive substepping scheme is implemented where the size of steps are adaptively selected depending on the success of constitutive update at the element. The algorithm used for this adaptive substepping scheme is summarized in Table 6.3.

tactic II: Depending on the frequency of evaluation of tangent stiffness matrix, different Newton-Raphson schemes could be employed to solve the nonlinear FE equations. The "full" Newton-Raphson scheme pertains to the case where the tangent stiffness matrix is evaluated at every iteration. Another class of Newton-Raphson schemes is the quasi-Newton methods where tangent stiffness matrix is evaluated either at the beginning of each time step or just the first iteration of the first time step [128]. Due to the infrequent update of the tangent stiffness matrix in quasi-Newton methods, combining quasi-Newton methods with direct linear solvers is favorable. Once the tangent stiffness matrix is factorized, direct solvers spend a negligible time to

I	initialize required variables $level = 1\ ,\quad t_{old} = t - \triangle t\ ,\quad ISV_{old} = ISV_{t-\triangle t}$
II	determine trial time increment and update trial time $\triangle t_{tr} = \frac{\triangle t}{2^{level}}\ ,\quad t_{new} = t_{old} + \triangle t_{tr}$
III	linearly interpolate $\mathbf{F}$ and s $\mathbf{F}_{new} = \mathbf{F}_{t-\triangle t} + \frac{t_{new}-(t-\triangle t)}{\triangle t}(\mathbf{F} - \mathbf{F}_{t-\triangle t})$ $s_{new} = s_{t-\triangle t} + \frac{t_{new}-(t-\triangle t)}{\triangle t}(s - s_{t-\triangle t})$
IV	perform constitutive update using $\mathbf{F}_{new}$, s_{new} and ISV_{old} and store the updated state variables in ISV_{new}
V	if constitutive update failed, then $level \leftarrow level + 1$ and go to step II
VI	update required variables $t_{old} \leftarrow t_{new}\ ,\quad ISV_{old} \leftarrow ISV_{new}$
VII	if $t = t_{new}$, the full time increment is marched and exit substepping. Otherwise, go to step II

Table 6.3: Sequence of computational operations to perform adaptive substepping for CP constitutive update

do back-substitution and solve the linear system of equations in a relatively short period of time. In order to accelerate fracture simulations and save time in solving the linear systems, one may use the quasi-Newton method from the beginning of the simulation up to the point when the softening starts. Beyond this point, due to the drastic changes in tangent stiffness matrix per iteration per time step, quasi-Newton methods often do not perform well and one has to switch the solver to the "full" Newton-Raphson scheme.

tactic III: For simulating a mechanical process over a period of time, the FE solvers start with an initial time increment and then adaptively increase it based on some criterion such as the number of Newton-Raphson iterations required for convergence. In fracture simulations beyond the point of softening when cracks start to propagate, if large time increments are taken, the FE solvers generally face some problems with respect to the convergence, resulting in cutbacks. It is often seen that at some stages of fracture, the FE solver executes multiple cutbacks consecutively to make time increment sufficiently small for convergence to happen. One would like to minimize the number of cutbacks to avoid wasting computational resources.

An effective tactic in these cases is to disable the adaptive time incrementation when the FE solver goes through a user-defined number of consecutive cutbacks $n_{cutback}^{user}$. After these cutbacks, the FE solver will eventually converge for a sufficiently small time increment, here referred to as the *stable time increment*. The FE solver is then instructed to march in time with a time increment as large as the stable

one for the next n_{guard}^{user} time steps (a user-defined variable) before the adaptive time incrementation is reactivated.

Chapter 7

Numerical results on fracture

This chapter provides some numerical examples on brittle and ductile fracture. When possible, comparisons with analytical solutions and experimental observations are made to validate the fracture modeling framework. Numerical examples include 2D and 3D simulations of fracture in isotropic and anisotropic materials. It is worthy to mention that 2D simulations are carried out under plain strain conditions. For brittle fracture simulations, conventional linear triangular/tetrahedral elements are used; however, modified F-bar-patch element is used for ductile fracture simulations to alleviate the adverse effects of volumetric locking.

Following the results of [65], the regularization length scale l_c in the numerical examples is chosen to be twice the size of elements. Moreover, the residual strength parameter κ_s is set to zero, unless mentioned otherwise.

Parameters	E	ν	l_c	g_c	β_{lu}	β_{gu}	β_{gs}
unit	GPa	$-$	mm	$\frac{J}{m^2}$	$Pa \cdot s$	$\frac{Pa \cdot s}{m^2}$	$Pa \cdot s$
Value	210	0.3	7.5×10^{-3}	2700	1	0	10^3

Table 7.1: material/numerical parameters for problem in Section 7.1 and 7.2

7.1 Single edge notched plate under tension

Consider a single edge notched square plate, as shown in Figure 7.1. The plate is subject to an applied velocity of $\dot{u}_y = 10^{-5} mm/s$. The notch has zero thickness and is created by duplicating the nodes on the notch line. The material is assumed to be nonlinear isotropic elastic. The required material/numerical parameters are given in Table 7.1. The resulting crack profile at different stages of deformation is given in 7.2. As expected, under mode I fracture, the crack grows normal to the direction loading in a fairly straight path. The corresponding load-deflection curve is shown in Figure 7.3 where a sudden drop in load is observed once fracture starts. This is a signature of brittle failure.

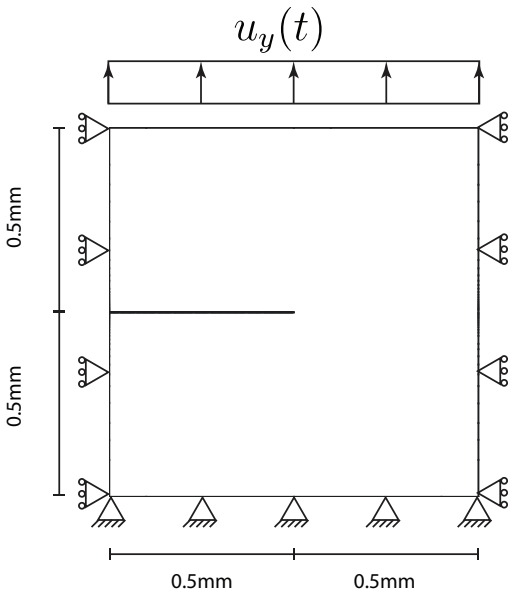

Figure 7.1: geometry and boundary conditions for the single edge notched square plate under tension

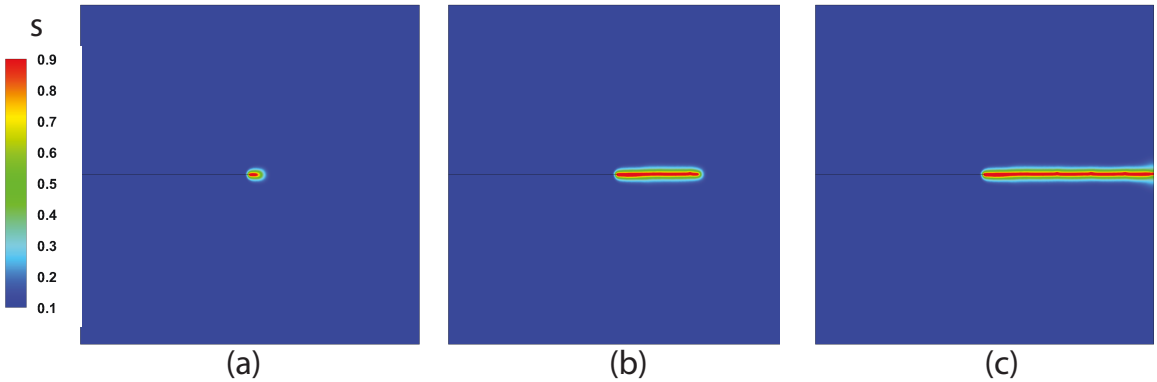

Figure 7.2: crack profile in single edge notched square plate under tension at (a) $t = 600.236s$, (b) $t = 639.8048s$ and (c) $t = 639.8049s$

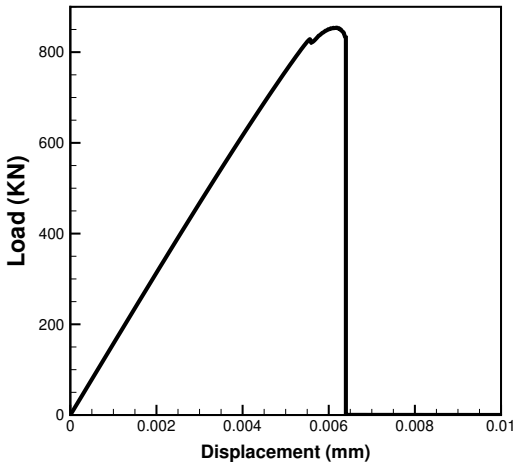

Figure 7.3: load-deflection curve for single edge notched square plate under tension

7.2 Notched square plate under pure shear

The boundary conditions for the problem in Section 7.1 are modified such that the single edge notched plate is under pure shear conditions, as shown in Figure 7.4. The plate is subject to an applied velocity of $\dot{u}_x = 10^{-5} mm/s$ and The parameters given in Table 7.1 are used for FE simulations.

The resulting crack profile at different stages of deformation is given in 7.5. The crack is observed to kink down to the tensile region due to the choice of SEED which respects the unilateral condition. This is as opposed to the crack branching shown earlier in Figure 5.2. The crack propagates with an angle of $\approx -59.4^\circ$ relative to the crack line, which is comparable with -70.5° predicted by the maximum tensile stress criterion [129]. The corresponding load-deflection curve for this problem is shown in Figure 7.6.

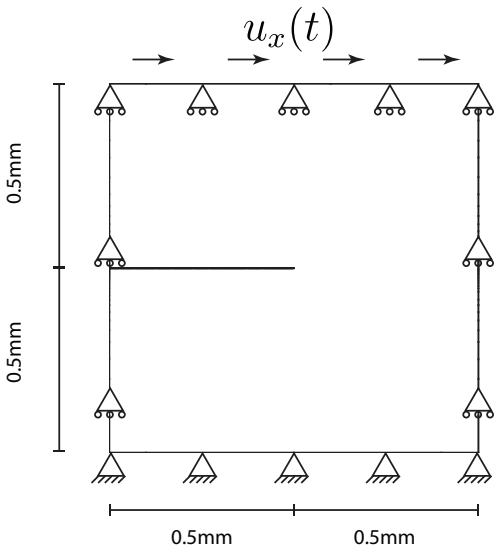

Figure 7.4: geometry and boundary conditions for the single edge notched square plate under pure shear conditions

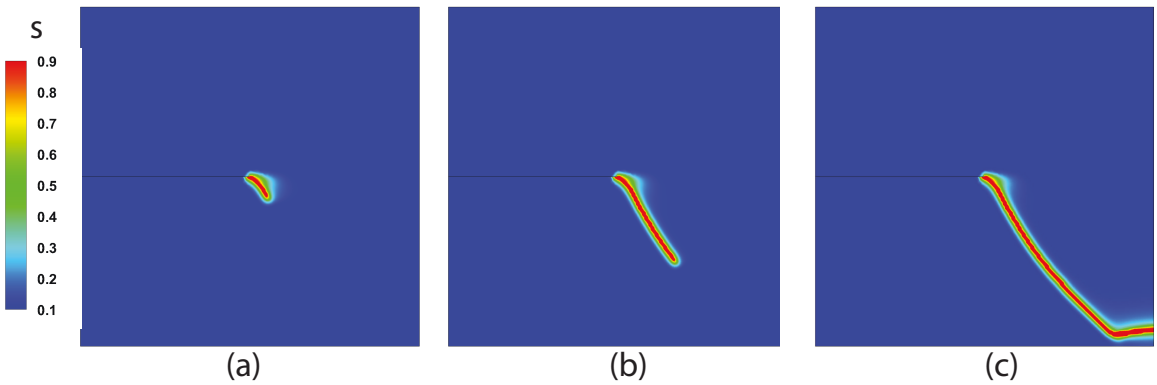

Figure 7.5: crack profile in single edge notched square plate under pure shear at (a) $t = 1058.721s$, (b) $t = 1146.840s$ and (c) $t = 1219.265s$

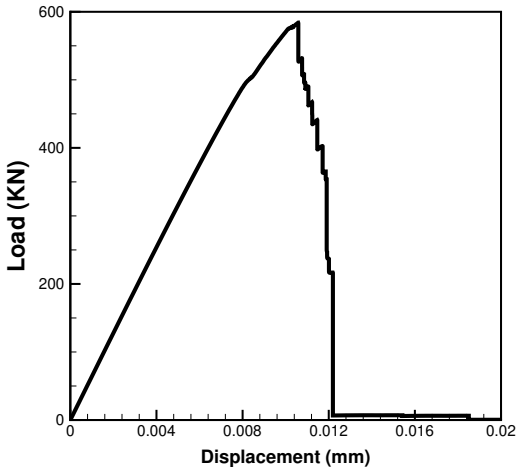

Figure 7.6: load-deflection curve for single edge notched square plate under pure shear

7.3 Effect of convergence criteria on crack profile

There are generally three measures which could be used to determine convergence of the nonlinear FE solver for the displacement field. These measures examine whether the displacement field, residual force or internal energy have converged. It is recommended [109] that two of these measures should be employed to confirm convergence of the solver. An excellent discussion on different convergence criteria is provided in the seminal work of Bathe and Cimento [109]. In this work, convergence of the solver is determined using the displacement field and residual force.

As pointed out in [109], in problems involving softening like fracture simulations, a strict tolerance should be used for the criterion involving displacement field. For the

purpose of this discussion, the $i-th$ iteration of Newton-Raphson for displacement field at time t, given earlier in Equation 4.35b, is recalled as:

$$\{u_t\}^{i+1} = \{u_t\}^i + \{d_u\} \tag{7.1}$$

Conventionally the following relative convergence criterion is used for the displacement field

$$\frac{\|\{d_u\}\|}{\|\{u_t\}^i\|} \leq \epsilon_d \tag{7.2}$$

in which ϵ_d is a small positive tolerance. This criterion examines whether the norm of correction to the displacement field $\|\{d_u\}\|$ is small enough with respect to the norm of total displacement field $\|\{u_t\}^i\|$. Alternatively, one may examine convergence of displacement field by comparing the norm of correction to the norm of displacement increment; that is,

$$\frac{\|\{d_u\}\|}{\|\{u_t\}^i - \{u_{t-\triangle t}\}\|} \leq \epsilon_d \tag{7.3}$$

This alternative convergence criterion is clearly stricter compared to the conventional one. Figure 7.7 shows the effect of convergence criteria and its tolerance on the prediction of crack profile for the problem illustrated in Figure 7.5. It is observed in Figure 7.7a that the conventional convergence criterion with $\epsilon_d = 10^{-3}$ predicts an incorrect crack path. Reducing ϵ_d, the convergence criterion becomes stricter and the correct crack kinking is obtained. The convergence criterion in Equation 7.3 with a

larger tolerance, $\epsilon_d = 10^{-2}$, can correctly predict the correct crack profile, as shown in Figure 7.7d. More details with respect to this problem will be discussed in Section 7.9.

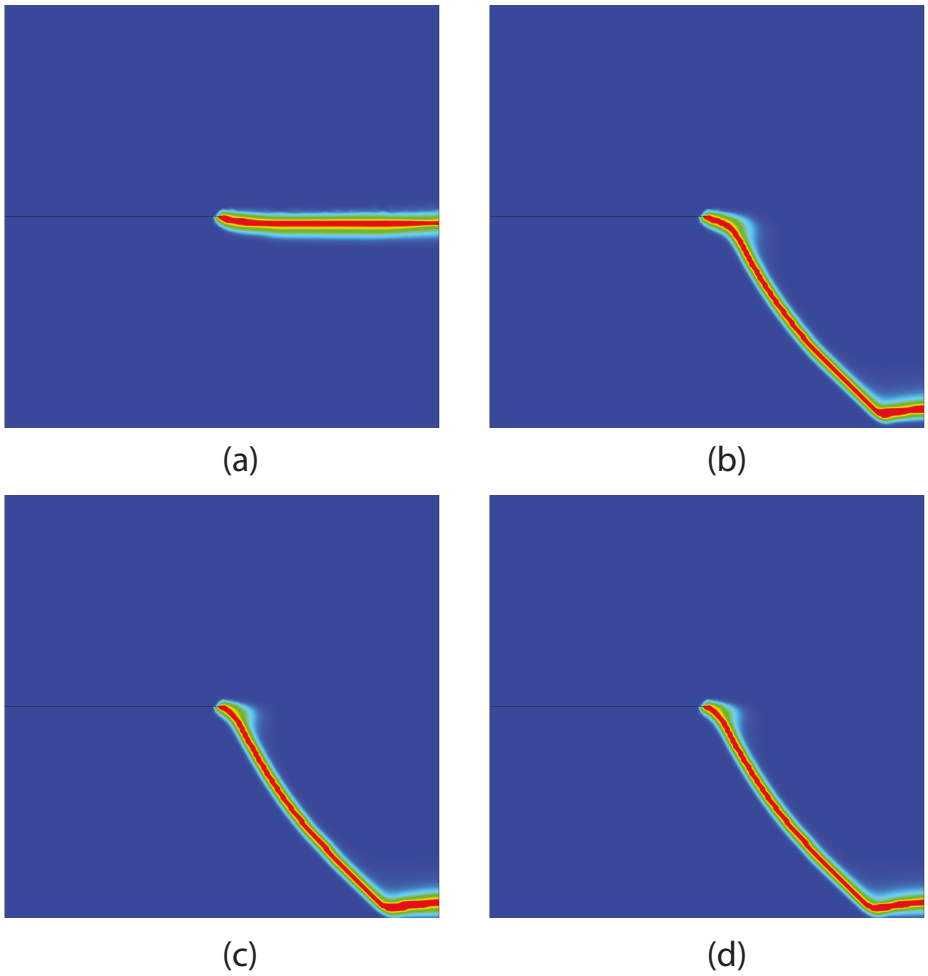

Figure 7.7: crack profile in single edge notched square plate under pure shear using Equation 7.2 with (a) $\epsilon_d = 10^{-3}$, (b) $\epsilon_d = 10^{-4}$ and (c) $\epsilon_d = 10^{-5}$. Figure (d) is obtained by using Equation 7.3 with $\epsilon_d = 10^{-2}$

.

7.4 Fracture using PF model with threshold

As mentioned in Section 5.1, the crack surface energy density in Equation 5.9 permits material degradation upon loading and therefore has no energy density threshold for damage nucleation. Equation 5.10, on the other hand, has a threshold for the damage nucleation and material degradation starts only after certain amount energy density has been stored in the material. Figure 7.8 compares the two models for the problems illustrated in Figures 7.1 and 7.4. w_c in the PF model with threshold is set to $180MPa$ and the other parameters are given in Table 7.1. It is observed that the model with threshold yields a sharper representation of fracture; that is, the material degradation is more localized to the immediate vicinity of crack path. It is also seen that the final stages of fracture under pure shear loading conditions are different in these two models. In the model with threshold, crack moves along the lower boundary whereas it propagates with a distance off the lower boundary in the model without threshold.

7.5 L-shaped plate

A series of experimental fracture tests were done on an L-shaped $10cm$ thick concrete plate by Winkler [3]. The geometry and boundary conditions for this problem

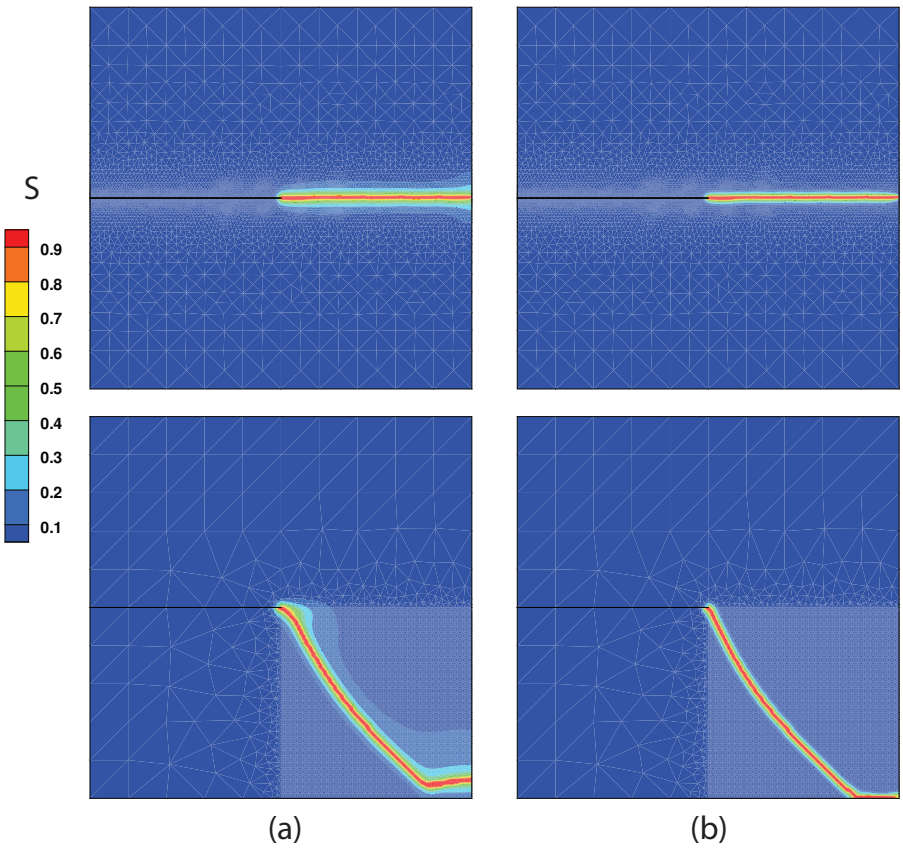

Figure 7.8: crack profile in single edge notched square plate using the fracture model (a) without and (b) with threshold

Parameters	E	ν	l_c	g_c	w_c	β_{lu}	β_{gu}	β_{gs}
unit	GPa	$-$	mm	$\frac{J}{m^2}$	MPa	$Pa \cdot s$	$\frac{Pa \cdot s}{m^2}$	$Pa \cdot s$
Value	25.84	0.18	3	89	0.015	1	0	10

Table 7.2: material/numerical parameters for L-shaped plate

are shown in Figure 7.9. The displacement is applied at a rate of $10^{-3} mm/s$. This test has been often used in the literature to validate the crack phase field models [4,5,130]. The material is assumed to be isotropic elastic. The required material/numerical parameters are given in Table 7.2.

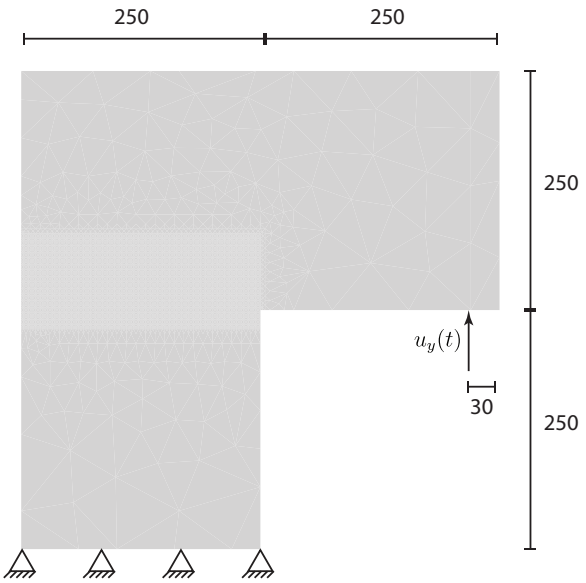

Figure 7.9: geometry and boundary conditions for the L-shaped plate (all dimensions are in mm)

Different stages of crack propagation predicted by the models with and without

threshold are given in Figure 7.10. It is observed again that the model with threshold has a sharper representation of crack. The predicted crack profile is compared with the experimental [3] and numerical [4] results in Figure 7.11. The predicted crack path is observed to fall in the range of experimental observations.

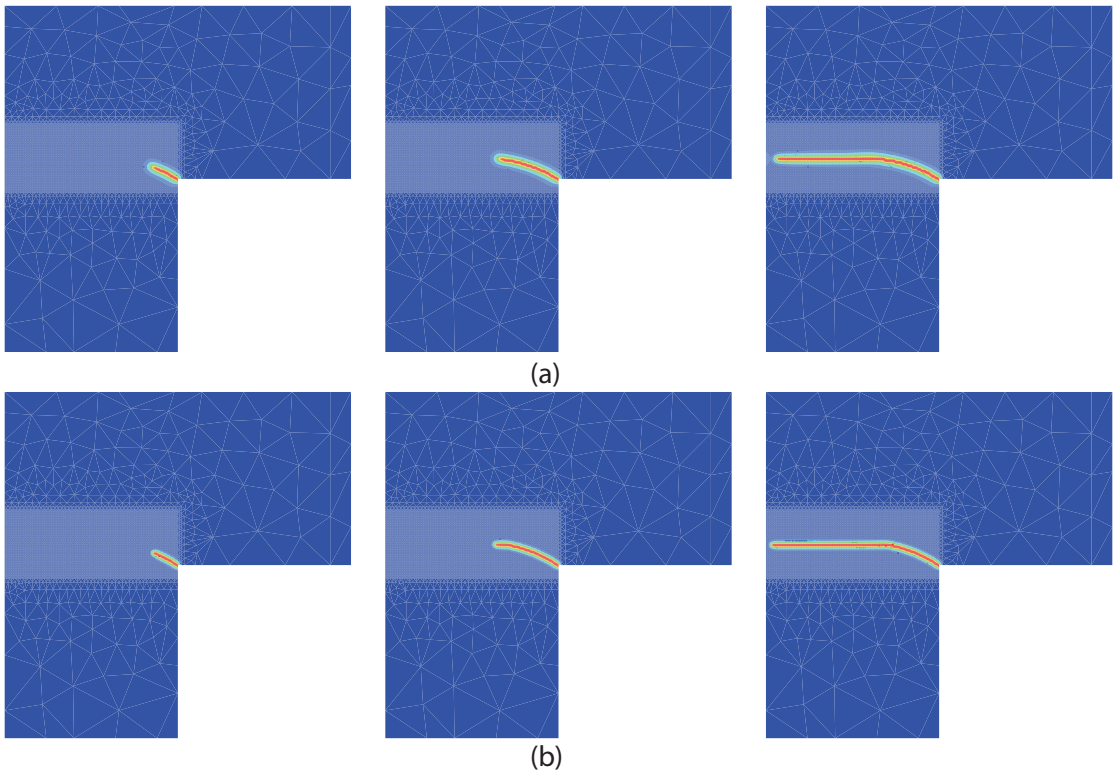

Figure 7.10: different stages of crack propagation in L-shaped plate using fracture model (a) without and (b) with threshold

The proposed model respects the unilateral condition; that is, under compressive volume change, the volumetric strains are not degraded and do contribute to the SEED and stress in the full extent while the deviatoric strains are degraded and do not contribute to the stress in full extent. Therefore, it is expected that the degraded

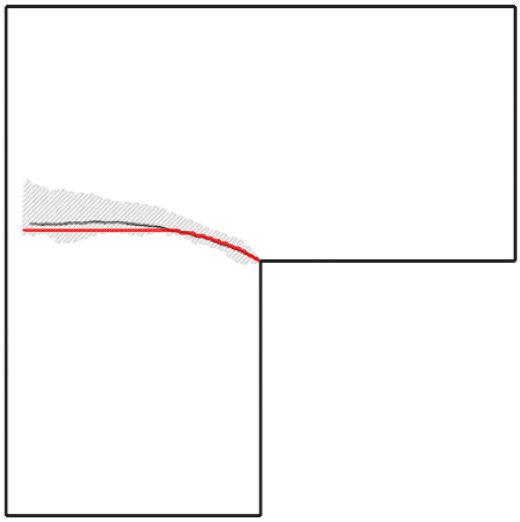

Figure 7.11: comparison of the predicted crack path (red line) with the experimental (gray area) [3] and numerical (black line) [4] results. The red line represents $0.9 \leq s \leq 1$

material regains part of its loading-bearing capacity in the compression. To observe the effect of the unilaterial conditions, the L-shaped plate is subject to a displacement history given in Figure 7.12a which involves load reversals. The fracture model with threshold is used to simulate this problem. The load-deflection curve is given in Figure 7.12b. It is observed that upon the first load reversal at $t = 400s$, the structure unloaded with a degraded slope until $t = 800s$ when the applied displacement changes sign. From $t = 800s$ to $t = 1200s$, the applied displacement is negative and the crack closure takes place. It is observed that during this period due to the unilateral conditions the structure shows a mechanical response, almost similar to that of an intact material. There is $\approx 5\%$ difference between the slopes since the deviatoric strains are degraded in the compression.

7.6 Notched plate with hole

An interesting experiment was done by Ambati et al. [5] on a notched concrete plate with a hole. A displacement-controlled loading with a rate of $0.1mm/min$ was applied on the top pin while holding the lower pin fixed. The geometry and boundary conditions for this problem are illustrated in Figure 7.13. The fracture model with threshold is used to predict the crack profile. The material/numerical parameters are tabulated in Table 7.3. Different stages of crack propagation are shown in Figure 7.14 and the predicted crack path is compared with the experimental observations

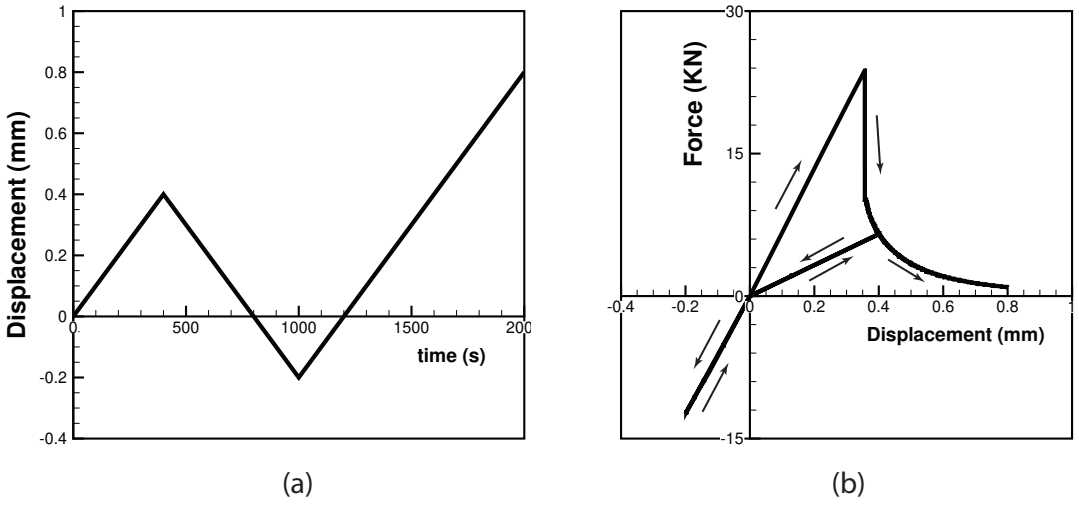

Figure 7.12: effect of unilateral conditions on the L-shaped plate. (a) displacement history involving load reversals, (b) load-deflection curve

in Figure 7.15. It is seen that the predicted crack path compares very well with the range observed in the experiments.

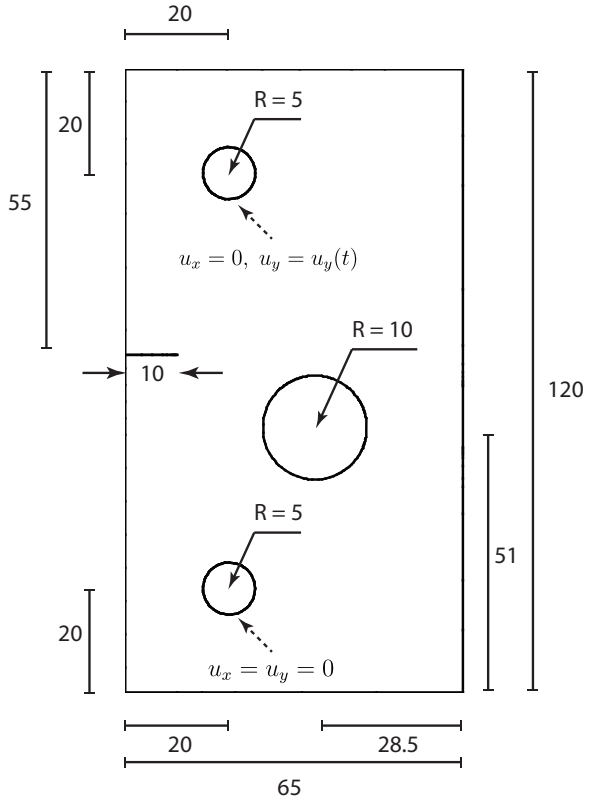

Figure 7.13: geometry and boundary conditions for the notched plate with hole (all dimensions are in mm)

We have a closer look at the effects of different viscous stabilization techniques discussed in Section 3.5 on the mechanical response. Here the effects of each technique is investigated separately; that is, one of the viscosity parameters β_{lu}, β_{gu} or β_{gs} is changed while the others are set to zero. In order to study the effect of β_{gs}, the residual strength parameter κ_s is set to 10^{-4} to avoid ill-conditioning of the tangent stiffness matrix for the displacement problem. When investigating the effects of β_{lu} or

Parameters	E	ν	l_c	w_c	β_{lu}	β_{gu}	β_{gs}
unit	GPa	$-$	mm	MPa	$Pa \cdot s$	$\frac{Pa \cdot s}{m^2}$	$Pa \cdot s$
Value	5.89	0.22	0.5	2.28	0	10^2	0

Table 7.3: material/numerical parameters for notched plate with hole

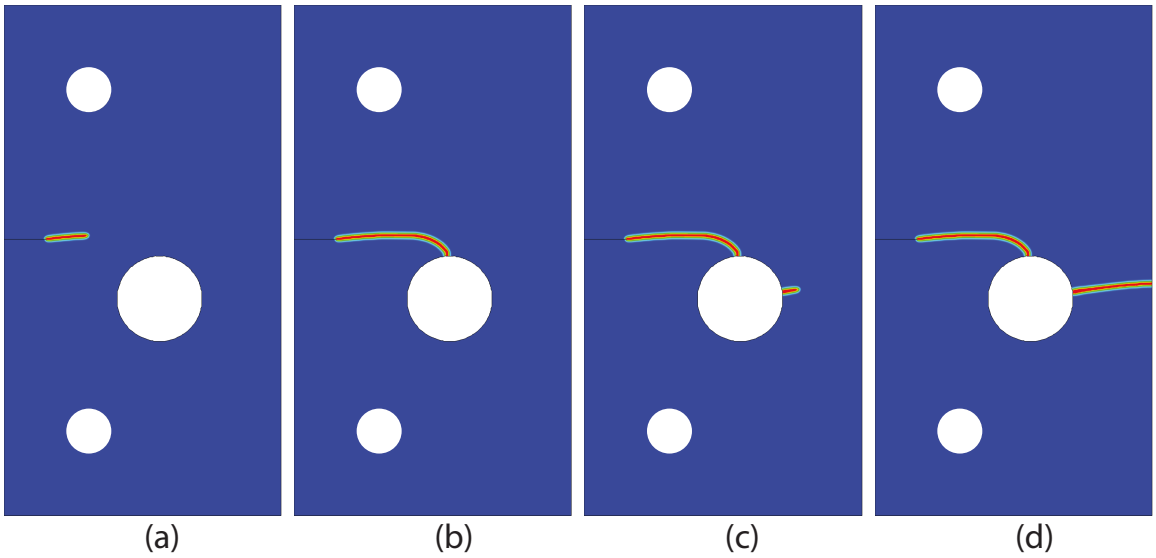

Figure 7.14: different stages of crack propagation in notched plate with hole. (a) $t = 429.65s$,(b) $t = 565.03s$, (c) $t = 1554.30145s$ and (d) $t = 1554.30146s$

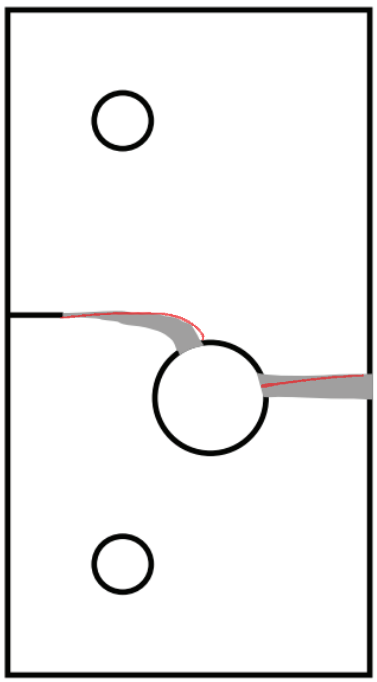

Figure 7.15: comparison of the predicted crack path (red line) with the experimental observations (gray area) [5]. The red line represents $0.9 \leq s \leq 1$

β_{gu}, κ_s is set to zero since the viscous stabilization of the displacement field prevents ill-conditioning of the tangent stiffness matrix. The load-deflection plots for different viscous stabilization techniques are given in Figure 7.16. It is observed that for the small amount of artificial viscosity, all three methods predict nearly identical load-deflection curves. However for higher values of artificial viscosity, they behave differently. It is seen that the critical points A and B shown in Figure 7.16a (these points correspond to nucleation of crack from the notch and hole) are more sensitive to β_{gs} and less sensitive to β_{gu}. With respect to the viscous stabilization of displacement field, the load levels are observed to be more sensitive to β_{lu}, than β_{gu}.

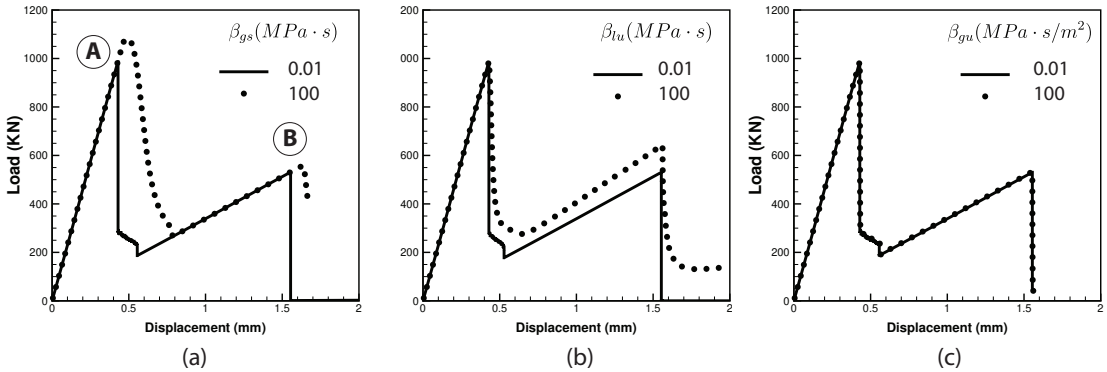

Figure 7.16: load-deflection plots for notched plate with hole for different viscous stabilization techniques. (a) global viscous stabilization of crack phase field, (b) local viscous stabilization of displacement field and (c) global viscous stabilization of displacement field

7.7 Asymmetric double notched plate

This numerical example concludes the 2d examples of fracture. Consider a plate with asymmetric notches, as shown in Figure 7.17. The bottom edge is fixed whereas the top edge is constrained to move horizontally. A displacement controlled loading with a rate of $5 \times 10^{-3} mm/s$ is applied on the top edge. This example has been studied in Ambati et al. [131]. The material/numerical parameters for this problem are given in Table 7.4.

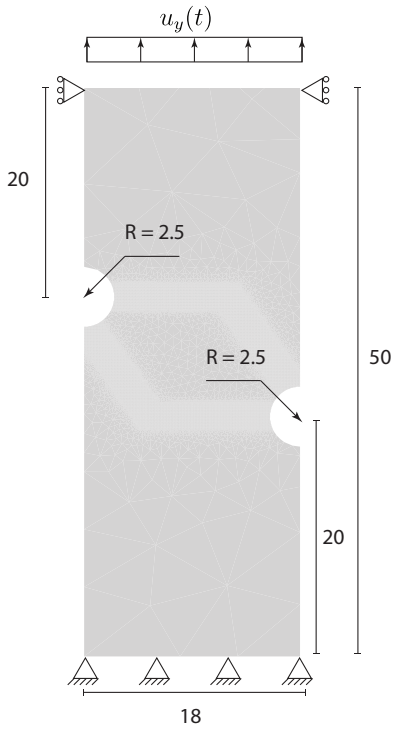

Figure 7.17: geometry and boundary conditions for the asymmetric double notched plate (all dimensions are in mm)

The crack profile for this problem is shown in Figure 7.18. It is observed that

Parameters	E	ν	l_c	g_c	β_{lu}	β_{gu}	β_{gs}
unit	GPa	$-$	mm	$\frac{J}{m^2}$	$Pa \cdot s$	$\frac{Pa \cdot s}{m^2}$	$Pa \cdot s$
Value	72.62	0.33	0.1	9310	10^4	10^{46}	1

Table 7.4: material/numerical parameters for asymmetric double notched plate

the cracks initiate at the notches and then follow curvilinear path towards the other notch. The hydrostatic stress is also seen to move with the crack tips. The final damaged state of this problem is plotted in the deformed configuration in Figure 7.19.

7.8 3D single edge notched plate

This example studies fracture in a 3D single edge notched plate, shown in Figure 7.20. Two different types of displacement-controlled loading, namely tensile and shear loadings, are simulated. For the tensile loading, the bottom and top yz planes are fixed in x and z directions. The bottom xz plane is fixed in y and z directions and a displacement in y direction with a rate of $10^{-5} mm/sec$ is applied on the top xz plane. For the shear loading, the bottom and top yz planes are fixed in y and z directions. The bottom xz plane is fixed in all directions. The top xz plane is fixed in y direction. A displacement in x direction with a rate of $10^{-5} mm/sec$ is applied on the top xz plane.

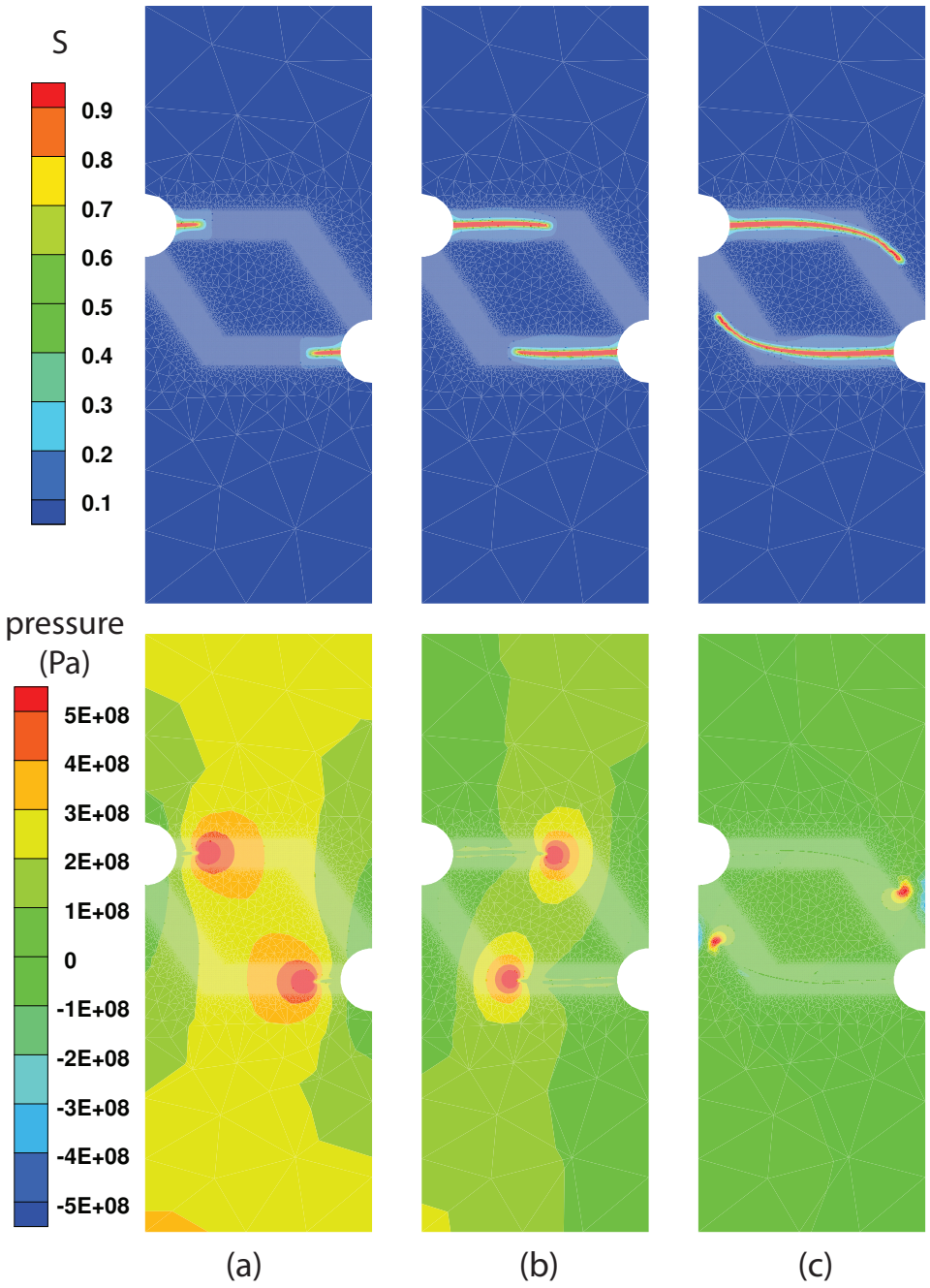

Figure 7.18: different stages of crack propagation in asymmetric double notch plate. (a) $t = 62.4257s$,(b) $t = 62.4258s$ and (c) $t = 130.58s$

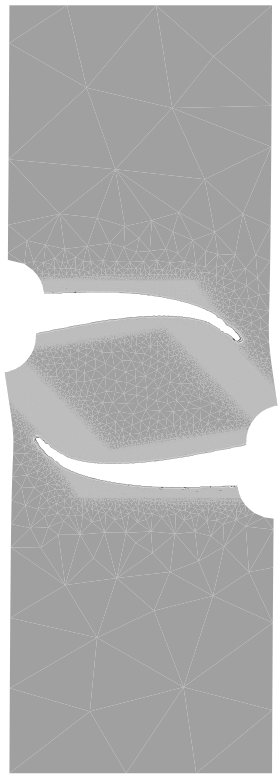

Figure 7.19: fracture in asymmetric double notch plate in deformed configuration. Here the deformation is magnified 4 times and the elements with $0.9 \leq s \leq 1$ are removed to visualize cracks

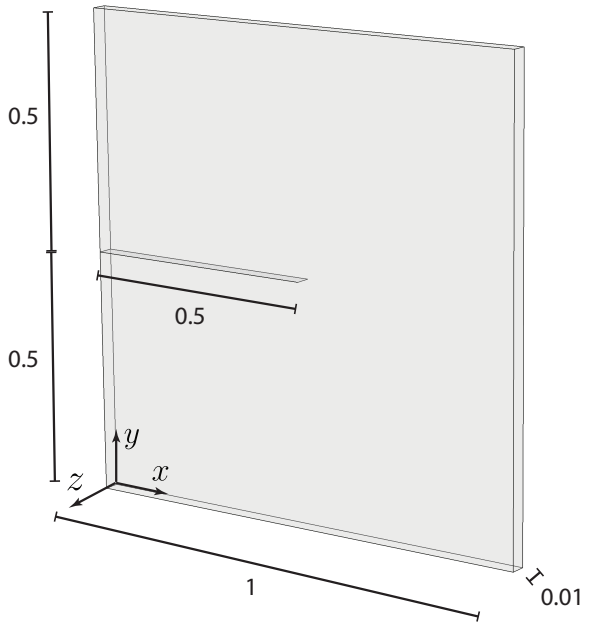

Figure 7.20: geometry for the 3D single edge notched plate (all dimensions are in mm)

The material is assumed to be nonlinear isotropic elastic. The material/numerical parameters for this problem are given in Table 7.5. The crack profiles for tensile and shear loadings are shown in Figure 7.21. The elements with $0.9 \leq s \leq 1$ are visualized in this figure to see crack surfaces.

Parameters	E	ν	l_c	g_c	β_{lu}	β_{gu}	β_{gs}
unit	GPa	$-$	mm	$\frac{J}{m^2}$	$Pa \cdot s$	$\frac{Pa \cdot s}{m^2}$	$Pa \cdot s$
Value	210	0.3	0.01	2700	10^4	0	10^3

Table 7.5: material/numerical parameters for the 3D single edge notched plate

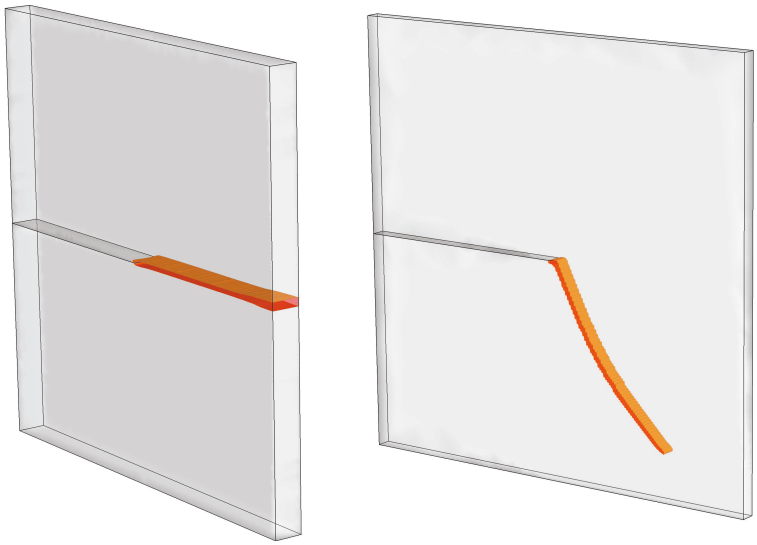

Figure 7.21: crack profile in 3D single edge notched plate under (a) tensile and (b) shear loading. Only elements with $0.9 \leq s \leq 1$ are visualized

7.9 Single-pass vs. multi-pass staggered solver

The importance of proper convergence criteria in predicting the correct crack path was discussed in Section 7.3. This section highlights the significance of staggered solver and its effect on crack path predictions. The 3D single notched plate under shear which involves crack kinking is chosen for this study. For all simulations in this section, the strict convergence criteria given in Equation 7.3 is used with $\epsilon_d = 10^{-2}$. The time incrementation is instructed to adaptively change time increment depending on the number of Newton-Raphson iterations with some safeguard considerations

pointed out in Section 6.6. The maximum allowable time increment is set to $200s$. This problem is solved using single-pass and multi-pass staggered solvers. The crack predicted by these two solvers are shown in Figure 7.22. Although the simulations are 3D, the crack profile on the xy plane is shown for better visualization of fracture pattern. It is observed that the multi-pass staggered solver can successfully predict the crack path whereas the single-pass one fails to capture the correct crack profile. It is also observed that the crack width is larger in the case of single-pass solver. This example shows sensitivity of the single-pass solver to time increments due to its *semi-explicit* algorithm. Although single-pass solver is faster; however, one should pay extra caution in choosing the time increments.

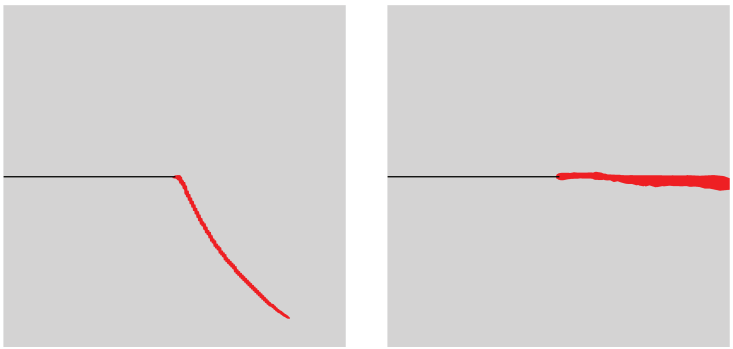

Figure 7.22: crack profile in 3D single edge notched plate under shear using (a) multi-pass and (b) single-pass staggered solver

Generally fracture simulations require small time incrementation since crack evolution is accompanied by the significant re-balancing of loads and forces in the structure. The fracture process is comprised of unstable and stable stages. In the unstable

regime, the fracture is manifested by brutal crack network development and small time increments should therefore be taken. In the stable regime, on the other hand, the cracks evolve slowly and large time increments could be taken. From this perspective, it might be a better idea to limit the increment in nodal crack phase field, rather than limiting the time increment. In other words, once the staggered solver converged, maximum increment in any crack phase field DOF is examined. If it exceeds the user-defined maximum allowable increment, the solver is instructed to restart the time step with a smaller time increment.

Post-analysis of the results in Figure 7.22 indicates that the maximum increment in nodal crack phase field (not norm) is 0.2 and 0.22 for the multi-pass and single-pass solvers, respectively. The average increment in nodal crack phase field for the multi-pass solver is 5.9×10^{-3} whereas it is 1×10^{-3} for the single-pass one. Figure 7.23 shows the crack profile predicted by the single-pass solver if the maximum allowable increment in nodal crack phase field is set to 0.16 and 0.1. It is observed that the single-pass solver can predict the correct crack path for small enough allowable increments in crack phase field, here 0.1.

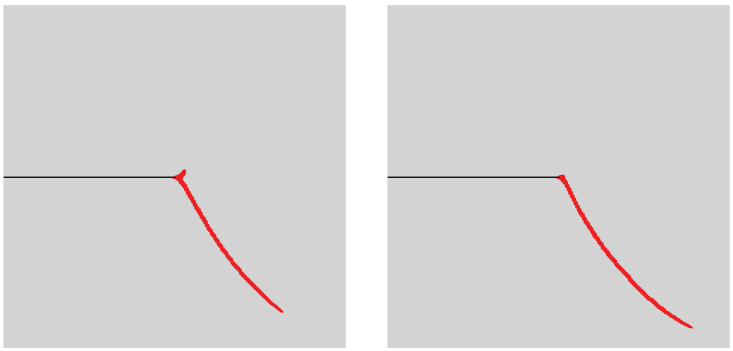

Figure 7.23: crack profile in 3D single edge notched plate under shear predicted by the single-pass staggered solver subject to maximum allowable increment in nodal crack phase field being (a) 0.16 and (b) 0.1

7.10 Brittle fracture in polycrystalline Al7075-T651 alloy

This example studies the fracture process in a single edge notched rolled polycrystalline Al7075-T651 plate, shown in Figure 7.24. This alloy consists of crystalline Al grains and brittle intermetallic Fe-rich particles. The particles are shown in dark blue. A detailed characterization of this alloy can be found in [132–134]. The origin is fixed in all directions. The z axis is fixed in x direction. The bottom xz plane is fixed in y direction while the top xz plane is subject to displacement controlled loading with a rate of $2.4 \times 10^{-3} \mu m/s$ along y direction.

The elastic constants for the crystalline Al phase with cubic symmetry were calibrated using experiments in [135]. The brittle intermetallic particles show isotropic

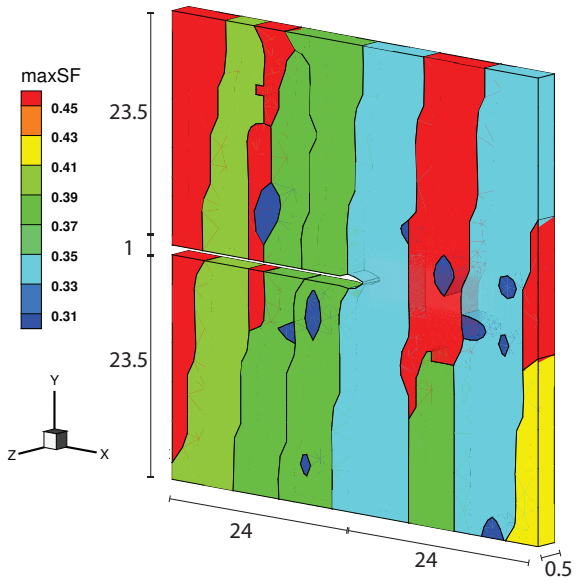

Figure 7.24: plot of maximum Schmid factor for loading along y in single edge notched rolled polycrystalline Al7075-T651 plate. Dark blue regions correspond to Fe-rich particles (all dimensions are in micrometer)

					Al grains				particles	
Parameters	β_{lu}	β_{gu}	β_{gs}	l_c	C_{11}	C_{12}	C_{44}	g_c	E	ν
unit	$MPa \cdot s$	$\frac{MPa \cdot s}{m^2}$	$Pa \cdot s$	μm	GPa	GPa	GPa	$\frac{J}{m^2}$	GPa	$-$
	10^{-2}	1	10^2	0.24	107.3	60.9	28.3	110	160.9	0.3

Table 7.6: material/numerical parameters for the single edge notched rolled polycrystalline Al7075-T651 plate

elastic response. The mechanical properties of particles were measured in [132] using an atomic probe microscope equipped with a nanoindenter. The required material/numerical parameters are given in Table 7.6.

A nonlinear crystal elasticity is used to represent the constitutive behavior of the Al grains whereas a nonlinear isotropic elastic model is used for the brittle particles. The load-deflection curve for different values of g_c in particles is given in Figure 7.25. It is observed that the changes in fracture energy of particles does not have an appreciable effect on the load-deflection curve. This is mainly due to the fact that particles occupy a small volume fraction of the sample and most of the fracture path goes through the crystalline Al phase.

Although the load-deflection curve is almost insensitive to g_c of particles, the local fracture path is significantly affected by this parameter. Figure 7.26 shows different stages of fracture for $g_c = 10J/m^2$. Attention is specifically drawn to particles A and B, marked in Figure 7.26a. Crack is observed to nucleate at the notch root and

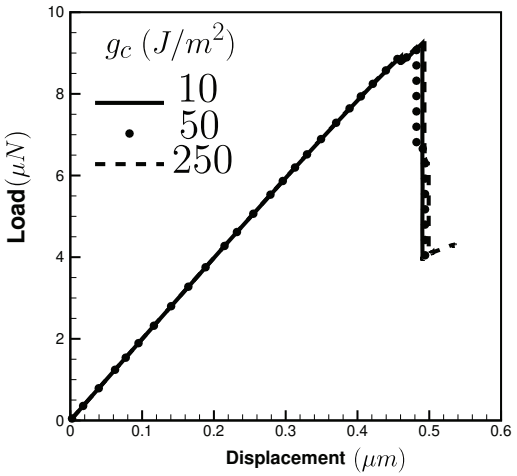

Figure 7.25: load-deflection plots for single edge notched rolled polycrystalline Al7075-T651 plate for different value of g_c for particles

propagates forward with the normal to crack surface being nearly aligned with the loading direction. Upon further loading, it is observed that particle A fractures as well and the cracks in the Al matrix and particle A coalesce (Figure 7.26c) while another crack develops in particle B (Figure 7.26d). It is later seen that the coalesced crack will propagate further while the one in particle B gets arrested at the interface with Al matrix.

For larger values of g_c in particles, the crack profile is quite different. Figure 7.27 shows the crack path for $g_c = 50J/m^2$ and $g_c = 250J/m^2$. It is observed that as the value of g_c for particles increases, particle B does not fracture. Moreover, a crack does not nucleate in particle A, rather the crack developed in the Al matrix cuts through it for $g_c = 50J/m^2$. For higher value of g_c, it is observed that the crack does

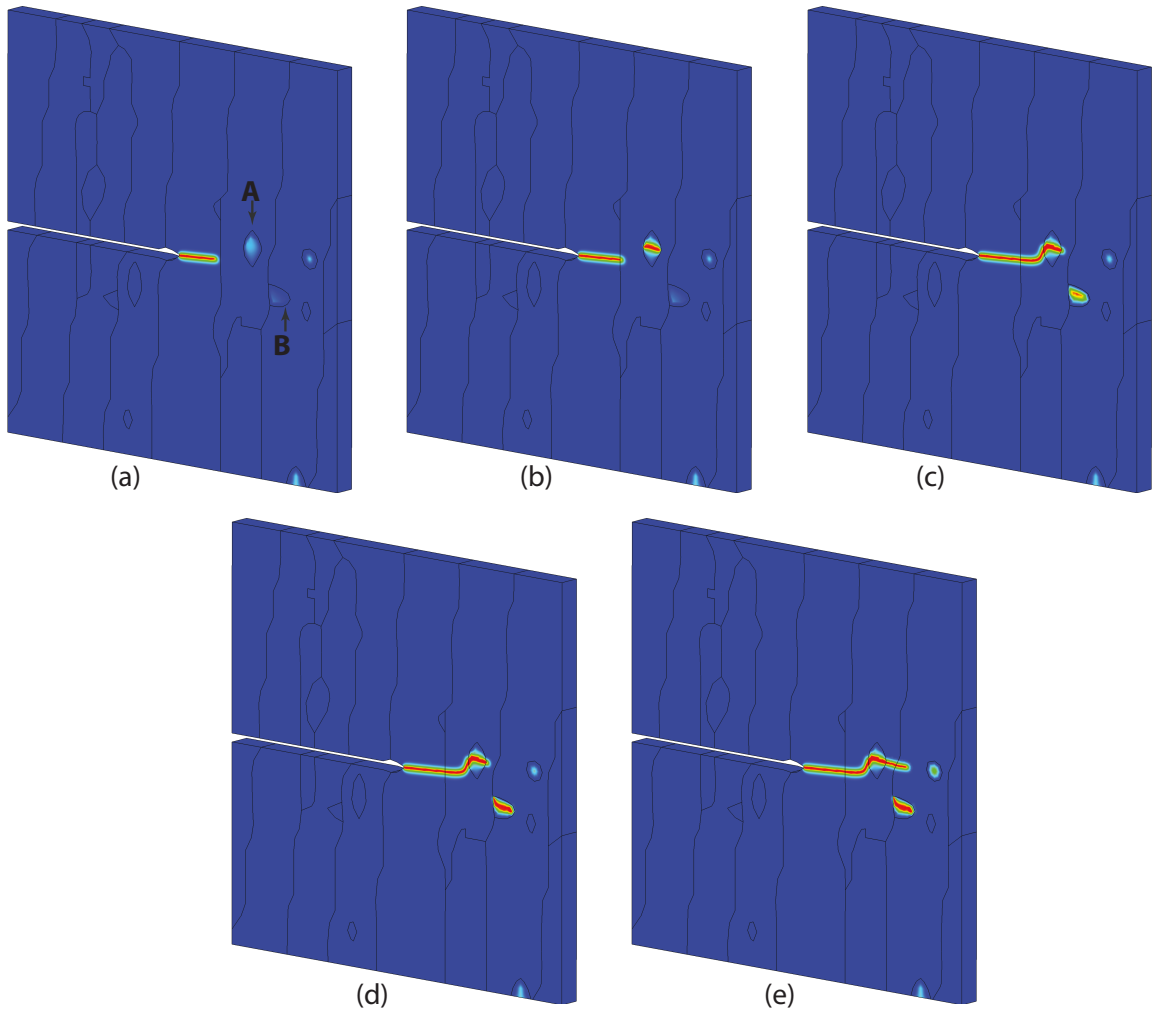

Figure 7.26: different stages of fracture in single edge notched rolled polycrystalline Al7075-T651 plate with $g_c = 10J/m^2$ in particles

not penetrate into particle A and rather the particle deflects the crack and makes it change its path to go around the particle. The same behavior can be also seen if the elastic moduli of the particles are magnified. This is qualitatively consistent with the analytical results in [136], indicating that crack deflection is favored over penetration as the stiffness of the potentially penetrable material increases. Parametric studies, like the one in Clayton and Knap [137], can be conducted to determine the critical ratio of stiffnesses and fracture energies which will favor crack deflection over penetration in media with heterogeneities.

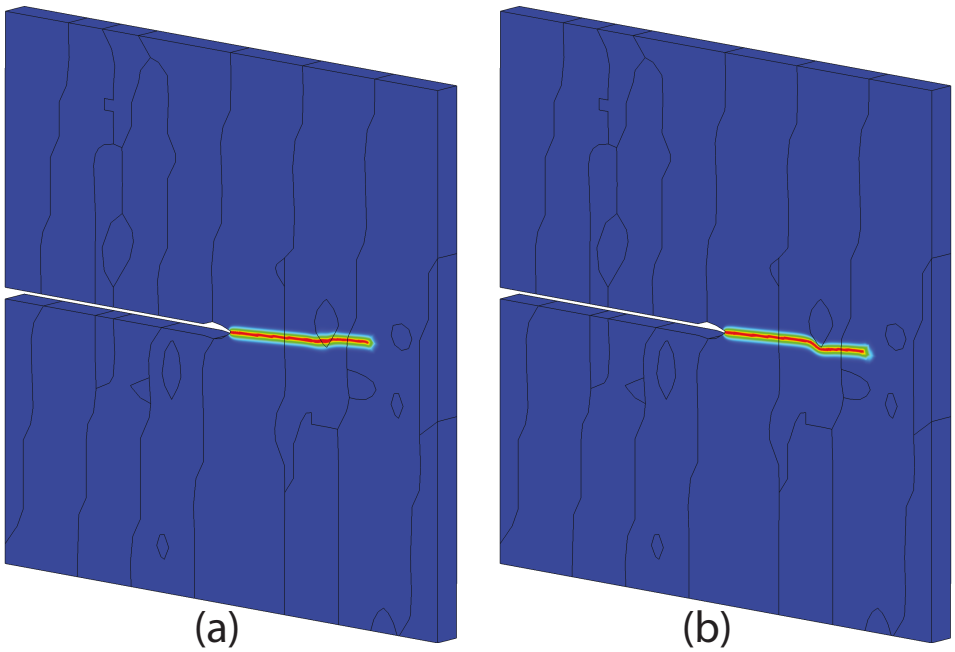

Figure 7.27: crack profile in single edge notched rolled polycrystalline Al7075-T651 plate for (a) $g_c = 50J/m^2$ and (b) $g_c = 250J/m^2$

7.11 Edge notched single crystal Al plate

Consider a single edge notched plate made of single crystal Al, as shown in Figure 7.28a. The origin is fixed in all directions. y axis is fixed in x direction. The bottom xy plane is fixed in z direction while a displacement-controlled loading with a rate of $10^{-4}\mu m/s$ is applied on the top xy plane in z direction. Crystal plasticity is used to represent the constitutive behavior of the material. CP material constants are calibrated and validated using the experimental results in [135]. The material/numerical parameters are give in Table 7.7. The elasticity constants are already given in Table 7.6. The Bunge Euler angles are set to $(0°, 0°, 0°)$ and the fracture energy is $g_c = 0.45J/m^2$. The crack profile is shown in Figure 7.28b.

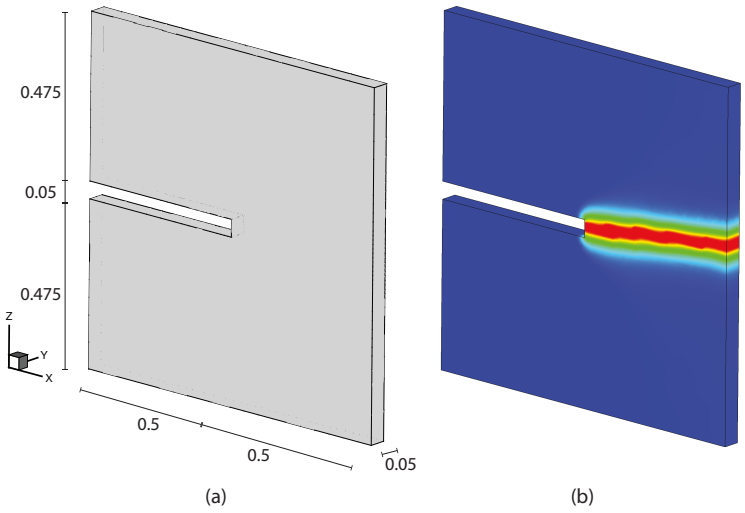

Figure 7.28: (a) geometry of edge notched single crystal Al plate (all dimensions are in micrometer), (b) crack profile

Parameters	κ_s	l_c	β_{lu}	β_{gu}	β_{gs}	β_p	ν_{att}	c_2^α	B_0	b^α
unit	–	μm	$Pa \cdot s$	$\frac{MPa \cdot s}{m^2}$	$Pa \cdot s$	–	s^{-1}	–	$N \cdot s$	m
Value	0.01	0.025	0	100	10^4	0.1	10^{10}	10^4	5×10^{-4}	2.86×10^{-10}
Parameters	Q^α	p	q	$a_{\dot{\gamma}}$	$s^\alpha_{0,(a)th}$	$h^\alpha_{ref,(a)th}$	r^α	$s^\alpha_{sat,(a)th}$	c^α_χ	d^α_χ
unit	J	–	–	m^{-1}	MPa	MPa	–	GPa	MPa	–
Value	4.8×10^{-19}	0.78	1.15	1.78×10^3	76.1	55	1.115	5	0	0

Table 7.7: material/numerical parameters for the edge notched single crystal Al plate

The critical point (deformation state corresponding to load drop) takes place once the crack nucleates from the notch root. This point is determined by the amount of energy density stored in the material which is in turn dependent on the material properties. Here the effects of two properties, i.e. reference hardening parameter $h^\alpha_{ref,(a)th}$ and fracture energy density g_c, on the critical point are studied. It is observed from Figure 7.29a that by increasing the fracture energy density the critical point is pushed to higher displacement levels since the material needs to store more energy density to be able to drive fracture from the notch root. On the other hand, the critical point is pushed to lower displacements as the reference hardening parameter increases. This is due to the increase in rate of strain hardening (manifested by the increase in hardening slope in Figure 7.29b) and therefore storage of more energy density.

Besides material parameters, the crystallographic properties such as crystal orientation can also affect the critical point. Three sets of Euler angles are used to study the effect of crystal orientation on the critical point. These sets,$O_1 = (0°, 54.73°, 45°)$,

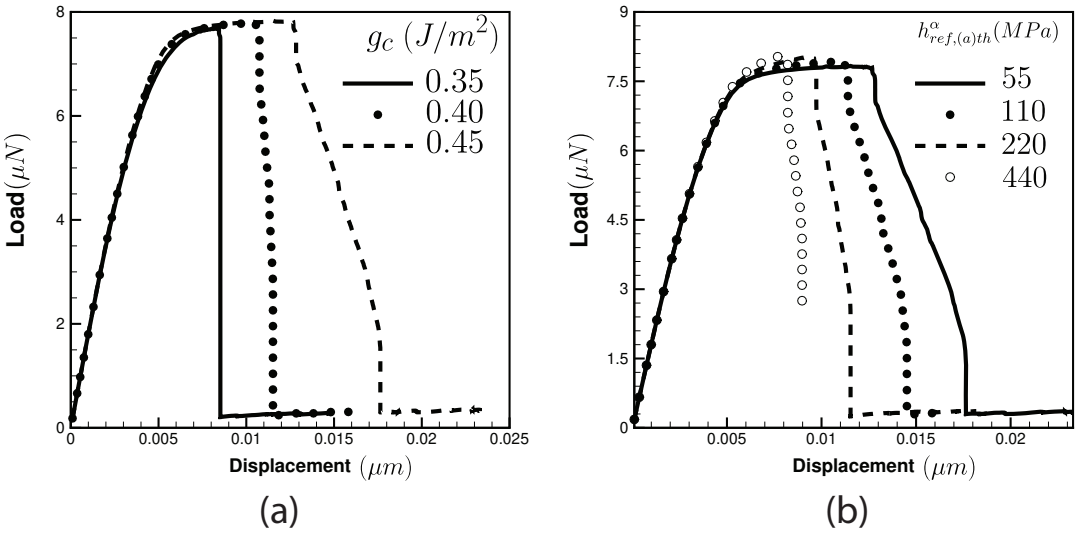

Figure 7.29: sensitivity of critical point to (a) fracture energy density and (b) reference hardening parameter

$O_2 = (0°, 45°, 0°)$ and $O_3 = (0°, 0°, 0°)$, are special in the sense that they make the loading axis z align with the crystal $< 111 >$, $< 011 >$ and $< 001 >$ directions, respectively. Among these three sets, O_1 and O_2 produce an elastically stiffer material response. O_1 corresponds to an orientation with low Schmid factors on the slip systems; therefore, it has the highest yield stress among these three orientations [138]. Due to the high stiffness and yield stress corresponding to O_1, it is observed in Figure 7.30 that its critical point occurs at a lower displacement level compared to those of O_2 and O_3.

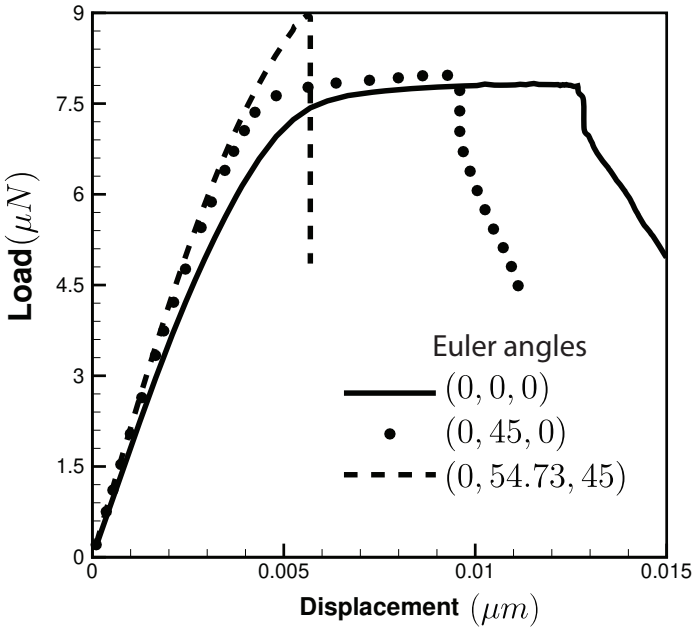

Figure 7.30: sensitivity of critical point to crystalline orientation (Euler angles are in degrees)

7.12 Ductile fracture in polycrystalline Al7075-T651 alloy

This example studies the process of fracture in a polycrystalline Al7075-T651 plate, shown in Figure 7.31. In contract with the example given in Section 7.10, here the constitutive behavior of the Al matrix is described by crystal plasticity laws. Bozek et al. [132] observed that many of the brittle particles are pre-cracked in the as-received sample. In order to represent this observation in the microstructure, a crack is seeded in the center of particle A, shown in Figure 7.31. The crack is introduced as a Dirichlet condition in the phase field problem. The boundary and loading conditions for this example are identical to the ones described in Section 7.10.

The material constants used in this example are similar to the ones given in Table 7.7, except for $\kappa_s = 0.001$, $l_c = 0.1\mu m$, $\beta_{lu} = 0.01MPa \cdot s$, $\beta_{gu} = 0MPa \cdot s/m^2$, $\beta_{lu} = 10^{-4}MPa \cdot s$. With respect to the fracture energy parameter for Al matrix and brittle particles, two cases are considered: (case I) $g_c = 1.25J/m^2$ for particles and $g_c = 2.25J/m^2$ Al matrix and (case II) $g_c = 1.5J/m^2$ for particles and $g_c = 2.5J/m^2$ for Al matrix. The loading-direction volume-averaged stress-strain plot is shown in Figure 7.32. As expected, the critical point for case II happens at a later stage of deformation due to its higher fracture energy densities.

Besides the critical point, the stress-strain plots for the two cases are different after the critical point. This is due to the fact that the fracture process which takes

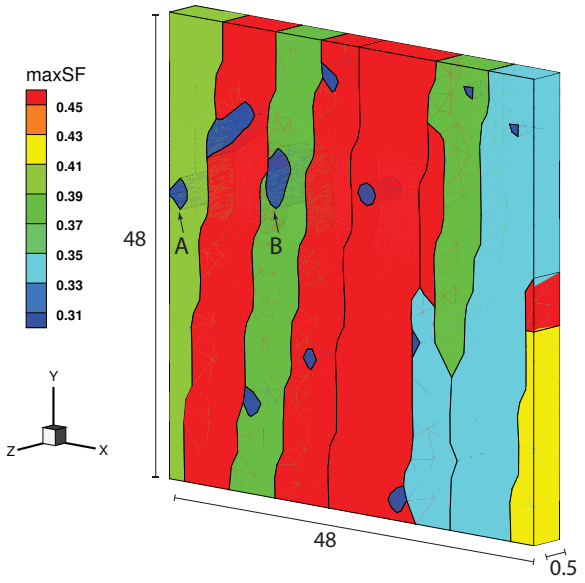

Figure 7.31: plot of maximum Schmid factor for loading along y in single edge notched rolled polycrystalline Al7075-T651 plate. Dark blue regions correspond to Fe-rich particles (all dimensions are in micrometer)

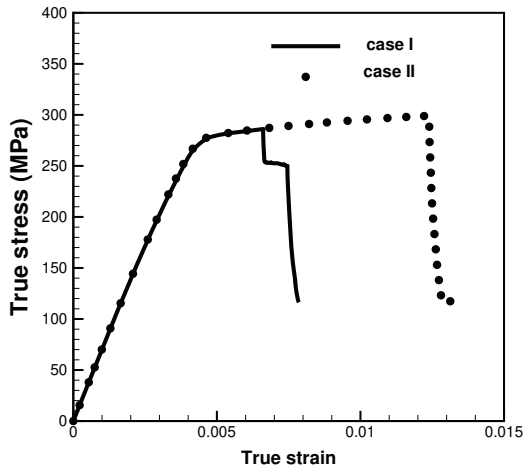

Figure 7.32: loading-direction volume-averaged stress-strain plot for fracture in polycrystalline Al7075-T651 alloy

place at the microstructure scale is different. Figure 7.33 shows the stages of crack development for the two cases. As it is seen in Figure 7.33a, for case I, the crack nucleates from the pre-existing one in particle A and then extends into the neighboring Al crystal. Meanwhile, another crack forms near the interface of particle B and Al matrix which will coalesce later with the crack originating from particle A. On the other hand, for case II in Figure 7.33b, the fracture does not start from the pre-existing one. Indeed the crack starts from the interface of particle B and the Al matrix and then extends outward. Later another crack nucleates from the pre-existing one which will coalesce with the first one. Although the final crack profile for the two cases look similar, due to these differences in the sequence of events, the stress-strain plots look different.

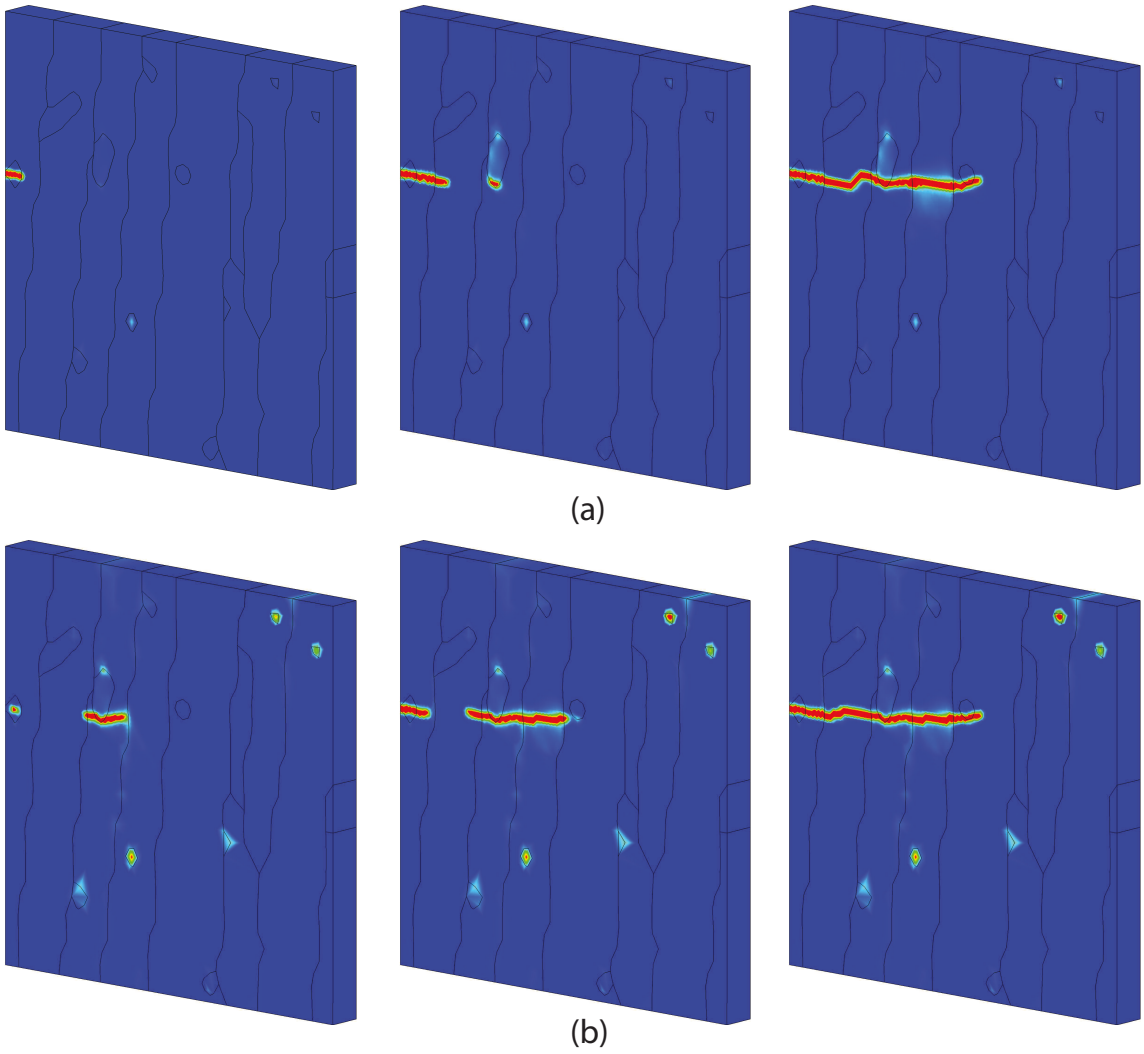

Figure 7.33: different stages of crack development in polycrystalline Al7075-T651 alloy for (a) case I and (b) case II

Chapter 8

Unified flow rule for high strain rate deformation of Ti alloys

In this chapter, we will discuss the development a unified flow rule in the context of dislocation density-based crystal plasticity for modeling deformation of *hcp* Ti alloys under a wide range of strain rates. Similar to the dislocation velocity law in Equation 2.11, a composite dislocation velocity law is developed here from a dislocation mechanism point of view. Unlike the phenomenological framework explained in Section 2.3, the CP constitutive model presented here keeps track of dislocation densities as internal state variables.

It is worthy to mention that the simulations reported in this chapter focus on the deformation aspect of the microstructure under different loading conditions and material degradation, i.e. fracture, is ignored. Except for a few equations which will

be pointed out, many of the derivation given in the previous chapters can also be employed here by setting the order parameter to zero ($s = 0$). The results presented in this chapter have been published in [110, 139].

8.1 Motivation for development of unified models

Titanium alloys are widely used in various industrial applications like compressor blades of jet engines or armor of ground combat vehicles [140], due to their superior properties such as high strength to weight ratio, high fracture toughness, as well as good corrosion resistance. The extensive commercial use of these alloys that have a predominantly hexagonal close-packed (*hcp*) crystalline structure, has motivated researchers to study their mechanical responses over a wide range of strain-rates and temperatures. For example, high strain-rate behavior, such as in ballistic impact problems, have been investigated by [121, 141–145], while low to moderate strain-rate studies in cyclic and dwell fatigue conditions have been conducted in [146, 147]. When modeling for different applied rates, it is important to realize that even if the loading is at a certain strain-rate (high or low), different points in the material microstructure may undergo a wide range of strain-rates depending on the material point location and deformation history. For instance, in microstructures of *hcp* Ti alloys with significant slip system resistance anisotropy, large strain gradients can develop between

soft and *hard* grains, even with moderate applied strain-rates [95, 148, 149]. This can lead to locally large strain-rates in their polycrystalline microstructures. Similarly, a polycrystalline microstructure that is macroscopically subjected to high strain-rates can locally undergo location-dependent lower rates of deformation, especially near stationary boundaries. Conventionally used rate-dependent plasticity models are incapable of smoothly transitioning across strain-rates. Thus, it is desirable to develop unified constitutive relations from consideration of physics-based mechanisms that can transcend a wide range of strain-rates without having to change constitutive parameters or models.

Plastic deformation in polycrystalline microstructures of Ti alloys are strongly dependent on the grain morphology and crystallographic lattice orientations. This, in part, is attributed to the large differences in the critical resolved shear stress (CRSS) for different *hcp* slip systems shown in Figure 8.1. For example, the CRSS of the first and second order $< c + a >$ pyramidal systems have been shown to be ∼2-4 times higher than those of the basal and prism $< a >$ systems [148,150]. This difference can cause localized stress concentrations leading to crack nucleation in creep loading and dwell fatigue [95, 148, 151, 152]. Crystal plasticity finite element method (CPFEM) is conventionally used to model deformation and failure in these alloys using a variety of constitutive laws [8, 95, 143, 148, 149, 153–155]. The predictive capability of CPFE models is strongly dependent on the accuracy of constitutive models along with their

flow rules.

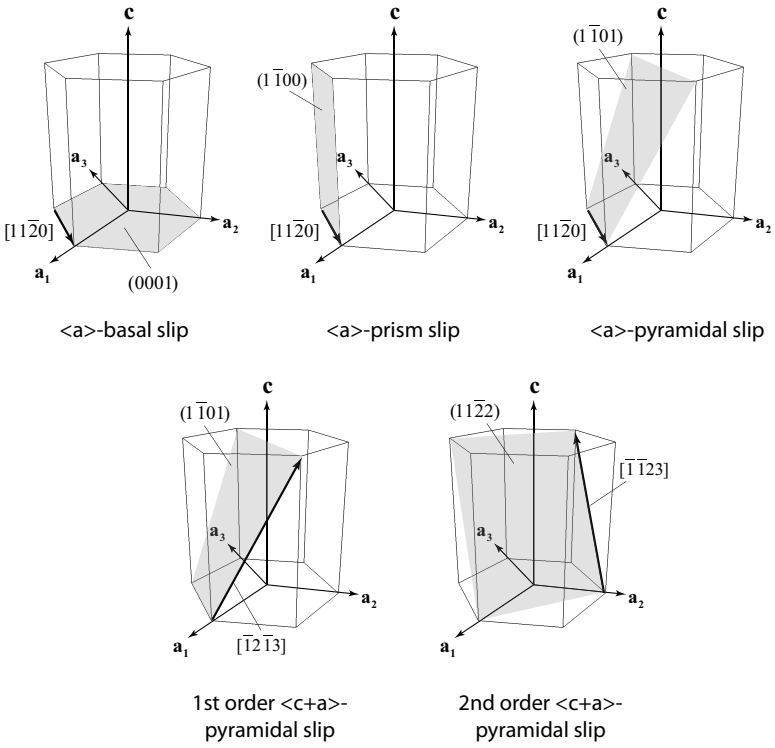

Figure 8.1: Schematic view of non-orthogonal base vectors $\{\mathbf{a_1}, \mathbf{a_2}, \mathbf{a_3}, \mathbf{c}\}$ and slip system families in *hcp* metals and alloys.

Various forms of the flow rule have been proposed in the literature. Among the most commonly used flow rules are (i) the phenomenological power law model [6], (ii) the Arrhenius-type activation energy-based model [88] and (iii) the linear model [88]. The power law model expresses the plastic slip-rate on a slip system α with a power law dependence on the resolved shear stress and the slip system deformation resistances [6, 96, 152] as:

$$\dot{\gamma}^{\alpha} = \dot{\gamma}_0^{\alpha} \left| \frac{\tau_p^{\alpha} - s_{ath}^{\alpha}}{s_{th}^{\alpha}} \right|^{\frac{1}{m}} sign(\tau_p^{\alpha} - s_{ath}^{\alpha}) \tag{8.1}$$

where m is the strain-rate sensitivity exponent. This flow rule, that implicitly accounts for temperature, is appropriate for modeling low to moderate strain-rates in the range $< 10^4 s^{-1}$. The Arrhenius-type activation energy-based mobility law in Equation 2.9 explicitly accounts for the temperature in the thermally-activated processes governing dislocation glide, and is also applicable to deformations at low to moderate strain-rates. Its explicit dependence on the temperature makes it effective for simulating temperature-sensitive phenomena. Finally, at very high strain-rates exceeding $10^4 s^{-1}$, the dislocation motion is dominated by viscous drag-dominated processes. Correspondingly, the flow rule in this range is expressed as a linear function of the effective resolved shear stress as shown earlier in Eqaution 2.10

Here it is intended to develop a unified flow rule that can transcend the range of strain-rates corresponding to the progression from thermally-activated to drag-dominated stages of dislocation motion. Figure 8.2 demonstrates the deformation mechanisms for Ti alloys, in which screw dislocations glide by a double-kink mechanism in multiple stages. The thermally-activated stage corresponds to the nucleation of the kink pair whereas the drag-dominated stage corresponds to the broadening of the kink pair and moving the dislocation line to the next Peierls valley. The flow rule to be developed will account for the time lapsed in each stage of dislocation glide and the distance dislocation traveled during the motion over Peierls hills in the glide

plane.

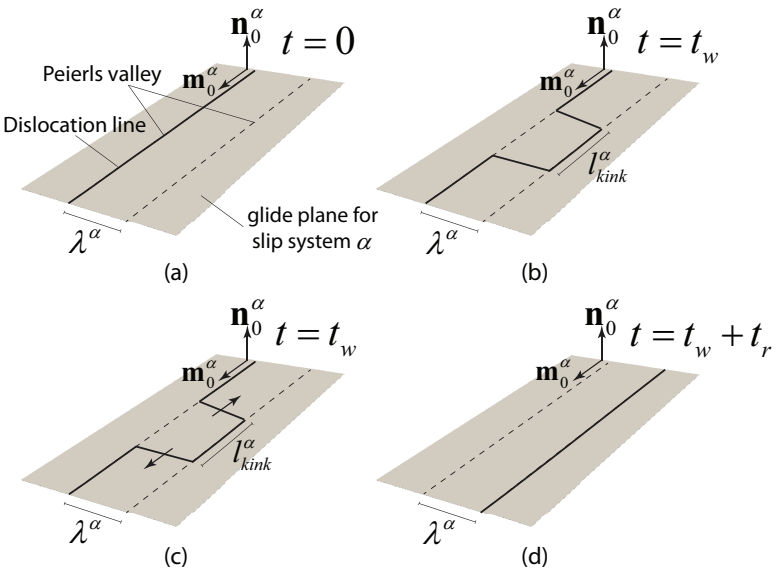

Figure 8.2: Illustration of a screw dislocation motion over Peierls hills in the glide plane via a double-kink mechanism: (a) dislocation lying in a Peierls valley, (b) nucleation of kink-pair due to thermal activation, (c) kink-pairs moving apart under drag forces, and (d) dislocation moving to the next Peierls valley.

8.2 Crystal plasticity model

The crystal plasticity model developed in this study is for single-phase Ti alloys such as α-Ti-6AL and α-Ti-7AL with a *hcp* crystal structure. Figure 8.1 shows the crystal structure with atoms stacked in an axial ratio of ~ 1.587 for titanium [148,156]. Plastic deformation in these alloys occurs predominantly by dislocation slip, where dislocations are distributed non-homogeneously in planar arrays due to short range

ordering of Ti and Al atoms on the *hcp* lattice [157]. Dislocation slip in *hcp* crystals occurs on 5 different families of slip systems as shown in Figure 8.1. This corresponds to a total of 30 possible slip systems. Differential slip on these systems result in strong anisotropic behavior of Ti alloys, both in elasticity and plasticity. The $\langle a \rangle$ - basal and prism slip families have the lowest critical resolved shear stress (CRSS), making them the most active of slip families. The $\langle c + a \rangle$ - pyramidal slip families have the largest CRSS, $\sim 2 - 4$ times that of the basal or prism slip systems [150]. The proposed constitutive model is developed for finite deformation under general non-isothermal conditions. While deformation twinning has been observed in pure Ti at temperatures below $500°C$ [142, 158], the alloying of Ti with Al inhibits this process. Ti alloyed with %6 Al is found not to twin even at temperatures as low as $100K$ [159, 160]. Hence, twinning is not considered in the constitutive model.

As pointed out in Section 5.3, the majority of plastic work is dissipated and converted into heat. Under high strain rate conditions, the generated heat does not have enough time to get conducted out the system and therefore the temperature increases locally. This process in known as *adiabatic heating*. In order to address these temperature effects, one needs to introduce a thermal deformation gradient $\mathbf{F}^{\theta}$ in the multiplicative decomposition of deformation gradient in Equation 2.4. As illustrated in Figure 8.3, the total deformation gradient $\mathbf{F}$ is multiplicatively decomposed into elastic, thermal and plastic components [86, 89], expressed as:

$$\mathbf{F} = \mathbf{F}^e \, \mathbf{F}^\theta \, \mathbf{F}^p \tag{8.2}$$

Here $\mathbf{F}^\theta$ represents the deformation of the crystal lattice due to temperature changes that evolves as [161]:

$$\dot{\mathbf{F}}^\theta = \dot{T} \, \boldsymbol{\alpha} \, \mathbf{F}^\theta \tag{8.3}$$

where $\dot{T}$ is the rate of temperature change and $\boldsymbol{\alpha}$ is an anisotropic thermal expansion coefficient tensor. The latter can reduce to a diagonal matrix if expressed in the material crystallographic coordinate system. *Ab initio* calculations in [162, 163] and experimental observations in [164] have corroborated the existence of anisotropic thermal expansion coefficient tensor for α Ti alloys over a wide range of temperatures.

It can be easily shown that the constitutive model in the thermally-expanded configuration read as:

$$\mathbf{S}_\theta = \det\left(\mathbf{F}^e\right) \mathbf{F}^{e-1} \boldsymbol{\sigma} \mathbf{F}^{e-T} = \mathbb{C}^e : \mathbf{E}^e \tag{8.4}$$

Moreover, the resolved shear stress in the thermally-expanded configuration is obtained as:

$$\tau_\theta^\alpha = \det\left(\mathbf{F}^\theta\right) \left(\mathbf{C}^e \mathbf{S}_\theta\right) : \left(\mathbf{F}^\theta \mathbf{m}_0^\alpha \otimes \mathbf{n}_0^\alpha \mathbf{F}^{\theta\,-1}\right) \tag{8.5}$$

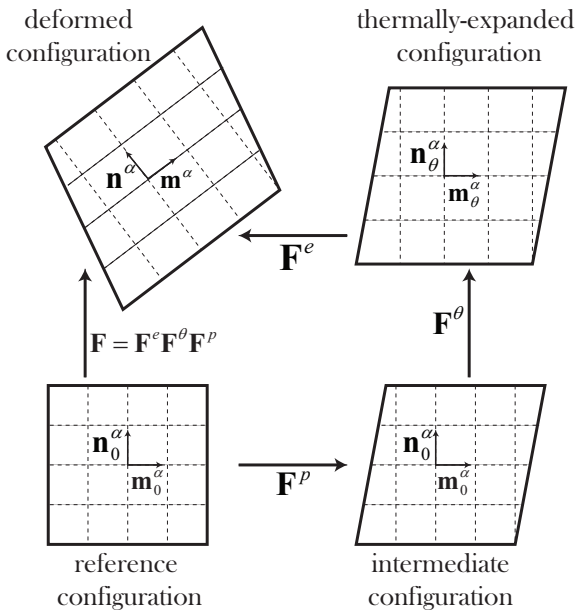

Figure 8.3: Multiplicative decomposition of the total deformation gradient $\mathbf{F}$ into elastic $\mathbf{F}^e$, thermal $\mathbf{F}^\theta$ and plastic $\mathbf{F}^p$ components.

8.2.1 Unified flow rule

The flow rule in a crystal plasticity constitutive model expresses slip-rates as a function of the local stress state and relevant internal state variables. Dislocation motion on glide planes is generally controlled by both thermal activation and drag mechanisms. The relative strength of these mechanisms changes with the level of stresses and strain-rate. Thermally-activated processes are the dominant mechanism up to strain rates of $10^4 s^{-1}$ while drag processes control the dislocation glide at strain rates above $10^4 s^{-1}$. The physics-based unified flow rule derived here, represents a combination of thermally-activated and drag dominated mechanisms, while reducing to the activation energy-based and linear flow rules as limiting cases.

Given that a dislocation density-based crystal plasticity model is developed in this work, the Orowan equation can be used for express the flow rule.

$$\dot{\gamma}^{\alpha} = \rho^{\alpha} b^{\alpha} v^{\alpha} \text{sign}\left(\tau_{\theta}^{\alpha}\right) \tag{8.6}$$

Experimental observations in [160, 165] have concluded that predominantly screw dislocations are responsible for plastic deformation in Ti alloys. These screw dislocations move over the Peierls hills in the glide plane by the double-kink mechanism that involves thermally-activated nucleation of kink pairs. Assuming nucleation of one kink pair per dislocation line, the dislocation motion by this mechanism takes place in two stages as shown in Figure 8.2. In the first stage, the dislocation lies in a Peierls valley and waits for a period *waiting time* t_w^{α} until a successful local thermal activation takes place and a pair of kinks with a separation distance of l_{kink}^{α} nucleates and moves to the next Peierls valley [166]. In the subsequent drag-dominated stage, the kinks move apart and bring the whole dislocation line to the next Peierls valley [88]. The time spent in this stage is *running time* t_r^{α}. The average dislocation velocity can then be formulated in terms of the waiting and running times as [25]:

$$v^{\alpha} = \frac{\lambda^{\alpha}}{t_w^{\alpha} + t_r^{\alpha}} \tag{8.7}$$

where λ^{α} is the spacing between two consecutive Peierls valleys that may be approximated as b^{α}. Since t_w^{α} corresponds to the thermally-activated nucleation of a kink pair, it is defined by a temperature-dependent Arrhenius-type relationship as [167]:

$$t_w^\alpha = \left[2\,\frac{\nu_{\mathrm{D}} b^\alpha}{l_{kink}^\alpha}\,\frac{l^\alpha}{l_{kink}^\alpha} \exp\left(-\frac{Q^\alpha}{K_{\mathrm{B}}T}\right) \sinh\left(\frac{|\tau_\theta^\alpha| - s_{ath}^\alpha}{s_{th}^\alpha}\right)\right]^{-1} \tag{8.8}$$

in which l^α is the average length of a straight dislocation line that is inversely proportional to the square root of the forest dislocation population ρ_{F}^α. This is expressed as $l^\alpha = c_l^\alpha/\sqrt{\rho_{\mathrm{F}}^\alpha}$, where c_l^α is a material constant [154]. ν_{D} is the Debye frequency, which is known to be $9.13 \times 10^{13} s^{-1}$ for titanium. Experimental observations in [168, 169] suggest that the effective activation energy is generally temperature-dependent. Correspondingly a temperature dependent form:

$$Q^\alpha(T) = Q_{ref}^\alpha + c_Q^\alpha \left(T/T_{ref} - 1\right)^{p_Q^\alpha} \tag{8.9}$$

is adopted in this paper, where c_Q^α and p_Q^α are material constants and Q_{ref}^α and T_{ref} are respectively the reference effective activation energy and temperature. The term $\frac{\nu_{\mathrm{D}} b^\alpha}{l_{kink}^\alpha}$ corresponds to the attempt frequency for nucleation of a kink pair and the term $\frac{l^\alpha}{l_{kink}^\alpha}$ is the number of competing sites for kink nucleation on the dislocation line. The equations describing the athermal and thermal resistances will be detailed in section 8.2.3.

The running time t_r^α corresponds to the stage, where retarding drag forces due to the phonon-dislocation interactions govern dislocation motion, effectively broadening the kink band. It is written in terms of viscous drag velocity v_d^α as [24, 25]:

$$t_r^\alpha = \frac{\lambda^\alpha}{v_d^\alpha} \tag{8.10}$$

Depending on the temperature, various types of phonon-dislocation interactions, e.g. flutter, scattering, or radiation mechanisms, are possible [24, 88]. These interactions yield a temperature-dependent drag coefficient B_0, given by the relation [88]:

$$B_0 = \frac{c_d K_{\mathrm{B}} T}{v_s b^{\alpha 2}} \tag{8.11}$$

where v_s is the shear wave speed and c_d is the drag constant. Assuming that the change in rate-sensitivity of the flow stress occurs around $10^5 s^{-1}$, as observed in experiments on titanium alloys [170], the drag coefficient is derived to be $c_d = 45$. Given the ratio of the effective dislocation line mass density to the drag coefficient B_0 that represents a decaying time scale is very small, the equation of motion for a unit length of dislocation line is solved to yield the viscous drag velocity as [171]:

$$v_d^\alpha = \frac{\left(|\tau_\theta^\alpha| - s_{ath}^\alpha\right) b^\alpha}{B_0} \tag{8.12}$$

In [28], the drag coefficient has been modified to ensure that the dislocation drag velocity does not exceed the shear wave speed, by incorporating relativistic effects as:

$$B = \frac{B_0}{1 - \left(\frac{v_d^\alpha}{v_s}\right)^2} \tag{8.13}$$

This modification implies that as the dislocation drag velocity v_d^α approaches the shear wave speed, the drag coefficient B grows to be large. Consequently very large resolved shear stresses are needed for dislocation glide. Replacing B_0 in Equation 8.12 with B and solving for v_d^α, the modified dislocation drag velocity is obtained as [28]:

$$v_d^\alpha = v_s \left[\sqrt{1 + \left(\frac{B_0 v_s}{2\left(|\tau_\theta^\alpha| - s_{ath}^\alpha\right) b^\alpha} \right)^2} - \frac{B_0 v_s}{2\left(|\tau_\theta^\alpha| - s_{ath}^\alpha\right) b^\alpha} \right] \tag{8.14}$$

Substituting Equations 8.10 and 8.8 into Equation 8.7, the expression for the unified average dislocation velocity, incorporating both thermally-activated and drag-dominated processes, is written as:

$$v^\alpha = \frac{v_d^\alpha}{\frac{v_d^\alpha}{\lambda^\alpha}\left[2\,\frac{\nu_D b^\alpha}{l_{kink}^\alpha}\,\frac{l^\alpha}{l_{kink}^\alpha}\exp\left(-\frac{Q^\alpha}{K_B T}\right)\sinh\left(\frac{|\tau_\theta^\alpha| - s_{ath}^\alpha}{s_{th}^\alpha}\right)\right]^{-1} + 1} \tag{8.15}$$

***Remark* 10** *For low strain-rate deformations corresponding to lower stress levels, $t_r^\alpha << t_w^\alpha$, i.e. $t_r^\alpha \approx 0$. In this case, the average dislocation velocity in Equation 8.7 reduces to:*

$$v^\alpha = \frac{\lambda^\alpha}{t_w^\alpha} = 2\lambda^\alpha \frac{\nu_D b^\alpha}{l_{kink}^\alpha}\,\frac{l^\alpha}{l_{kink}^\alpha}\exp\left(-\frac{Q^\alpha}{K_B T}\right)\sinh\left(\frac{|\tau_\theta^\alpha| - s_{ath}^\alpha}{s_{th}^\alpha}\right) \tag{8.16}$$

As is expected, this dislocation velocity expression is used in the Arrhenius type thermal activation-based flow rule.

***Remark* 11** *At high strain-rates corresponding to high stress levels, $t_w^\alpha << t_r^\alpha$, i.e. $t_w^\alpha \approx 0$. Correspondingly for these drag-dominated processes the average dislocation velocity in Equation 8.7 reduces to:*

$$v^\alpha = \frac{\lambda^\alpha}{t_r^\alpha} = v_d^\alpha = \frac{\left(|\tau_\theta^\alpha| - s_{ath}^\alpha\right) b^\alpha}{B_0} \tag{8.17}$$

which is the velocity used in the linear flow rule.

Parameters (unit)	Q^{α}_{ref} (J)	b^{α} (m)	l^{α}_{kink} (b^{α})	ν_D (s^{-1})	v_s (ms^{-1})
Value	2.1×10^{-19}	2.94×10^{-10}	20	9.13×10^{13}	3312

Table 8.1: Parameters for basal slip system at room temperature.

The slip rates on different slip systems can then be derived using Equation 8.6 with known dislocation densities, whose evolution will be discussed in section 8.2.2.

The average dislocation velocity for the unified flow rule in Equation 8.15, as well as the velocities for the thermally-activated and drag-dominated dislocation motions in Equations 8.16 and 8.17 respectively are plotted in Figures 8.4(a,b). In Figure 8.4(b), the velocities are plotted on a log-scale for improved clarity. The resolved shear stress is increased to calculate the average dislocation velocity as a function of stress at room temperature $T = 300K$. The forest dislocation density is kept fixed at $30.49\mu m^{-2}$. The parameters used to simulate these plots are given in table 8.1. The material constants used are $c^{\alpha}_{ath} = 0.8$, $c^{\alpha}_{act} = 0.7$ and $c^{\alpha}_{l} = 8.0$. At lower stresses and strain-rates, the velocity profile by the unified rule agrees well with the velocity predicted by the activation energy based rule. With increasing stresses and strain-rates, the rate of successful thermal activation is boosted and t^{α}_{w} decreases exponentially. Consequently at around $90m/s$, the velocity by the unified rule smoothly transitions to the velocity by the linear rule for the drag-dominated dislocation motion. This transition point is close to predictions of $\sim 100m/s$ made by a multi-scale strength model for screw dislocations in tantalum [26].

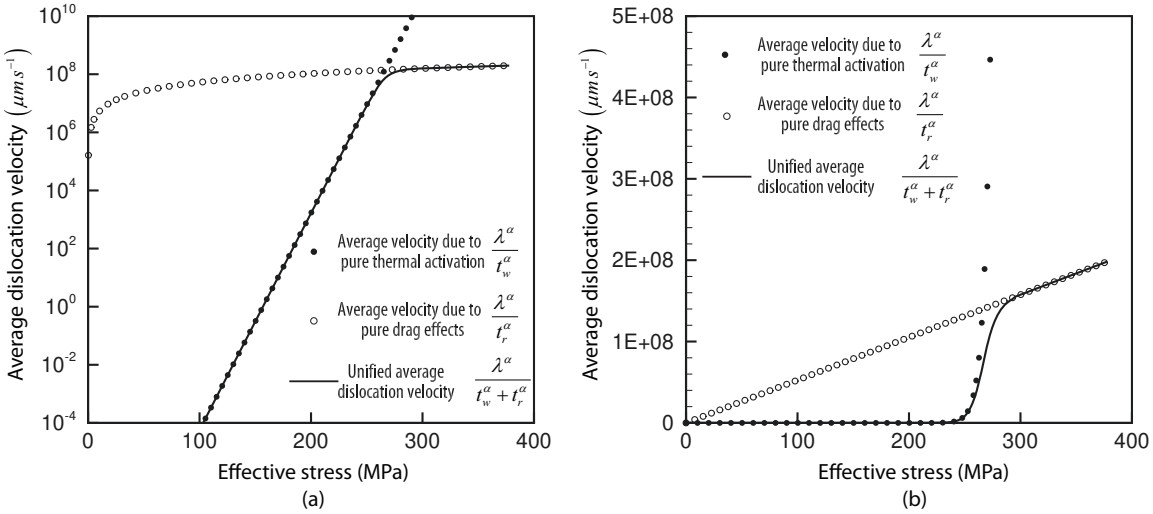

Figure 8.4: Comparison of the average dislocation velocity by the unified flow rule with the velocities with the thermally-activated and drag-dominated dislocation motions, plotted on (a) regular scale and (b) log-scale.

8.2.2 Evolution of dislocation densities

The evolution of SSDs is predominantly governed by two competing mechanisms of dislocation multiplication and annihilation. Other less dominant mechanisms are ignored in the present formulation. The multiplication rate on a slip system α has been related to the inverse of dislocation length (or equivalently square root of dislocation density) in [172] as:

$$\dot{\rho}^\alpha_{mult} = c^\alpha_{multi}\sqrt{\rho^\alpha}\,|\dot{\gamma}^\alpha| \tag{8.18}$$

where c^α_{multi} is a material constant. This equation was originally derived for *fcc* metals with the assumption of emission of rectangular shaped dislocation loops from disloca-

tion sources. This work makes the same assumption for the *hcp* alloys. Dislocations of opposite sign can annihilate each other athermally if they come within a critical distance. The rate of athermal annihilation is given as [154, 172]:

$$\dot{\rho}^{\alpha}_{anni} = c^{\alpha}_{annih}\rho^{\alpha}\left|\dot{\gamma}^{\alpha}\right| \tag{8.19}$$

with c^{α}_{annih} as a material constant. The rate of dislocation evolution is written as:

$$\dot{\rho}^{\alpha} = \dot{\rho}^{\alpha}_{mult} - \dot{\rho}^{\alpha}_{anni} \tag{8.20}$$

following the simplified form in [173].

8.2.3 Slip system resistances

The SSD and GND densities are internal state variables in the unified flow rule that contribute to the slip system hardening. The athermal and thermal resistances to dislocation motion on slip system α are given as [87]:

$$s^{\alpha}_{ath} = c^{\alpha}_{ath}\mu^{\alpha}b^{\alpha}\sqrt{\rho^{\alpha}_{\mathrm{P}}} + s^{\alpha}_{0,ath} + \frac{K^{\alpha}}{\sqrt{D_g}} \tag{8.21a}$$

$$s^{\alpha}_{th} = \frac{K_{\mathrm{B}}T}{c^{\alpha}_{act}l^{\alpha}_{kink}b^{\alpha 2}} \tag{8.21b}$$

where c^{α}_{ath} and c^{α}_{act} are model parameters and μ^{α} is the projection of the shear modulus μ on the slip system α. The denominator $c^{\alpha}_{act}l^{\alpha}_{kink}b^{\alpha 2}$ in equation (8.21b)

corresponds to the activation volume. In Equation 8.21a $\rho_{\mathrm{P}}^{\alpha}$ is the parallel dislocation density on the slip system α, while $\rho_{\mathrm{F}}^{\alpha}$ corresponds to the forest dislocation density perpendicular to it. The parallel and forest dislocation densities are calculated as [93]:

$$\rho_{\mathrm{P}}^{\alpha} = \sum_{\beta=1}^{n_{slip}} \chi^{\alpha\beta} \left[\left| \rho_{\mathrm{GNDs}}^{\beta} \sin\left(\mathbf{n}_0^{\alpha}, \mathbf{m}_0^{\beta}\right) \right| + \left| \rho_{\mathrm{GNDet}}^{\beta} \sin\left(\mathbf{n}_0^{\alpha}, \mathbf{t}_0^{\beta}\right) \right| + \left| \rho_{\mathrm{GNDen}}^{\beta} \sin\left(\mathbf{n}_0^{\alpha}, \mathbf{n}_0^{\beta}\right) \right| + \left| \rho^{\beta} \sin\left(\mathbf{n}_0^{\alpha}, \mathbf{m}_0^{\beta}\right) \right| \right] \tag{8.22a}$$

$$\rho_{\mathrm{F}}^{\alpha} = \sum_{\beta=1}^{n_{slip}} \chi^{\alpha\beta} \left[\left| \rho_{\mathrm{GNDs}}^{\beta} \cos\left(\mathbf{n}_0^{\alpha}, \mathbf{m}_0^{\beta}\right) \right| + \left| \rho_{\mathrm{GNDet}}^{\beta} \cos\left(\mathbf{n}_0^{\alpha}, \mathbf{t}_0^{\beta}\right) \right| + \left| \rho_{\mathrm{GNDen}}^{\beta} \cos\left(\mathbf{n}_0^{\alpha}, \mathbf{n}_0^{\beta}\right) \right| + \left| \rho^{\beta} \cos\left(\mathbf{n}_0^{\alpha}, \mathbf{m}_0^{\beta}\right) \right| \right] \tag{8.22b}$$

where $\chi^{\alpha\beta}$ is the interaction factor, taken as 1 in this work. In the last term on the RHS of Equations 8.22a and 8.22b, the angle between $\mathbf{n}_0^{\alpha}$ and $\mathbf{m}_0^{\beta}$ is used to project ρ^{β} onto the slip system α. $\mathbf{m}_0^{\beta}$ is used here since the tangent line is parallel to the Burgers vector for screw dislocations.

Computational procedure to perform time integration of the unified model can be formulated similar to the one given in Table 6.1. Alternatively one can set up a nonlinear equation on the second Piola-Kirchhoff stress in the inner loop. Interested readers are referred to [139] for more details.

8.3 A phenomenological flow rule for comparison

Rate-dependent phenomenological flow rules, especially those using the power law, have been used to describe crystallographic slip-rates for metals and alloys in various studies e.g. in [7,148,149,156]. In these rules, the average velocity of dislocations has a power-law dependence on the resolved shear stress, and the slip-rate is expressed as:

$$\dot{\gamma}^{\alpha} = \dot{\gamma}_0^{\alpha} \left(\frac{\left|\tau_{\theta}^{\alpha}\right| - s_{ath}^{\alpha}}{s_{th}^{\alpha}} \right)^{\frac{1}{m}} \operatorname{sign}\left(\tau_{\theta}^{\alpha}\right) \tag{8.23}$$

For Ti alloys, the effect of SSDs on the slip system resistances are taken into account through phenomenological relationships [95, 96]:

$$s_{ath}^{\alpha} = c_1^{\alpha} \mu^{\alpha} b^{\alpha} \sqrt{\rho_{\mathrm{GND,P}}^{\alpha}} \tag{8.24a}$$

$$s_{th}^{\alpha} = s_{0,th}^{\alpha} + \frac{K^{\alpha}}{\sqrt{D_g}} + \int_{t'=0}^{t'=t} \sum_{\beta=1}^{n_{slip}} h_{th}^{\alpha\beta} \left|\dot{\gamma}^{\beta}\right| dt' + \frac{Q^{\alpha}}{c_2^{\alpha} c_3^{\alpha} b^{\alpha 2}} \sqrt{\rho_{\mathrm{GND,F}}^{\alpha}} \tag{8.24b}$$

Q^{α} is the activation energy to overcome forest GND dislocation population, which is approximated as $Q^{\alpha} = 10\mu^{\alpha} b^{\alpha}$ for *hcp* crystals in [96]. $h_{th}^{\alpha\beta}$ is the hardening matrix that accounts for self and latent hardening and is given as:

$$h_{th}^{\alpha\beta} = \chi^{\alpha\beta} h_{th,ref}^{\beta} \left| 1 - \frac{s_{th}^{\beta}}{s_{th,sat}^{\beta}} \right|^{r} \text{sign}\left(1 - \frac{s_{th}^{\beta}}{s_{th,sat}^{\beta}} \right) \quad \text{where} \quad s_{th,sat}^{\beta} = \tilde{s}_{th}^{\beta} \left| \frac{\dot{\gamma}^{\beta}}{\dot{\gamma}_0^{\beta}} \right|^{n} \tag{8.25}$$

This phenomenological flow rule is used for comparing numerical results with the unified flow rule.

8.4 Adiabatic heating

Plastic deformation is an exothermic process that releases energy in the form of heat. A large fraction ($\approx 90\%$) of the energy dissipated due to the plasticity is converted into heat, while some is stored in the microstructure as stored and defect energy [86, 121]. At lower strain-rates, the localized heat generated has time to conduct away into the material. However, at high rates of deformation, the time afforded for transient heat conduction is very short. This leads to a localized increase in the temperature adiabatically. Even deformations at moderate strain-rates can lead to adiabatic heating processes [121].

Temperature increase due to adiabatic heating, in turn, promotes additional plastic deformation through an increase in the rate of thermal activation. This cycle is more relevant for high strain-rate problems. The rate of temperature increase due to adiabatic heating is expressed as:

$$\dot{T} = \frac{\beta_t}{\rho \hat{c}} \dot{W}_p \tag{8.26}$$

where $\hat{c}$ is the temperature-dependent specific heat capacity at constant volume. For Ti alloys the values are $\rho = 4428kg/m^3$ and $\hat{c} = 559.77 - 0.1473T + 0.00042949T^2\ JKg^{-1}K^{-1}$ for the temperature range $278K < T < 1144K$ from [174]. $\dot{W}_p = \boldsymbol{\sigma} : \mathbf{d}^p$ is the plastic power per unit deformed volume, where $\mathbf{d}^p$ is the symmetric part of the plastic velocity gradient in the current configuration $\mathbf{l}^p = \mathbf{F}^e\mathbf{F}^\theta\dot{\mathbf{F}}^p\mathbf{F}^{p^{-1}}\mathbf{F}^{\theta^{-1}}\mathbf{F}^{e^{-1}}$. The parameter β_t corresponds to the fraction of plastic work that is converted to heat and is taken to be 0.9 in this study. While the heat energy has been largely assumed to be 90% of the plastic dissipation in studies on various metals, experimental studies e.g. in [121] have shown some variations. When modeling shock events [175], the incorporation of thermo-elastic effects in equation (8.26) may be necessary, in addition to plastic work.

8.5 Microstructural characterization and statistically equivalent representative volume elements

This section briefly discusses the material characterization and reconstruction methods for 3D virtual microstructures from 2D measurements. The material studied in this paper is Ti-7.02Al-0.11O-0.015Fe (wt%), better known as Ti-7Al alloy, with a predominantly *hcp* crystallographic structure [165]. The composition of this alloy is

very close to the α phase of many commercially available titanium alloys [147]. Mechanical testing is done on two variants of this alloy, based on their pre-test processing. They are the purely rolled (AR) samples and the rolled-annealed (RA) samples, which are first rolled and subsequently annealed to increase the grain size and improve its ductility.

8.5.1 Microstructural Characterization

Ti-7Al specimens are imaged using electron back-scattered diffraction (EBSD) in a scanning electron microscopy system, provided in [176]. For the AR and RA samples, surface EBSD scans quantifying the texture are respectively collected on regions with dimension $5425 \times 2190 \mu m^2$ and $5175 \times 2135 \mu m^2$, at $5 \mu m$ step size. A portion of the surface EBSD scans for both the samples are shown in figure 8.5. The scans have been filtered to remove noise from the data based on a confidence index. The pole figures for the $\{0001\}$ and $\{\bar{2}110\}$ orientations in figure 8.5 indicate that the crystallographic c-axis of grains is mostly aligned with the normal direction (ND) for both the AR and RA microstructures. The most significant morphological difference between these two sample microstructures is the grain size due to the annealing process. The averaged diameters of the equivalent 2D circular grains are $34.9 \mu m$ and $83.4 \mu m$, for the AR and RA samples respectively.

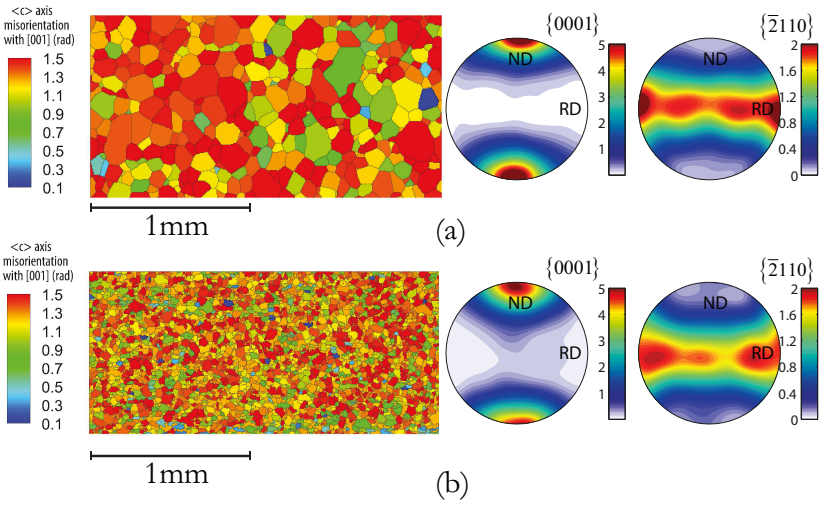

Figure 8.5: Filtered EBSD scans and pole figures for the (a) RA and (b) AR samples

8.5.2 Generating Virtual Microstructures

Methods of reconstructing 3D virtual microstructures have been developed using techniques like serial-sectioning using focused ion beam [177–179], manual polishing [180] and X-ray tomography [181]. However, these methods need 3D data for microstructure reconstruction. In the present work, 3D statistics are estimated from extrapolation of 2D surface EBSD data on polycrystalline specimens as done in [8] for other alloys. The 2D EBSD images for both samples in Figure 8.5 are characterized. Crystallographic distributions, e.g. orientation and misorientation distributions, and morphological distribution, e.g. distribution of 2D equivalent circular grain diameters (ECD), are obtained. To generate 3D statistics from 2D distributions, a procedure based on stereology principles in [182] is employed. Assuming equiaxed grains, the average equivalent spherical grain diameter ($\overline{ESD}$) is expressed in terms of the average

equivalent grain diameter $\overline{ECD}$ as:

$$\overline{ESD} = \frac{4}{\pi}\overline{ECD} \tag{8.27}$$

The standard deviation of the 2D and 3D grain idealizations, C^{sd} and S^{sd} respectively, are assumed to be the same. The averaged 3D grain diameters $\overline{ESD}$ and its standard deviation S^{sd}, calculated from the 2D distributions in the images of Figure 8.5 are given in Table 8.2 for both the AR and RA samples. The log-normal probability

Microstructure (Process)	$\overline{ESD}$ (μm)	S^{sd} (μm)
Annealed (AR)	44.4	15.4
Rolled Annealed (RA)	106.2	51.7

Table 8.2: Average and standard deviation of the 3D equivalent grain diameter for RA and AR samples

density function has been found to reasonably represent the grain size distribution in metallic alloys such as Ni-based superalloys in [11] and Ti alloys in [8]. This distribution function is defined in terms of two parameters viz. the average μ and standard deviation σ of the population. They can be computed in terms of the grain size average and standard deviation values in table 8.2 using the following formulae given in [183]:

$$\mu = \ln\left(\overline{ESD}^2/\sqrt{S^{sd2} + \overline{ESD}^2}\right) \tag{8.28a}$$

$$\sigma = \sqrt{\ln\left[\left(\frac{S^{sd}}{\overline{ESD}}\right)^2 + 1\right]} \tag{8.28b}$$

Alternatively one can employ the method of maximum-likelihood to obtain the parameters of the log-normal distribution.

The morphological and crystallographic orientation, misorientation and micro-texture distribution data are input into the DREAM.3D software [10] to create 3D statistically-equivalent virtual microstructures using methods described in [11, 184]. For generating synthetic microstructures, this software relaxes the assumption of equiaxed grains used in the development of morphological statistics. Grains are allowed to have complex shapes with random morphological orientations. These grains are then packed in the synthetic microstructure based on neighborhood constraints. Following previous reconstructions for Ti alloys in [8] and IN100 superalloys in [11], the average number of neighbors to a grain in the 3D ensemble is assumed to be 14.

Crystallographic orientations are assigned to the grains in the synthetic microstructure by sampling from the experimentally obtained orientation distribution function. Subsequently, the misorientation and micro-texture distributions are matched by an error minimization routine, in which orientations are swapped among grains and/or perturbed. A total of 180 different synthetic microstructures with varying number of grains are reconstructed for the RA sample. These microstructures are grouped into different bins based on the number of grains in the ensemble. Each bin has a width of 10, i.e. the increase in the number of grains for every bin is by 10. Error measures for the average grain size and the standard deviation are defined to quantitatively study

the convergence in grain size distribution. They are:

$$E_{av}^{(i)} = \frac{1}{n^{(i)}} \sqrt{\sum_{j=1}^{n^{(i)}} \left(\frac{\overline{ESD}_j^{(i)}}{\overline{ESD}} - 1 \right)^2} \tag{8.29a}$$

$$E_{sd}^{(i)} = \frac{1}{n^{(i)}} \sqrt{\sum_{j=1}^{n^{(i)}} \left(\frac{S^{sd}{}_j^{(i)}}{S^{sd}} - 1 \right)^2} \tag{8.29b}$$

For microstructures in the ith bin, $E_{av}^{(i)}$ and $E_{sd}^{(i)}$ respectively quantify the error in the average and standard deviation of the grain size. $n^{(i)}$ is the number of microstructural instantiations that belong to the bin i. $\overline{ESD}_j^{(i)}$ and $S^{sd}{}_j^{(i)}$ represent the average and standard deviation of the diameter of the equivalent spherical grain in the jth synthetic microstructure belonging to bin i. $\overline{ESD}$ and S^{sd}, on the other hand, correspond to values from stereological analysis of EBSD maps in table 8.2. Figure 8.6 shows the error in the average and standard deviation as a function of the number of grains in the synthetic microstructure. The error generally decreases rapidly with increasing number of grains. Less than 2% error is seen for both parameters for microstructures containing more than 480 grains.

To assess the fidelity of crystallographic distribution representation in the synthetic microstructure, the misorientation distribution is examined. The error in the misorientation distribution is evaluated by the Kolmogorov-Smirnov (KS) test [185]. It is a distribution-free test of goodness of fit, which quantifies the maximum difference between two cumulative distribution functions (CDFs). Figure 8.7 shows that the KS statistic generally decreases rapidly with increase in the number of grains in the microstructure. In other words, the misorientation CDF of the synthetic mi-

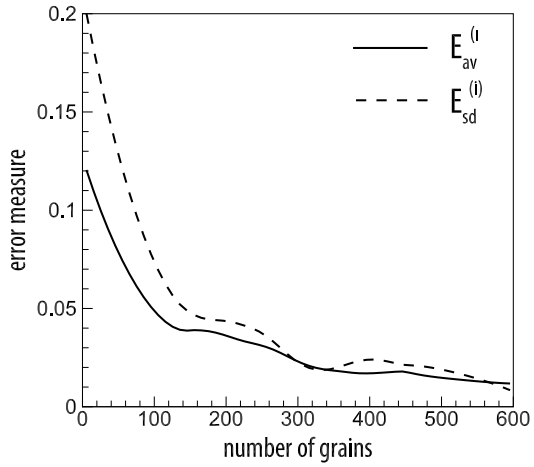

Figure 8.6: Error in the the average and standard deviation of 3D grain size for the rolled-annealed (RA) microstructures.

crostructure compares better to the one obtained from EBSD maps with increasing the number of grains.

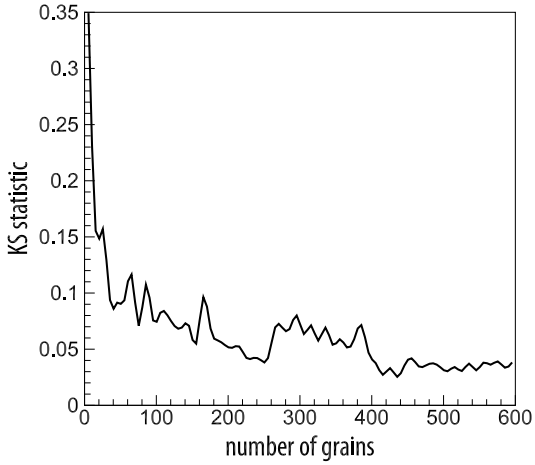

Figure 8.7: Kolmogorov-Smirnov test for the misorientation distribution in the rolled-annealed (RA) microstructures.

From the results in figures 8.6 and 8.7 for the RA microstructure, a statistically equivalent microstructure of dimensions $960 \times 960 \times 960 \mu m^3$ containing 529 grains is chosen for crystal plasticity FE simulations. Figure 8.8(a) shows the contour plot of the $< c >$-axis misorientation of a microstructure containing 529 grains. The pole figures, misorientation and grain size distribution of the 529-grain simulated microstructure are compared with those obtained from EBSD maps in figures 8.8(b-d). Very good agreement is seen between the simulated and the experimental probability density functions.

With an analogous reconstruction process and convergence study, a statistically equivalent RVE of dimensions $300 \times 300 \times 300 \mu m^3$ containing 515 grains is simulated for the AR sample. Figure 8.9(a) shows the $< c >$-axis misorientation contour plot, while pole figures, misorientation and grain size distribution of the simulated microstructure are compared with EBSD based results in figures 8.9(b-d).

8.5.3 Mesh Generation and Convergence Study

The 3D simulated statistically equivalent microstructures, developed in the previous section, are represented as voxelized volumes with each voxel in a grain identified by a common set of 3 Euler angles. For crystal plasticity FE analysis, these voxelized volumes should be transformed into domains with smooth grain boundaries that can be discretized into a finite element mesh.

For discretization of the computational domain, the voxelized synthetic microstruc-

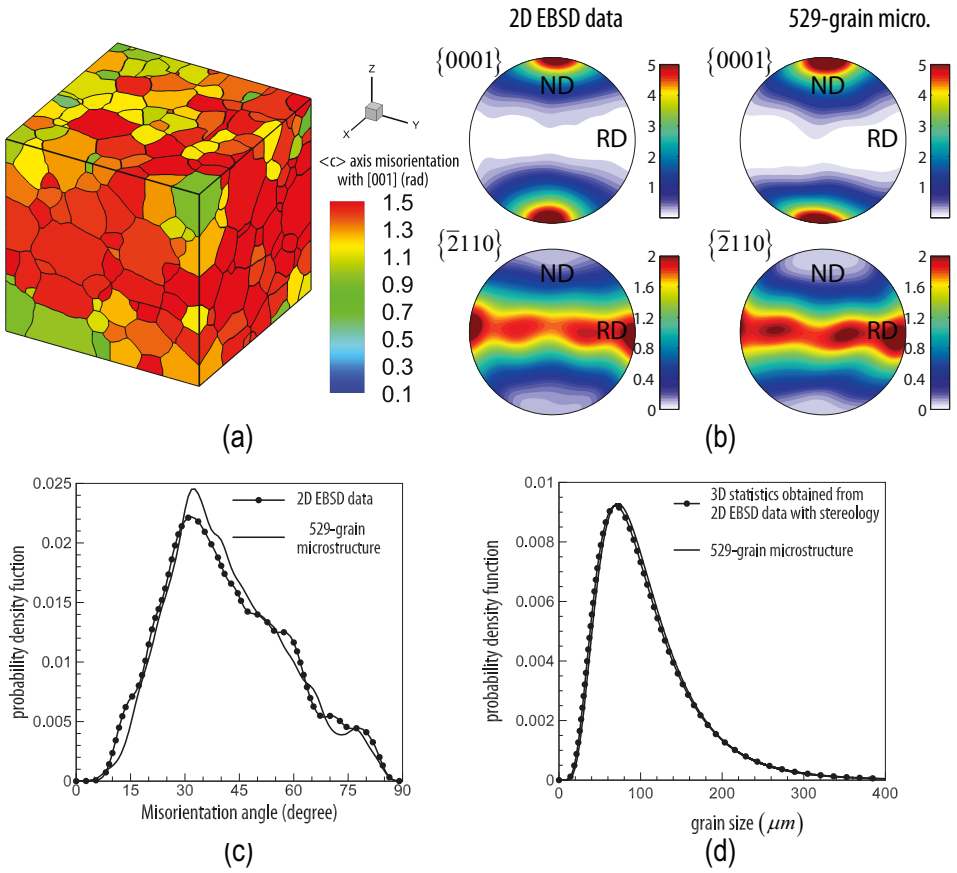

Figure 8.8: (a) Contour plot of $< c >$-axis misorientation for the 529-grain statistically equivalent RA virtual microstructure; Comparison of (b) orientation distribution, (c) misorientation distribution and (d) grain size distribution of the simulated microstructure with those from the EBSD data.

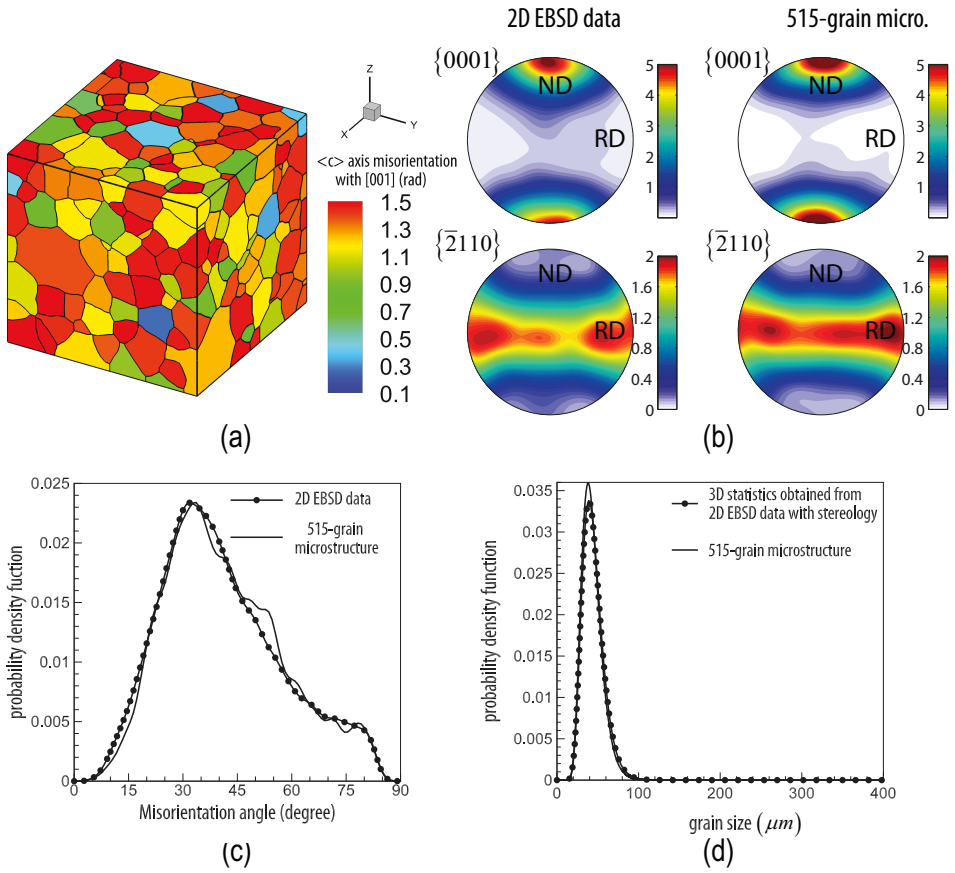

Figure 8.9: (a) Contour plot of $< c >$-axis misorientation for the 515-grain statistically equivalent AR virtual microstructure; Comparison of (b) orientation distribution, (c) misorientation distribution and (d) grain size distribution of the simulated microstructure with those from the EBSD data.

tures are input into the Simmetrix® software [12]. For enhancing mesh quality, this software applies some basic filters to remove the small features and smoothen the grain boundaries. Stabilized four-node tetrahedral or TET4 elements, with linear interpolation functions for displacements, discretize the polycrystalline domains. The aspect ratio of elements in the mesh is kept below 70 and less than 0.01% of elements have an aspect ratio higher than 40.

It is necessary to conduct a mesh convergence study with respect to both macroscopic and microscopic variables, prior to conducting major CPFE simulations [186]. For this study, a CPFE analysis of the virtual RA microstructure in Figure 8.8(a) is conducted under constant strain-rate $\dot{\epsilon} = 1.1 \times 10^3 s^{-1}$ along the [100] or x-direction. Two mesh densities with 536090 and 754916 elements are considered for comparison. Figure 8.10(a) shows the comparison of the macroscopic volume-averaged stress-strain response, while Figure 8.10(b) compares the distribution of microscopic von Mises stress along an X-directed line passing through the centroid of the microstructure. The mesh convergence study concludes that the 536090-element mesh provides sufficient resolution for the CPFE simulations. A similar study for the AR microstructure converges to a 517023-element mesh to provide adequate accuracy.

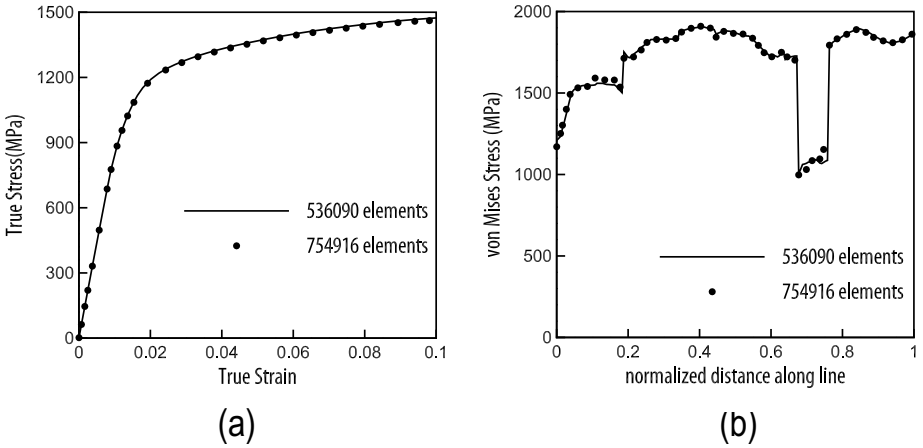

Figure 8.10: Mesh convergence study for the RA microstructure by comparing results of two mesh densities: (a) volume-averaged loading direction stress-strain response and (b) von Mises stress at 2% strain along an X-directed line.

8.6 Calibration and Validation of the Crystal Plasticity FE Model

The unified flow rule (UL) and phenomenological (PL) crystal plasticity models are calibrated and validated using experiments that are conducted at Army Research Laboratories in Aberdeen. Room temperature, uniaxial compression experiments are conducted to determine the mechanical behavior of both the as-rolled (AR) and rolled-annealed (RA) materials. The tests are performed at both, quasi-static ($10^{-3}s^{-1}$) and dynamic strain rates (1000 - $4000s^{-1}$) to investigate strain-rate sensitivity. Given the texture in both materials, it was necessary to run the experiments with loading along the three orthogonal directions (normal (ND), rolled (RD), and transverse (TD)) to

probe possible anisotropic behavior.

8.6.1 Experimental Methods

The quasi-static (QS) tests are conducted on a screw-driven Instron load frame under displacement control conditions. The specimens are machined from the bulk materials using a wire-EDM to dimensions of $3.5 \times 3.5 \times 7mm$ (aspect ratio of 2). A compression subpress fixture ensures proper axial alignment during loading. To minimize the frictional effects, the ends of the specimens are lubricated. The displacement is measured using a stereoscopic digital image correlation (DIC) system consisting of two 2.3 MP cameras. The choice of a two-camera system is made to eliminate the effect of out of plane motion on the strain measurements. DIC speckle pattern is applied to the surface of the specimen using a fine airbrush. VicSnap and Vic3D are used to acquire the images and perform the correlation (subset 29, step 10). Uniaxial strain is calculated using a digital extensometer. None of the specimens failed during testing. Unloading is initiated either after sufficient data is obtained or the specimen begins to deform in a non-uniform manner upon which the data becomes invalid.

The dynamic (DY) strain-rate tests are conducted on a compression Kolsky (Split-Hopkinson) bar, a technique originally suggested in [187] and subsequently modified in [188]. It is currently the most popular technique for testing of high strain-rate ($10^3 - 10^4\ s^{-1}$) behavior of materials. The Kolsky bar consists of two $9.5mm$ maraging steel bars, referred to as the input and output bars, with the specimen sandwiched

between them. A gas gun accelerates a projectile, which strikes the input bar, creating a compressive stress pulse that travels down the input bar and loads the specimen [189]. The foil strain gages, located on the input and output bars, record the reflected and transmitted stress pulses respectively. These data are used to calculate the stress and strain rate history of the specimen once it has reached stress equilibrium. The strain-rate history is integrated over time to obtain the strain history, which is correlated with the stress history to form stress-strain curves. A complete description of the Kolsky bar experimental technique is provided in [190]. The specimens are machined from the bulk materials to dimensions of $3.5 \times 3.5 \times 2.5mm$ (aspect ratio of 0.7). The smaller aspect ratio reduced the inertial effects during testing and is inversely related to the achievable strain rate. The specimen ends were polished and lubricated to limit the effects of friction.

8.6.2 Experimental Results

Figure 8.11 shows the representative compressive true stress-strain curves for the rolled-annealed (RA) and as-rolled (AR) materials. Valid measurement of stresses and strain-rates using the Kolsky bar experiments requires stress equilibrium within the specimen. Since this condition may not be satisfied at the early stages of deformation, corresponding to very small strains, the calculated strain-rates and stresses are not representative of the mechanical response of the material under uniaxial loading conditions. In this work, the strains at which stress equilibrium is reached is

calculated to be $\sim 2-3\%$. The Young's modulus and the 0.2% offset yield stress are therefore obtained from the QS data only. The transverse and rolled directions for the RA material have similar response. However, the normal direction shows increased strength and strain hardening. The 0.2% yield strengths for the RD, TD, and ND are $613MPa$, $620MPa$, and $909MPa$ respectively, which corresponds to an increase in strength of over 30% in the ND. The 5% flow stress shows increased strength of $265MPa$, $302MPa$, and $209MPa$ for the RD, TD, and ND respectively. The direction-averaged Young's modulus is $122GPa$.

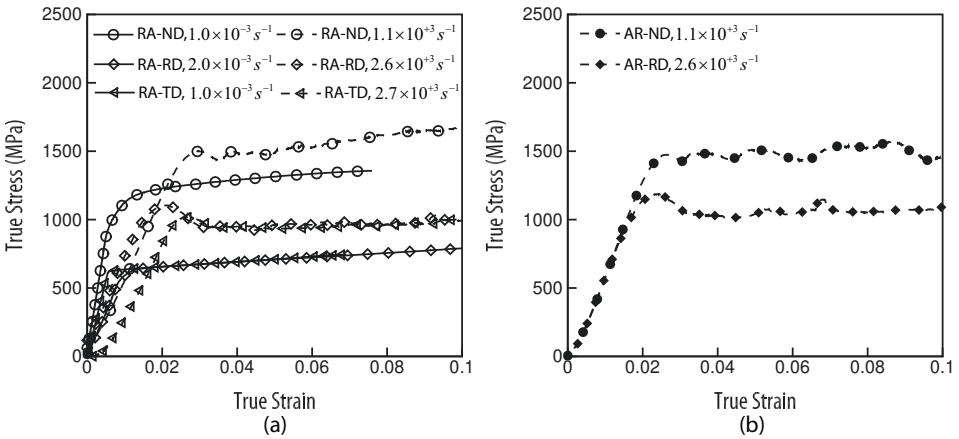

Figure 8.11: Representative compression true stress-strain curve for the Ti-7Al alloy tested at QS and DY strain rates with: (a) RA and (b) AR material microstructures.

8.6.3 Choosing calibration and validation set of experiments

Image-based CPFE models need robust constitutive models for predicting the material response. The constitutive models are calibrated and validated using the results of the quasi-static and dynamic experiments discussed in section 8.6. Results from eight experiments are used for calibration of the crystal plasticity constitutive model parameters and also validation of the CPFE model. The parameters and conditions for these tests are tabulated in tables 8.3 and 8.4. The different variables in the table corresponds to:

(i) the microstructure variations due to variation in the processing conditions: as-rolled (AR) or rolled-annealed (RA),

(ii) the applied strain-rate corresponding to quasi-static (QS) or dynamic (DY) loading classification, and

(iii) the loading direction that may be normal (ND), rolling (RD) or transverse (TD) direction.

The ND, RD and TD directions correspond to the global [100], [010] and [001] directions respectively in the simulations. Four of the eight experiments given in table 8.3 are used for calibration of constitutive parameters, while the other four in table 8.4 are used for CPFE model validation. Both the calibration and validation experiments incorporate a diverse set of conditions.

Microstructure	Strain-rate (s^{-1})	Classification	Loading direction
RA	1.0×10^{-3}	QS	ND
RA	$1.1 \times 10^{+3}$	DY	ND
RA	2.0×10^{-3}	QS	RD
RA	$2.6 \times 10^{+3}$	DY	RD

Table 8.3: Specifics of calibration experiments.

Microstructure	Strain-rate (s^{-1})	Classification	Loading direction
RA	1.0×10^{-3}	QS	TD
RA	$2.7 \times 10^{+3}$	DY	TD
AR	$1.1 \times 10^{+3}$	DY	ND
AR	$2.6 \times 10^{+3}$	DY	RD

Table 8.4: Specifics of validation experiments.

8.6.4 Calibration of Constitutive Parameters

The constitutive equations for the unified flow rule (UL) and phenomenological (PL) crystal plasticity models are calibrated in this section. Constitutive parameters to be calibrated include the anisotropic elastic constants and slip system-dependent crystal plasticity parameters. The α titanium alloys with a *hcp* lattice-parameter ratio of $c/a = 1.59$ shows a transversely isotropic elastic response. The elastic stiffness coefficients are expressed in a material coordinate system that is defined by the orthonormal basis $(\mathbf{e}_1^c, \mathbf{e}_2^c, \mathbf{e}_3^c)$. Here, the directions 1, 2 and 3 correspond respectively to $[\bar{1}2\bar{1}0]$, $[\bar{1}010]$ and $[0001]$ directions of the *hcp* crystal lattice. The anisotropic elasticity tensor in this coordinate system is expressed in the Voigt notation as $[C_{IJ}^e]$, $I, J = 1 \cdots 6$. For transversely isotropic elastic behavior, there are only 5 independent elastic constants, viz. $C_{11} = C_{22}$, C_{12}, $C_{13} = C_{23}$, C_{33}, $C_{55} = C_{66}$ and $C_{44} = (C_{11} - C_{12})/2$. The elastic constants are measured using resonant ultrasound spectroscopy experiments on Ti-7 single crystal samples at room temperature in [1] and tabulated in Table 8.5.

Experimental measurements of elastic constants of α-Ti have shown a near linear dependence on temperature [2]. Stiffness components decrease almost linearly with increasing temperature but with different slopes. Experimental results in [2] are used to obtain the thermal gradients of the stiffness components. The linear slopes of elastic coefficients with temperature are given in Table 8.5.

The crystal plasticity parameters for the (UL) and (PL) models are calibrated in

Stiffness Parameters	unit	$IJ = 11$	$IJ = 12$	$IJ = 13$	$IJ = 33$	$IJ = 55$
C_{IJ}	GPa	164.7	82.5	61.8	175.2	48.5
$-\frac{\partial C_{IJ}}{\partial T}$	MPa/K	48	8.9	21	21	21.9

Table 8.5: Experimentally measured elastic stiffness components at room temperature in [1], and their slopes with temperature [2].

an iterative manner. For the (PL) model, the parameters that have been calibrated for the Ti-6Al alloy in [148] are taken as the starting values since its chemical composition is relatively close to that of Ti-7Al alloy. From sensitivity analysis, it is revealed that $\dot{\gamma}_0^\alpha$, $s_{0,th}^\alpha$ and m are the parameters that control the onset of plasticity i.e. yield point. Also the parameters $h_{ref,th}^\alpha$, $\tilde{s}^\alpha$, r^α and n^α are the ones controlling the hardening rate. The exponent m is found to be the primary parameter controlling rate-sensitivity. The calibration process is designed to use quasi-static tests at room temperature to calibrate parameters that control the onset of plasticity as well as hardening. Dynamic tests are utilized to calibrate the rate-controlling parameter m that affects the yield stress, as well.

Using the four calibration tests categorized in table 8.3, parameters in the (PL) model are calibrated. The volume-averaged stress-strain plots, comparing simulated results with experiments are shown in Figure 8.12. The hatched area in Figure 8.12a corresponds to a period at which stress equilibrium is not necessarily reached in the sample during high-rate experiments. Therefore, the experimental stress-strain

response is not reliable during this period. The calibrated parameters for the (PL) model are given in table 8.6. The response to loading in the ND direction is stiffer than in the RD direction. This is the effect of the rolling process, which aligns the $\langle c \rangle$ - axis of grains along the ND direction. Therefore, loading along the ND direction will favor activation of $\langle c + a \rangle$ - pyramidal slip systems whose critical resolved shear stress is $2 \sim 3$ times larger than the $\langle a \rangle$ - basal or prismatic slip systems [150].

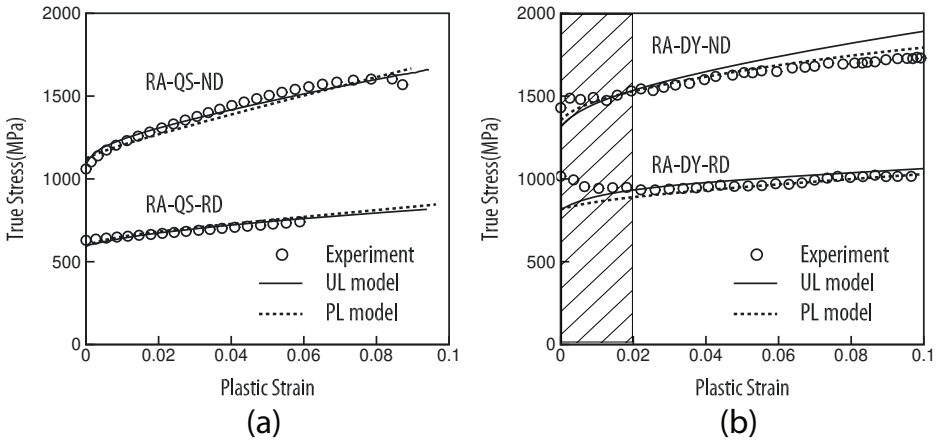

Figure 8.12: Stress-strain plots used in the calibration of the (PL) and (UL) model parameters using: (a) quasi-static (QS) and (b) dynamic (DY) experiments. The hatched region corresponds to the range where stress equilibrium is not attained in the dynamic experiments.

It is also important to account for the effect of temperature increase on plastic deformation in high strain-rate simulations due to adiabatic heating. Increasing temperature boosts the rate of successful thermal activation attempts and consequently

Parameters (units)	$< a >$ basal	$< a >$prismatic	$< a >$ pyramidal	$< c + a >$ pyramidal
$s^{\alpha}_{0,th}$ (MPa)	230	205	500	610
$\dot{\gamma}^{\alpha}_{0}$ (s^{-1})	0.003	0.003	0.003	0.003
$h^{\alpha}_{th,ref}$ (MPa)	250	250	1200	2000
m	0.019	0.019	0.019	0.019
r^{α}	0.02	0.02	0.02	0.02
n^{α}	0.3	0.3	0.3	0.3
$\tilde{s}^{\alpha}$ (MPa)	1600	1600	1600	1800

Table 8.6: Calibrated parameters of the (PL) constitutive model for different slip systems.

plastic flow is enhanced. In other words, the resistance to plastic flow reduces with rising temperature. In the (PL) model, this is phenomenologically accounted for by scaling the slip system resistances with temperature as: $s^{\alpha}_{th} = s^{\alpha}_{th,ref}\,(T/T_{ref})^{p}$, where $s^{\alpha}_{th,ref}$ is the slip system resistance at reference temperature T_{ref} and p is a fitting parameter [86]. In the present work, T_{ref} is set to room temperature, for which $s^{\alpha}_{th,ref}$ will correspond to $s^{\alpha}_{0,th}$. The p exponent is set to -1 using the experimental results in [160] on α-Ti alloys. They have measured the variation of yield stress and critical resolved shear stresses for different slip systems at a wide range of temperatures. The results in [160] are laterally shifted such that yield stress at room temperature matches the one using the calibrated parameters in table 8.6. Figure 8.13 shows the variation of 0.2% yield stress with temperature, for single crystal Ti-7Al that is oriented for activation of $\langle a \rangle$-basal and $\langle c+a \rangle$-pyramidal slip systems. The results of $\langle a \rangle$-prism slip are not shown since it is very close to the response of $\langle a \rangle$-basal slip.

The crystal plasticity parameters for the unified flow rule (UL) crystal plasticity model are calibrated in the same way as for the (PL) model. The calibrated parameters for the (UL) model are delineated in Table 8.7. The corresponding comparison with experimental stress-strain plots are shown in Figure 8.12.

Parameters (units)	$\langle a \rangle$ -basal	$\langle a \rangle$ -prismatic	$\langle a \rangle$ -pyramidal	$\langle c+a \rangle$ -pyramidal
Q^{α}_{ref} (J)	2.1×10^{-19}	2.2×10^{-19}	3.0×10^{-19}	2.6×10^{-19}
l^{α}_{kink} (b^{α})	20	20	20	20
$s^{\alpha}_{0,th}$ (MPa)	5.0	5.0	5.0	5.0
c^{α}_{ath}	0.8	0.62	0.7	0.5
c^{α}_{act}	0.7	0.7	0.1	0.04
c^{α}_{l}	8.0	8.0	8.0	8.0
c^{α}_{multi} (μm^{-1})	150	230	500	500
c^{α}_{annih}	10	10	10	10
c^{α}_{Q}(J)	2.3×10^{-20}	3.7×10^{-20}	1.8×10^{-20}	0.9×10^{-20}
p^{α}_{Q}	1.6	1.6	1.6	1.6

Table 8.7: Calibrated parameters of the (UL) model for different slip systems.

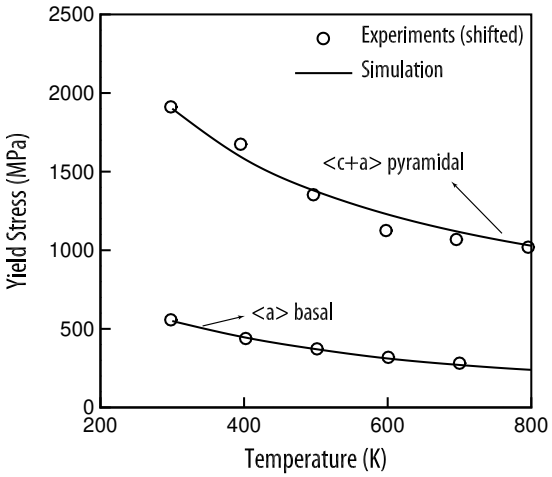

Figure 8.13: Variation of yield stress with temperature for single crystals oriented for activation of different slip systems.

8.6.5 Validation of the CPFE Model with Experimental Results

Validation of both the (UL) and (PL) models with respect to the fidelity of calibrated parameters is achieved by simulating the four experiments described in table 8.4. The image-based CPFE models for the AR and RA materials, developed in section 8.5, are used for these simulations and boundary conditions are applied commensurate with the experimental loading conditions. Results of the simulations are compared with corresponding experiments in Figure 8.14. Generally a good agreement is observed between the models and experiments for the range of strain-rates considered. Even though the parameters are calibrated using the RA materials, the models predict the deformation of AR microstructure very well. This concludes that

the grain size-dependence mechanisms in the model, i.e. the GND hardening and Hall-Petch type effects are properly represented, since the primary difference between the AR and RA microstructures is the average grain size.

Uniqueness of the calibrated parameters is always an issue when limited experimental results are available, as in this problem. The combination of sensitivity analysis and least-squares minimization routine, however yields the best possible combination of parameters to reproduce the experimentally observed response.

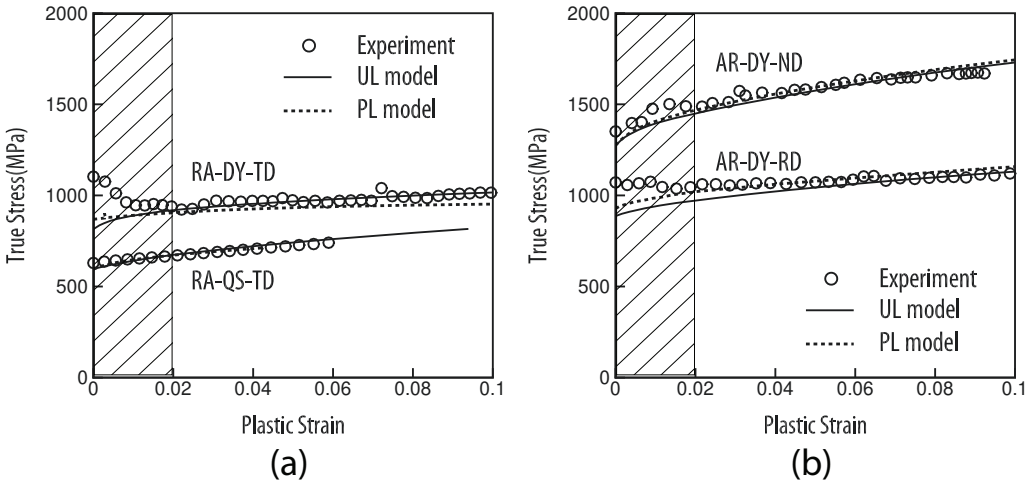

Figure 8.14: Validation of (UL) and (PL) models for the quasi-static (QS) and dynamic (DY) experiments on (a) RA and (b) AR material microstructures.

8.6.6 Validation of temperature-dependence of the flow stress

Temperature changes affect both the elastic and plastic responses of Ti alloys. With increasing temperature, elastic stiffnesses decrease in value. This affects the slip-driven plasticity through a reduction in the shear modulus dependent slip system strength represented by the athermal stress [191]. Increasing temperature also promotes plasticity by boosting up the rate of successful thermal activation attempts. The effects of temperature on plastic deformation by the (UL) model is studied here under isothermal conditions.

Compression tests are simulated for the AR microstructure along ND and RD at a strain-rate of $10^{-3}s^{-1}$ under isothermal conditions, but at different initial temperatures. The volume-averaged stress-strain responses in the loading direction are plotted in Figure 8.15a. With temperature increase, the yield stress decreases significantly but the reduction of elastic stiffness is negligible. Figure 8.15b shows the variation of the yield stress with temperature in the temperature range of $300K$ to $700K$. It is observed that the yield stress decreases almost linearly with temperature, consistent with the experimental results in [143] performed on Ti-6Al-4V. The yield stress for the AR material in the ND direction decreases more rapidly in comparison with the RD direction. This is due to the crystallographic orientation of the grains and the dissimilar variation of critical resolved shear stress (CRSS) with temperature

for different slip systems. Crystallographic orientations of grains in the AR material are such that the $\langle a \rangle$-basal and prism slip systems are the favorable modes of slip when the sample is loaded along the RD. On the other hand, $\langle c + a \rangle$-pyramidal slip is the favorable one for loading along the ND. As shown in Figure 8.13, the CRSS for the $\langle c + a \rangle$-pyramidal slip system reduces at a faster rate with temperature, compared to that for the $\langle a \rangle$-basal and prism slip systems. This explains why the yield stress for the AR-ND simulations decreases more rapidly with temperature in Figure 8.15b.

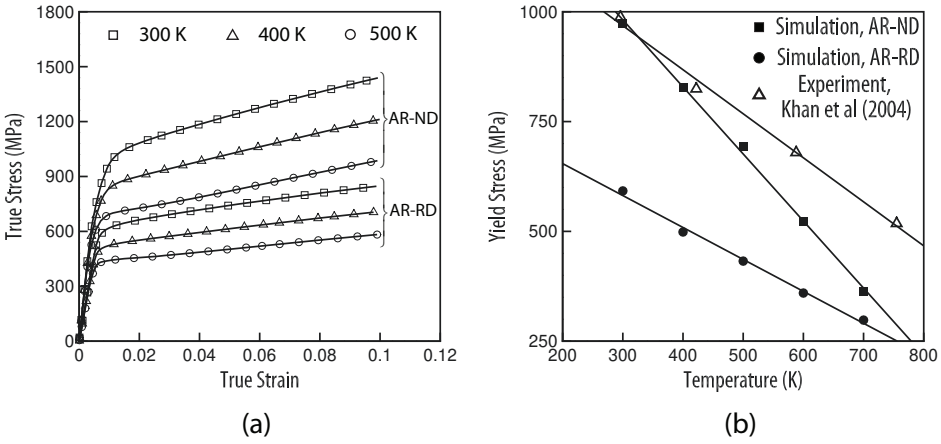

Figure 8.15: CPFE simulation of the AR microstructure at different initial temperatures, subject to strain-rate of $10^{-3}s^{-1}$: (a) loading direction stress-strain response, (b) variation of yield stress with temperature.

8.7 Numerical results

8.7.1 Strain-rate Variations in Polycrystalline Microstructures for CPFE Simulations

The unified flow-rule is applicable to a wide range of applied strain-rates. Strain-rates at different locations in a heterogeneous and plastically anisotropic polycrystalline microstructure can vary significantly even for a uniformly applied macroscopic strain-rate. The unified flow-rule is uniquely capable of seamlessly accounting for the effects of location-dependent thermally-activated and drag-dominated mechanisms of dislocation glide without any user intervention. This capability is of importance in CPFE modeling, where the local strain-rates could be orders of magnitude different from the macroscopic applied strain-rate.

To investigate the distribution of the local strain-rate in a polycrystalline Ti-7Al microstructure, the CPFE simulation is conducted for an applied compressive strain-rate of $5 \times 10^3 s^{-1}$ along the X direction. Figure 8.16a is a contour plot of the plastic strain-rate in the loading direction at 2% macroscopic strain. The heterogeneity in the strain-rate, especially over a plane parallel to the YZ plane is clearly depicted in this plot. Furthermore, the plastic strain-rate along the dashed line in Figure 8.16a is plotted for different overall strain levels in Figure 8.16b. The local plastic strain-rate field shows large variations at the early stages of plastic deformation. This variation

decreases with increasing deformation. Figure 8.16d shows the maximum Schmid factor on the basal and prism planes along the dashed line. The grains A and B in the plot have high and low values of the Schmid factor respectively, corresponding to most favorable and least favorable regions for time-dependent plastic deformation. The local plastic strain-rate in grain A reaches as high as ~ 5 times the macroscopic strain-rate at 2% strain. On the other hand, the grain B is not favorably oriented for plasticity and the local plastic strain-rate in this grain ranges from 6 to 3 orders of magnitude lower than the macroscopic applied strain-rate, depending on the strain level. This observation is not only limited to high strain-rate deformations. Figure 8.16c depicts the variation of local plastic strain-rate along the same line in the microstructure under an applied compressive strain-rate of $5 \times 10^{-4} s^{-1}$.

Next, the waiting (t_w^α) and running (t_r^α) times on individual slip systems are studied. To measure the relative effects of thermally-activated and drag-dominated processes, a *drag fraction* is introduced as the ratio of the time spent on the drag-dominated stage over the total travel time, i.e.

$$f_d^\alpha = \frac{t_r^\alpha}{(t_w^\alpha + t_r^\alpha)} \quad \text{s.t.} \quad 0 < f_d^\alpha \leq 1$$

The fraction is only defined for active slip systems. $f_d^\alpha \to 0$ corresponds to a predominantly thermally-activated dislocation glide, whereas $f_d^\alpha = 1$ denotes a purely drag-dominated dislocation glide. If f_d^α exceeds 0.1, the drag-dominated processes are significant as they constitute over 10% of the total dislocation travel time. Fig-

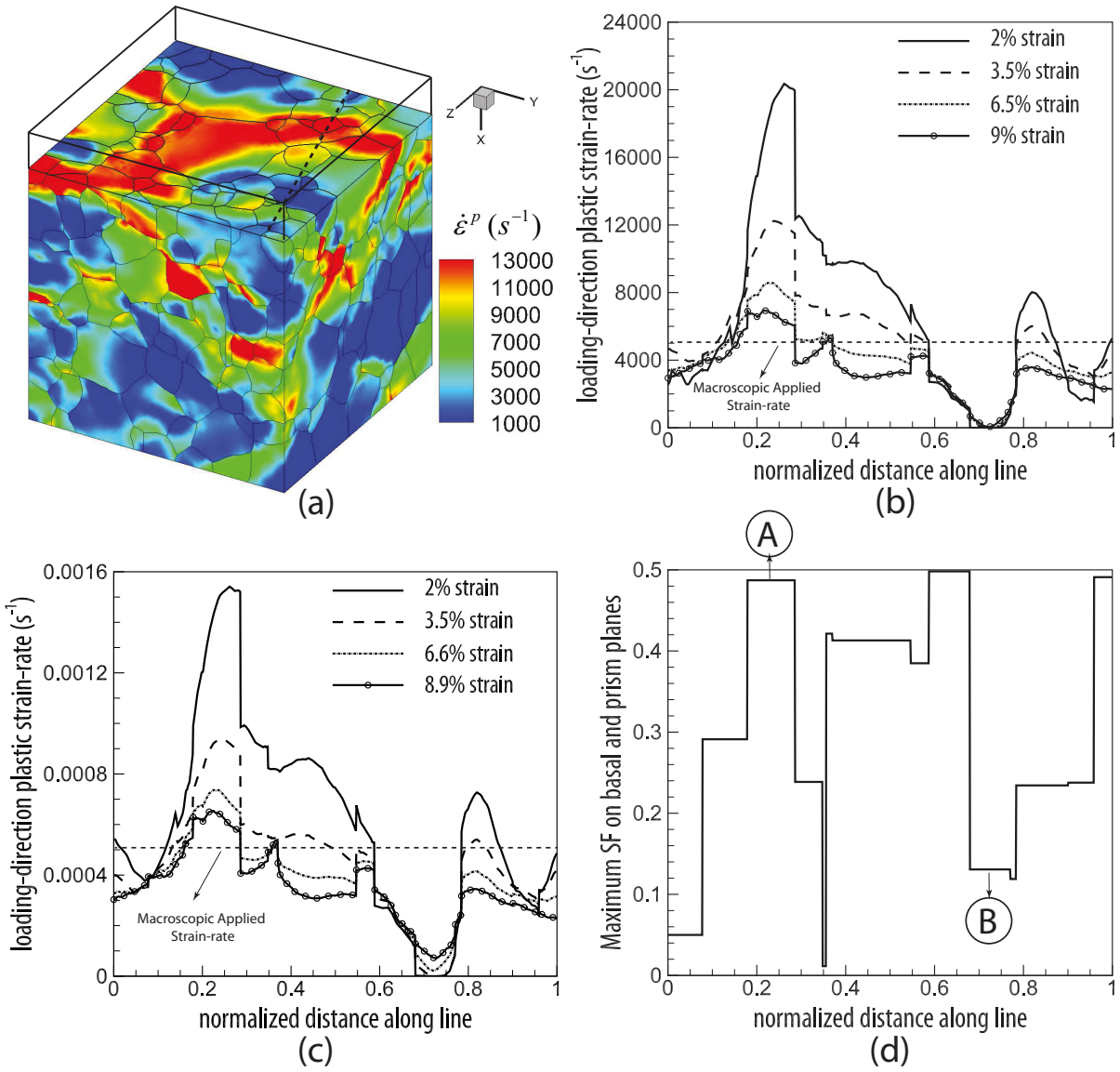

Figure 8.16: (a) Contour plot of the loading-direction plastic strain-rate at 2% strain applied compressive strain-rate of $5 \times 10^3 s^{-1}$, plot of evolution of the loading-direction plastic strain-rate along the dashed line at different strain levels under an applied compressive strain-rate of (b) $5 \times 10^3 s^{-1}$, (c) $5 \times 10^{-4} s^{-1}$ and (d) maximum Schmid factor on the basal and prism planes along the dashed line.

ure 8.17 shows the evolution of volume fraction of elements with considerable drag-dominated dislocation glide. It is calculated by probing element integration points, for which $f_d^\alpha > 0.1$ on any active slip system. In the early stages of plastic deformation, the drag-dominated processes contribute to plasticity in up to 20% of the microstructural volume. With continuing deformation, the effects of drag-dominated processes gradually fade and the mode of dislocation glide smoothly transitions to a purely thermally-activated mode. The results demonstrate that the local state of the material points in the polycrystalline aggregates could be very different from the macroscopic applied loading and hence the need for the unified flow rule.

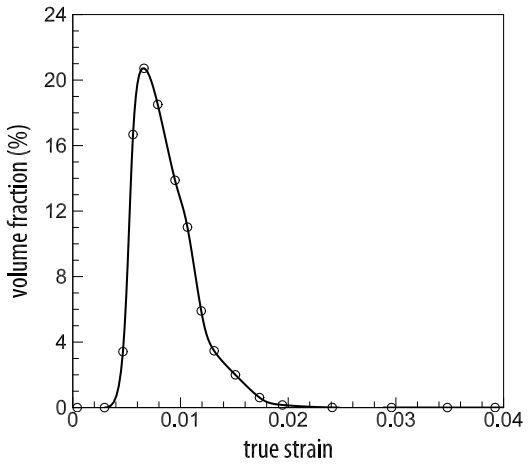

Figure 8.17: Evolution of volume of fraction of elements with significant drag-dominated processes

	Figure 8.18a	Figure 8.18b	Figure 8.18c
Euler-angles	$[0°, 45°, 30°]$	$[0°, 90°, 0°]$	$[0°, 0°, 0°]$
max. SF on $\langle a \rangle$ - Basal	0.5	0.00	0.00
max. SF on $\langle a \rangle$ - Prism	0.22	0.43	0.00
max. SF on $\langle a \rangle$ - Pyramidal	0.31	0.38	0.00
max. SF on first-order $\langle c + a \rangle$ - Pyramidal	0.36	0.41	0.41
max. SF on second-order $\langle c + a \rangle$ - Pyramidal	0.28	0.34	0.45

Table 8.8: Euler-angles and the maximum Schmid factor on different slip planes for different single crystal simulations.

8.7.2 Rate Sensitive Flow Rule in CPFE Modeling of Single Crystals

To investigate the effectiveness of the rate-sensitive unified flow rule in CPFE modeling, uniaxial deformation simulation of single crystals are conducted. Three single crystal models with different orientations, illustrated in Figure 8.18, are simulated in this study. The crystal models are oriented in a manner such that slip on specific crystallographic systems are dominant for each model. The corresponding Euler angles defining each orientation, along with the maximum Schmid factor (SF) on different slip planes are reported in table 8.8.

The single crystal models are loaded under different strain-rates to comprehend the

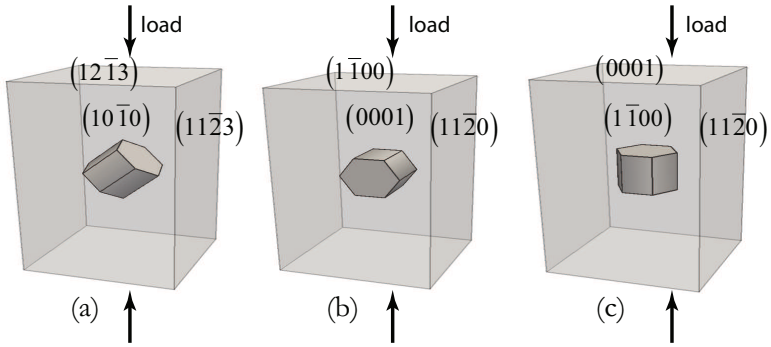

Figure 8.18: Single crystal model oriented for dominant activation of (a) $\langle a \rangle$ - basal, (b) $\langle a \rangle$ - prismatic, and (c) $\langle c + a \rangle$ - pyramidal slip systems.

underlying dislocation glide behavior across a range of strain-rates. Figure 8.19 shows the dependence of the flow stress on strain-rates ranging from 10^{-4} to $10^{+7}s^{-1}$ at 8% true strain, as predicted by the unified (UL) and phenomenological (PL) models. The resulting basal and pyramidal system flow stresses exhibit a linear dependence on the logarithm of strain-rates. Predictions by the two models are in good agreement up to strain-rates of $\sim 10^5 s^{-1}$. Beyond this, the slope predicted by the unified model is considerably higher than that by the phenomenological model. Similar trends are also observed for the prism dominated slip (not shown) and for other orientations. This change in the rate-sensitivity has also been observed for many metals e.g. in [192]. The results in Figure 8.19 suggest that the phenomenological model can be reliably used up to strain-rates of $\sim 10^5 s^{-1}$.

Figure 8.20 depicts the loading direction stress-strain response for a single crystal

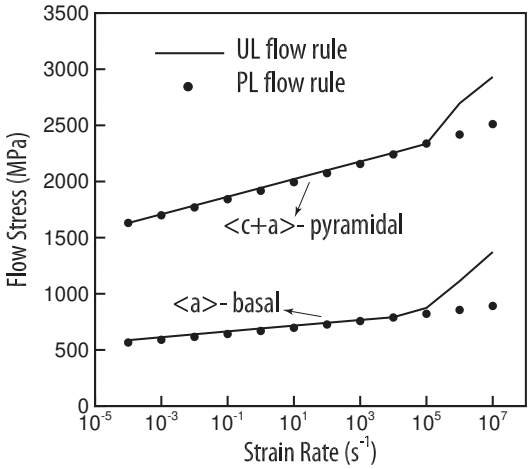

Figure 8.19: Strain-rate sensitivity of flow stress in the single crystal model at 8% strain, as predicted by the unified (UL) and phenomenological (PL) models.

model that is oriented favorably for $\langle a \rangle$ - basal slip, at a range of strain-rates. An elastic overshoot occurs in the stress response at strain-rates beyond $10^6 s^{-1}$, which becomes more pronounced as the applied strain-rate is increased. Such elastic overshoot has been reported in simulations of copper [171] and vanadium [26] at high deformation rates. The initial peak in the stress profile is explained in terms of dislocation activity on individual slip systems, which can be understood through a Schmid factor analysis given in table 8.9. It indicates that the $\left[\bar{2}110\right]$ basal slip system has the highest Schmid factor, leading to a dominant single-slip mode. Slip activities on the $\langle a \rangle$ - pyramidal and $\langle c + a \rangle$ - pyramidal systems are relatively dormant for this loading case.

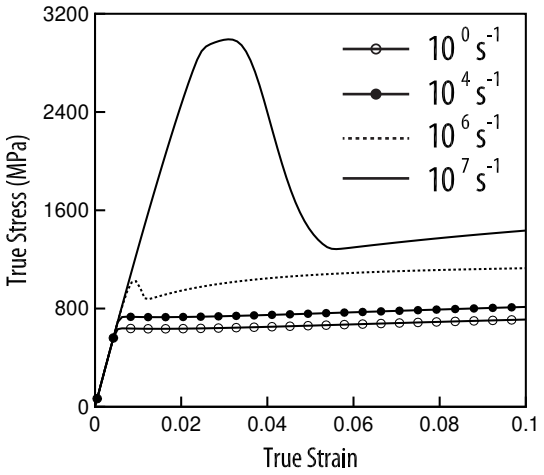

Figure 8.20: Loading direction stress-strain response at different strain-rates for a single crystal model oriented favorably for $\langle a \rangle$ - basal slip.

Slip system	Miller-Bravais index	Label	Schmid factor
basal	$(0001)\,[1\bar{2}10]$	B1	-0.25
	$(0001)\,[\bar{2}110]$	B2	0.50
	$(0001)\,[11\bar{2}0]$	B3	-0.25
prism	$(10\bar{1}0)\,[\bar{1}2\bar{1}0]$	P1	0.22
	$(01\bar{1}0)\,[\bar{2}110]$	P2	0.00
	$(\bar{1}100)\,[\bar{1}\bar{1}20]$	P3	-0.22

Table 8.9: Schmid factors for the basal and prism slip families for the single crystal model oriented favorably for $\langle a \rangle$ - basal slip.

8.7.2.1 Evolution of temperature and plastic strains in single crystals

Figure 8.21 shows the evolution of temperature, plastic shearing-rate and drag fraction on the basal and prism slip system families at a strain-rate of $10^7 s^{-1}$. All slip systems in the basal and prism families become active with deformation except for P2. Consequently, it is not included in the plots in Figure 8.21. The overall deformation may be generally partitioned into multiple stages, as enumerated in Figure 8.21. Stage I corresponds to a purely elastic regime where the resolved shear stress on all slip systems is smaller than the long-range stress, viz. the passing stress τ^{α}_{pass} that occurs by interaction of mobile dislocations with other dislocations and their networks. In stage II, dislocation slip starts to occur on B2. However, the initial dislocation density is not sufficient to sustain plastic deformation for the applied strain-rate. The material should deform elastically until a sufficient amount of dislocation density is available. This translates into an increase in the stress level and consequently provides adequate resolved shear stress to activate the other basal and prism slip systems with lower Schmid factors, as shown in Figure 8.21b. Figure 8.21d shows the transition of dislocation glide from a thermally-activated to drag-dominated mechanism in this stage. In stage III, there is collectively sufficient dislocation content to cause plastic shearing for the applied strain-rate. Thus the macroscopic stress-strain response deviates clearly from a predominantly elastic response. During this stage, drag-dominated dislocation glide persists and plastic shearing rate on active

slip systems, specifically on B2, increases. This causes the self and latent hardening to become more pronounced. Figure 8.21c shows the evolution of temperature in this stage due to the significant development of plastic and dissipative work. During stage IV, dislocation glide on B2 remains drag-dominated and sufficient dislocation density accumulates on B2 to accommodate further plastic deformation. This causes a drop in the stress level in this stage. As the stress decreases, the plastic contribution of slip systems with lower Schmid factor, viz. B1, B3, P1 and P3, progressively reduces until these slip systems become inactive at the end of this stage. In Stage V, B2 is the sole active slip system. Self hardening through the evolution of the parallel dislocation population is the main source of strain hardening, as observed in Figure 8.21a. During this step, thermally-activated processes become more significant, and the mechanism governing dislocation glide transitions from a drag-dominated mode to a mixed mode.

The high stresses induced by the elastic overshoot at very high strain-rates can be relieved in real materials by either nucleating new dislocations (in addition to dislocation multiplication) [28] or by deformation twinning [141, 142, 158]. Considering the contributions of homogeneous and heterogeneous dislocation nucleation to the evolution of dislocation population may be of benefit in the simulation of polycrystals subject to very high strain-rates and shock loading [193, 194]. The model in this paper considers dislocation slip as the major deformation mechanism, based on experimental results in [159, 160] where twinning was not reported for Ti alloys with

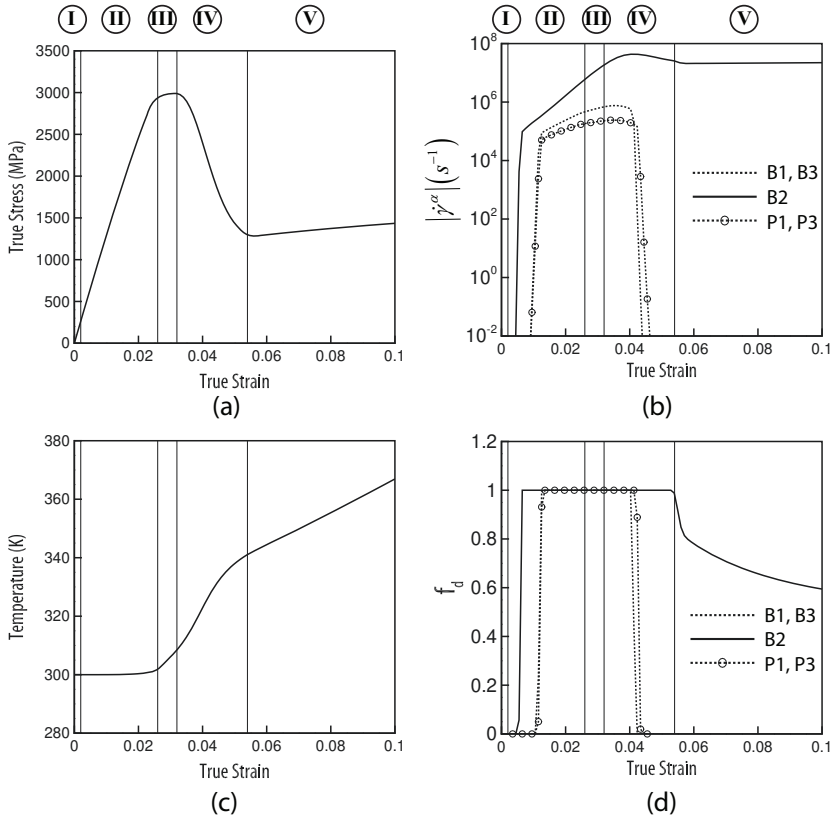

Figure 8.21: Results of single crystal CPFE simulation for $\langle a \rangle$-basal slip at strain rate of $10^7 s^{-1}$: (a) the loading direction stress-strain response, and evolution of: (b) plastic shearing rate, (c) temperature and (d) drag fraction. (the Roman numerals denote different stages of deformation).

high Al concentration.

8.7.3 Rate Sensitive Flow Rule in CPFE Modeling of Polycrystals

Experiments on polycrystalline Ti samples have shown an increasing rate sensitivity to the logarithm of strain-rate [142]. Based on the rate sensitivity study of single crystals, it is expected that the unified model will show the change in rate sensitivity of flow stress for polycrystalline microstructures. The polycrystalline Ti-7Al microstructural volume is compressed in the X direction (the ND direction) at various strain-rates. The flow stress from the CPFE analyses at 6% strain is plotted in Figure 8.22. These results are compared with some experimental results for Ti-6Al-4V in [170] and commercially-pure Ti [142]. Results with the unified model show a change in the rate sensitivity for strain-rates higher than $10^5 s^{-1}$. This is in good agreement with the experimental results of [170], where an enhanced hardening effect is observed beyond strain rates of $10^4 s^{-1}$. The phenomenological model exhibits a constant rate sensitivity across a range of strain-rates.

8.7.4 CPFE Simulations with Adiabatic Heating

This section explores the role of local adiabatic heating associated with high strain-rates on the deformation response of polycrystalline Ti-7Al alloys. The image-based

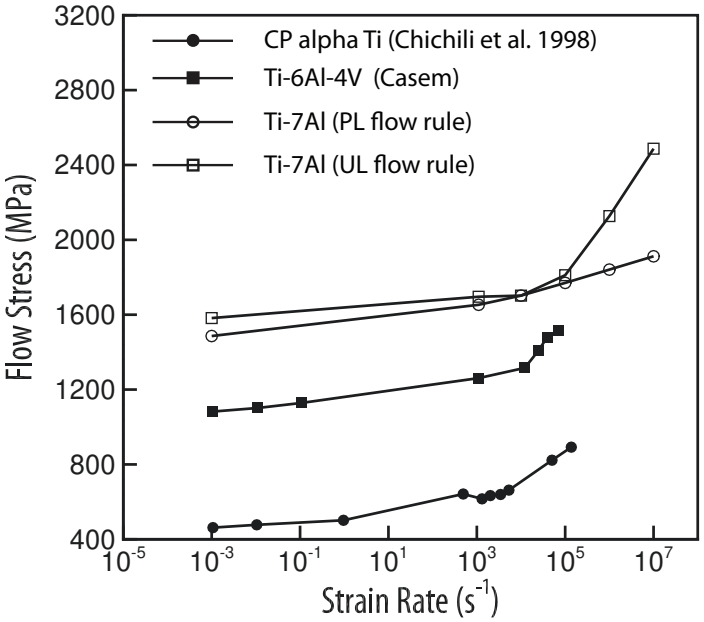

Figure 8.22: Rate sensitivity of the flow stress in polycrystalline Ti alloys at 6% strain by the unified (UL) and phenomenological (PL) flow rules.

CPFE models developed in section 8.5 are used for these simulations. The as-rolled (AR) material microstructural RVE is subjected to a compressive strain rate of $10^4 s^{-1}$ along the normal direction (ND). Different case studies are considered for these simulations.

- **Case I**: Simulation in which local adiabatic heating is turned off, i.e. simulation is under isothermal conditions.
- **Case II**: Simulation in which local adiabatic heating is accounted for, but the reduction of elastic constants with temperature is neglected.
- **Case III**: Simulation in which both local adiabatic heating and reduction of elastic constants with temperature are considered.

The macroscopic stress-strain response for the three cases are shown in Figure 8.23. Comparing the responses, it is observed that the pre-yield portion of the stress-strain response is not affected much by the adiabatic heating, since the amount of plastic work and consequently the local temperature rise is very small in this stage of deformation. The effect of adiabatic heating becomes more evident with rise in the local temperature at higher strains. A lower strain hardening is seen for case III in comparison with case I for which the temperature evolution is suppressed. Moreover, based on the macroscopic response for cases II and III in Figure 8.23, it is inferred that the effect of decrease in elastic constants with temperature becomes noticeable only at higher strains above 0.15. Thus, the consideration of elastic softening is of secondary

importance if material failure due to nucleation and evolution of microstructural defects starts at early stages of deformation. This is consistent with observations in [195], where the effect of temperature on the failure of Ti alloys were investigated.

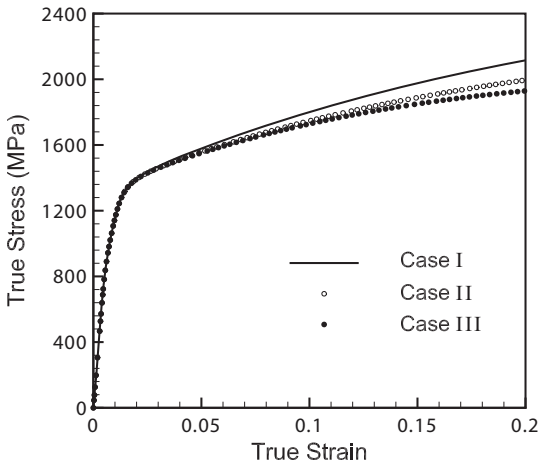

Figure 8.23: Stress-strain response in the loading (ND) direction, for an applied compressive strain-rate of $10^4 s^{-1}$ on the AR microstructural RVE.

Failure of Ti alloys at high strain-rates is attributed to formation of adiabatic shear bands (ASBs), which in turn is related to the emergence of hot spots due to adiabatic heating. The case III simulations are analyzed for local temperature evolution in each grain. A temperature increase $\Delta\overline{T}_g$ is calculated for each grain g, and its distribution over the entire microstructure at four different stages of deformation is plotted in Figure 8.24a. The average temperature increase in the grain g is evaluated as:

$$\Delta\overline{T}_g = \frac{\sum_{i=1}^{N_e^{(g)}} \Omega_i \, \Delta\overline{T}_i}{\sum_{i=1}^{N_e^{(g)}} \Omega_i} \tag{8.30}$$

where $N_e^{(g)}$ is the number of elements and Ω_i and $\Delta\overline{T}_i$ are respectively the volume and

temperature increase in the i-th element of the grain g. The $\Delta\overline{T}_g$ distribution evolution indicates that not only the average temperature in individual grains, but also its standard deviation increases with deformation. A similar trend is observed in the distribution of the effective plastic strain in each grain, shown in Figure 8.24b. The increase in heterogeneity of the plastic strain field implies that the micro-plasticity transitions from a nearly uniform state in the early stages of deformation to a non-uniform state in the later stages. This tendency of deformation towards a non-uniform distribution of the plastic strain implies the realization of severely plastically-deformed grains. Depending on the contiguity of these grains, large regions of localized deformation can be created. Figure 8.25 shows the formation of such a region over an XZ slice in the 3D microstructure. In this region, the temperature is also locally high due to significant dissipative plastic work, as observed in Figure 8.26. These regions can facilitate the nucleation of the adiabatic shear bands, initiating a failure process.

Since the adiabatic heating is a consequence of plastic deformation, it may be reasonable to assume that the distributions in Figure 8.24 are complementary. This implies that with increased plastic localization in certain grains, the temperature rises adiabatically and causes an increase in the standard deviation in those grains in Figure 8.24a. However, a close analysis of the plastic strain and temperature contours in the microstructure reveals that the regions with a high plastic strain do not necessarily correspond to hot spots of the temperature field and vice versa. For example, the effective plastic strain contour plot in Figure 8.27a shows that grain A is

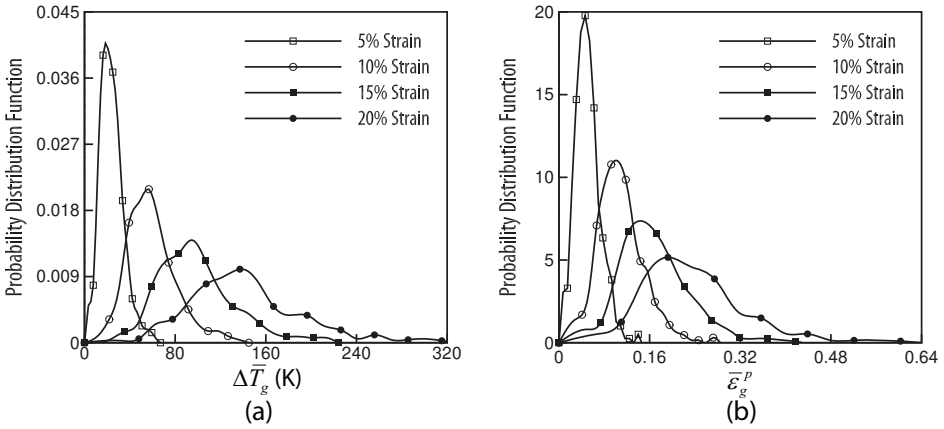

Figure 8.24: Probability distribution functions of: (a) $\Delta\overline{T}_g$ and (b) $\overline{\epsilon}_g^p$ at different stages of deformation, in CPFE simulations of the AR microstructure at strain-rate of $10^4 s^{-1}$.

highly plastically deformed. However the contour plot of temperature field in Figure 8.27b does not suggest an elevated temperature in this grain. On the other hand, grains B, C and D experience elevated thermal fields, although they are undergoing moderate plastic deformation. To comprehend this anomalous behavior, the plastic power density definition is recalled as:

$$\dot{W}_p = \boldsymbol{\sigma} : \mathbf{d}^p \tag{8.31}$$

where $\boldsymbol{\sigma}$ and $\mathbf{d}^p$ are respectively the Cauchy stress and plastic part of the rate of deformation tensor in the current configuration. $\dot{W}_p$ is dependent on the stress level and the rate of plastic deformation in the multiplicative form. Hence, a high value of plastic strain by itself does not constitute a high value of plastic work and consequently

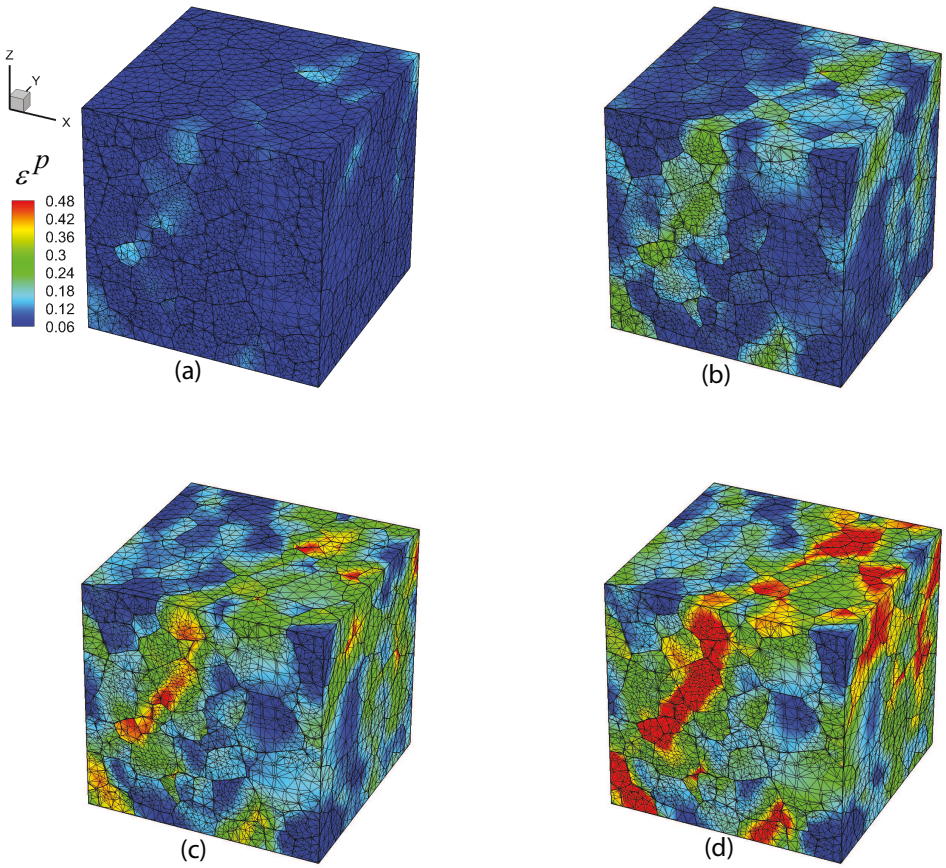

Figure 8.25: Development of regions of plastic localization in the AR microstructure under a compressive strain-rate of $10^4 s^{-1}$ along the ND direction, at: (a) 5%, (b) 10%, (c) 15% and (d) 20% strain. (The contours are shown in the undeformed configuration).

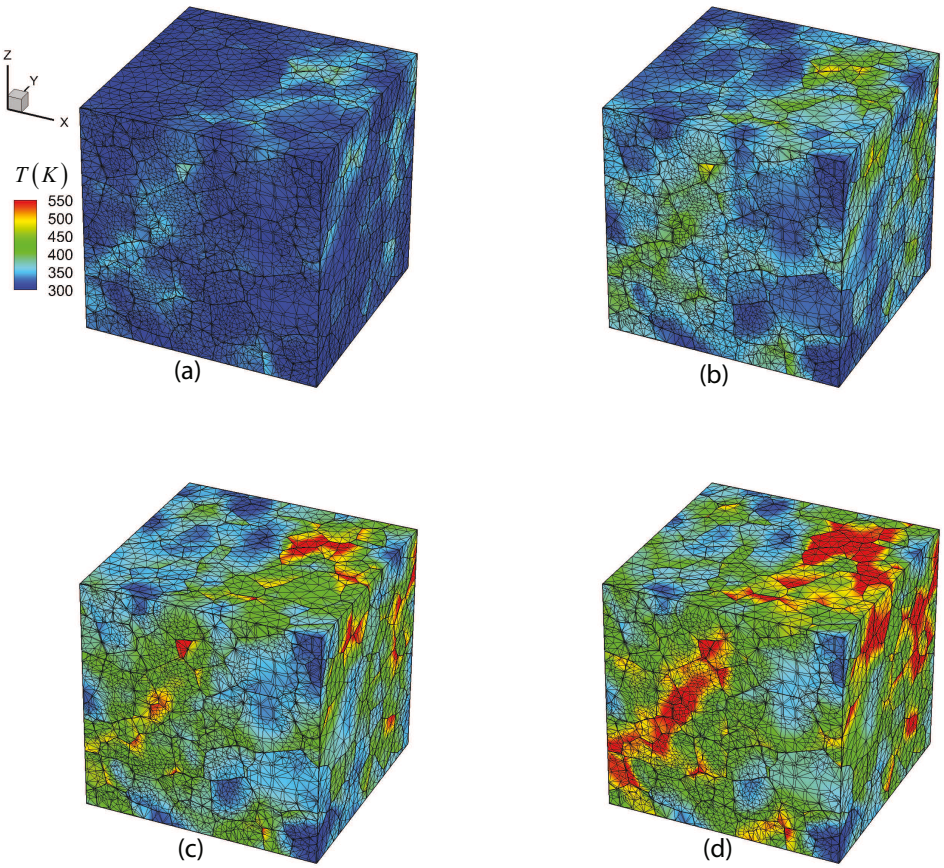

Figure 8.26: Evolution of temperature in the AR microstructure under a compressive strain-rate of $10^4 s^{-1}$ along the ND direction, at: (a) 5%, (b) 10%, (c) 15% and (d) 20% strain. (The contours are shown in the undeformed configuration)

adiabatic heating. Temperature may increase more at a material point with high level of stress but low plastic strain, compared to another material point with higher plastic strain and lower stress. Hence the temperature trends in grains A, B, C and D are more congruent with the contour plot of the von Mises stress, as a measure of stress tensor, as shown in Figure 8.27c.

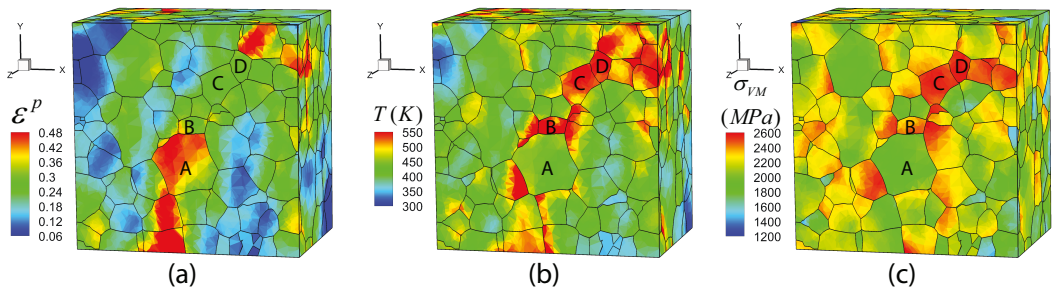

Figure 8.27: Contour plots of: (a) effective plastic strain, (b) temperature and (c) von Mises stress at 20% strain, from CPFE simulations of the AR microstructure under a compressive strain-rate of $10^4 s^{-1}$ along the ND direction.

To study this further, a bi-crystal model consisting of a *hard* and *soft* grain is generated as shown in Figure 8.28a. The orientation induces a much higher level of plastic strain in the soft grain. Figure 8.28b plots the macroscopic stress-strain response in the direction of loading, for this bi-crystal model with an applied compressive strain-rate of $10^4 s^{-1}$ in the [001] direction. Three stages of deformation are selected as indicated in Figure 8.28b. The evolution of relevant micro-mechanical variables are investigated at these stages along a line in the X-direction that passes

through the centroid of the model. At stage I, the plastic flow has already started in the soft grain, whereas the hard grain has barely deformed plastically. As shown in Figure 8.29a, the temperature in the soft grain is slightly higher than that in the hard grain. In the subsequent stages of deformation, the temperature in the hard grain increases significantly in comparison with the soft grain. Here again the rate of adiabatic heating is governed by the stress state. The temperature difference between the two grains grows larger with deformation as shown in figures 8.29b and 8.29c.

The results of the bi-crystal problem in Figure 8.29 also provides some insight on the formation of adiabatic shear bands or ASBs at high strain-rates. Different criteria have been proposed for estimating the formation of adiabatic shear bands, based on thermo-mechanical variables, such as plastic shear strain in [196], temperature in [197] or stored energy of cold work in [195, 198]. The model developed in this paper with reference to Figure 8.29 has the ability to comprehend the source of nucleation of such ASBs that will be studied more in future work.

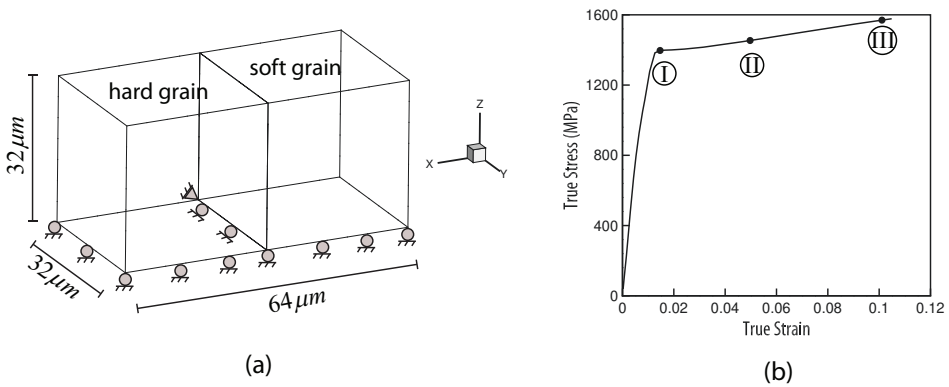

Figure 8.28: (a) A bi-crystal model discretized into 5103 linear tetrahedral elements, and (b) macroscopic stress-strain response in the loading direction, for applied compressive strain-rate of $10^4 s^{-1}$ along the [001] direction.

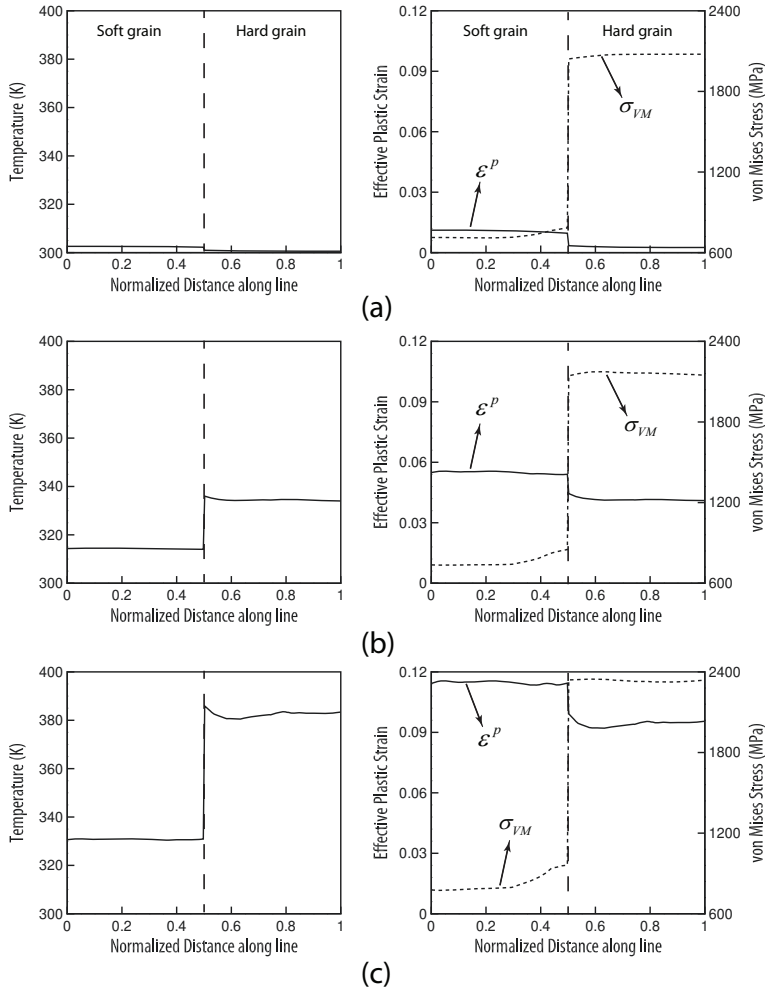

Figure 8.29: Profiles of temperature, effective plastic strain and von Mises stress along a line at (a) 1.5% strain (stage I), (b) 5% strain (stage II) and (c) 10% strain (stage III).

Chapter 9

Conclusions and future work

This work focused on different aspects of crystal plasticity framework. Regarding modeling fracture, a thermodynamically-consistent coupled crystal plasticity-crack phase field was developed. For modeling deformation, multiple improvements to the computational and constitutive aspects of the theory was proposed. In the following, a summary of these efforts is given.

9.1 Coupled CP-PF framework

Using principles of thermodynamics and virtual power, the coupled differential equations governing the displacement and crack phase field were derived. These equations are two-way coupled via the Helmholtz free energy density. Recognizing that the available models in the literature are not applicable to anisotropic materials

under finite strain conditions, a novel Helmholtz free energy density (HFED) was proposed in this work in terms of a *degraded elastic Green-Lagrange strain*. This degraded elastic strain tensor was obtained via volumetric-deviatoric decomposition of the elastic deformation gradient. This definition of HFED requires that the deviatoric part of elastic strain is degraded with order parameter whereas the volumetric part is degraded only if the volume change is tensile. Therefore, this definition of HFED respects the unilateral condition of damage.

Finite element solvers often suffer from convergence issues in modeling degradable materials. The traditional arc-length methods are not applicable due to the rate-dependency of the CP constitutive models. In order to overcome the instabilities and convergence issues, three viscous stabilization techniques were proposed. They include global viscous stabilizations of the displacement and crack phase fields by introducing artificial viscous forces in the governing differential equations. Also local viscous stabilization of the displacement field is proposed where an artificial viscous stress term in added to the conventional stress tensor.

9.2 volumetric locking

An F-bar-patch element formulation was proposed in the context of crystal plasticity framework to overcome volumetric locking associated with application of linear tetrahedral elements in modeling (nearly-) incompressible materials. It was shown

that this element formulation can effectively alleviate volumetric locking by reducing the number of incompressibility constraints.

For fracture simulations, some modifications to the F-bar-patch element formulation was proposed to seamlessly remove fully degraded elements from the element patches on the fly. The tangent stiffness matrix and residual vector corresponding to this modified F-bar-patch formulation were derived by linearizing the weak form.

9.3 unified CP laws

Motivated by the fact that the local strain rate experienced by different material points in polycrystalline microstructures could be orders of magnitude different from the applied macroscopic strain rate, a unified flow rule was developed in the context of dislocation density-based CP framework. Unlike most of the flow rule formulations in the literature, the unified flow rule is applicable over a wide range of strain rates and can seamlessly model transition of dislocation glide from thermally-activated regime to the drag-dominated one as strain rate increases.

It was shown that this formulation can predict the experimentally-observed change in rate sensitivity of flow stress. Moreover, it was observed that surprisingly the thermal hot spots do not necessarily correspond to the material points undergoing significant plastic strain. Indeed hard grains, which do not deform plastically as much, may experience higher adiabatic temperatures. This observation was linked to the

multiplicative dependence of plastic work on the stress and plastic deformation rate.

9.4 future work

As pointed out in Section 5.1, sharpness of the phase field representation of crack is controlled by parameter l_c. Choosing small l_c will result in more realistic order parameter distribution which mimics the sharp crack, as shown in Figure 9.1. Ideally one would like to use a small l_c to obtain realistic crack profiles; however, it should be noted that the finite element mesh is required to be fine enough to resolve this length scale. This requirement incurs significant computational costs in 3D fracture simulations and problems where the crack path is not known *a priori*. In these cases, the modelers have to discretize the entire computational domain with a fine mesh which makes fracture simulations computationally cumbersome. Developing computational tools which can detect/predict the fracture path on the fly and enrich the solution space only in the regions of interest would be significantly helpful. This enrichment could be done by either simply refining the mesh or improving the interpolation functions (e.g. higher-order or hierarchical shape functions).

Most of the degradation forms used in the literature are of the linear $(1-s)$ or quadratic $(1-s)^2$ forms. Recently there has been some work on alternative degradation functions, for example higher-order functions [68], plasticity-dependent power laws [131, 199] and exponential forms [200]. This is still an open question. More

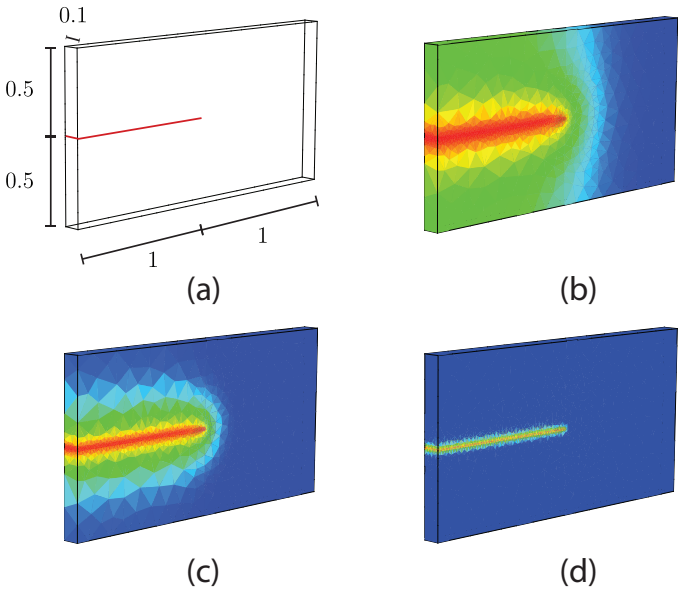

Figure 9.1: phase field representation of a sharp crack using different l_c (a) sharp crack geometry shown with red line, (b) $l_c = 4 \times 10^{-1}$, (c) $l_c = 2 \times 10^{-1}$ and (d) $l_c = 2 \times 10^{-2}$. (all units are in micrometer)

detailed fracture experiments and some insight from molecular dynamics simulations may help modelers choose the most appropriate form of the degradation function. Moreover, detailed experimental observations are needed to calibrate and validate fracture models in polycrystalline microstructures.

In this work, a crack phase field model was developed for materials with anisotropic material response. Yet there is another anisotropy which was not addressed in this work and needs to be developed. Cracks in crystalline materials tend to propagate on some favorable planes and directions. In order to represent this fact numerically, one needs to develop anisotropic fracture energy density formulations. Such an anisotropic fracture energy density would promote phase field evolution in favorable directions while penalizing propagation of fracture in other directions by requiring higher energy levels. This is an active area of research and more experiments may help one formulate such an anisotropic fracture energy.

Bibliography

[1] P. Shade, "Unpublished work," Air Force Research Laboratory, Wright-Patterson AFB, Dayton OH, 2015.

[2] H. Ogi, S. Kai, H. Ledbetter, R. Tarumi, M. Hirao, and K. Takashima, "Titanium's high-temperature elastic constants through the hcp–bcc phase transformation," *Acta Mater.*, vol. 52, no. 7, pp. 2075–2080, 2004.

[3] B. Winkler, "Traglastuntersuchungen von unbewehrten und bewehrten betonstrukturen auf der grundlage eines objektiven werkstoffgesetzes für beton," Ph.D. dissertation, Innsbruck University Press, 2001.

[4] A. Mesgarnejad, B. Bourdin, and M. Khonsari, "Validation simulations for the variational approach to fracture," *Computer Methods in Applied Mechanics and Engineering*, vol. 290, pp. 420 – 437, 2015.

[5] M. Ambati, T. Gerasimov, and L. De Lorenzis, "A review on phase-field models of brittle fracture and a new fast hybrid formulation," *Computational Mechanics*, vol. 55, no. 2, pp. 383–405, 2015.

BIBLIOGRAPHY

[6] D. Peirce, R. Asaro, and A. Needleman, "An analysis of nonuniform and localized deformation in ductile single crystals," *Acta Metal.*, vol. 30, no. 6, pp. 1087 – 1119, 1982.

[7] R. Asaro and J. Rice, "Strain localization in ductile single crystals," *Journal of the Mechanics and Physics of Solids*, vol. 25, no. 5, pp. 309 – 338, 1977.

[8] J. Thomas, M. Groeber, and S. Ghosh, "Image-based crystal plasticity FE framework for microstructure dependent properties of Ti–6Al–4V alloys," *Mater. Sci. Eng. A*, vol. 553, no. 15, pp. 164–175, 2012.

[9] M. Groeber, S. Ghosh, M. Uchic, and D. Dimiduk, "A framework for automated analysis and representation of 3d polycrystalline microstructures, part 1: Statistical characterization," *Acta Mater.*, vol. 56, pp. 1257–1273, 2008.

[10] M. Groeber and M. Jackson, "DREAM.3D: A digital representation environment for the analysis of microstructure in 3D," *Integr. Mater. Manuf. Innov.*, vol. 3, no. 5, pp. 1–17, 2014.

[11] M. Groeber, S. Ghosh, M. Uchic, and D. Dimiduk, "A framework for automated analysis and simulation of 3D polycrystalline microstructures: Part 1: statistical characterization," *Acta Mater.*, vol. 56, no. 6, pp. 1257–1273, 2008.

[12] Simulation Modeling Suite, "Simmetrix Inc." http://www.simmetrix.com, 2015.

[13] J. Cheng, J. Shen, R. K. Mishra, and S. Ghosh, "Discrete twin evolution in mg alloys using a novel crystal plasticity finite element model," *Acta Materialia*, vol. 149, pp. 142 – 153, 2018.

[14] M. Knezevic, A. Levinson, R. Harris, R. K. Mishra, R. D. Doherty, and S. R. Kalidindi, "Deformation twinning in az31: Influence on strain hardening and texture evolution," *Acta Materialia*, vol. 58, no. 19, pp. 6230 – 6242, 2010.

[15] H. Abdolvand and M. R. Daymond, "Multi-scale modeling and experimental study of twin inception and propagation in hexagonal close-packed materials using a crystal plasticity finite element approach; part ii: Local behavior," *Journal of the Mechanics and Physics of Solids*, vol. 61, no. 3, pp. 803 – 818, 2013.

[16] J. Zhang and S. P. Joshi, "Phenomenological crystal plasticity modeling and detailed micromechanical investigations of pure magnesium," *Journal of the Mechanics and Physics of Solids*, vol. 60, no. 5, pp. 945 – 972, 2012.

[17] M. Knezevic, H. F. Al-Harbi, and S. R. Kalidindi, "Crystal plasticity simulations using discrete fourier transforms," *Acta Materialia*, vol. 57, no. 6, pp. 1777 – 1784, 2009.

[18] J. Michel, H. Moulinec, and P. Suquet, "Effective properties of composite materials with periodic microstructure: a computational approach," *Computer*

Methods in Applied Mechanics and Engineering, vol. 172, no. 1, pp. 109 – 143, 1999.

[19] R. Lebensohn, A. Kanjarla, and P. Eisenlohr, "An elasto-viscoplastic formulation based on fast fourier transforms for the prediction of micromechanical fields in polycrystalline materials," *Int. J. Plast.*, vol. 32–33, pp. 59 – 69, 2012.

[20] Y. Azdoud, J. Cheng, and S. Ghosh, "Wavelet-enriched adaptive crystal plasticity finite element model for polycrystalline microstructures," *Computer Methods in Applied Mechanics and Engineering*, vol. 327, pp. 36 – 57, 2017.

[21] Y. Azdoud and S. Ghosh, "Adaptive wavelet-enriched hierarchical finite element model for polycrystalline microstructures," *Computer Methods in Applied Mechanics and Engineering*, vol. 321, pp. 337 – 360, 2017.

[22] H. J. Frost and M. F. Ashby, "Motion of a dislocation acted on by a viscous drag through an array of discrete obstacles," *J. Appl. Physics*, vol. 42, no. 13, pp. 5273–5279, 1971.

[23] R. D. Isaac and A. V. Granato, "Rate theory of dislocation motion: Thermal activation and inertial effects," *Phys. Rev. B*, vol. 37, pp. 9278–9285, 1988.

[24] M. Hiratani and E. Nadgorny, "Combined model of dislocation motion with thermally activated and drag-dependent stages," *Acta Mater.*, vol. 49, no. 20, pp. 4337 – 4346, 2001.

[25] M. Hiratani, H. Zbib, and M. Khaleel, "Modeling of thermally activated dislocation glide and plastic flow through local obstacles," *Int. J. Plasticity*, vol. 19, no. 9, pp. 1271 – 1296, 2003.

[26] N. Barton, J. Bernier, R. Becker, A. Arsenlis, R. Cavallo, J. Marian, M. Rhee, H. Park, B. Remington, and R. Olson, "A multiscale strength model for extreme loading conditions," *J. Appl. Physics*, vol. 109, no. 7, 2011.

[27] R. Becker, A. Arsenlis, J. Marian, M. Rhee, M. Tang, and L. Yang, "Continuum level formulation and implementation of a multi-scale model for vanadium," Lawrence Livermore National Laboratory, Tech. Rep., 2009.

[28] R. Austin and D. McDowell, "A dislocation-based constitutive model for viscoplastic deformation of fcc metals at very high strain rates," *Int. J. Plasticity*, vol. 27, no. 1, pp. 1 – 24, 2011.

[29] J. Lloyd, J. Clayton, R. Austin, and D. McDowell, "Plane wave simulation of elastic-viscoplastic single crystals," *J. Mech. Physics Solids*, vol. 69, pp. 14 – 32, 2014.

[30] D. Cereceda, M. Diehl, F. Roters, D. Raabe, J. M. Perlado, and J. Marian, "Unraveling the temperature dependence of the yield strength in single-crystal tungsten using atomistically-informed crystal plasticity calculations," *International Journal of Plasticity*, vol. 78, pp. 242 – 265, 2016.

[31] K. Matouš and A. Maniatty, "Finite element formulation for modelling large deformations in elasto-viscoplastic polycrystals," *Int. J. Numer. Meth. Eng.*, vol. 60, pp. 2313 – 2333, 2004.

[32] C. Dohrmann, M. Heinstein, J. Jung, S. Key, and W. Witkowski, "Node-based uniform strain elements for three-node triangular and four-node tetrahedral meshes," *Int. J. Numer. Meth. Eng.*, vol. 47, pp. 1549 – 1568, 2000.

[33] M. Gee, C. Dohrmann, S. Key, and W. Wall, "A uniform nodal strain tetrahedron with isochoric stabilization," *Int. J. Numer. Meth. Eng.*, vol. 78, pp. 429 – 443, 2009.

[34] E. de Souza Neto, F. Andrade Pires, and D. Owen, "F-bar-based linear triangles and tetrahedra for finite strain analysis of nearly incompressible solids. part i: formulation and benchmarking," *Int. J. Numer. Meth. Eng.*, vol. 62, pp. 353 – 383, 2005.

[35] E. de Souza Neto, D. Peric, and D. Owen, *Computational methods for plasticity: theory and applications.* John Wiley and Sons Ltd., 2008.

[36] J. Bonet, H. Marriott, and O. Hassan, "Stability and comparison of different linear tetrahedral formulations for nearly incompressible explicit dynamic applications," *Int. J. Numer. Meth. Eng.*, vol. 50, pp. 119 – 133, 2001.

[37] M. A. Puso and J. Solberg, "A stabilized nodally integrated tetrahedral," *Int. J. Numer. Meth. Eng.*, vol. 67, pp. 841 – 867, 2006.

[38] G. Laschet, I. Caylak, S. Benke, and R. Mahnken, "Locally integrated node-based formulations for four-node tetrahedral meshes," *Private communication*.

[39] G. Liu, T. Nguyen-Thoi, H. Nguyen-Xuan, and K. Lam, "A node-based smoothed finite element method (ns-fem) for upper bound solutions to solid mechanics problems," *Comput. struc.*, vol. 87, pp. 14–26, 2009.

[40] H. Nguyen-Xuan and G. Liu, "An edge-based smoothed finite element method softened with a bubble function (bes-fem) for solid mechanics." *Comput. struc.*, vol. 128, pp. 14–30, 2013.

[41] G. Liu, T. Nguyen-Thoi, and L. K.Y., "An edge-based smoothed finite element method (es-fem) for static, free and forced vibration analyses of solids." *J Sound Vib*, vol. 320, pp. 1100–1130, 2009.

[42] T. Nguyen-Thoi, G. Liu, L. K.Y., and Z. G.Y., "A face-based smoothed finite element method (fs-fem) for 3d linear and non-linear solid mechanics problems using 4-node tetrahedral elements," *Int. J. Numer. Meth. Eng.*, vol. 78, pp. 324–353, 2009.

[43] E. de Souza Neto, D. Peric, M. Dutko, and D. Owen, "Design of simple low

order finite elements for large strain analysis of nearly incompressible solids," *Int. J. Solids Struct.*, vol. 33, pp. 3277 – 3296, 1996.

[44] W. S. and B. C., "A finite element method based on c0 continuous assumed gradients," *Int. J. Numer. Meth. Eng.*, vol. 86, pp. 876–914, 2011.

[45] R. Mahnken and I. Caylak, "Stabilization of bi-mixed finite elements for tetrahedral with enhanced interpolation using volume and area bubble functions," *Int. J. Numer. Meth. Eng.*, vol. 75, pp. 377–413, 2008.

[46] R. Mahnken, I. Caylak, and G. Laschet, "Two mixed finite element formulations with area bubble functions for tetrahedral elements," *Comput. Meth. in Appl. Mech. And Eng.*, vol. 197, pp. 1147–1165, 2008.

[47] J. Rice, "A path independent integral and the approximate analysis of strain concentration by notches and cracks," *Journal of Applied Mechanics*, vol. 35, no. 2, pp. 379–386, 1968.

[48] M. Yoda, "The j-integral fracture toughness for mode ii," *International Journal of Fracture*, vol. 16, no. 4, pp. 175–178, 1980.

[49] B. E. Amstutz, M. A. Sutton, and D. S. Dawicke, "An experimental study of ctod for mode i/mode ii stable crack growth in thin aluminium specimens," *ASTM Special*, vol. 26, pp. 256–271, 1995.

[50] J. N. Jr and M. James, "A review of the ctoa/ctod fracture criterion – why it

works!" ser. 42nd AIAA/ASME/ASCE/AH/ASC Structures, Structural Dynamics, and Materials Conference and Exhibit, 2001.

[51] N. Moes, J. Dolbow, and T. Belytschko, "A finite element method for crack growth without remeshing," *International Journal for Numerical Methods in Engineering*, vol. 46, pp. 131–150, 1999.

[52] M. Ortiz and A. Pandolfi, "Finite-deformation irreversible cohesive elements for three-dimensional crack-propagation analysis," *International Journal for Numerical Methods in Engineering*, vol. 44, no. 9, pp. 1267–1282, 1999.

[53] K. Park and G. H. Paulino, "Cohesive Zone Models: A Critical Review of Traction-Separation Relationships Across Fracture Surfaces," *Applied Mechanics Reviews*, vol. 64, no. 6, p. 061002, 2011.

[54] S. Ghosh, Y. Ling, B. Majumdar, and R. Kim, "Interfacial debonding analysis in multiple fiber reinforced composites," *Mechanics of Materials*, vol. 32, no. 10, pp. 561 – 591, 2000.

[55] V. Tvergaard and A. Needleman, "Analysis of the cup-cone fracture in a round tensile bar," *Acta Metallurgica*, vol. 32, no. 1, pp. 157 – 169, 1984.

[56] C. C. Chu and A. Needleman, "Void nucleation effects in biaxially stretched sheets," *Journal of Engineering Materials and Technology*, vol. 102, pp. 249–256, 1980.

BIBLIOGRAPHY

[57] H. Lippmann and J. Lemaitre, *A Course on Damage Mechanics*. Springer Berlin Heidelberg, 1996.

[58] G. Voyiadjis, *Advances in Damage Mechanics: Metals and Metal Matrix Composites*. Elsevier Science, 2012.

[59] J. R. Jain and S. Ghosh, "Damage evolution in composites with a homogenization-based continuum damage mechanics model," *International Journal of Damage Mechanics*, vol. 18, no. 6, pp. 533–568, 2009.

[60] Z. Bazant and G. Pijaudier-Cabot, "Nonlocal Continuum Damage, Localization Instability and Convergence," *Journal of Applied Mechanics*, vol. 55, p. 287, 1988.

[61] G. Z. Voyiadjis, R. K. A. Al-Rub, and A. N. Palazotto, "Thermodynamic framework for coupling of non-local viscoplasticity and non-local anisotropic viscodamage for dynamic localization problems using gradient theory," *International Journal of Plasticity*, vol. 20, no. 6, pp. 981 – 1038, 2004.

[62] Z. Li, S. Ghosh, N. Getinet, and D. J. O'Brien, "Micromechanical modeling and characterization of damage evolution in glass fiber epoxy matrix composites," *Mechanics of Materials*, vol. 99, pp. 37 – 52, 2016.

[63] H. Amor, J.-J. Marigo, and C. Maurini, "Regularized formulation of the varia-

tional brittle fracture with unilateral contact: Numerical experiments," *Journal of the Mechanics and Physics of Solids*, vol. 57, no. 8, pp. 1209 – 1229, 2009.

[64] B. Bourdin, G. Francfort, and J.-J. Marigo, "Numerical experiments in revisited brittle fracture," *Journal of the Mechanics and Physics of Solids*, vol. 48, no. 4, pp. 797 – 826, 2000.

[65] C. Miehe, F. Welschinger, and M. Hofacker, "Thermodynamically consistent phase-field models of fracture: Variational principles and multi-field fe implementations," *International Journal for Numerical Methods in Engineering*, vol. 83, no. 10, pp. 1273–1311, 2010.

[66] C. Miehe, M. Hofacker, and F. Welschinger, "A phase field model for rate-independent crack propagation: Robust algorithmic implementation based on operator splits," *Computer Methods in Applied Mechanics and Engineering*, vol. 199, no. 45, pp. 2765 – 2778, 2010.

[67] C. Miehe, L.-M. Schänzel, and H. Ulmer, "Phase field modeling of fracture in multi-physics problems. part i. balance of crack surface and failure criteria for brittle crack propagation in thermo-elastic solids," *Computer Methods in Applied Mechanics and Engineering*, vol. 294, pp. 449 – 485, 2015.

[68] M. J. Borden, T. J. Hughes, C. M. Landis, A. Anvari, and I. J. Lee, "A phase-field formulation for fracture in ductile materials: Finite deformation balance

law derivation, plastic degradation, and stress triaxiality effects," *Computer Methods in Applied Mechanics and Engineering*, vol. 312, pp. 130 – 166, 2016.

[69] L. D. Lorenzis, A. McBride, and B. Reddy, "Phase-field modelling of fracture in single crystal plasticity," *GAMM-Mitteilungen*, vol. 39, no. 1, pp. 7–34, 2016.

[70] C. Miehe, M. Hofacker, L.-M. Schänzel, and F. Aldakheel, "Phase field modeling of fracture in multi-physics problems. part ii. coupled brittle-to-ductile failure criteria and crack propagation in thermo-elastic–plastic solids," *Computer Methods in Applied Mechanics and Engineering*, vol. 294, pp. 486 – 522, 2015.

[71] P. Shanthraj, L. Sharma, B. Svendsen, F. Roters, and D. Raabe, "A phase field model for damage in elasto-viscoplastic materials," *Computer Methods in Applied Mechanics and Engineering*, vol. 312, pp. 167 – 185, 2016.

[72] P. Shanthraj, B. Svendsen, L. Sharma, F. Roters, and D. Raabe, "Elasto-viscoplastic phase field modelling of anisotropic cleavage fracture," *Journal of the Mechanics and Physics of Solids*, vol. 99, pp. 19 – 34, 2017.

[73] M. Klinsmann, D. Rosato, M. Kamlah, and R. M. McMeeking, "An assessment of the phase field formulation for crack growth," *Computer Methods in Applied Mechanics and Engineering*, vol. 294, pp. 313 – 330, 2015.

[74] G. Liu, Q. Li, M. A. Msekh, and Z. Zuo, "Abaqus implementation of monolithic

and staggered schemes for quasi-static and dynamic fracture phase-field model," *Computational Materials Science*, vol. 121, pp. 35 – 47, 2016.

[75] M. J. Borden, C. V. Verhoosel, M. A. Scott, T. J. Hughes, and C. M. Landis, "A phase-field description of dynamic brittle fracture," *Computer Methods in Applied Mechanics and Engineering*, vol. 217-220, pp. 77 – 95, 2012.

[76] E. G. Kakouris and S. P. Triantafyllou, "Phase-field material point method for brittle fracture," *International Journal for Numerical Methods in Engineering*, vol. 112, no. 12, pp. 1750–1776, 2017.

[77] ——, "Material point method for crack propagation in anisotropic media: a phase field approach," *Archive of Applied Mechanics*, vol. 88, no. 1, pp. 287–316, 2018.

[78] V. Ziaei-Rad and Y. Shen, "Massive parallelization of the phase field formulation for crack propagation with time adaptivity," *Computer Methods in Applied Mechanics and Engineering*, vol. 312, pp. 224 – 253, 2016.

[79] E. Riks, "An incremental approach to the solution of snapping and buckling problems," *International Journal of Solids and Structures*, vol. 15, no. 7, pp. 529 – 551, 1979.

[80] M. Crisfield, "A fast incremental/iterative solution procedure that handles snap-through," *Computers and Structures*, vol. 13, no. 1, pp. 55 – 62, 1981.

BIBLIOGRAPHY

[81] I. May and Y. Duan, "A local arc-length procedure for strain softening," *Computers and Structures*, vol. 64, no. 1, pp. 297 – 303, 1997.

[82] N. Singh, C. Verhoosel, R. de Borst, and E. van Brummelen, "A fracture-controlled path-following technique for phase-field modeling of brittle fracture," *Finite Elements in Analysis and Design*, vol. 113, pp. 14 – 29, 2016.

[83] S. May, J. Vignollet, and R. de Borst, "A new arc-length control method based on the rates of the internal and the dissipated energy," *Engineering Computations*, vol. 33, no. 1, pp. 100–115, 2016.

[84] A. Mouritz and A. Gibson, *Fire Properties of Polymer Composite Materials*, ser. Solid Mechanics and Its Applications. Springer Netherlands, 2007.

[85] D. Systemes, *ABAQUS/Standard User's Manual, Version 6.9*, Providence, RI, 2009. [Online]. Available: www.simulia.com

[86] J. Clayton, "Dynamic plasticity and fracture in high density polycrystals: constitutive modeling and numerical simulation," *J. Mech. Phys. Solids*, vol. 53, p. 261–301, 2005.

[87] A. Ma, F. Roters, and D. Raabe, "A dislocation density based constitutive model for crystal plasticity FEM including geometrically necessary dislocations," *Acta Mater.*, vol. 54, no. 8, pp. 2169 – 2179, 2006.

[88] U. Kocks, A. Argon, and M. Ashby, "Thermodynamics and kinetics of slip," *Prog. Mater. Sci.*, vol. 19, 1975.

[89] F. Meissonnier, E. Busso, and N. O'Dowd, "Finite element implementation of a generalised non-local rate-dependent crystallographic formulation for finite strains," *Int. J. Plasticity*, vol. 17, pp. 601 – 640, 2001.

[90] M. Kothari and L. Anand, "Elasto-viscoplastic constitutive equations for polycrystalline metals: Application to tantalum," *Journal of the Mechanics and Physics of Solids*, vol. 46, no. 1, pp. 51 – 83, 1998.

[91] D. Hull and D. Bacon, *Introduction to Dislocations*. Oxford: Butterworth-Heinemann, 2011.

[92] A. Arsenlis and D. M. Parks, "Crystallographic aspects of geometrically-necessary and statistically-stored dislocation density," *Acta Mater.*, vol. 47, pp. 1597–1611, 1998.

[93] S. Keshavarz and S. Ghosh, "Multi-scale crystal plasticity finite element model approach to modeling nickel-based superalloys," *Acta Mater.*, vol. 61, no. 17, pp. 6549 – 6561, 2013.

[94] S. Nemat-Nasser, W. Guo, and J. Cheng, "Mechanical properties and deformation mechanisms of a commercially pure titanium," *Acta Mater.*, vol. 47, no. 13, pp. 3705 – 3720, 1999.

BIBLIOGRAPHY

[95] G. Venkataramani, S. Ghosh, and M. J. Mills, "A size dependent crystal plasticity finite element model for creep and load-shedding in polycrystalline Titanium alloys," *Acta Mater.*, vol. 55, pp. 3971–3986, 2007.

[96] J. Cheng and S. Ghosh, "A crystal plasticity FE model for deformation with twin nucleation in magnesium alloys," *Int. J. Plasticity*, vol. 67, pp. 148 – 170, 2015.

[97] V. Bennett and D. McDowell, "Polycrystal orientation distribution effects on microslip in high cycle fatigue," *International Journal of Fatigue*, vol. 25, no. 1, pp. 27 – 39, 2003.

[98] D. Ozturk, A. Shahba, and S. Ghosh, "Crystal plasticity fe study of the effect of thermo-mechanical loading on fatigue crack nucleation in titanium alloys," *Fatigue & Fracture of Engineering Materials & Structures*, vol. 39, no. 6, pp. 752–769, 2016.

[99] C. Banfi, A. Marzocchi, and A. Musesti, "On the principle of virtual powers in continuum mechanics," *Ricerche di Matematica*, vol. 55, no. 2, pp. 139–150, 2006.

[100] M. E. Gurtin, "Generalized ginzburg-landau and cahn-hilliard equations based on a microforce balance," *Physica D: Nonlinear Phenomena*, vol. 92, no. 3, pp. 178 – 192, 1996.

[101] G. Holzapfel, *Nonlinear Solid Mechanics: A Continuum Approach for Engineering*. Wiley, 2000.

[102] F. Patrick and M. Corrado, "Linear and nonlinear solvers for variational phase-field models of brittle fracture," *International Journal for Numerical Methods in Engineering*, vol. 109, no. 5, pp. 648–667, 2016.

[103] Y. Gu, J. Jung, Q. Yang, and W. Chen, "An inertia-based stabilizing method for quasi-static simulation of unstable crack initiation and propagation," *Journal of Applied Mechanics, Transactions ASME*, vol. 82, no. 10, 2015.

[104] Y. F. Gao and A. F. Bower, "A simple technique for avoiding convergence problems in finite element simulations of crack nucleation and growth on cohesive interfaces," *Modelling and Simulation in Materials Science and Engineering*, vol. 12, no. 3, p. 453, 2004.

[105] W. Liu, D. Schesser, Q. Yang, and D. Ling, "A consistency-check based algorithm for element condensation in augmented finite element methods for fracture analysis," *Engineering Fracture Mechanics*, vol. 139, pp. 78 – 97, 2015.

[106] I. Simonovski and L. Cizelj, "Cohesive zone modeling of intergranular cracking in polycrystalline aggregates," *Nuclear Engineering and Design*, vol. 283, pp. 139 – 147, 2015.

[107] S. Reese and S. Govindjee, "A theory of finite viscoelasticity and numerical

aspects," *International Journal of Solids and Structures*, vol. 35, no. 26, pp. 3455 – 3482, 1998.

[108] T. Gerasimov and L. D. Lorenzis, "A line search assisted monolithic approach for phase-field computing of brittle fracture," *Computer Methods in Applied Mechanics and Engineering*, vol. 312, pp. 276 – 303, 2016.

[109] K. J. Bathe and A. P. Cimento, "Some practical procedures for the solution of nonlinear finite element equations," *Computer Methods in Applied Mechanics and Engineering*, vol. 22, no. 1, pp. 59 – 85, 1980.

[110] S. Ghosh, A. Shahba, X. Tu, E. L. Huskins, and B. E. Schuster, "Crystal plasticity fe modeling of ti alloys for a range of strain-rates. part ii: Image-based model with experimental validation," *International Journal of Plasticity*, vol. 87, pp. 69 – 85, 2016.

[111] J. Cheng, A. Shahba, and S. Ghosh, "Stabilized tetrahedral elements for crystal plasticity finite element analysis overcoming volumetric locking," *Computational Mechanics*, vol. 57, no. 5, pp. 733–753, 2016.

[112] O. Zienkiewicz and R. Taylor, *The Finite Element Method for Solid and Structural Mechanics*. Elsevier Science, 2013.

[113] T. Hughes, *The finite element method: linear Static and dynamic finite element analysis*. Prentice-Hall, Inc, 1987.

[114] J. Marsden and T. Hughes, *Mathematical Foundations of Elasticity*, ser. Dover Civil and Mechanical Engineering Series. Dover, 1994.

[115] H. C. and W. K., "Thermodynamically consistent algorithms for a finite-deformation phase-field approach to fracture," *International Journal for Numerical Methods in Engineering*, vol. 99, no. 12, pp. 906–924, 2014.

[116] K. Weinberg and C. Hesch, "A high-order finite deformation phase-field approach to fracture," *Continuum Mechanics and Thermodynamics*, vol. 29, no. 4, pp. 935–945, 2017.

[117] M. Frémond and B. Nedjar, "Damage, gradient of damage and principle of virtual power," *International Journal of Solids and Structures*, vol. 33, no. 8, pp. 1083 – 1103, 1996.

[118] K. Pham, H. Amor, J.-J. Marigo, and C. Maurini, "Gradient damage models and their use to approximate brittle fracture," *International Journal of Damage Mechanics*, vol. 20, no. 4, pp. 618–652, 2011.

[119] J. L. Chaboche, "Development of continuum damage mechanics for elastic solids sustaining anisotropic and unilateral damage," *International Journal of Damage Mechanics*, vol. 2, no. 4, pp. 311–329, 1993.

[120] J. Clayton and J. Knap, "Phase field modeling of directional fracture in

anisotropic polycrystals," *Computational Materials Science*, vol. 98, pp. 158 – 169, 2015.

[121] G. Ravichandran, A. J. Rosakis, J. Hodowany, and P. Rosakis, "On the conversion of plastic work into heat during high-strain-rate deformation," in *Shock Compression of Condensed Matter*, ser. American Institute of Physics Conference Series, vol. 620, 2002, pp. 557–562.

[122] T. Wick, "Modified newton methods for solving fully monolithic phase-field quasi-static brittle fracture propagation," *Computer Methods in Applied Mechanics and Engineering*, vol. 325, pp. 577 – 611, 2017.

[123] X. Ling, M. F. Horstemeyer, and G. P. Potirniche, "On the numerical implementation of 3d rate-dependent single crystal plasticity formulations," *Int. J. Numer. Meth. Eng.*, vol. 63, no. 4, pp. 548–568, 2005.

[124] G. Weber and L. Anand, "Finite deformation constitutive equations and a time integrated procedure for isotropic hyperelastic—viscoplastic solids," *Comput. Methods Appl. Mech. Eng.*, vol. 79, no. 2, pp. 173–202, 1990.

[125] S. Kalidindi, C. Bronkhorst, and L. Anand, "Crystallographic texture evolution in bulk deformation processing of fcc metals," *Journal of the Mechanics and Physics of Solids*, vol. 40, no. 3, pp. 537 – 569, 1992.

[126] A. M. Maniatty, P. R. Dawson, and Y. S. Lee, "A time integration algorithm

for elasto-viscoplastic cubic crystals applied to modelling polycrystalline deformation," *International Journal for Numerical Methods in Engineering*, vol. 35, no. 8, pp. 1565–1588, 1992.

[127] S. W. Sloan, "Substepping schemes for the numerical integration of elastoplastic stress–strain relations," *International Journal for Numerical Methods in Engineering*, vol. 24, no. 5, pp. 893–911, 1987.

[128] J. Bonnans, J. Gilbert, C. Lemaréchal, and C. Sagastizábal, *Numerical Optimization: theoretical and practical aspects*. Springer, 2003.

[129] F. Erdogan and G. C. Sih, "On the crack extension in plates under plane loading and transverse shear," *Journal of Basic Engineering*, vol. 85, no. 4, pp. 519–527, 1963.

[130] X. Zhang, C. Vignes, S. W. Sloan, and D. Sheng, "Numerical evaluation of the phase-field model for brittle fracture with emphasis on the length scale," *Computational Mechanics*, vol. 59, no. 5, pp. 737–752, 2017.

[131] M. Ambati, T. Gerasimov, and L. De Lorenzis, "Phase-field modeling of ductile fracture," *Computational Mechanics*, vol. 55, no. 5, pp. 1017–1040, 2015.

[132] J. E. Bozek, J. D. Hochhalter, M. G. Veilleux, M. Liu, G. Heber, S. D. Sintay, A. D. Rollett, D. J. Littlewood, A. M. Maniatty, H. Weiland, R. J. C. Jr, J. Payne, G. Welsh, D. G. Harlow, P. A. Wawrzynek, and A. R. Ingraf-

fea, "A geometric approach to modeling microstructurally small fatigue crack formation: I. probabilistic simulation of constituent particle cracking in aa 7075-t651," *Modelling and Simulation in Materials Science and Engineering*, vol. 16, no. 6, p. 065007, 2008.

[133] J. Jordon, M. Horstemeyer, K. Solanki, J. Bernard, J. Berry, and T. Williams, "Damage characterization and modeling of a 7075-t651 aluminum plate," *Materials Science and Engineering: A*, vol. 527, no. 1, pp. 169 – 178, 2009.

[134] J. D. Hochhalter, D. J. Littlewood, R. J. C. Jr, M. G. Veilleux, J. E. Bozek, A. R. Ingraffea, and A. M. Maniatty, "A geometric approach to modeling microstructurally small fatigue crack formation: Ii. physically based modeling of microstructure-dependent slip localization and actuation of the crack nucleation mechanism in aa 7075-t651," *Modelling and Simulation in Materials Science and Engineering*, vol. 18, no. 4, p. 045004, 2010.

[135] J. Jordon, M. Horstemeyer, K. Solanki, and Y. Xue, "Damage and stress state influence on the bauschinger effect in aluminum alloys," *Mechanics of Materials*, vol. 39, no. 10, pp. 920 – 931, 2007.

[136] H. Ming-Yuan and J. W. Hutchinson, "Crack deflection at an interface between dissimilar elastic materials," *International Journal of Solids and Structures*, vol. 25, no. 9, pp. 1053 – 1067, 1989.

[137] J. D. Clayton and J. Knap, "A geometrically nonlinear phase field theory of

brittle fracture," *International Journal of Fracture*, vol. 189, no. 2, pp. 139–148, 2014.

[138] G. R. Weber and S. Ghosh, "Thermo-mechanical deformation evolution in polycrystalline ni-based superalloys by a hierarchical crystal plasticity model," *Materials at High Temperatures*, vol. 33, no. 4-5, pp. 401–411, 2016.

[139] A. Shahba and S. Ghosh, "Crystal plasticity fe modeling of ti alloys for a range of strain-rates. part i: A unified constitutive model and flow rule," *International Journal of Plasticity*, vol. 87, pp. 48 – 68, 2016.

[140] J. Montgomery, M. Wells, B. Roopchand, and J. Ogilvy, "Low-cost titanium armors for combat vehicles," *JOM*, vol. 49, no. 5, pp. 45–47, 1997.

[141] P. Follansbee and G. Gray, "An analysis of the low temperature, low and high strain-rate deformation of Ti-6Al-4V," *Metall. Trans. A*, vol. 20, pp. 863 – 874, 1989.

[142] D. Chichili, K. Ramesh, and K. Hemker, "The high-strain-rate response of alpha-titanium: experiments, deformation mechanisms and modeling," *Acta Mater.*, vol. 46, no. 3, pp. 1025 – 1043, 1998.

[143] A. Khan, Y. Suh, and R. Kazmi, "Quasi-static and dynamic loading responses and constitutive modeling of titanium alloys," *Int. J. Plasticity*, vol. 20, no. 12, pp. 2233 – 2248, 2004.

[144] A. Khan, R. Kazmi, and B. Farrokh, "Multiaxial and non-proportional loading responses, anisotropy and modeling of Ti–6Al–4V titanium alloy over wide ranges of strain rates and temperatures," *Int. J. Plasticity*, vol. 23, no. 6, pp. 931 – 950, 2007.

[145] A. Khan and S. Yu, "Deformation induced anisotropic responses of Ti–6Al–4V alloy. part i: Experiments," *Int. J. Plasticity*, vol. 38, pp. 1 – 13, 2012.

[146] V. Sinha, M. Mills, and J. Williams, "Determination of crystallographic orientation of dwell-fatigue fracture facets in Ti-6242 alloy," *J. Mater. Sci.*, vol. 42, no. 19, pp. 8334–8341, 2007.

[147] A. Pilchak, "Fatigue crack growth rates in alpha titanium: Faceted vs. striation growth," *Scripta Mater.*, vol. 68, no. 5, pp. 277 – 280, 2013.

[148] V. Hasija, S. Ghosh, M. J. Mills, and D. S. Joseph, "Deformation and creep modeling in polycrystalline Ti–6Al alloys," *Acta Mater.*, vol. 51, pp. 4533–4549, 2003.

[149] D. Deka, D. S. Joseph, S. Ghosh, and M. J. Mills, "Crystal plasticity modeling of deformation and creep in polycrystalline Ti-6242," *Metall. Trans. A*, vol. 37A(5), pp. 1371–1388, 2006.

[150] H. Li, D. Mason, T. Bieler, C. Boehlert, and M. Crimp, "Methodology for

estimating the critical resolved shear stress ratios of α-phase ti using ebsd-based trace analysis," *Acta Mater.*, vol. 61, no. 20, pp. 7555 – 7567, 2013.

[151] G. Venkataramani, K. Kirane, and S. Ghosh, "Microstructural parameters affecting creep induced load shedding in Ti-6242 by a size dependent crystal plasticity FE model," *Int. J. Plasticity*, vol. 24, pp. 428–454, 2008.

[152] M. Anahid, M. Samal, and S. Ghosh, "Dwell fatigue crack nucleation model based on crystal plasticity finite element simulations of polycrystalline titanium alloys," *J. Mech. Phys. Solids*, vol. 59, no. 10, pp. 2157 – 2176, 2011.

[153] S. Schoenfeld and B. Kad, "Texture effects on shear response in ti–6al–4v plates," *Int. J. Plasticity*, vol. 18, pp. 461–486, 2002.

[154] A. Alankar, P. Eisenlohr, and D. Raabe, "A dislocation density-based crystal plasticity constitutive model for prismatic slip in α-titanium," *Acta Mater.*, vol. 59, no. 18, pp. 7003 – 7009, 2011.

[155] F. Dunne, D. Rugg, and A. Walker, "Length scale-dependent, elastically anisotropic, physically-based hcp crystal plasticity: Application to cold-dwell fatigue in Ti alloys," *Int. J. Plasticity*, vol. 23, no. 6, pp. 1061 – 1083, 2007.

[156] S. Balasubramanian and L. Anand, "Plasticity of initially textured hexagonal polycrystals at high homologous temperatures: application to titanium," *Acta Mater.*, vol. 50, no. 1, pp. 133–148, 2002.

[157] T. Neeraj and M. Mills, "Short-range order (SRO) and its effect on the primary creep behavior of a Ti–6wt. % Al alloy," *Mater. Sci. Eng. A*, vol. 319–321, pp. 415 – 419, 2001.

[158] B. Morrow, R. Lebensohn, C. Trujillo, D. Martinez, F. Addessio, C. Bronkhorst, T. Lookman, and E. Cerreta, "Characterization and modeling of mechanical behavior of single crystal titanium deformed by split-hopkinson pressure bar," *Int. J. Plasticity*, vol. 82, pp. 225 – 240, 2016.

[159] N. Paton, R. Baggerly, and J. Williams, "Deformation and solid solution strengthening of titanium-aluminum single crystals," Rockwell Int. Report, Tech. Rep., 1976.

[160] J. Williams, R. Baggerly, and N. Paton, "Deformation behavior of HCP Ti-Al alloy single crystals," *Metall. Mater. Trans. A*, vol. 33, p. 837 – 850, 2002.

[161] B. Lee, K. Vecchio, S. Ahzi, and S. Schoenfeld, "Modeling the mechanical behavior of tantalum," *Metal. Mater. Trans. A*, vol. 28, no. 1, pp. 113–122, 1997.

[162] Y. Nie and Y. Xie, "*Ab initio* thermodynamics of the hcp metals Mg, Ti, and Zr," *Phys. Rev. B*, vol. 75, p. 174117, 2007.

[163] P. Souvatzis, O. Eriksson, and M. I. Katsnelson, "Anomalous thermal expansion in α-titanium," *Phys. Rev. Lett.*, vol. 99, p. 015901, 2007.

[164] V. Nizhankovskii, M. Katsnelson, G. Peschanskikh, and A. Trefilov,

"Anisotropy of the thermal-expansion of titanium due to proximity to an electronic topological transition," *JETP Lett.*, vol. 59, pp. 733–737, 1994.

[165] M. Brandes, "Creep, fatigue, and deformation of alpha and alpha-beta titanium alloys at ambient temperature," Ph.D. dissertation, Materials science and engineering, Ohio State University,USA, 2008.

[166] P. Guyot and J. Dorn, "a critical review of the Peierls mechanism," *Canadian J. Physics*, vol. 45, no. 2, pp. 983–1016, 1967.

[167] M. Tang, L. Kubin, and G. Canova, "Dislocation mobility and the mechanical response of b.c.c. single crystals: A mesoscopic approach," *Acta Mater.*, vol. 46, no. 9, pp. 3221 – 3235, 1998.

[168] A. Akhtar and E. Teghtsoonian, "Prismatic slip in α-titanium single crystals," *Metall. Mater. Trans. A*, vol. 6, pp. 2201–2208, 1975.

[169] T. Tanaka and H. Conrad, "Deformation kinetics for $10\bar{1}0 < 11\bar{2}0 >$ slip in titanium single crystals below $0.4t_m$," *Acta Metal.*, vol. 20, no. 8, pp. 1019 – 1029, 1972.

[170] D. Casem, "Unpublished work," U.S. Army Research Laboratory, Aberdeen Proving Ground, MD, 2015.

[171] B. Hansen, I. Beyerlein, C. Bronkhorst, E. Cerreta, and D. Dennis-Koller, "A

dislocation-based multi-rate single crystal plasticity model," *Int. J. Plasticity*, vol. 44, pp. 129 – 146, 2013.

[172] U. Essmann and H. Mughrabi, "Annihilation of dislocations during tensile and cyclic deformation and limits of dislocation densities," *Phil. Mag. A*, vol. 40, no. 6, pp. 731–756, 1979.

[173] H. Mecking and U. Kocks, "Kinetics of flow and strain-hardening," *Acta Metal.*, vol. 29, no. 11, pp. 1865 – 1875, 1981.

[174] Military Handbook, *Metallic Materials and Elements for Aerospace Vehicle Structures*. Wright Lab., Wright-Patterson AFB, OH. Materials Directorate, 1998.

[175] J. Clayton, *Nonlinear Mechanics of Crystals*. Springer Verlag, 2010.

[176] A. Pilchak, "Unpublished Report," Air Force Research Laboratories, Wright Patterson Air Force Base, Dayton, OH, 2015.

[177] S. Ghosh, Y. Bhandari, and M. Groeber, "CAD-based reconstruction of 3D polycrystalline alloy microstructures from FIB generated serial sections," *Computer-Aided Design*, vol. 40, no. 3, pp. 293 – 310, 2008.

[178] Y. Bhandari, S. Sarkar, M. Groeber, M. Uchic, D. Dimiduk, and S. Ghosh, "3D polycrystalline microstructure reconstruction from FIB generated serial sections for FE analysis," *Comput. Mater. Sci.*, vol. 41, no. 2, pp. 222 – 235, 2007.

[179] M. Groeber, S. Ghosh, M. Uchic, and D. Dimiduk, "Development of a robust 3d characterization-representation framework for modeling polycrystalline materials," *JOM J. Miner., Met. Materials Soc.*, vol. 59, no. 9, pp. 32–36, 2007.

[180] D. Rowenhorst and P. Voorhees, "Measurements of the grain boundary energy and anisotropy in tin," *Metall. Mater. Trans. A*, vol. 36A, pp. 2127–2135, 2005.

[181] E. Lauridsen, S. Schmidt, S. Nielsen, L. Margulies, H. Poulsen, and D. Jensen, "Non-destructive characterization of recrystallization kinetics using three-dimensional x-ray diffraction microscopy," *Scripta Mater.*, vol. 55, no. 1, pp. 51–56, 2006.

[182] J. Russ and R. Dehoff, *Practical streology, 2nd edition.* Plenum press, 1999.

[183] A. Mood, F. Graybill, and D. Boes, *Introduction to the Theory of Statistics, 3rd edition.* McGraw-Hill, 1974.

[184] M. Groeber, S. Ghosh, M. Uchic, and D. Dimiduk, "A framework for automated analysis and simulation of 3D polycrystalline microstructures. part 2: Synthetic structure generation," *Acta Mater.*, vol. 56, no. 6, p. 1274–1287, 2008.

[185] E. Massey, "The kolmogorov-smirnov test for goodness of fit," *J. Amer. Statis. Assoc.*, vol. 46, no. 253, pp. 68–78, 1951.

[186] O. Diard, S. Leclercq, G. Rousselier, and G. Cailletaud, "Evaluation of finite element based analysis of 3d multicrystalline aggregates plasticity: Application

to crystal plasticity model identification and the study of stress and strain fields near grain boundaries," *Int. J. Plasticity*, vol. 21, no. 4, pp. 691 – 722, 2005.

[187] B. Hopkinson, "A method of measuring the pressure produced in the detonation of high explosives or by the impact of bullets," *Phil. Trans. R. Soc London*, vol. A213, pp. 437–456, 1914.

[188] ——, "An investigation of the mechanical properties of materials at very high rates of loading," *Phil. Trans. R. Soc London*, vol. B62, pp. 676–700, 1949.

[189] E. Huskins, B. Cao, and K. Ramesh, "Strengthening mechanisms in an Al–Mg alloy," *Mater. Sci. Eng. A*, vol. 527, no. 6, pp. 1292 – 1298, 2010.

[190] W. Chen and B. Song, *Split Hopkinson (Kolsky) Bar: Design, Testing and Applications*. Boston, MA: Springer Science+Business Media, LLC, 2011.

[191] M. Ashby, "The deformation of plastically non-homogeneous materials," *Phil. Magazine*, vol. 21, no. 170, pp. 399–424, 1970.

[192] P. Follansbee, G. Regazzoni, and U. Kocks, *Mechanical Properties at High Rates of Strain, Proceedings of the Third Conference on the Mechanical Properties of Materials at High Rates of Strain Held in Oxford, 9-12 April 1984*, ser. Conference series. Inst. of Physics, 1984.

[193] M. Meyers, F. Gregori, B. Kad, M. Schneider, D. Kalantar, B. Remington, G. Ravichandran, T. Boehly, and J. Wark, "Laser-induced shock compression

of monocrystalline copper: characterization and analysis," *Acta Mater.*, vol. 51, no. 5, pp. 1211 – 1228, 2003.

[194] L. Capolungo, D. Spearot, M. Cherkaoui, D. McDowell, J. Qu, and K. Jacob, "Dislocation nucleation from bicrystal interfaces and grain boundary ledges: Relationship to nanocrystalline deformation," *J. Mech. Phys. Solids*, vol. 55, no. 11, pp. 2300 – 2327, 2007.

[195] S. Osovski, D. Rittel, and A. Venkert, "The respective influence of microstructural and thermal softening on adiabatic shear localization," *Mech. Mater.*, vol. 56, pp. 11 – 22, 2013.

[196] R. Culver, *Thermal instability strain in dynamic plastic deformation*, ser. Metallurgical efects at high strain rates. Plenum press, 1973.

[197] S. Medyanik, W. Liu, and S. Li, "On criteria for dynamic adiabatic shear band propagation," *J. Mech. Phys. Solids*, vol. 55, no. 7, pp. 1439 – 1461, 2007.

[198] D. Rittel, Z. G. Wang, and M. Merzer, "Adiabatic shear failure and dynamic stored energy of cold work," *Phys. Rev. Lett.*, vol. 96, p. 075502, 2006.

[199] M. Ambati, R. Kruse, and L. De Lorenzis, "A phase-field model for ductile fracture at finite strains and its experimental verification," *Computational Mechanics*, vol. 57, no. 1, pp. 149–167, 2016.

[200] J. M. Sargado, E. Keilegavlen, I. Berre, and J. M. Nordbotten, "High-accuracy

phase-field models for brittle fracture based on a new family of degradation functions," *Journal of the Mechanics and Physics of Solids*, vol. 111, pp. 458 – 489, 2018.

Vita

Ahmad Shahba received a Bachelor of Science in Civil Engineering from University of Tehran in 2011. He was an undergraduate research assistant in Centre of Numerical Methods in Engineering where he worked on developing novel numerical and analytical methods to study stability, static and dynamic response of structural members with non-uniform cross-section. He subsequently started graduate school under advising of Professor Somnath Ghosh at Johns Hopkins University in 2012. Ahmad received a Master of Science in Mechanical Engineering in 2016. His PhD research focused on improving and developing different aspects of crystal plasticity finite element simulation of deformation and fracture in polycrystalline microstructures.